

Developing Novel Functional Laser- Induced Carbon Nanofibers for Miniaturized Electroanalytical Biosensors



Dissertation zur Erlangung des
Doktorgrades der Naturwissenschaften

(Dr. rer. nat.)

an der Fakultät Chemie und Pharmazie

der Universität Regensburg

Deutschland

Vorgelegt von

Christoph Bruckschlegel

aus Leonberg

im Jahr 2024

Die vorliegende Dissertation entstand in der Zeit von Dezember 2021 bis November 2024 am Institut für Analytische Chemie, Chemo- und Biosensorik der Universität Regensburg.

Die Arbeit wurde angeleitet von Prof. Dr. Antje J. Bäumner und Dr. Nongnoot Wongkaew.

Promotionsgesuch eingereicht am: 27.11.2024

Kolloquiumstermin: 28.03.2025

Prüfungsausschuss

Vorsitzender: Prof. Dr. Werner Kunz

Erstgutachterin: Prof. Dr. Antje J. Bäumner

Zweitgutachter: Dr. Pierre Bauduin

Drittprüfer: Apl. Prof. Dr. Rainer Müller

Acknowledgements

To begin with, I would like to thank **Prof. Dr. Antje J. Bäumner**, who offered me the opportunity to join her working group, even though she did not know me personally before I started. This decision enabled me to work on a topic I loved with the best colleagues I could have imagined. I want to thank you for your support whenever I needed it, starting from your help at the beginning of my thesis, which enabled the cooperation with the ICSM during my PhD thesis, and did not even stop when I was searching for a job in the chemical industry. I always enjoyed your motivating scientific curiosity in every seminar.

I wish to express my warmest and sincere thanks to **Dr. Pierre Bauduin**, who left a significant impact on me both scientifically and personally. From you, I learned to always be open to new topics and to eagerly solve even the hardest questions. Thank you for supervising me from my master's thesis through to the end of my PhD thesis! Beyond science, I would like to thank you for always extending a warm welcome to me whenever I visited the ICSM, making southern France a second home for me. Furthermore, I would like to thank you for your willingness to be my second reviewer.

Additionally, I thank **Apl. Prof. Dr. Rainer Müller** for all the lectures and lab courses on physical chemistry, which had a huge impact on my scientific work, and for your willingness to be my third reviewer.

I also want to thank **Prof. Dr. Werner Kunz** for making the COSOM master program possible, which was the best master program I could have imagined, and for being the chairman in my doctoral examination.

Furthermore, I am deeply thankful to **Dr. Nongnoot Wongkaew** for being my supervisor. I would like to thank you for your patience and for always having an open ear for me. I really enjoyed working with you, and I think we made a great team. Your positive mindset motivated me and helped me to never give up, which was invaluable both professionally and personally. You significantly contributed to my scientific and personal development.

Furthermore, I would like to thank all of my **colleagues** for creating a perfect lab atmosphere and making my time at the university very pleasant. I am thankful to all **members of the Nanofiber Club** for the very enjoyable meetings. I want to thank the **members of the 4th floor** for the very amusing lunch breaks and the overall atmosphere. A special thank you goes to **Alissa Wieberneit** for being a perfect lab mate from the beginning to the end. You gave me advice and helped me whenever needed. I am also sure that your supply of the coffee machine really saved my life ^^. Another special thank you goes to

Antonia Perju, who really helped me get into the topic of my thesis by sharing a lot of her knowledge with me. I would also like to thank **Vivien Fleischmann** for being the best master student I could have imagined supervising. Even though MIPs made us desperate, your way of not letting it get you down, your humor, and your personality always made me enjoy working with you. I am also thankful to **Barbara Grotz, Sarah Dietrich, Katharina Weiß, Michaela Ziebegk, and Selene Fiori** for creating a perfect lab and office atmosphere and for being great colleagues. Another thank you goes to the not yet mentioned members of the Demo-group, **Prof. Dr. Axel Dürkop, Florian Weinzierl, and Michael Lößl**, for making the long Friday afternoons very enjoyable. I would also like to thank **Dr. Olivier Diat, Prof. Dr. Luc Girard and Dr. Coralie Pasquier** for always extending a warm welcome and for their help during my stays at the ICSM.

Finally, I want to thank my parents, **Anita** and **Konrad**, my brother, **Stefan**, my sister-in-law, **Tina**, and my nephew and niece, **Jonas** and **Lena**, for their constant love and support.

Declaration of Collaborations

This work was conducted in large degrees of experimental and theoretical work solely by the author. However, at some points collaborations with other researchers were conducted to generate results, which is stated in this chapter in accordance with §8 Abs. 1 Satz 2 Ziff. 7 of the “Ordnung zum Erwerb des akademischen Grades eines Doktors der Naturwissenschaften (Dr. rer. nat.) an der Universität Regensburg vom 18. Juni 2009“.

Non-enzymatic electrochemical sensors for point-of-care testing: Current status, challenges, and future prospects (Chapter 1)

Parts of this chapter will be further used as a manuscript that is intended to be submitted to *Talanta* as a critical review article. The author and Dr. Nongnoot Wongkaew contributed equally to literature search and manuscript preparation.

Investigating nanocatalyst-embedding laser-induced carbon nanofibers for non-enzymatic electrochemical sensing of hydrogen peroxide (Chapter 3)

This chapter has been published. The author and Dr. Nongnoot Wongkaew contributed equally to design of the experiments. The author conducted the experiments and evaluated the data. Dr. Marc Schlosser conducted SEM-EDX measurements shown in Figure 3.2. The author and Dr. Nongnoot Wongkaew equally contributed to the manuscript draft. Dr. Nongnoot Wongkaew led the project administration.

Laser generated Pt/Ni nanocatalysts-carbon nanofibers enabling ratiometric enzyme-free glucose detection at physiological pH (Chapter 4)

This chapter has been submitted as an original research article in *Sensors and Actuators B*. The author contributed to the conceptualization, design of the study, experimental investigation, data acquisition, interpretation of the data, and writing original draft. Vivien Fleischmann supported the experimental investigation. Dr. Aladin Ullrich conducted the TEM-EDX measurements and contributed to Figure 4.2 and its interpretation. Prof. Luc Girard supported us with XPS measurements, interpretation of the data and reviewing. Dr. Pierre Bauduin contributed with project administration, funding acquisition, supervision, writing – review & editing, Prof. Antje Bäumner contributed with project administration, funding acquisition, reviewing and supervision. Dr. Nongnoot Wongkaew led the conceptualization, project administration, funding acquisition, supervision, and writing of the original draft.

Laser-induced Carbon Nanofibers as Permeable Non-enzymatic sensor for Biomarker Detection in Breath Aerosol (Chapter 5)

This chapter will be further used as a manuscript that is intended to be submitted to Analytical Chemistry as a technical note article. The author and Selene Fiori contributed equally to conceptualization, design of the study, experimental investigation, data acquisition, interpretation of the data, and writing original draft. Katharina Weiß, Keyu Su, and Michael Födlmeier helped during initial experimental investigations. Prof. Flavio Della Pelle, Dr. Annalisa Scroccarello, and Prof. Dario Compagnone revised the original draft and contributed to funding acquisition and supervision. Prof. Antje J. Bäumner contributed to project administration and supervision. Dr. Nongnoot Wongkaew lead conceptualization, project administration, funding acquisition, supervision, and writing of the original draft.

Table of Contents

Acknowledgements	II
Declaration of Collaborations	IV
Table of Contents.....	VI
List of used Symbols and Abbreviations.....	X
List of Figures	XII
List of Tables	XIX
1. Non-enzymatic electrochemical sensors for point-of-care testing: Current status, challenges, and future prospects	1
1.1 Abstract.....	1
1.2 Author distribution	1
1.3 Introduction	1
1.4 Definition, principle, and mechanism	6
1.5 Fabrication of non-enzymatic electrodes.....	7
1.5.1 Conventional strategy	7
1.5.2 Laser-induced functional hybrid electrodes as emerging technology.....	13
1.6 Effects of matrices on sensing performance.....	17
1.6.1 Clinical sample	17
1.6.2 Non-clinical sample.....	21
1.7 Other challenges and promising studies	26
1.7.1 Anti-fouling	26
1.7.2 Measurements performed under physiological conditions	26
1.7.3 Biocompatibility	27
1.7.4 Long-term stability and storage conditions	28
1.7.5 Mobility and placement.....	28
1.7.6 Efficiency, cost, and simplicity.....	29
1.7.7 Practical considerations	29
1.8 Conclusion and outlook.....	31

2. Motivation and Structure of the Thesis	33
3. Investigating nanocatalyst-embedding laser-induced carbon nanofibers for non-enzymatic electrochemical sensing of hydrogen peroxide	36
3.1 Abstract.....	36
3.2 Author contributions.....	36
3.3 Graphical abstract.....	37
3.4 Introduction	37
3.5 Materials and methods.....	39
3.5.1 Preparation of LCNF	39
3.5.2 Morphology characterization.....	39
3.5.3 Electrochemical characterization.....	40
3.6 Results and discussion.....	41
3.6.1 Characterization of nanocatalyst embedding LCNFs	41
3.6.2 Electrochemical characterization towards H ₂ O ₂	43
3.6.3 Influence of various Pt and Ni content on analytical performance	45
3.6.4 Investigating strategies for suppressing signals from UA, AA, and DA	49
3.7 Conclusions	52
3.8 Supporting information	53
3.8.1 Optimized conditions for preparing LCNFs-embedded with nanocatalysts at various metal compositions.....	53
3.8.2 Morphological characterization of LCNFs by SEM.....	54
3.8.3 Determining electroactive surface area	55
3.8.4 The linear range of 100% Pt-LCNF	56
3.8.5 Evaluating impact of Pt at various mol-%.....	57
3.8.6 Effect of anionic polymer coating on minimizing signal interference from ascorbic acid (AA)	58
3.9 Additional studies towards H ₂ O ₂ detection – lower measurement potential	59
3.9.1 Motivation and strategy	59
3.9.2 Experimental	59
3.9.3 Results and discussion.....	60

3.9.4 Conclusions	63
3.10 Additional studies towards H ₂ O ₂ detection – Polyoxometalates as catalysts	64
3.10.1 Motivation and strategy	64
3.10.2 Experimental	65
3.10.3 Results and discussion.....	67
3.10.4 Conclusions	78
4. Laser generated Pt/Ni nanocatalysts-carbon nanofibers enabling ratiometric enzyme-free glucose detection at physiological pH	79
4.1 Abstract.....	79
4.2 Author contribution	79
4.3 Graphical abstract.....	80
4.4 Introduction	80
4.5 Materials and methods.....	83
4.5.1 Fabrication of laser-induced carbon nanofibers	83
4.5.2 Characterization methods	83
4.5.3 Electrochemical measurements	84
4.6 Results and discussion.....	86
4.6.1 Structural and composition analysis	86
4.6.2 Pt/Ni-LCNFs for glucose detection – single measurement per electrode.....	91
4.6.4 Selectivity study	97
4.6.5 Recovery study	98
4.7 Conclusions	101
4.8 Supporting information	102
4.8.1 Price per electrode	102
4.8.2 Characterization of surface chemistry focusing on carbon and oxygen	103
4.8.3 Characterization of surface chemistry focusing on Pt and Ni	104
4.8.4 Small Angle X-ray Scattering (SAXS) analysis	105
4.8.5 Electrocatalytic oxidation of glucose at various pHs and metal compositions.....	106
4.8.6 Optimization of pretreatment conditions for electrocatalytic oxidation of glucose present in physiological pH.....	107

4.8.7 Effect of electrode ageing.....	108
4.8.8 Effect of sterilizations.....	108
4.8.9 Reusability of electrodes	109
4.8.10 Measurement in undiluted and diluted human serum.....	109
5. Laser-induced Carbon Nanofibers as Permeable Non-enzymatic sensor for Biomarker Detection in Breath Aerosol.....	111
5.1 Abstract.....	111
5.2 Author distribution	111
5.3 Graphical abstract.....	112
5.4 Introduction	112
5.5 Materials and methods.....	114
5.5.1 Chemicals and materials.....	114
5.5.2 Apparatus.....	114
5.5.3 Sensor manufacturing.....	115
5.5.4 Measurement setup.....	116
5.5.5 Morphological characterization.....	116
5.6 Results and discussion.....	117
5.6.1 Sensor fabrication.....	117
5.6.2 Measuring glucose by direct detection mode	117
5.6.3 Optimization of sensor production	119
5.6.4 Sensor electroanalytical performance.....	119
5.6.5 Capturing and measurement of aerosolized glucose	120
5.7 Conclusions	123
5.8 Supporting information	124
6. Conclusion and Future Perspectives.....	127
7. Summary	132
8. Zusammenfassung	134
9. References	136
Curriculum Vitae	160
Eidesstattliche Erklärung.....	162

List of used Symbols and Abbreviations

In the following, all used symbols and abbreviations, besides common abbreviations, are explained.

Abbreviation/Symbol	Meaning
A	Ampere
AA	Ascorbic acid
bidest	Double-distilled
c(x)	Concentration of x
CA	Chronoamperometry
CV	Cyclovoltammetry
DA	Dopamine
EC	Electrochemical
ESA	Effective surface area. The active surface of an electrode which takes part in an electrochemical reaction.
Fe-LCNFs	Laser-induced carbon nanofibers which contain Fe-nanoparticles
Glu	Glucose
HRP	Horseradish peroxidase
HR-TEM	High resolution Transmission electron microscopy
I	Current in ampere
ICP-MS	Inductively coupled plasma mass spectrometry
ITO-PET	Polyethylene terephthalate coated with a layer of indium-tin-oxide to make it conductive.
kWh	Kilowatt-hour
LCNFs	Laser-induced carbon nanofibers
LIG	Laser-induced graphene
LIG-LCNFs	Laser-induced carbon nanofibers that do not contain any metals. For a better laser scribing, laser induced graphene was added to the spinning solution.
LOD	Limit of detection ($= 3 \cdot \text{Std(blank)} / \text{slope}$)
LOQ	Limit of quantification
LP	Laser power
MWCNT	Multi-walled carbon nanotube
NF	Nanofibers

Ni-LCNFs	Laser-induced carbon nanofibers which contain Ni-nanoparticles
OPP	Organophosphorus pesticides
PBS	Phosphate buffered solution
PEG	Polyethylen glycol
Pegylation	Coating a surface with polyethylen glycol
PET	Polyethylene terephthalate
pH	-lg(c(H ₃ O ⁺))
PI	Polyimide
POC	Point of care. Medical diagnostic testing that is at or near the place of the patient with a small waiting time.
POM	Polyoxometalate
Pot. (vs. Ag/AgCl)	Potential versus an Ag/AgCl (3 M KCl) reference electrode in Volt.
Pt-LCNFs	Laser-induced carbon nanofibers which contain Pt-nanoparticles
Pt-Ni-LCNFs	Laser-induced carbon nanofibers which contain Pt-Ni-alloyed nanoparticles
R2R	Roll-to-roll
SAXS	Small Angle X-ray scattering
SEM	Scanning electron microscope
SEM EDX	Scanning electron microscope coupled with energy-dispersive X-ray spectroscopy
SiMo	H ₄ SiMo ₁₂ O ₄₀
Std	Standard deviation
TEM	Transmission electron microscopy
TEM-EDX	Transmission electron microscopy coupled with energy-dispersive X ray spectroscopy
UA	Uric acid
V	Volt
w/	With
w/o	Without
w%	Weight-percent
XPS	X-ray photoelectron spectroscopy
XRD	X-ray diffraction
μ-	Micro-

List of Figures

Figure 1. 1: The growth of research published in the past 11 years when searching with the terms “non-enzymatic electrochemical sensors”, “enzyme-free electrochemical sensors”, and “enzymeless electrochemical sensors” combined with the specific analyte (blank columns), and representation of the search with the same keywords but with enzyme-based strategies instead (patterned columns). Web of Science searched on July 2nd, 2024.....	4
Figure 1. 2: Structure of this review.	5
Figure 1. 3: Setup of Roll to Roll (R2R) gravure printing and Flexography.....	12
Figure 1. 4: Examples for coating catalyst precursor on carbonizable substrate by (i) attaching a metal leave on polyimide (PI) substrate, (ii) spin coating a PI substrate with an ethyl cellulose + metal salt solution, and (iii) by knife coating a PAA + metal salt solution onto a PI substrate.	14
Figure 1. 5: Examples for blending catalyst precursor with carbonizable substrate by (i) distributing polymer-metal salt solution on a surface, drying, and a consecutive heat treatment, (ii) electrospinning a polymer-metal salt solution, and (iii) by preparing a graphene oxide (GO)-metal salt solution and consecutive filtration.	15
Figure 3. 1: Graphical abstract of chapter 3.	37
Figure 3. 2: (A) Elemental mapping of Ni and Pt for a (50% Pt + 50% Ni)-LCNFs by SEM-EDX. (B) EDX spectra of various LCNF hybrids focused on Ni and Pt for an area with the size of the SEM image shown in (A), i.e., of around 520 $\mu\text{m} \times 350 \mu\text{m}$	42
Figure 3. 3: Cyclic voltammograms of LCNFs with various metal compositions where A to E are from (100% Ni)-LCNFs, (75% Ni + 25% Pt)-LCNFs, (50% Ni + 50% Pt)-LCNFs, (25% Ni + 75% Pt)-LCNFs, and (100% Pt)-LCNFs, respectively, (mol-% are given). (F) LCNFs without metal. The characterizations were performed in PBS (pH = 7.4) with and without 10 mM H_2O_2 (n=3). The potential (Pot.) is given against Ag/AgCl reference electrode. Scan rate of 50 mV/s was used.	44
Figure 3. 4: Analytical performance of various LCNFs hybrid electrodes. (A) Calibration curves of the various metal LCNFs for the detection of H_2O_2 obtained by non-stirred chronoamperometry at +0.5 V (n \geq 6). (B) Limit of detection for LCNFs with various Pt-ratios.	46
Figure 3. 5: Impact of Pt on the normalized sensitivities shown in Figure 3A of various Pt/Ni-LCNF hybrids.	48
Figure 3. 6: Selectivity of LCNFs with various metal compositions (A: 100% Ni, B: 75% Ni + 25% Pt, C: 50% Ni + 50% Pt, D: 25% Ni + 75% Pt, E: 100% Pt, F: no metal) in PBS solution (pH = 7.4) towards H_2O_2 , ascorbic acid (AA), uric acid (UA), dopamine (DA) and glucos e (Glu) (n=3). The diagrams show the amperometric response of 100 μM substance in PBS from which the signal in pure PBS solution was subtracted.	49

Figure 3. 7: (A) Calibration curves of pure Pt-LCNFs with different metal-to-polymer ratios for the detection of H_2O_2 obtained by non-stirred chronoamperometry at +0.5 V (n≥3). (B) The % relative signal (at +0.5V) of AA, UA, and DA (100 μM in PBS) compared to the signal of a 100 μM H_2O_2 solution in PBS for investigated metal ratios (compared to dry mass of the polymer in the spinning solution). ... 50
Figure 3. 8: The current response of 50 μM and 100 μM of H_2O_2 added to a blank minus the current response of the blank without any H_2O_2 . Hereby, the blank is either pure PBS, a 50:50 mixture of PBS and human serum, or pure human serum for (A) the 25% metal pure Pt- LCNF and for (B) the 25% metal pure Pt-LCNF with a 1 μL of 5 w% Nylon-coating. The green numbers refer to the recovery, whereas current responses in pure PBS solution are defined as 100% (n≥3)..... 51
Figure S3. 1: SEM pictures of various LCNFs with a magnification of 300 in the left and 3000 in the right column. The red arrows point at the fibrous samples that may be under carbonized. 54
Figure S3. 2: Cyclic voltammograms at various scan rates of LCNFs (A: 100% Ni, B: 75% Ni + 25% Pt, C: 50% Ni + 50% Pt, D: 25% Ni + 75% Pt, E: 100% Pt, F: no metal) in 1mM ferri/ferrocyanide in PBS-solution (pH = 7.4) (n≥5), the respective Randles-Sevcik plot of the ferri/ferrocyanide peak (~300 mV, oxidation scan (IUPAC)) and the resulting effective surface area (ESA). The peak couple above +0.6 V in A-C (also slightly visible in D) relate to the formation of nickel hexacyanoferrate species. 55
Figure S3. 3: LCNFs with 100% Pt data from Figure 3.4A ; a plot of low concentrations shows that there is a perfect linear correlation from at least 5-500 μM H_2O_2 56
Figure S3. 4: Mass of the Pt- and Ni-salt per mL spinning solution of the investigated LCNFs and the resulting ESAs from Figure S1. 57
Figure S3. 5: Effect of polymer coatings of 25% Pt-LCNF on the selectivity shown by the signal ratios of H_2O_2 to ascorbic acid (AA). The H_2O_2 and AA concentrations were prepared at 100 μM in PBS (n=3). 58
Figure S3. 6: Cyclic voltammograms of LCNF electrodes with various Pt and Ni compositions running from +0.3 V to -0.3 V. The characterizations were performed in 40 μL solution droplet (PBS with and without H_2O_2 , pH = 7.4) using scan rate of 50 mVs-1. 60
Figure S3. 7: Dose response curve of H_2O_2 measured by chronoamperometry at -0.2 V under stagnant condition using 100Pt-LCNF electrodes. H_2O_2 solutions were prepared in PBS buffer (pH 7.4). (n = 5) Inset (i) and (ii) represents the exemplary chronoamperograms for data evaluation, and the background-subtracted signals at low H_2O_2 concentrations. 61
Figure S3. 8: Characterization of analytical performance of the electrodes for H_2O_2 detection. (A) Dose response curves obtained from chronoamperometric measurements when applying the potential at (i) +0.1 V, (ii) 0.0 V, and (iii) -0.1V (n=6). (B) Chronoamperometric signals (blank was subtracted) for selectivity studies against AA performed at (i) +0.1 V, (ii) 0.0 V, and (iii) -0.1V (n=6). 62

Figure S3. 9: CV scan of laser induced graphene-LCNFs (LIG-LCNF) with 1 mM SiMo in citrate buffered solution (pH= 3) with and without 10 mM H ₂ O ₂ . Numbers in brackets refer to reactions shown above.	64
Figure S3. 10: CVs (50 mV/s) of 1 mM SiMo in solutions with various pH-values on LIG-LCNFs with and without 10 mM H ₂ O ₂	67
Figure S3. 11: CV measurements of SiMo-co-spun LCNF (i) for ten consecutive times in citrate buffered solution (pH= 3) and (ii) the 10 th scan in buffer versus an additional scan in citrate buffered solution with 1 mM H ₂ O ₂ . For (A), 15 w% POM @ Matrimid® fibers, for (B), 5 w% POM + 20 w% Ni @ Matrimid® fibers, and, for (C), 5 w% POM + 20 w% Pt @ Matrimid® fibers were used.	69
Figure S3. 12: CV measurements of SiMo-co-spun LCNF (i) for ten consecutive times in phosphate buffered solution (pH= 7.4) and (ii) the 10 th scan in buffer versus an additional scan in phosphate buffered solution with 1 mM H ₂ O ₂ . For (A), 15 w% POM @ Matrimid® fibers, for (B), 5 w% POM + 20 w% Ni @ Matrimid® fibers, and, for (C), 5 w% POM + 20 w% Pt @ Matrimid® fibers were used.	70
Figure S3. 13: SAXS spectra of aqueous SiMo samples (0, 1.5, 15, 50, 150 mM)(left) and the spectra after subtraction of scattering from water (right)....	71
Figure S3. 14: SAXS spectra of 1.5 mM SiMo (water subtracted) and a fit by using a monodisperse sphere-model (r= 0.456 nm; SASfit).	72
Figure S3. 15: SAXS spectra of (A) SiMo in aqueous solution (50 mM) and Matrimid-nanofibers with SiMo embedded (co-spun) and (B) Matrimid-nanofibers with and without SiMo embedded.	72
Figure S3. 16: SAXS spectra of Matrimid-nanofibers with SiMo embedded before (fibers_POM) and after (LCNF_POM) laser scribing and in comparison, a laser scribed LCNF without POMs (LCNF_25Pt). The form factor of SiMo present in LCNF_POM is implied by the black arrow.	73
Figure S3. 17: Two consecutive measurements of POM deposited on LIG-LCNF by dropcoating in citrate buffered solution.	74
Figure S3. 18: CV measurements of SiMo dropcoated on (A) Pt-LCNF and on (B) PEGylated Pt-LCNF (i) for ten consecutive times in citrate buffered solution (pH= 3), and (ii) the 10 th scan in buffer versus an additional scan in citrate buffered solution with 1 mM H ₂ O ₂	74
Figure S3. 19: CV measurements of SiMo dropcoated on (A) Pt-LCNF and on (B) PEGylated Pt-LCNF (i) for ten consecutive times in phosphate buffered solution (pH= 7.4), and (ii) the 10 th scan in buffer versus an additional scan in phosphate buffered solution with 1 mM H ₂ O ₂	75
Figure S3. 20: CV measurements with a smaller scan range of SiMo dropcoated on PEGylated Pt-LCNF in (A) citrate buffer (pH= 3) and (B) phosphate buffer (pH= 7.4), (i) for ten consecutive times in buffered solution, and (ii) the 10 th scan in buffer versus an additional scan in buffered solution with 1 mM H ₂ O ₂	76
Figure S3. 21: CV measurements of SiMo dropcoated on (A) laser induced graphene (LIG) LCNF, (B) oxygen-plasma treated LIG LCNF, (C) Ethomeen C/25 dropcoated LIG-LCNF, and (D)) oxygen-	

plasma treated, Ethomeen C/25 dropcoated LIG-LCNF in citrate buffered solution (pH= 3). CV measurements show the first and the fifth scan in one solution. The sixth and the tenth scan of a consecutive measurement after washing the electrode are shown as well. After that, a scan in 1 mM H₂O₂ was recorded..... 77

Figure S3. 22: CV measurement of pure Pt-LCNF (15 w%) in phosphate and citrate buffered solution with and without 1 mM H₂O₂..... 78

Figure 4. 1: Graphical abstract of chapter 4. 80

Figure 4. 2: Structural and composition analysis of the laser-generated LCNFs with various Pt and Ni content. (A) An overview of TEM images and the respective size distribution (radius of nanoparticles) of (i) LCNFs, (ii) 100Pt-LCNFs, (iii) 50Pt/50Ni-LCNFs, and (iv) 100Ni-LCNFs. (B) The crystalline structure of (i) LCNFs, (ii) 100Pt-LCNFs, (iii) 50Pt/50Ni-LCNFs, and (iv) 100Ni-LCNFs revealed by HRTEM. (C) STEM-EDS image showing (i) the mapping area of 50Pt/50Ni alloy core-shell nanoparticle focused on (ii) Pt, (iii) Ni, and (iv) Pt-Ni overlay. (D) STEM-EDS image showing (i) the mapping area of 50Pt/50Ni alloy non-core-shell nanoparticle focused on (ii) Pt, (iii) Ni, and (iv) Pt-Ni overlay. 87

Figure 4. 3: XPS analysis of surface chemistries at (A) C1s orbitals, (B) Pt4f orbitals (Pt⁰ and Pt²⁺ and their satellites are combined), and (C) Ni2p orbitals (Ni³⁺ and its satellite are combined). 88

Figure 4. 4: I(q) · q³ vs. q plot of 100Pt-LCNFs (A), 50Pt/50Ni-LCNFs (B) and 100Ni-LCNFs with various metal concentrations. 90

Figure 4. 5: Electrochemical characterizations of electrodes for glucose detection. (A) Impact of Ni content on the sensitivity of glucose considering the anodic currents at +0.7 V and a pH above 11.5 (**Figure S4.5**). (B) Optimization of electrochemical pretreatment conditions for increasing pH locally (n=3). 92

Figure 4. 6: Electrochemical detection of glucose using in situ generation of OH- strategy prior to CV measurement. (A) Proof-of-principle of electrocatalytic reaction (i) without and (ii) with glucose characterized by CV. (B) (i) Exemplary CVs at various concentrations of glucose using pretreatment strategy (-0.9 V for 20s), and (ii and iii) improving reliability of data acquisition (n= 6). The CV measurement was conducted using a 50 mVs⁻¹ scan rate..... 93

Figure 4. 7: Effect of electrode ageing on the detection sensitivity of glucose when electrodes were stored under ambient conditions for 0, 2, 8, and 18 days (A-D, respectively), where the insets display water contact angles for each case. (E) Improvement of analytical performance of 20-day old electrodes by the addition of Tween-20 to the measurement solution (n=5). (F) Summary of LODs from A-E .. 94

Figure 4. 8: Continuous measurements of glucose on one electrode. A pretreatment of -0.9 V before each CV measurement was conducted for 20 s. (A) Stabilization of signal and diminishing of background current after 5 CV measurements in PBS. (B) CVs of various glucose concentrations measured consecutively. The CV of PBS is the same CV as the 5th measurement in (A). (C) Dose-

response curve considering the anodic current at +0.7 V. (D) Dose response curve considering the ratio between the current at +0.7 V and the reduction peak at +0.5 V. Since the ratio is a negative value, the absolute value was plotted.....	96
Figure 4. 9: Selectivity study. (A) single measurement per electrode approach: (i) the exemplary CVs randomly chosen from all measurements, and (ii) the corresponding ratiometric signals ($n \geq 3$). (B) multiple measurements per electrode approach: (i) CVs and (ii) the corresponding ratiometric signals ($n=1$) where the dash line indicated the mean value of PBS + 1 Glu mM and the highlight indicated its error range.	98
Figure 4. 10: Measurement in 20% human serum. (A) CVs of calibration in PBS solution and consecutive measurement in diluted human serum. (B) Respective ratios of (A).....	99
Figure S4. 1: Price estimation per electrode when using the scribing pattern shown in (B). (C) SEM pictures of the produced electrode material (LCNF) with a 1000- and 5000-fold and magnification. 102	
Figure S4. 2: Deconvoluted XPS spectra with background subtracted of (A) C1S orbitals, and (B) O1s orbitals for (i) 100Pt-LCNFs, (ii) 50Pt/50Ni-LCNFs, and (iii) 100Ni-LCNFs. Blue- and purple-colored arrows indicate an increase of oxygen-containing groups with increasing Ni-content. The red arrow highlights an increasing appearance of O^{2-} with increasing Ni-content, arising from Ni-oxide species.	103
Figure S4. 3: Deconvoluted XPS spectra with background subtracted of (A) Pt4f orbitals, and (B) Ni2p orbitals for (i) individual metal either 100Pt-LCNFs or 100Ni-LCNFs, and (ii) 50Pt/50Ni-LCNFs.. 104	
Figure S4. 4: Full range SAXS spectra and fitted patterns of the as-generated materials..... 105	
Figure S4. 5: HRTEM of (A)100Ni and (B)100Pt LCNFs focusing on rGO structure. An additional zoom highlights the more ordered structure within 100Ni-LCNFs compared to 100Pt-LCNFs, explaining the appearance of the 18.6 nm^{-1} reflex in SAXS spectra of 100Ni-LCNFs..... 105	
Figure S4. 6: Cyclic voltammograms (CVs) of 10 mM glucose (solid line) compared with 0 mM glucose (dash line) from LCNF electrodes contained various metal compositions measured under different pHs. Glucose solutions were prepared in PBS buffer adjusted to the desired pHs by NaOH (1 M). CV was performed using scan rate of 0.05 V/s. Each CV was from the averaged current obtained from individual triplicate measurements..... 106	
Figure S4. 7: CVs of 10 mM glucose (solid line) compared with 0 mM glucose (dash line) from LCNF electrodes contained various metal compositions after pretreatment at various times and applied voltages. Here, the pretreatment condition was applied directly before the respective CV scan, either in the absence or presence of glucose. Glucose solution was prepared in PBS buffer (pH 7.4). The absence of the oxidation peak at around 0.15 V is due to the fact that the electrodes were no fresh electrodes and already performed measurements for Figure S4.6 107	

Figure S4. 8: Effect of electrode ageing on detection sensitivity of glucose when electrodes were stored under ambient conditions for (A) 1 day, and (B) 4 days.) where the insets display water contact angle for each case. (n = 5)	108
Figure S4. 9: Comparison of the glucose signals obtained from electrodes without and without sterilization by (A) autoclaved at 121°C for 15 min, and (B) exposed to 70% ethanol for 10 min. For both conditions, electrodes were dried prior to the measurements.....	108
Figure S4. 10: (A) Reusing an electrode for several consecutive measurements in PBS + 10 mM glucose solution. After each CV measurement, a fresh drop of solution was placed. (B) Impact of an electrode cleaning. The procedure was: pretreatment (-0.9 V for 20 s) - measurement (CV) - recovery treatment (-0.2/0.0/+0.2 V for 60 s) – place fresh drop on electrode. After 6 consecutive measurements in 10 mM glucose solution, a 0 mM, 5 mM, 10 mM, 15 mM, and 20 mM glucose in PBS was measured. For a better comparison between the electrodes, the ratio I(0.7 V)/I(0.1 V of first measurement) was used.	109
Figure S4. 11: (A) The stabilized, 5 th measurement in PBS and a consecutive measurement in undiluted human serum. (B) CVs with various pretreatments in undiluted human serum.....	109
Figure S4. 12: Calibration and measurements of (A) 20 % human serum (0.96 mM glucose according to Roche AccuChec) and (B) 20% human serum spiked with 0.25 mM glucose (in total 1.21 mM glucose. Due to good linearity of electrodes 1, 2 and 4, calibration measurements were reduced for electrodes 3, 5 and 6.	110
Figure 5. 1: Graphical abstract of chapter 5.	112
Figure 5. 2: Schematic representation of sensor fabrication and measurement procedure. (A) Preparation of the spinning solution. (B) Electrospinning set-up to produce a nanofiber mat on filter paper. (C) Laser-induced carbon nanofibers (LCNFs) embedding Ni nanocatalysts generation using CO ₂ laser. (D) UV-Ozone treatment for enhancing the hydrophilicity of sensors' surface. (E) Wax transferring to confine the sensor working area. (F) Experimental set-up to test the potentiality of the sensor when integrated into a breathing mask. (G) Electrochemical measurement set-up for determining the glucose aerosol after capturing in a closed configuration. (H) Example of cyclic voltammograms in absence and presence of glucose. (I) Picture of the Ni-LCNFs device (i). SEM micrograph of the sensor's side-view (ii). Micrograph of the as-spun nanofibers (iii) and the Ni-LCNFs after device assembly (iv).	115
Figure 5. 3: (A) High signal variations of CVs obtained from three different Ni-LCNF sensors performed in 0.1 M NaOH without glucose. (B) Anodic peak current (iox) obtained with glucose 5, 10 and 25 µM.(C) Peak intensity ratio (iox/ire) determined at glucose 5, 10 and 25 µM. The data in B and C were extrapolated from the same CVs. (D) Comparison of relative standard deviation (RSD) calculated from anodic peak current (red) and iox/ire (blue) evaluated at concentrations of glucose enclosed between 0.1 and 10 µM. All data were obtained using the individual sensors (open device configuration) (n=3).	117

Figure 5. 4: (A) Exemplary CVs obtained with increasing concentrations of glucose using the closed device configuration. (B) Calibration curve obtained with the closed device configuration (n=3). Linear fit equation $y=0.0161[\pm 0.0011]x + 1.3701 [\pm 0.0038]$, $R^2= 0.9709$	120
Figure 5. 5: (A) The concentration of glucose measured with the close device configuration after nebulization of 0.4 mM glucose solution at different times. (B) Optimization of the distance between sensor surface and nebulization source. Graph reports the glucose concentrations obtained from nebulizing 0.4 mM glucose for 5 min, placing the sensor at 0, 1 and 3 cm of distance from the nebulizer. Red dashed lines represent the LOD and the superior limit of linear range. (C) Correlation between concentrations of glucose in the nebulized solutions and the captured glucose measured with the device (n=3).....	121
Figure 5. 6: (A) Stability of the sensor of the complete devices shown in Figure 5.2E . Graph reports the electrochemical response from nebulized glucose solution at 0.4 mM. (B) Selectivity study for potential interference found in breath. Glucose and interfering species at concentration of 0.4 mM were used in nebulized solutions.....	122
Figure S5. 1: Cyclic voltammograms obtained in presence of different amount of glucose. CVs obtained from Ni-LCNF sensor performed in 0.1 M NaOH (blank) and with 5, 10 and 25 μ M of glucose.	124
Figure S5. 2: Effect of UV-ozone treatment. (A) Cyclic voltammograms obtained from Ni-LCNF sensor untreated and treated with UV-ozone (5 min, and 0.5 L min ⁻¹ O ₂ flow rate). Measurements were performed in 40 μ L of 0.1 M NaOH without (dashed lines) and with 50 μ M glucose (continuous lines). (B) Comparison of signal ratio obtained in presence of different amount of glucose, after UV-ozone treatment performed with different duration.	124
Figure S5. 3: Influence of laser power on the limit of detection. Limit of detections calculated from the dose response curve (glucose concentration range 0-500 μ M in 0.1 M NaOH). The measurements were performed using the open device configuration with triplicate measurement.....	125
Figure S5. 4: Dose response curve obtained from open device configuration. Linear fit of the data extrapolated from CV in the range 0-500 μ M of glucose in 0.1 M NaOH. Equation: $y=0.0014 [\pm 1.6422 \times 10^{-4}] x + 1.4503 [\pm 0.0165]$, $R^2= 0.9362$ (n=3).....	125
Figure S5. 5: Cyclic voltammograms obtained from different glucose concentrations nebulized.	125
Figure S5. 6: Glucose measurement using Ni-modified commercial screen-printed electrodes (A) Electrochemical behavior of SPEs with and without electrodeposited Ni. The inset reports the zoomed signal of the unmodified SPE. The CVs of SPE-Ni _{drop} were obtained from drop-testing for 0.1 M NaOH (dashed line) and 0.4 mM of glucose (solid line). The CVs of SPE-Ni _{nab} were obtained after capturing nebulized glucose using 0 mM (dashed line) or 0.4 mM (solid line). (B) Comparison of the I_{ox}/I_{re} with (0.4 mM glucose) and without glucose for drop and aerosol measurements using SPE-Ni electrodes.	126

List of Tables

Table 1. 1: Comparison of fabrication techniques.....	16
Table 1. 2: Sample matrices, their properties, and considerations for enzyme-free sensor development.....	24
.....	
Table 3. 1: Summary of the results from EDX-spectra shown in Figure 1B.....	42
Table 3. 2: Comparison of Pt-LCNF with various Pt- and carbon-nanomaterial-based electrodes considering the effort of production, Limit of detection (LOD), measurement conditions, linear range, and applied potential.....	47
.....	
Table S3. 1: Composition of metal precursors, electrospinning conditions, laser settings, and their electroactive surface area determined by Randles–Ševčík equation.....	53
.....	
Table 4. 1: Measurement in undiluted and diluted (20%) human serum. Concentrations are calculated from data shown in Figure S4.12 (n=3).....	100

1. Non-enzymatic electrochemical sensors for point-of-care testing: Current status, challenges, and future prospects

1.1 Abstract

Current electrochemical sensors in point-of-care (POC) testing devices mainly rely on enzyme-based sensors owing to superior sensitivity and selectivity. Nevertheless, the poor stability, high reagent cost, complex fabrication and requirement of specific operational conditions make their adaptability in real-world applications unfavorable. Non-enzymatic electrochemical sensors are thus developed as they are more robust and cost-effective. The advancement in material science and nanotechnology enables the development of novel non-enzymatic electrodes with favorable analytical performance. However, the developments are yet far from being adopted as viable products. This review therefore aims to gain insight into the field and evaluate the current progress and challenges to eventually propose future research directions. Here, fabrication strategies based on traditional and emerging technology are discussed in the light of analytical performance and cost-effectiveness. Moreover, the discussion is given on the pros and cons of non-enzymatic sensors when they are employed with various kinds of sample matrices, i.e., clinical and non-clinical samples, which must be taken into consideration for sensor development. Finally, promising strategies from literature for solving the remaining challenges are included which could facilitate further development of robust POC testing devices based non-enzymatic sensors. We believe that once researchers and technology developers have reached the point where most problems are solved, non-enzymatic sensors are going to be the robust choice for POC testing in clinical diagnostic, ensuring food safety, monitoring contaminants in environment, and bioprocess control.

This chapter will be further used as a manuscript that is intended to be submitted to Talanta as a critical review article.

1.2 Author distribution

The author and Dr. Nongnoot Wongkaew contributed equally to literature search and manuscript preparation.

1.3 Introduction

In 2004, Wild et al. estimated that global diabetes cases would rise from 171 million in the year 2000 to 366 million by 2030¹. However, by 2021, diabetes already far exceeded this estimation, i.e., with 537 million people suffering from diabetes, a majority of whom resided in low- and middle-income countries². This significant deviation from projections not only raises questions about the current prevalence of diabetes but also highlights the urgency of developing affordable point-of-care (POC)

sensors. This need is particularly critical in economically disadvantaged regions where access to advanced healthcare facilities is limited. Such POC sensors will enable individuals who are suffering from diabetes to monitor their blood glucose levels inexpensively and without the need for elaborate laboratory tests.

POC sensors play a crucial role not only in diabetes management but also in addressing other diseases. The POC diagnostics market reached a substantial size of over 44 billion dollars in 2023, and it is projected to grow annually at a rate of 6.1% until 2030³. This remarkable growth is primarily driven by the increasing lifespan of people and the anticipated surge in cancer screening POC devices³. In addition, the recent pandemic has remarkably emphasized the necessity of POC testing that should be able to get access by anyone to allow disease containment in a rapid and effective manner. Beyond diagnostics in healthcare settings, POC testing also holds significance in broader contexts such as in environmental monitoring, and quality control in food/beverage or bioprocess industry.

Electrochemical sensors are emerging as ideal candidates for POC applications due to their miniaturized design, rapid response times, robustness, cost-effectiveness, sensitivity, versatility, scalability, ease of use, low power consumption, and portability. Typical measurement methods used in electrochemical sensors include amperometry, cyclic voltammetry, differential pulse voltammetry, or square-wave voltammetry, potentiometry, and impedance spectroscopy. Generally, the analyte can be detected either directly through oxidation or reduction of electroactive analytes, or indirectly, via affinity elements, e.g., antibody, and aptamer, that specifically bind to the analyte. The interaction in the latter case leads to changes in the current which can be monitored directly or indirectly through an additional redox marker. Presently, commercially successful diagnostic tools in this domain are predominantly enabled by biosensors, with a strong reliance on enzyme-based systems⁴. This is not surprising as enzymes offer a superior combination of high selectivity, sensitivity, biocompatibility, and the ability to function effectively under physiological conditions. In principle, there are three generations of enzymatic biosensors that have been developed so far⁵. First-generation sensors rely on the measurement of current resulted from co-substrate (e.g., oxygen) consumption or co-product generation (e.g., H₂O₂) as a consequent of enzymatic reaction. However, electroactive interferences and the requirement of a sufficient amount of free oxygen in the samples make the first-generation sensors problematic. This issue has thus led to the development of the second-generation sensors which use synthetic mediators, e.g., ferrocene or osmium, for shuttling electrons between the enzyme's redox active center and electrode. Nevertheless, maintaining the presence of the redox mediator constantly near the electrode has proved to be challenging. As a result, the third-generation enzymatic sensors have been developed and aimed for promoting direct electron transfer between the enzyme and the electrode, eliminating the need for redox mediators. In this context, advances in nanostructures and porous materials have contributed to achieving mediator-free oxidation and reducing interference effects.

Although enzyme-based biosensors with various configurations have served as a goal standard platform for POC testing devices, they yet suffer from high material and fabrication cost⁶⁻⁸, instability during

sterilization, vulnerability to changes in temperature, pH or other environmental factors⁹, the need for specific storage conditions, and short-term stability, that seek for more robust approaches. To overcome the challenges, there has been attempts to promote the detection of analyte of interest directly on electrode material which is considered as ‘the fourth-generation sensor’. The term, e.g., ‘non-enzymatic’, ‘enzyme-free’, or ‘enzyme-less’ has been used interchangeably for this type of sensors. In fact, analytes can be directly undergone redox reaction at any electrode. Nevertheless, electron transfer kinetics of many electrodes are too sluggish, thus requiring high overpotential to drive the redox reaction of interest. For example, a bare glassy carbon electrode (GCE) allows oxidation of glucose at 1.0 V to 1.4 V (in an alkaline solution)¹⁰. Such high overpotentials are not favorable as they tend to cause side reactions, e.g., oxygen evolution, concomitantly occur with the intended reaction, making the measurements of analyte at low concentrations troublesome. In addition, other electroactive species, e.g., ascorbic acid (AA), can easily undergo redox reactions at lower potentials, further generating false-positive signals. Therefore, researchers are attempting to develop electrodes that permit the redox reaction at relatively low over potentials.

Various kinds of electrodes have been introduced in which the significant progress in this field has been promoted majorly through the remarkable advancement in synthesis and fabrication of nanomaterials and nanostructures¹¹⁻¹³. The research on enzyme-free sensor has been continually active over the past decade as it can be seen from an impressive high number of publications reported each year (**Figure 1.1**). The numbers of enzyme-free sensors are considered highly comparable to the enzyme-based electrochemical sensors (**Figure 1.1: blank vs. patterned columns**). It is interesting to see that in 2016 enzyme-free sensors started to gain more attention compared to enzyme-based strategies. Glucose, H₂O₂, and uric acid have been widely investigated for both enzyme- and enzyme-less sensors but pesticides and cholesterol have seen to rely majorly on using enzymes which suggests further research on enzyme-less strategies for these analytes.

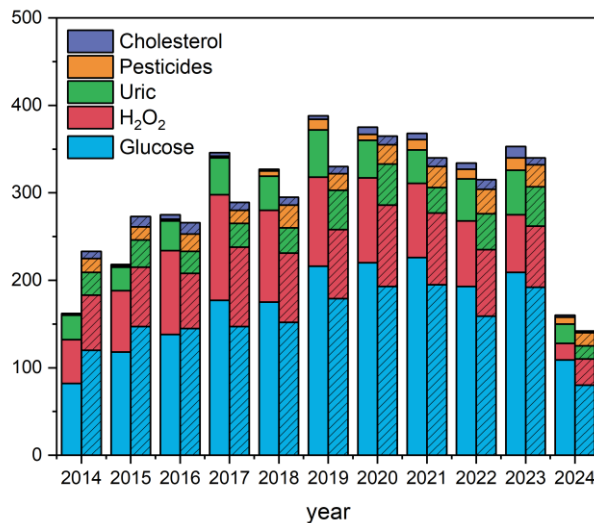


Figure 1. 1: The growth of research published in the past 11 years when searching with the terms “non-enzymatic electrochemical sensors”, “enzyme-free electrochemical sensors”, and “enzyme-less electrochemical sensors” combined with the specific analyte (blank columns), and representation of the search with the same keywords but with enzyme-based strategies instead (patterned columns). Web of Science searched on July 2nd, 2024.

Up to now enzyme-free sensors have been seen as a promising platform to address the needs for POC testing. However, most researchers attempted to develop novel electrode materials and improve analytical performance which have been successfully demonstrated mostly in ideal environments, e.g., pure buffer medium, where the electrodes can yield the greatest performance. Besides, the as-reported excellent sensing performance must be typically traded off with high costs of nanomaterial and fabrication methods, difficulty in large-scale manufacturing, and, for some cases, requirements of strict operational conditions, e.g., in alkaline media. Moreover, the biocompatibility of nanomaterials used for enzyme-free electrodes has been doubtful so far. These raise some crucial questions, i.e., are enzyme-less sensors able to be implemented in the field of POC testing, are there any restrictions/issues in using them, and what else should researchers do to facilitate the efficient translation of enzyme-less sensor into commercial products and to be practical in real-world applications?

So far, a great number of review articles related to non-enzymatic electrochemical sensors have been provided. For example, He et al. focused on a certain type of catalyst and reported the recent advances of perovskite oxide-based detection, highlighting their synthesis methods, electrocatalytic mechanisms, and the need for composites to overcome limitations in electron transfer kinetics, stability, and selectivity¹⁴. Govindaraj et al. on the other side focused on a certain analyte¹⁵. Their review covered recent advancements and future perspectives in enzymatic and non-enzymatic glucose detection such as fabrication processes, materials, detection principles, and effectiveness in various bodily fluids. Furthermore, strides made in wearable sensors and in the development of new nanomaterials and biomolecules for improved glucose detection are highlighted. As a last example, Panahi et al. focusses on the detection of hydrophobic analytes in biofluids, highlighting recent advances and surface

modification technologies in non-enzymatic electrochemical biosensors, addressing challenges in sensitivity and selectivity in complex biological fluids¹⁶. Despite significant merits of the previous review articles, to our knowledge, none of them has addressed the aforementioned questions. Even though these reviews provide significant value to the respective community by sharing general methods and strategies to improve electrochemical sensors, there is a risk that researchers focusing on other catalysts, analytes, or matrices may never read them.

In this review, we aim to provide a comprehensive overview of the entire development process for non-enzymatic electrochemical sensors (**Figure 1.2**). First, we give the basic principles and mechanism of enzyme-free sensors to not only help non-experienced readers in entering the field but also to define the definition in our review. This section also included the discussion on the most common materials used in sensors development. We will then highlight the current state-of-the-art of fabrication methods for non-enzymatic electrochemical sensors and evaluate their advantages and disadvantages, particularly in the context of their implementation in POC testing devices. With this, we will highlight laser-induced non-enzymatic electrochemical sensors as an emerging technology that offers mass-production capability and high-performing electrodes at low cost. We will also discuss current challenges that need to be addressed in future research. Additionally, we will critically evaluate specific sensor requirements for POC detection with respect to properties of sample matrices and the design of measurement and devices. This is crucial for researchers to consider from the outset in employing enzyme-less sensor strategies in the development process based on the intended application. Finally, we will emphasize the remaining challenges and promising strategies that may apply in the future before concluding with future prospects.

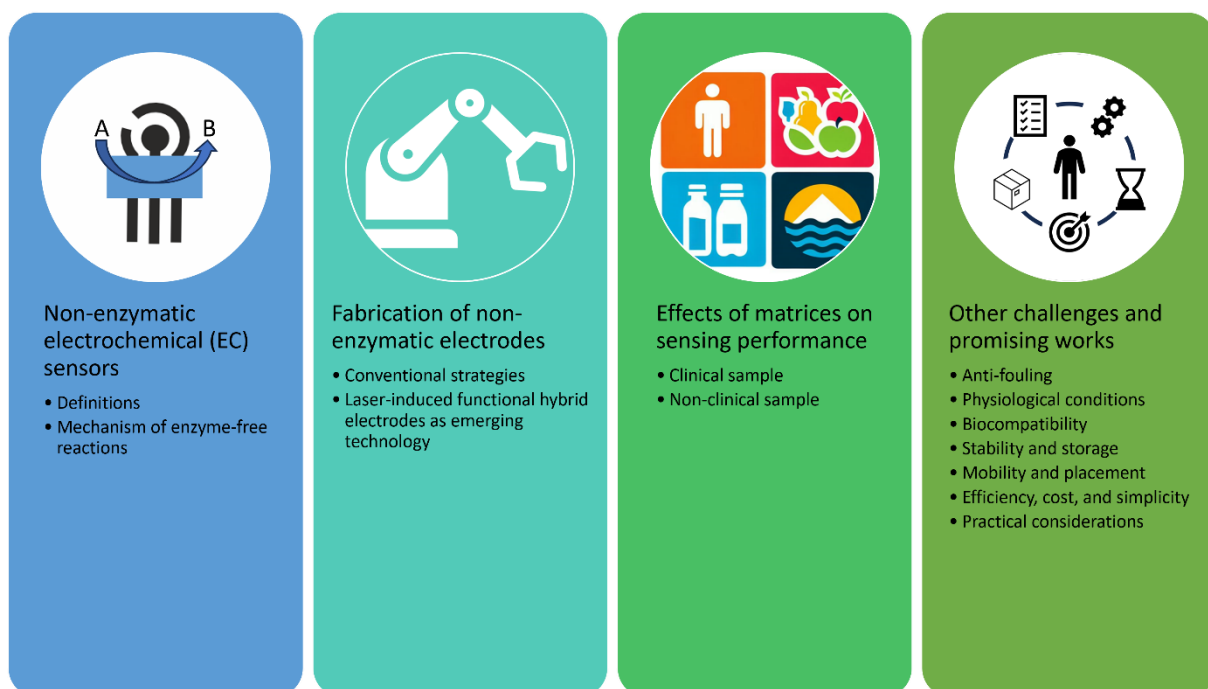


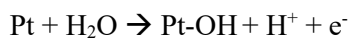
Figure 1. 2: Structure of this review.

1.4 Definition, principle, and mechanism

To our knowledge, the term “non-enzymatic electrochemical sensors” or the other (as-mentioned earlier) have been ambiguously used for various meanings where it tends to broadly cover any electrochemical sensors without the use of enzyme. Therefore, it is not surprising to see the use of this term in many affinity biosensors, e.g., using molecular imprinted polymers, aptamers, or antibodies, and detecting changes upon analyte binding through impedance or signal blocking. However, in this review we will focus only on non-enzymatic sensors-based electrocatalytic reactions induced by inorganic catalysts. In general, non-enzymatic electrochemical sensors consist of a functional material embedded or modified on the electrode surface in which an electrochemical signal can be obtained by catalytic reaction of the analyte^{17,18}. Hereby, the functional electrode material enhances electron transfer kinetics, i.e., lowering the required potential compared to pristine electrodes¹⁹. Various kinds of functional material have been reported for this purpose, namely 1) metal- or metal oxide-based materials, e.g., noble and transition metal and their composites, 2) carbon-based materials, e.g., graphene and its derivatives, and 3) combinations of carbon and metals or metal oxide.

In non-enzymatic detection, electrocatalysts play an important role in triggering redox reaction of the analyte. To understand the basic mechanism, an exemplary catalytic reaction of glucose, the most-studied analyte, is discussed as follows. Catalysis is in fact a complex topic, and in principle, each catalyst material could follow a different mechanism. Additionally, for a single catalyst, multiple adsorption geometries can exist²⁰, and even the crystal plane facing the analyte significantly influences the catalytic properties²¹. However, by simplifying this topic and reducing it to a common denominator, we can generally distinguish between two fundamental mechanisms in glucose oxidation, i.e., 1) reactions based on noble metal surfaces and 2) reactions based on non-noble metal surfaces⁵.

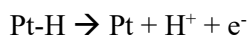
Both mechanisms basically involve hydroxide species adsorbed on the surface. However, noble metal can catalyze its reaction in neutral conditions, while base metal usually requires basic conditions. For noble metals, e.g., Pt or Au, at neutral pH, water can be oxidized at low potentials on their surface, forming a covalently attached layer of hydroxide species according to the ‘Incipient Hydrous Oxide Adatom Mediator (IHOAM)’ model^{5,22}:



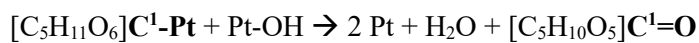
According to the concentric adsorption theory, glucose also adsorbs on the surface of the noble metal by breaking the bond between the hydrogen atom and the C¹-atom of glucose^{5,23}:



The hydrogen-atom is then oxidized:



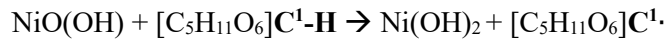
Both the covalently bound hydroxide species and the glucose subsequently react with each other on the Pt surface to form gluconolactone and water:



In contrast, for non-nobel metals such as Ni or Cu, basic conditions are required to form hydroxides such as Ni(OH)_2 ²⁴. These hydroxide ions are not covalently bound but interact ionically. During oxidation of Ni(OH)_2 in a basic medium, Ni(III) oxyhydroxide is formed:



This species can abstract the hydrogen atom at the C¹-atom in glucose in a rate-determining step, forming radicals:



The radical further reacts with a hydroxide ion to form gluconolactone and water:



In summary, on the catalyst surface of noble metals, water is first oxidized, and hydroxide is covalently bound to the noble metal. Additionally, glucose can adsorb to the surface by breaking the bond between the C¹ and hydrogen atoms, with both fragments being covalently bound. The glucose fragment then reacts with hydroxide to form gluconolactone. In contrast, for non-noble metals, hydroxide ions must be present in solution (basic conditions), and glucose is oxidized by the strong oxidant, i.e., Ni(III)-oxyhydroxide. Considering both mechanisms, the key difference between noble and base metals lies in their electron composition. Here, the 5d orbitals of Pt (electron configuration: [Xe]4f¹⁴5d⁹6s¹) or noble metals in general, should effectively overlap with the orbitals of glucose due to their geometric size and energy levels. This overlap enables the adsorption of glucose and direct participation in redox reactions²⁵. On the contrary, non-noble metals such as Ni (electron configuration: [Ar]3d⁸4s²) only have 3d orbitals, which are likely not able to interact with other molecular orbitals as effective as 5d orbitals. Therefore, the surrounding hydroxide species are necessary to enable electrocatalytic oxidation of glucose.

1.5 Fabrication of non-enzymatic electrodes

1.5.1 Conventional strategy

1.5.1.1 Drop-casting and dip-coating

Drop-casting and dip coating are straightforward methods used to modify the surface of an electrode with nanocatalysts. In drop-casting, catalyst material suspension in a small volume is placed and adsorbed directly onto the electrode, while in dip coating, the electrode is immersed in the catalyst solution which requires a greater volume of suspension. The former technique is superior in terms of material usage, as the catalyst material is selectively deposited only on the electrode's surface, unlike the latter one. After electrode drying, the modification process is complete. Although both methods are highly facile and widely employed for generating enzyme-free POC sensors, the major drawback of these methods is the inhomogeneous distribution of the catalyst material caused by the coffee ring effect²⁶. This effect occurs during liquid droplet evaporation. As liquid evaporates from the edge, it is replaced by interior liquid, creating radial flow. This flow carries dispersed material to the edge, resulting

in a characteristic ring pattern. To mitigate this effect, co-solvents with low evaporation rates and higher viscosity can be added^{27,28}. These two properties will reduce the driving force of radial flow and increase resistance towards radial flow, respectively. Furthermore, various other attempts have been conducted to overcome the issue as reviewed by Kumar et al.²⁶. These include (i) using substrates with super hydrophobic surfaces²⁹, (ii) employing electrowetting³⁰, (iii) utilizing anisotropic particles³¹, (iv) introducing surface acoustic waves³², and (v) enhancing Marangoni flow³³. Among these, adjusting the solvent to enhance the Marangoni flow (e.g., by using a mixture of solvents with different surface tensions) and using anisotropic particles appear to be the most practical solutions.

1.5.1.2 Electro- or electroless deposition

Electro- or electroless deposition is a technique that has gained prominence in the field of enzyme-free sensors. In case of electrodeposition, ion precursors from the surrounding solution deposit on the electrode by applying an oxidative or reductive potential. Alternatively, the formation of metal ion precursors into catalyst nanoparticles is also feasible without application of external potential, termed electroless deposition. For example, Kawakami et al. electropolymerized polypyrrole onto Pt electrode followed by drop-casting KAuCl_4 solution on the as-prepared electrode³⁴. After drying, AuNPs with diameters ranging from 20-40 nm, depending on the volume of KAuCl_4 solution introduced, were formed and the electrodes were used for glucose detection. Both methods are a highly controllable manner with relatively high precision. Here, the morphological structures and sizes of nanocatalysts obtained from electrodeposition can be precisely controlled by fine-tuning the solution compositions, time, and/or the applied current and potential³⁵. Similarly, the nanocatalyst' features based electroless deposition can be controlled via chemical compositions introduced, deposition time, and/or volume used for deposition³⁴. In addition, the techniques allow ones to exclusively deposit the nanoparticle catalysts on the specified working area, thus avoiding contamination of any other unwanted sensor components.

Nevertheless, during electrocatalytic reaction the deposited nanocatalyst films can be unstable and peeled off from electrode surface easily. To address the issue, Viswanathan et al. used methionine to strengthen electrodeposited copper-cobalt nanostructures on indium tin oxide electrodes³⁶. Hereby, the thiol group of methionine interacts with metal ions (Cu^{2+} and Co^{2+}) during electrodeposition. This interaction stabilizes the films by forming a protective layer on the electrode surface, preventing the detachment during electrocatalysis. Apart from instability during electrocatalysis, mechanical force such as from solution stirring can raise the issue during operation, especially when deposition of nanocatalysts is carried out on 3D-porous electrodes containing high number of edges and defects. Our research group has demonstrated that under shaking at 50 rpm continuously for 5 h, nearly 100% of the electrodeposited Ni nanoparticles on carbon nanofiber electrode detached from the surface²⁴. The electrodeposition of nanocatalysts on 3D-porous carbon or any rough surface electrodes can suffer from poor adhesion stability apart from poor fabrication reproducibility. Therefore, a learning study is mandatory to carry out when sensor operation has to be performed inline, real-time, and under flow-condition.

1.5.1.3 Printing

Screen-printing

Screen printing, a versatile, cost-effective, and user-friendly technique, is commonly used for manufacturing electrochemical sensors³⁷. It relies on applying conductive ink such as carbon and metallic inks, or their mixture onto a substrate support, e.g., ceramic or plastic, using a screen mesh containing electrode patterns³⁷. The formulation of conductive ink is critical in this process. Typically, the inks consist of conductive material such as carbon or metal powder/particles to ensure electrical conductivity, and binders to enhance interactions between the conductive material and the substrate as well as the material itself³⁷. Solvents regulate ink rheology and viscosity, aiding printability³⁷. Additionally, some additives, e.g. surfactants or chelating agents, improve wettability and drying rate, and prevent agglomeration of conductive particles³⁷. However, the use of binders and other additives, while essential in ink formulation, can lead to poor electron transfer kinetics of the embedding nanocatalysts, necessitating surface activation prior their uses of electrodes³⁷. The electrode surface can be activated by electrochemical pretreatment or plasma treatment. For example, Su et al. investigated effect of electrochemical pretreatment procedures with varying scan ranges and observed significant changes such as increased porosity, enhanced electron transfer kinetics, and a larger effective surface area³⁸.

In principle catalytic functionalities such as metal nanoparticles can be principally incorporated into the ink to fabricate enzyme-free sensors by screen printing. However, to our knowledge, there are relatively few publications on this method which is probably due to the challenge of preventing nanoparticle agglomeration within the ink^{39,40}. Agglomeration, especially during drying, leads to the formation of larger particle clusters, diminishing the overall high catalyst surface area achieved by the nanometric size of the nanoparticles. Addition of stabilizing agents to prevent agglomeration of nanoparticles is possible but their excess amount can adversely reduce viscosity and subsequently diminish printability⁴¹. Furthermore, since nanoparticles are distributed throughout the entire ink (not just on the surface), the portion of nanoparticles contributing to the catalytic reaction is significantly lower than the total number of nanoparticles added. This aspect is especially important when working with costly catalyst materials, e.g., platinum or gold nanoparticles.

For real-world applications, a screen-printed electrode that does not require pretreatments to overcome the limitations of additives would be highly beneficial. Therefore, the catalyst material in the binder-free ink must exhibit thixotropic properties to ensure printability³⁷. In their comprehensive review, Suresh et al. proposed that water-based ink containing rGO nanofibers could be particularly interesting³⁷. The basic idea is that the catalyst material itself includes structural elements necessary for a printable ink. We suggest that these rGO nanofibers could be functionalized, for example, by attaching nanocatalysts. To name an example that proofed such approaches, Abdolhosseinzadeh et al. used MXene sediments, which are two-dimensional inorganic compounds consisting of carbides and nitrides of transition metals, to formulate an additive-free ink with suitable rheological properties⁴².

Inkjet printing

Inkjet printing is a versatile, fast, and low-cost production method for creating electrochemical sensors. With inkjet printing, electrodes can be directly printed onto a substrate using a commercial inkjet printer. Its high adaptability comes from the fact that inkjet printing is a digital printing technique, allowing us to print a digital file (e.g., a PDF file with the electrode designs) directly, without the need for masks, unlike screen printing or photolithography⁴³. The printing technique can be either continuous (a jet of ink deflected by an electric field) or drop-on-demand, where either an oscillating crystal (piezo inkjet printing) or a heating element (thermal inkjet printing) ejects a drop as needed. Each of these techniques has different advantages (speed, cost, robustness) and requires different ink properties, such as viscosity or thermal stability. Lab-compatible inkjet printers, such as the EPSON L130, are affordable (available for under €300) and can be used with ink tanks instead of ink cartridges for easier refilling purpose⁴⁴. The printing process efficiently utilizes inks and is highly scalable⁴³. Substrates for inkjet printing range from commercial A4 paper⁴⁴ to flexible PET plastic⁴³. However, precise ink formulation is crucial. While screen printing can handle higher ink viscosities and solid loadings, inkjet printing may face nozzle clogging and printability issues⁴⁵. Additionally, the wettability of the ink on the substrate impacts overall resolution, which can be fine-tuned through ink formulation or substrate treatment⁴⁵. For inkjet printing, the coffee ring effect (**chapter 1.5.1.1**) plays a crucial role but can be solved by the same strategies as mentioned before. In addition, nanofibers (e.g. cellulose nanofibers in aqueous solution) also reduce the coffee-ring effect by preventing the rush hour phenomenon, which is a drastic acceleration of radial flow at the final stage of the drying⁴⁶. However, a possible nozzle clogging needs to be kept in mind with these approaches.

There have been attempts to formulate the ink by combining nanocatalysts with carbon nanomaterials such as graphene^{47,48}. However, metal nanoparticles alone can be successfully fabricated via inkjet-printing method as well⁴⁹. The authors ensured homogeneity of the ink solution by filtering through a 0.45 µm membrane⁴⁹. However, to improve conductivity when electrodes are printed on substrates like paper, it may be necessary to print several times on the same position⁴⁸. Similar to screen-printing, additive free approaches using MXemes exist⁵⁰.

3D-printing

Three-dimensional (3D) printing is a versatile and cost-effective technique to create electrochemical sensors⁵¹. One significant advantage of 3D printing is the ability to produce complete, customized analytical systems. In addition to using conductive filament for the electrode, non-conductive filament can be employed for support or surrounding structures. However, there are some drawbacks to 3D printing. The specialized knowledge required for 3D design software and the steps involved in transitioning from a 3D model to a physical print can be challenging. Additionally, the cost of 3D printers varies significantly, ranging from as low as US\$ 150 to as high as US\$ 8300, depending on specifications such as resolution, compatible polymers, and dual nozzle printer for a faster printing when more

filaments are used⁵¹. Customized conductive filament with additive nanocatalysts also requires a filament extruder. Despite these challenges, there are user-friendly 3D modeling software options available, such as Autodesk's Fusion 360. These programs allow users to export STL files after designing their 3D models. The next step involves using a "slicer" software (such as PrusaSlicer) that converts the STL file into a "G-code" file- a set of precise instructions for the 3D printer. For learning about 3D-printing and modeling, YouTube offers a wealth of tutorials.

Commercial PLA conductive filament, e.g., Black Magic 3D Conductive Graphene Composite® (graphene contained PLA), can be used for printing 3D structure of electrode support. However, to construct non-enzymatic sensors, electrocatalysts have to be introduced via post-treatments such as electrodeposition. The technique is considered inconvenient, leading to many attempts in the direct incorporation of electrocatalysts into the filament to avoid such issue. For example, Rocha et al. synthesized Ni(OH)₂ microparticles and mixed them with a commercial conductive filament (cut into small pieces) in a proper solvent prior to drying and subsequently extruding into a filament for 3D printing⁵². However, the 3D-printed electrode requires polishing and electrochemical activating steps before detecting glucose performed in alkaline conditions⁵².

Roll-to-Roll (R2R) printing

Compared to previous printing techniques, Roll-to-Roll (R2R) printing works like a stamp which is alternately immersed into an ink and pressed onto the substrate. With that, R2R is a fast and high-throughput technique with low adaptability for sensor design and a significant entry barrier due to the investment required for R2R printing machines. Additionally, drying chambers are typically needed after each printing step, consuming a substantial amount of energy. However, once the design is finalized and the printing parameters, as well as ink formulation (rheology, printability, surface tension, stability), are optimized, the major advantage of R2R printing is its high throughput. Furthermore, additional electrodes containing different materials can be added consecutively by using additional printing rolls.

Substrates for R2R printing are thin polymer films such as poly(ethylene terephthalate)⁵³⁻⁵⁵ or flexible polyimide^{56,57}. There are two promising R2R printing techniques: R2R gravure printing and flexography. In R2R gravure printing⁵³ (**Figure 1.3**), a metal cylinder with a gravure (the negative imprint of the sensor design) dips into the ink solution. A doctor blade removes excess ink that is not in the engraved cavities of the roll. After the doctor blade, the ink-loaded gravure roll contacts the substrate, which is guided by the impression cylinder, transferring the ink to the substrate. As demonstrated by Bariya et al. multiple layers of various materials can be printed in a continuous process where the finished printing layer in each step is subjected to drying in between⁵³. The authors demonstrated that 150,000 electrodes on 150 meter-long of PET substrate with multiple materials can be printed within only 30 minutes⁵³.

In flexography⁵⁷ (**Figure 1.3**), ink is transferred onto the anilox roll, which has uniformly distributed engraved cavities capable of loading a defined amount of dye. After the removal of excess ink by a doctor blade, the defined amount of ink is transferred to the flexo plate, a positive imprint of the sensor

design. The ink on the flexo plate is then transferred to the substrate on the impression cylinder. Fung et al. used flexographic printing on a polyimide substrate to consecutively print an Ag/AgCl reference electrode, a carbon working and counter electrode, and a zinc acetate precursor layer on top of the working electrode⁵⁷. After each step, the ink was dried at 150°C for 10 minutes. During heating, the zinc acetate precursor formed zinc oxide (ZnO) nanowires⁵⁷. Even though the authors employed electrodes for enzymatic glucose sensors, the strategy is highly practical for enzyme-free sensors.

Comparing both methods, R2R gravure printing offers exceptional detail and high volumes, but it comes with a high upfront cost due to the need for cylinder engraving, making it an ideal technique for high-volume prints. Furthermore, it is more limited in terms of absorbent substrate material. Flexography, on the other hand, has lower upfront costs and setup time due to the easier adaptability of the flexo plate and is suitable for various substrates, making it an ideal candidate for lower volumes and more individualized prints due to its easier adaptability.

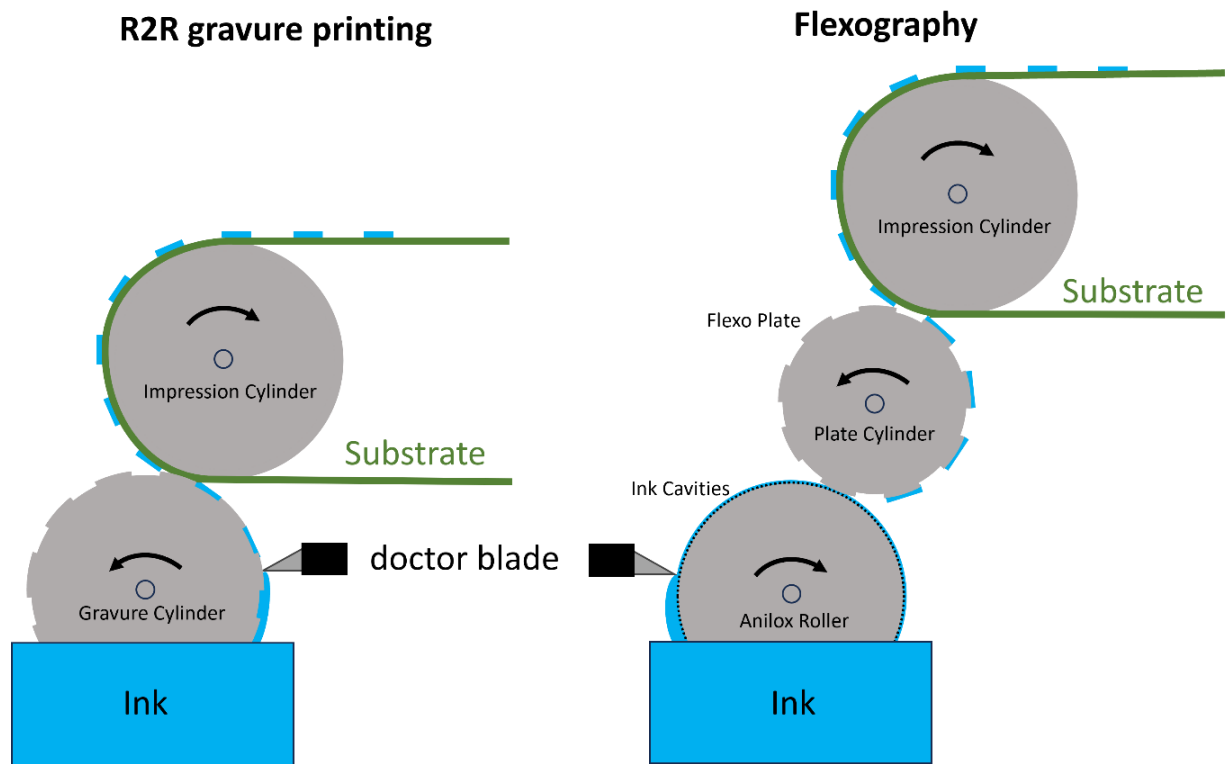


Figure 1.3: Setup of Roll to Roll (R2R) gravure printing and Flexography.

1.5.2 Laser-induced functional hybrid electrodes as emerging technology

Laser-induced catalyst synthesis is a promising single-step preparation method for non-enzymatic electrodes, as both the embedded catalyst and the conductive material (i.e., laser-induced graphene (LIG)) can be generated simultaneously, forming a functional hybrid material¹⁹. A wide range of precursors can be used for LIG, including polymers (such as polyimide), wood, cloth, or paper¹⁹. During the laser scribing process, the substrate (usually polymers) is carbonized, resulting in a reduced graphene oxide-like structure. This method is fast, inexpensive, and easy to adapt, as electrodes can be scribed in any pattern. Furthermore, it enables 3D-porous electrodes with immense surface area which is highly favorable for sensor development. The size, structure, and composition of LIG are highly dependent on the laser settings (e.g., power, speed, scribing mode, lens, atmosphere), and the laser power needed to convert material to LIG is very dependent on the thickness and composition of the precursor. In 2015, Tour's group conducted pioneering work by *in situ* generating metal oxide nanoparticles embedded in LIG using a CO₂ laser ($\lambda = 10.6 \mu\text{m}$) with a metal salt-containing polyimide film as the precursor material⁵⁸. The functional hybrids have been used for oxygen reduction reactions in the field of energy storage. This pioneered work has significantly enabled the fabrication of many novel carbon nanocatalyst hybrids for enzyme-free electrodes used in POC testing. In this section, discussion will be given based on how the substrate precursor is prepared prior to laser exposure.

1.5.2.1 Coating catalyst precursor on carbonizable substrate

To introduce metal nanocatalysts, coating a polyimide film substrate with metal precursors has been demonstrated. For example, Fan et al. covered a polyimide film with a thin metal leaf, e.g., gold, silver, platinum, palladium, and copper, prior to laser scribing the material with a CO₂ laser⁵⁹ (**Figure 1.4i**). In addition to generating monocatalyst-graphene hybrid, the authors also demonstrated that AuAg alloy could be facilely obtained via the combination of gold and silver leaf coating⁵⁹. The AuAg alloy LIG electrodes were successfully employed as enzyme-free electrodes for glucose detection in blood plasma sample⁵⁹. Although the authors have shown superior analytical performance, the stability of the as-generated nanoparticles remains a question as the initial interaction between metal leaves and PI substrate could be very weak. The nanocatalysts might be weakly bound to the LIG surface which may raise stability issue when applying the electrodes under stirred or flow-condition. Furthermore, applying very thin metal leaves may cause poor reproducibility when the process is not well-controlled. The method could be possibly circumvented through making a mixture of metal precursor together with a polymer matrix and homogeneously coated on a polyimide substrate as recently proposed by Zhang et al.⁶⁰ (**Figure 1.4ii**). Here, the mixture of Cu²⁺ precursor and ethyl cellulose in ethanol was spin-coated on a polyimide substrate⁶⁰. The ethyl cellulose may assist the spin-coating process and/or adhesion stability between precursor and polyimide film substrate. After drying the polymer film, a copper-embedded graphene electrode was generated using a CO₂ laser similar to the work shown by Feng et al. The authors successfully applied the resulting electrodes for determination of glucose in beverages.

Similarly, Zhao et al. knife-coated a polyamic acid mixed with Co^{2+} precursor on a polyimide substrate film and laser-generated Co_3O_4 nanoparticles-graphene hybrids⁶¹ (**Figure 1.4iii**). Here, polyamic acid is considered a carbon precursor and needs to be converted into polyimide via imidization process under high temperatures, e.g., 180°C, prior exposure to the CO_2 laser⁶¹. Unlike using ethyl cellulose as a matrix, the Co-doped PI layer could adhere better to polyimide layer underneath.

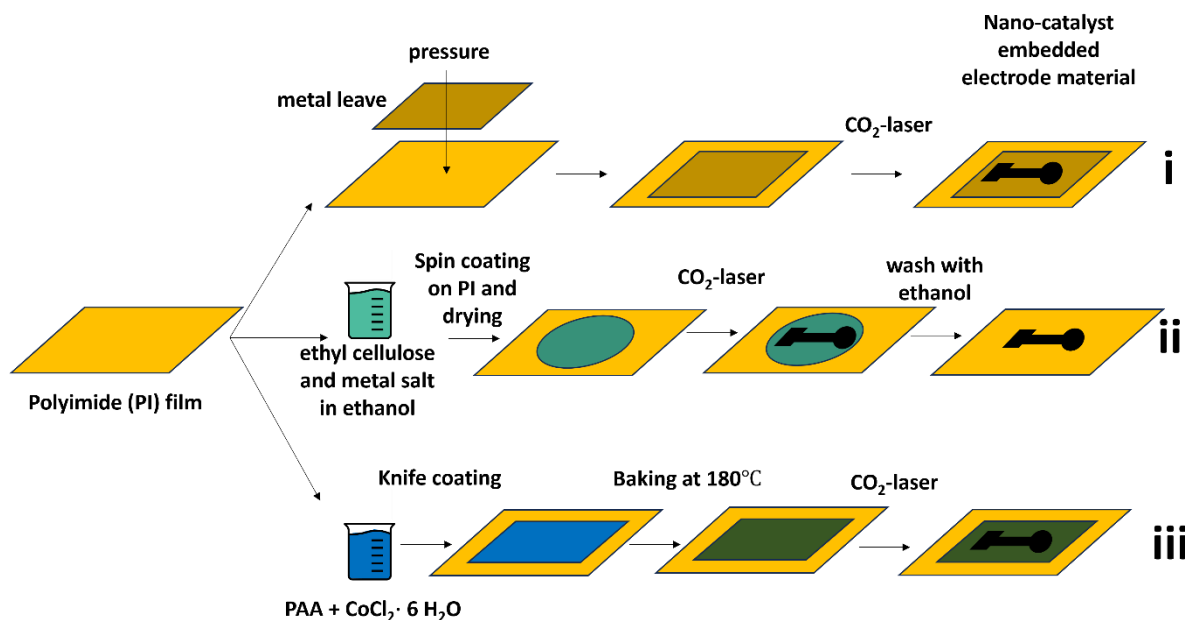


Figure 1.4: Examples for coating catalyst precursor on carbonizable substrate by (i) attaching a metal leave on polyimide (PI) substrate, (ii) spin coating a PI substrate with an ethyl cellulose + metal salt solution, and (iii) by knife coating a PAA + metal salt solution onto a PI substrate.

1.5.2.2 Blending catalyst precursor with carbonizable substrate

Although coating catalyst metal precursor on a carbonizable substrate, e.g., polyimide or Kapton, is high facile, direct doping the metal catalyst precursor with graphitizable materials is considered more effective as homogeneous distribution of catalysts through the entire 3D-electrodes can be expected. In this regard, the polymer precursor can be prepared similarly to the work proposed by Tour's group where polyamic acid precursor is blended with metal salt and later converted into metal-doped polyimide prior to laser scribing without the need of polyimide film underneath⁵⁸ (**Figure 1.5i**). Alternatively, a solvent soluble polyimide (Matrimid® 5218) is commercially available which allows direct preparation of metal salt-doped polyimide precursor without the need of imidization process. Our group has employed this material to create electrospun carbon nanofibers doped with nanocatalysts and develop non-enzymatic electrochemical sensors⁶² (**Figure 1.5ii**). For example, in the pioneered work, the spinning solution made from nickel acetyl acetate blended with Matrimid® 5218 was electrospun and later subjected to CO_2 laser for generating Ni embedded laser-induced carbon nanofibers (Ni-LCNFs)²⁴. The electrospun nanofibrous precursor facilitates the formation of 3D-porous structure and the homogenous distribution of Ni particles²⁴. The Ni-LCNF electrodes enabled glucose detection in sub-micromolar range which is attributed to high surface area and immense porosity of the electrodes²⁴. In addition, we have proven

that the stability of Ni within LCNFs is higher than the electrodeposited Ni counter parts when the electrodes were subjected to stirring condition²⁴. We also later generated Pt-LCNF electrodes and successfully employed them for H₂O₂, highlighting the versatility of the strategy⁶³.

Apart from the polymers mentioned earlier, graphene oxide film mixed with metal has been proposed. Recently, Scroccarello et al. prepared a film substrate by filtering a suspension of graphene oxide blended with metal salt, e.g., Au³⁺, Ag⁺, or Pt²⁺⁶⁴. After drying the film coated filter paper, non-enzymatic working electrodes were generated using CO₂ laser (Figure 1.5iii). The authors have demonstrated the utility of their electrodes, namely Au@rGO-, Ag@rGO-, and Pt@rGO for determination of caffeic acid nitrite, and hydrogen peroxide, respectively, with detection limits in sub-micromolar range⁶⁴. Nevertheless, the sensor manufacturing still requires transferring the metal/rGO film onto an additional substrate where counter and reference electrodes were accommodated. This may subsequently lead to poor reproducibility of the sensors due to additional steps required.

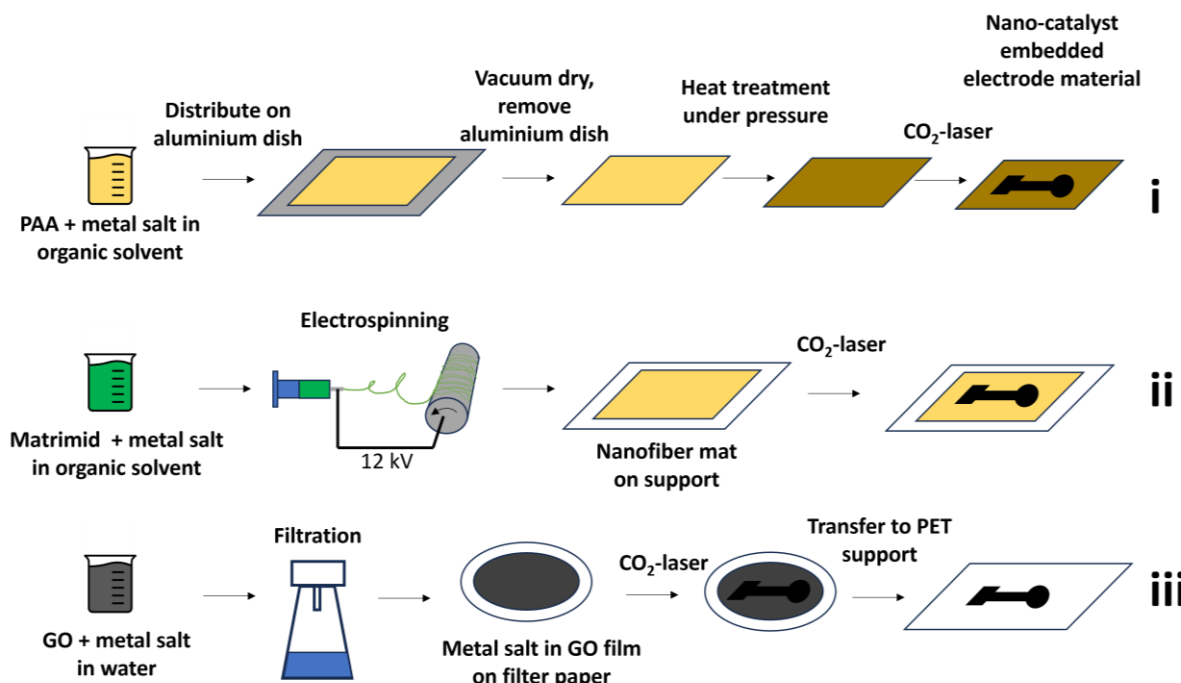


Figure 1.5: Examples for blending catalyst precursor with carbonizable substrate by (i) distributing polymer-metal salt solution on a surface, drying, and a consecutive heat treatment, (ii) electrospinning a polymer-metal salt solution, and (iii) by preparing a graphene oxide (GO)-metal salt solution and consecutive filtration.

Both coating and blending strategies are highly promising for upscaling the manufacturing process of non-enzymatic sensors. In comparison to the screen-printing technique, the 3D-porous structure of laser-generated non-enzymatic electrodes allows more efficient contact between analytes and catalysts anchored or embedded within LIG. However, to reach this favorable characteristic, wettability of LIG electrodes must be ensured as the roughness and microstructures could make the electrode surface highly hydrophobic, hindering the access to the inner porous structure. Oxygen-plasma or UV-zone treatment, and introduction of surfactant in the measuring samples could be conducted to hydrophilize LIG

electrodes. Nevertheless, it is necessary to ensure that such treatments do not adversely affect to the capability of nanocatalyst.

Table 1. 1: Comparison of fabrication techniques.

Strategy	Complexity and cost of instrumentation	Fabrication throughput/mass production capability	Strengths	Weakness
<i>Conventional method</i>	Drop casting & dip coating	Low	High	Simple, cheap Coffee-ring effect, stability (leaching), base electrode needed
	Electro- or electroless deposition	Low - Moderate	Low - Moderate	Simple, cheap, selective (coating only on working electrode) Electrodeposition on each individual electrode, stability (leaching), based electrode needed
	Screen printing	Low - Moderate	Moderate - High	Simple, cheap, complete electrode is produced, few manufacturing steps Need of a mask, surface activation needed, support needed
	Inkjet printing	Low - Moderate	Moderate - High	Simple, cheap, different electrode materials can be printed at the same time by using different inks Bad conductivity requires many layers, coffee-ring effect, particles can lead to nozzle blockage
	3D printing	High	Low	Very complex and individual systems printable, complete electrode is produced Slow, expensive, surface activation needed
	Roll-to-roll printing	High	High	Very high throughput, perfect for upscaling, complete electrode is produced Very expensive machine, offset print (hard to customize), support needed
<i>Laser-induced functional hybrid as emerging technology</i>	Coating catalyst precursor on carbonizable substrate	Moderate	Moderate - High	Simple, cheap, complete electrode is produced, few manufacturing steps Carbonizable substrate needed, laser scribe is expensive
	Blending catalyst precursor with carbonizable substrate	Moderate	Moderate - High	Simple, cheap, complete electrode is produced, freestanding material is possible, few manufacturing steps Laser scribe is expensive

1.6 Effects of matrices on sensing performance

1.6.1 Clinical sample

Blood

Blood is undoubtedly the most accurate biofluid in terms of analyte concentration found in the body and widely used sample in clinical settings and POC testing as seen from glucometers commonly used by diabetic patients. As analytes in blood are typically present in high concentrations (e.g., glucose levels ranging from 3.9 to 5.6 mmol/L)⁶⁵, the detection does not need highly sensitive enzyme-free electrodes. Instead, the sensor development should rather focus on selectivity and antibiofouling strategies due to the numerous interfering substances present. Since catalytic reactions are usually pH-dependent, all measurements and optimizations should be ideally carried out at the blood pH, i.e., 7.3-7.4⁶⁶, in order to enable a direct measurement without the need for sample preparation steps like pH-adjustments.

In selectivity studies, it is essential to consider key substances that can be easily oxidized or reduced during electrochemical measurements, depending on the potential used for analyte detection. Notably, urea and lactate are significant molecules commonly found in blood, with average concentrations around 5 mmol/L (tending to increase with age)⁶⁷ and below 2.2 mmol/L⁶⁸, respectively. In enzyme-free sensors, the same catalytic strategy, e.g., nickel oxide species in alkaline conditions, not only allows oxidation at similar potentials for both urea⁶⁹ and lactate⁷⁰ but also glucose²⁴. Therefore, careful attention has to be paid to the selectivity when one of these analytes is measured by non-enzymatic approach. Additionally, antioxidants like uric acid or ascorbic acid, both present in blood with concentrations at around 500 μ mol/L⁷¹ and below 114 μ mol/L⁷²⁻⁷⁴, respectively, should be also investigated. Even without metallic catalysts on reduced graphene oxide/graphene oxide-based electrodes, these antioxidants can be easily oxidized at low potentials⁶³. Other vitamins present in blood, such as biotin (<3.1 μ M)⁷⁵, folic acid (<45 nM)⁷⁶ or riboflavin (<98 nM)⁷⁷ do not require as much attention in selectivity studies due to their relatively low concentration. Neurotransmitter, i.e. dopamine, which can be easily oxidized at a low potential⁷⁸ without the need of a certain catalyst⁶³ are usually also negligible in selectivity studies due to their extremely low concentrations (pM to μ M range)^{68,79-81}. In blood, there are also unbound amino acids, which could possibly interfere with the analyte by oxidation reaction at relatively high potentials⁸². The concentration of free amino acids in blood varies from <20 μ M (i.e., glutamic acid) up to 780 μ M (i.e. glutamine)⁸³. Thus, if a high oxidation potential is needed for the analyte of interest (>0.5 V vs. Ag/AgCl), a selectivity study should at least take glutamine into account. In addition, although cholesterol is not soluble in water, its concentration in blood is approximately 5.5 mM⁸⁴ due to the presence of lipoproteins. Consequently, apart from selectivity studies it is essential to emphasize the importance of anti-biofouling strategies when performing measurements in pure blood or human serum, not only because of the possible interference of cholesterol, but also because of blocking of the electrode due to high protein levels (60-80 mg/mL)⁶⁶.

Dermal interstitial fluid

Interstitial fluid, a biofluid akin to blood, has been considered an alternative sample fluid as it can be accessible through minimally invasive means with just a few millimeters beneath the skin, holds great promise for continuous biomolecule monitoring through wearable enzyme-free sensor. In principle, analytes can enter the interstitial fluid in mainly three ways, (i) through the plasma membrane of endothelial cells (transcellular), (ii) by diffusion through the space between cells (paracellular), and (iii) within vesicles through cells (transcytosis)⁸⁵. One crucial parameter in such online-measurements is the lag-time, which denotes the duration from when a rise in blood concentration occurs to when it is mirrored in the biofluid concentration, i.e., interstitial fluid. The lag time of interstitial fluid varies depending on the patient⁴ and the study, typically ranging from 0 and 20 minutes⁸⁶. It is notable that the commercially available continuous glucose monitoring systems are using interstitial fluid, realized by microneedle electrode systems⁸⁷. The pH present in interstitial fluid is also similar to blood (pH= 7.2-7.4)⁶⁶.

Concentrations of analyte, e.g., glucose, cholesterol and lactate in interstitial fluid are highly similar to blood levels⁸⁷. As a result, similar considerations towards selectivity and anti-fouling studies should be performed as for blood, mentioned above. Nevertheless, in comparison to blood the total protein concentration in interstitial fluid is much (13-20 mg/mL)⁸⁷, making the measurement in interstitial fluid less prone to biofouling.

Sweat

Sweat is a non-invasive biofluid that provides easy access for sensors, which can be integrated into wearable devices typically placed on the skin⁴. Additionally, interstitial fluid surrounds sweat glands, allowing important analytes present in interstitial fluid to also be found in the sweat⁸⁵. However, the sweat rate varies depending on factors such as the patient's condition, the environmental humidity, the specific body location of the sensor, and the patient's activity level. There are additional challenges associated with sweat-based sensing itself. First, the skin is susceptible to contamination, and old sweat mixing with new sweat can lead to inaccurate result because the changes in analyte concentrations in the new sweat are altered by the presence of the old sweat. Second, the temperature of the sensor is highly dependent on its position on the body, the patient's activity, and the weather conditions. Last, the analyte-concentration levels and pH of the sweat are dependent on the specific body location of the sensor⁸⁸.

The pH of sweat typically ranges from 4.0 to 6.8^{66,89} and the lag time between blood and sweat measurements for both ethanol⁹⁰ and glucose⁹¹ are approximately 10 minutes. The sweat-glucose to blood-glucose ratio varies from 0.005 to 0.03, depending on the sweat rate⁹². Notably, a study by Moyer et al. observed a slightly higher sweat-glucose to blood-glucose ratio for increased sweat rates⁹². Despite these variations, changes in sweat-glucose levels do indeed indicate corresponding changes in blood-glucose levels⁹². Calibration by measuring glucose levels in both blood and sweat is however essential

to mitigate inaccuracies arising from individual patient differences. Given that glucose concentrations in human sweat are considered low (ranging from 0.06 to 0.2 mM⁹³ or in some studies up to 1.11 mM⁹⁴), thus achieving high sensitivity in sweat-based sensor is crucial compared to the sensors developed for measuring in blood or interstitial fluid. Although biofouling is less problematic due to low total protein concentrations in sweat (typically 0.1 to 0.7 mg/mL)⁶⁶, the presence of high metabolite concentrations necessitates a thorough selectivity study. Especially the high concentration of lactate (5-40 mM)⁹⁵ and of urea (4-12 mM)⁹⁵ highlights the need in investigating the interference of these two biomarkers when ones want to measure glucose in sweat, for instance. Ammonia, a waste product formed by bacteria during protein digestion, is found in sweat (1-8 mM) at higher concentrations than in blood⁹⁵. With that, also ammonia should be part of a selectivity study for non-enzymatic detection in sweat sensors, since it can be oxidized at low potentials by for example core-shell Pt–Ni(OH)₂ nanosheets on Ni foam electrodes⁹⁶. The low concentration of other metabolites like uric acid (~25 μM)⁹⁷ or ascorbic acid (~10 μM)⁹⁵ and free amino acids (<13 μM)⁹⁵ make them in selectivity studies negligible.

Saliva

Saliva is a non-invasive biofluid that provides easy access for sensors, which can be integrated into pacifiers⁹⁸ or mouth guards⁹⁹. Furthermore, saliva can be conveniently used for non-continuous measurements by spitting into a sample collector. The implementation of a sensor into a pacifier is especially relevant for newborns and babies. On average, a normal person produces 1000-1500 mL of saliva per day⁴. However, the secretion of saliva can vary significantly based on the patient's age, diseases or diet. Additionally, the average correlation between blood glucose and saliva glucose levels varies - sometimes better and sometimes worse- depending very much on the study and subject (study 1: R²= 0.629¹⁰⁰; study 2: R²= 0.881¹⁰¹). However, in a study with only one patient, blood and saliva glucose levels were measured at fasting state on different days, and a very good correlation between both body fluids was observed (R²=0.962)¹⁰². This indicates the need for individual calibration using both blood and saliva for each patient. Other analytes like cortisol are present in saliva in similar concentrations like in blood and the correlation between both levels seems to be very promising⁸⁵, especially since much less interferences are present in saliva compared to blood. Although saliva is a very promising biofluid, studies suggest that patients should fast during measurement to prevent contamination from food or drinks⁸⁵. With a saliva-to-blood concentration ratio of around 1:100¹⁰¹, low total protein concentrations (0.2-5 mg/mL)⁶⁶, and a pH range between 6.2 and 7.4⁶⁶, prioritizing sensitivity over anti-biofouling is advisable.

Considering a selectivity study, saliva consists of around 99% of water and the rest are inorganic compounds, such as electrolytes, and organic compounds such as uric acid (~200 μM)¹⁰³, creatinine (3-400 μM, mean: 11μM)¹⁰⁴, glucose (0-55 μM)¹⁰², cholesterol (up to 460 μM for patients with hyperlipidemia)¹⁰⁵, lactate (200-600 μM)¹⁰⁶, and polypeptides¹⁰⁷. Mashazi et al developed a glucose

sensor for saliva and investigated interference caused by sodium chloride, urea, sucrose, fructose, ascorbic acid, uric acid and dopamine at a concentration of 500 μM ¹⁰⁸.

Urine

Urine is a non-invasive biofluid that provides convenient access for sensors, which can be integrated into diapers¹⁰⁹, making it relevant for in-situ monitoring relevant biomarkers from newborns or babies. Furthermore, collecting a urine sample is painless and straightforward. The pH of urine varies from 4.5 to 8, and it primarily consists of waste substances that the body needs to excrete⁶⁶. However, measuring urine analytes can be challenging due to significant variations in concentration based on factors such as urine volume, sample collection time, and patient characteristics (e.g., gender, age, food intake, medication, and exercise)¹¹⁰. Additionally, urine analytes may differ in their existing form compared to their counterparts in blood due to metabolism. To obtain reliable data, it is essential to collect samples from the same patient over an extended period. Considering the lag time of urine is unnecessary since continuous sampling is not feasible.

With over 3000 metabolites identified, urine serves as an excellent matrix since it has the potential to be an indicator for various diseases, especially for diabetes and kidney disorders¹¹⁰. However, the abundance of diverse substances in urine can pose significant challenges to non-enzymatic sensors, in particular, in terms of selectivity. Nevertheless, the primary composition of urine includes water (95%), urea (2%), creatinine (0.1%), uric acid (0.03%), and ions (Na^+ , Cl^- , SO_4^{2-} , NH_4^+ , PO_4^{3-})¹¹⁰. For instance, when creatinine is the analyte of interest, researchers like Chen et al. have investigated interfering substances such as uric acid, ascorbic acid, ammonium, and urea¹¹¹. Due to the immense number of metabolites, the choice of additional interfering substances in a selectivity study should involve molecules present in urine that share a similar structure and concentration with the specific analyte. Notably, urine has the lowest protein concentration among all mentioned biofluids (below 0.1 mg/mL)⁶⁶, eliminating concerns related to antibiofouling.

Breath

Breath serves as a non-invasive sample of the body, offering high potential for early disease detection¹¹². Additionally, sensors can be easily integrated into a mask, enabling POC detection or even online measurements¹¹³. A significant advantage, even in continuous monitoring, is that the biocompatibility of the sensor is less concerned, because, when implemented in a mask, there is no direct contact between the sensor and the patient. The pH of exhaled breath condensate typically ranges from 7.8 to 8.1¹¹³, and respiratory fluid is believed to have a stable exchange with plasma, with short lag times¹¹⁴.

Regarding selectivity, exhaled breath primarily contains nitrogen, oxygen, carbon dioxide, water, and various compounds which are also found in blood. However, most of these compounds exist at concentrations 100 to 1000 times lower than in blood¹¹³. Sakumura et al. identified 63 volatile organic compounds (VOCs) in breath, with 43 of them approaching the limit of detection using gas-

chromatography/mass spectrometry¹¹⁵. These borderline VOCs can be disregarded in selectivity studies. The remaining VOCs are present at concentrations up to 0.3 ppb (e.g., CH₃CN), between 1 and 5 ppb (e.g., CHCl₃, CHN, 1-propanol, C₂H₃CN, limonene) and between 100 and 200 ppb (e.g., methanol, ethanol, isoprene)¹¹⁵. Other VOCs detected include butane, acetone, 2-propanol, C₈H₁₆, dichlorobenzene, C₈H₁₇OH, xylene, methylcyclohexane, toluene, and nonanal¹¹⁵. Furthermore, non-volatile components such as glucose or peptides are also present¹¹³. While the average concentration of glucose in respiratory fluid within the lungs is approximately 0.4 mM (diluted by a factor of 12 compared to blood), the concentration in exhaled breath condensate ranges from 0.24 to 5.5 μM¹¹⁴. Additionally, low molecular-weight components like ammonia and hydrogen peroxide are found in breath¹¹⁴. Ammonia levels can be elevated in exhaled breath condensate due to the high partial pressure of CO₂, creating an acidic environment that efficiently traps ammonia¹¹⁴. However, hydrogen peroxide levels are typically elevated in patients who are suffering from lung cancer and asthma¹¹⁴. When studying breath measurements, the focus should primarily be on sensitivity, and considerations related to antibiofouling may be less relevant, since total protein concentration of breath condensate is very low, i.e., at around 1 μg/mL^{116,117}.

1.6.2 Non-clinical sample

Water

Water serves as the foundation of human life, and the quality of drinking water significantly impacts human health and well-being. Although the release of pollutants into European water bodies due to economic activities has decreased over the last decade, there remains room for improvement. Notably, heavy metals releases -such as cadmium (Cd), mercury (Hg), nickel (Ni), and lead (Pb)- have not shown improvement between 2016 and 2021¹¹⁸. However, these heavy metals pose serious health risks even at low concentrations. Beyond Europe, underdeveloped and developing countries face even greater challenges due to lack of strict policies, insufficient capital for expensive waste treatment, and the prevalence of large-scale mining industries. Consequently, water pollution poses a significant problem in these regions.

Given this context, monitoring water pollution becomes crucial for efficient pollutant removal. Pollutants can be categorized into two main classes, i.e., organic pollutants (e.g., antibiotics and pesticides), originating from human and veterinary medicine¹¹⁹ or agricultural runoff¹²⁰, and inorganic pollutants (e.g. Cd, Hg, Ni, Pb, chromium (Cr), and arsenic (As) ions), usually caused by industrial processes¹²¹. Additionally, several other parameters warrant measurement, including pH, nitrogen-containing molecules (ammonia, nitrate, and nitrite), water hardness, dissolved oxygen levels, disinfectants (such as free chlorine or hydrogen peroxide), and sulfide/sulfite content¹²². Furthermore, the presence of microplastic caused by rising plastic waste in water has become increasingly more relevant due to their potential health impacts. A study by Goodman et al. demonstrated the need of

comprehensive microplastic monitoring, as microplastic intake can adversely affect kidney and liver function, thereby impacting human health negatively¹²³.

In the field of toxic metal ion detection, selectivity and anti-biofouling studies depend on the specific water being analyzed. Cho et al.'s review highlights typical ions studied for selectivity, including Cu(II), Fe(II), Fe(III), Ni(II), Zn(II), Cr(III), As(III), Sb(III), Se(IV), Pb(II), Al(III), Fe (III), Ni (II), Co (II), fluoride (F⁻), thiocyanate (SCN⁻), iodide (I⁻), phosphate (PO₄³⁻), sulfate (SO₄²⁻), nitrate (NO₃⁻), sodium (Na⁺), calcium (Ca(II)), magnesium (Mg(II)), potassium (K⁺), and carbonate (CO₃²⁻)¹²². Additionally, investigations have explored the interactions of benzene, xylene, surfactants, and ethylenediaminetetraacetic acid (EDTA) with analyte metal ion¹²².

Altahan et al. developed a non-enzymatic sensor for ammonium in water and tested its selectivity against interfering ions such as Na(I), Ca(II), Mg(II), nitrate, phosphate, F(-I), Cl(-I), formate, acetate, oxalate and β-phthalate¹²⁴. Furthermore, they measured the recovery after spiking tap and mineral water samples with ammonium¹²⁴. For such cases, anti-biofouling studies are not needed due to the expected low amount of proteins in the real samples.

Considering pesticides, especially organophosphorus pesticides (OPPs), which are derivatives of phosphoric, phosphinic, phosphonic acids, or phosphorothionate, are very popular due to their efficiency, selectivity, and fast degradation¹². However, OPPs pose significant ecological and health risks, necessitating the development of effective detection methods¹². Due to the low maximum residue limits of OPPs (ranging from 0.01 to single-digit ppm concentrations, depending on the country), achieving good selectivity through direct electrochemical detection is challenging¹². This is because fruits and vegetables contain many antioxidants in high concentrations, which, due to their function as antioxidants, have low oxidation potentials. Furthermore, non-enzymatic sensors offer hardly the ability to distinguish between structurally similar organophosphorus pesticides. Therefore, affinity-based approaches such as molecularly imprinted polymers (MIPs) seem to be more promising¹²⁵.

Food and beverages

Food and beverages play a crucial role in our daily lives, and ensuring their safety and quality is essential. Just as water quality affects human health, the composition of food and beverages can significantly impact consumers. Common analytes in food and beverage samples include contaminants¹²⁶ such as hydrazine (N₂H₄), malachite green, and bisphenol A), additives¹²⁶ (like ascorbic acid, caffeine, caffeic acid, sulfite, and nitrite), inorganic pollutions (as discussed in chapter 4.2, water), pesticides (categorized into insecticides, miticides, herbicides, nematicides, fungicides, molluscicides, and rodenticides)¹²⁷, pathogens¹²⁸ such as *Escherichia coli*, allergens¹²⁸ (e.g., gliadin, a protein component of gluten), and toxins¹²⁸ such as botulinum toxin. The vast majority of complex analytes highlights the need for affinity elements, including antibodies, aptamers, and molecular imprinted polymers¹²⁷.

Regarding antibiofouling and selectivity studies, given the wide variability in sample matrices, it is crucial to recognize that generalizing findings across all samples may not be appropriate. However, one approach we recommend for such studies is to measure the analyte in the real matrix of the final application (which is of course also essential for other matrices than food and beverage). Analyzing the analyte within the actual matrix of its intended application provides insights into real-world behavior, accounting for potential interferences and matrix effects. Researchers can spike the sample with the analyte at various concentrations and investigate reproducibility and recovery. Additionally, exploring structurally related compounds, especially those with similar applications, allows us to assess cross-reactivity and specificity (for example, investigating other pesticides when an insecticide is the analyte)¹²⁹. However, it is important to note that diluting the real matrix with a buffer is acceptable, but extreme dilution can distort results and is prone to cause errors especially when applied to analytes with extremely low concentrations. Researchers should aim for a dilution factor within the range of 1 to 10 to maintain relevance. Many recovery studies have reported great recovery rates. However, it should be noted that many of these studies typically performed sample dilution prior to spiking the analyte of interest. Such experiment does not well-reflect the real effects of matrix that has on the spiked analyte. Instead, the analyte should be spiked into undiluted samples, and later perform dilution to eliminate interfering effects from the food or beverage matrices.

Cell culture medium

Monitoring substrate consumption and product generation of bioreactor in a precise and, ideally, real-time manner is crucial in controlling productivity and product quality¹³⁰. Non-enzymatic electrodes are highly promising and practical in this area owing to their low cost and superior stability under common sterilization techniques. Bioreactor typically contains cell culture media that play a pivotal role in preserving, amplifying, and differentiating various cell types for bio-manufacturing products of interest. Cell culture media are essential for maintaining and growing cells *in vitro*, providing an artificial environment that simulates the natural conditions for cultured cells. The main tasks of cell culture media include supplying energy sources to the cells, maintaining proper salt balance and pH for a healthy cell growth, and facilitating the removal of cellular waste products.

Cell culture media typically contains well-defined composition. For example, a typical *E.coli* culture medium, namely LB-Bouillon (Lennox; Sigma Aldrich), contains 5 g/L NaCl, 10 g/L tryptone, 5 g/L yeast extract. It is buffered between a pH of 6.8 to 7.2 (usually using a phosphate buffer). Additionally, glucose, a crucial energy substrate, is added to cell culture media in concentrations, typically ranging from 5 to 25 mM. The typical high concentration of substrate makes the development of highly sensitive non-enzymatic sensors less concerned. However, a number of electroactive species in the culture media can potentially generate interfering signals which have to seriously take into account for selectivity studies. For example, tryptone and yeast extract contribute a variety of amino acids, e.g., glutamic acid, aspartic acid and lysine, in relative high concentrations, and vitamins, e.g., B₁, B₂, B₆, nicotinic acid,

biotin, pantothenic acid, and folacin¹³¹. Furthermore, yeast extract provides a rich source of proteins, emphasizing the need for anti-biofouling studies, in particular for online-monitoring purpose. It is also plausible to develop in situ cleaning procedure to recovery non-enzymatic electrode' functionality during operation.

Table 1. 2: Sample matrices, their properties, and considerations for enzyme-free sensor development.

Matrix (pH)	Relevant compound (concentration)	Advantages	Disadvantages	Concerns for enzyme-free sensors development
Clinical sample				
Blood (7.3-7.4)	<ul style="list-style-type: none"> -Glucose (3.9-5.6 mM) -Urea (~5 mM) -Lactate (<2.2 mM) -Uric acid (~0.5 mM) -Ascorbic acid (~0.1 mM) -Free amino acids (0.02-0.78 mM) -Cholesterol (5.5 mM) -Total protein (60-80 mg/mL) 	<ul style="list-style-type: none"> -High abundance of analytes -High accuracy 	<ul style="list-style-type: none"> -Invasive -High protein and interference concentration 	<ul style="list-style-type: none"> -Selectivity -Antibiofouling
Interstitial fluid (7.2-7.4)	<ul style="list-style-type: none"> Similar to blood -Total protein (13-30 mg/mL) 	<ul style="list-style-type: none"> -Continuous monitoring -Wearable devices 	<ul style="list-style-type: none"> -Minimal invasive 	<ul style="list-style-type: none"> -Selectivity -Antibiofouling -Lag time (0-20 min)
Sweat (4.0-6.8)	<ul style="list-style-type: none"> -Glucose (0.06-0.2 mM) -Lactate (5-40 mM) -Urea (4-12 mM) -Ammonia (1-8 mM) -Total protein (0.1- 0.7 mg/mL) 	<ul style="list-style-type: none"> -Continuous monitoring -wearable devices -Non-invasive 	<ul style="list-style-type: none"> -many factors that influence individual sweat rate 	<ul style="list-style-type: none"> -Sensitivity -Selectivity -Body location of sensor -Lag time (~10 min) -Correlation between blood and sweat level
Saliva (6.2-7.4)	<ul style="list-style-type: none"> -Glucose (<0.055 mM) -Uric acid (0.2 mM) -Creatinin (<0.4 mM) -Cholesterol (<0.46 mM) -Lactate (0.2-0.6 mM) -Total protein (0.2- 5 mg/mL) 	<ul style="list-style-type: none"> -Non-invasive -Continuous monitoring -Sensor integrateable in pacifier (newborn diagnostics) -low amount of interferents 	<ul style="list-style-type: none"> -many factors that influence secretion of saliva -Contamination from food and drinks 	<ul style="list-style-type: none"> -Sensitivity -(Selectivity) -Lag time -Correlation between blood and saliva level

Matrix (pH)	Relevant compound (concentration)	Advantages	Disadvantages	Concerns for enzyme-free sensors development
Urine (4.5-8.0)	-Urea (2 %) -Creatinine (0.1 %) -Uric acid (0.03 %) -Total protein (0.1 mg/mL)	-Non-invasive -Sensor integrateable in diapers -low protein content	-Continuous monitoring not possible -many factors that influence concentrations	-Sensitivity -(Selectivity) -Sample should be taken over a longer periode
Breath (7.8-8.1)	-Glucose (0.005 mM) -Volatile organic compounds -Ammonia -Hydrogen peroxide -Lactate -Total protein (0.001 mg/mL)	-Non-invasive -Sensor integrateable in mask -Continuous monitoring -low protein content		-Sensitivity -(Selectivity)
Non-clinical sample				
Water	-Heavy metals -Antibiotics -Pesticides -Fertilizer -pH	-Less fouling	-Many possible interferences -Hard to be selective	-Sensitivity -Selectivity
Food and beverages	-Contaminants -Additives (Vitamins) -Pesticides -Allergens -Toxins -pH	-Usually, matrix is very well known	-Many possible interferences -Hard to be selective	-Sensitivity -Selectivity -Fouling
Cell culture medium	-Glucose (5-25 mM) -Phosphate -Amino acids -Vitamins -pH	-Very defined matrix	-Too high conc. -High concentrated interferences (Tryptone (10 g/L); Yeast extract (5g/L))	-Selectivity -Fouling

1.7 Other challenges and promising studies

1.7.1 Anti-fouling

Fouling, the non-specific adsorption of biological materials such as proteins (biofouling) or reaction products, poses significant challenges in non-enzymatic sensors. In POC diagnostics, minimizing sample treatment is crucial to reduce errors associated with additional processing steps and to simplify detection. The goal is to measure the analyte of interest in the presence of these fouling molecules without any influence or minimal disturbance from them. To achieve this, effective antifouling strategies are essential, ensuring accurate and reliable measurements especially in complex biological environments. Antifouling strategies include the use of polymer coatings¹³²⁻¹³⁶ (e.g., electro-neutral, hydrophilic polymers such as PEG, zwitterionic polymers, or conducting polymers), hydrogels^{134,135,137}, biomolecules such as peptides^{132,134,135} or proteins¹³⁵, nanoporous membranes^{136,137}, and self-assembled monolayers^{132-134,136-138} (e.g., thiols on gold surfaces). For example, Moonla et al. applied a layer of chitosan and poly(vinyl chloride) onto their microneedle working electrode using a drop-coating technique¹³⁹. This layer reduced biofouling during ketone measurements in human interstitial fluid¹³⁹. Additionally, Shin et al. applied a conductive PEG-PEDOT hydrogel, which ensured the sensor's non-fouling properties even in bovine blood diluted 1:1 in PBS¹⁴⁰. They photopolymerized a PEG hydrogel on an ITO electrode and then electropolymerized PEDOT¹⁴⁰. In this setup, PEDOT within the hydrogel coating served as an electrochemical transducer. Furthermore, Zhu et al. utilized a branched-shaped zwitterionic peptide on electrodeposited gold nanoparticles to enhance electron transfer and antifouling properties¹⁴¹. The biosensor exhibited excellent stability in wastewater, retaining 91.8% of its initial signal after 15 days¹⁴¹.

Apart from coatings, an electrochemical cleaning step can be used before measurement to remove adsorbed molecules¹³⁶. Additionally, the composition of the catalyst can influence the adsorption energy of the reaction product, thereby affecting the fouling caused by the analyte itself. Xi et al. showed through density functional theory calculations that the reaction product of hydrogen peroxide reduction binds more strongly to pure platinum nanoparticles compared to Pt-Ni alloyed nanoparticles, leading to a significant increase in the reaction rate when the alloy was used¹⁴².

1.7.2 Measurements performed under physiological conditions

Often, enzyme-free reactions are highly pH-dependent and do not work under physiological conditions. For example, glucose only reacts with certain catalysts in an alkaline medium¹⁴³. However, some catalysts do work under neutral conditions, but they often consist of expensive materials such as Au/Pt alloys or require complex synthesis strategies, such as creating core-shell structures¹⁴⁴. Furthermore, not only the catalyst but also the carbon matrix plays an important role. Mei et al. observed that PtNi nanoparticles could oxidize glucose at physiological pH when the particles were attached to multi-walled carbon nanotubes, but they observed no catalytic effect when a pristine carbon black sample was used as the matrix¹⁴⁵. Hence, the question of whether a catalyst can oxidize the analyte under

physiological conditions may be more complex than expected, and strategies to adjust the pH on the catalyst surface seem to be very useful. In this regard, researchers have proposed various strategies. For example, Zhu et al. used an Ecoflex™ porous rubber membrane containing 0.05 mM NaOH as a layer on top of the electrode to provide an alkaline environment¹⁴⁶. The authors successfully demonstrated the practical utility of the porous membrane integrated microfluidic non-enzymatic glucose sensors in sampling sweat and detecting glucose in sweat¹⁴⁶. Alternatively, Strakosas et al. exploited an electrode containing Pd nanoparticles to generate hydroxide ions at -1.0 V (vs. Ag/AgCl)¹⁴⁷. These ions diffused to the closely placed cobalt-oxide working electrode, which, at the reduced local pH, was capable of oxidizing glucose at +0.5 V¹⁴⁷. In a similar manner, Zhu et al. used a gold rod as a working electrode and applied a potential of -2.0 V for 20 s (vs. a polypyrrole-coated Pt quasi-reference electrode) to increase the local pH on the working electrode and subsequently oxidized glucose at +0.2 V¹⁴⁸. After that, a potential of +1.0 V was used to clean the electrode surface, enabling nonenzymatic wearable sensor for continuous real-time monitoring of perspiration glucose during physical activities¹⁴⁸.

1.7.3 Biocompatibility

Since non-enzymatic electrochemical sensors contain reactive and nanometric-sized catalysts, biocompatibility needs to be considered, even though the catalyst material itself may be macroscopically safe, such as noble metals. Especially for continuous measurements where the sensor, for example, directly touches the patient's skin over weeks, the safety of the product needs to be ensured by minimizing possible adverse reactions such as inflammation or toxicity. Biocompatibility also maintains the functionality of devices in preventing immune responses from the patient. Thus, biocompatibility is not only essential for safety and the patient's well-being but also enhances the longevity and stability of devices, making them suitable for long-term use. Furthermore, regulatory compliance needs to be considered to gain approval for clinical use. In the literature, several approaches have been proposed to achieve or prove biocompatibility of electrode materials. For example, Dang et al. tested the biocompatibility of their Prussian blue (PB) nanoparticles intercalated Ti₃C₂ nanosheets biosensor by conducting cytotoxicity assays using L292 mammalian fibroblast cells¹⁴⁹. Cells were co-cultivated with various concentrations of the sensor components, i.e., PB, Ti₃C₂, and PB/Ti₃C₂¹⁴⁹. The cytotoxicity was assessed using the MTT method¹⁵⁰. The authors have proven that the PB/Ti₃C₂ did not cause significant cytotoxicity to the investigated skin cells for 48 hr¹⁴⁹. They further demonstrated the real-time and *in situ* detection of H₂O₂ secreted from living HeLa cells using glassy carbon electrode modified with PB/Ti₃C₂¹⁴⁹. Besides the *in vitro* study shown by Dang et al., Chen et al. recently developed a non-enzymatic glucose sensor for sweat by incorporating gold nanoparticles onto aminated multi-walled carbon nanotubes as a catalyst¹⁵¹. The material was cross-linked in a carboxylated styrene-butadiene rubber and PEDOT:PSS matrix, which was consecutively dropped-cast onto a screen-printed electrode¹⁵¹. Biocompatibility was demonstrated by observing no allergic reactions or skin irritations after 48 hours of contact with a volunteer's skin¹⁵¹.

1.7.4 Long-term stability and storage conditions

In sensor development, studying the long-term usability of a sensor is crucial as it enables continuous monitoring. Continuous monitoring provides comprehensive data on a patient's health, detecting short-lived but significant health events that single measurements might miss¹⁵². Additionally, it reduces the impact of temporary fluctuations, allowing for a more accurate determination of the patient's health status¹⁵². Therefore, investigating the aging of electrodes during long-term measurements is essential, ideally identifying and preventing its causes. Furthermore, examining the storage conditions of a sensor and the effect of aging is vital if the sensor is to become a viable product. Several studies in the literature address long-term measurements and aging during storage. For example, Li et al demonstrated that freshly prepared graphene/graphite is more hydrophilic than traditionally expected¹⁵³. The adsorption of hydrocarbon contaminants from the air increases hydrophobicity¹⁵³. In addition, Behrent et al. investigated the aging of LIG electrodes under various conditions¹⁵⁴. They found that storage environment such as the container (glass or plastic) and sources of hydrocarbon contaminants, e.g., glue or nail polish used to insulate the electrode, significantly impacted the electrochemical performance and contact angle during aging¹⁵⁴. These examples highlight the need of effective strategies in protecting LIG surface after scribing. Here, Zhang et al. electrodeposited gold on a LIG electrode and further coated it with chitosan¹⁵⁵. The super hydrophilic Chitosan-Au-LIG showed superior performance not only after storage in ambient conditions (bare LIG: 90% decrease in redox peak currents after 30 days; Chitosan-Au-LIG: 3% decrease in redox peak currents after 30 days) but also after reuse¹⁵⁵. While bare LIG electrodes lost 33% of redox peak currents in a second measurement one day later, Chitosan-Au-LIG only lost 5% of performance after 10 consecutive days with a measurement each day¹⁵⁵.

1.7.5 Mobility and placement

In real-life scenarios, the use of commercial reference and counter electrodes, such as an Ag/AgCl-reference electrode or a platinum wire as a counter electrode often presents mobility challenges and restricts the possible sensor placement locations. Consequently, it becomes crucial to explore alternative approaches with high reliability. One such approach involves testing the material of the working electrode itself as a counter electrode or even using it as a reference electrode. By doing so, the stability of the produced pseudo reference electrode can be investigated by measuring its open circuit potential versus a commercial reference electrode⁷⁸. Notably, printed electrodes offer a convenient solution. In a printed 3-electrode system, all three electrodes can be placed next to each other on a planar surface, simplifying handling, ensuring always the same distance between the electrodes to enhance reproducibility, and reducing overall system complexity. This streamlined design also enhances cost-effectiveness and facilitates mass production.

Considering wearable sensors, the comfort of the user is paramount. The device should be lightweight, flexible, unobtrusive, and easy to wear for extended periods. Furthermore, they should be mechanically

stable and have a long lifespan, particularly for wearable devices that may be exposed to various environmental conditions and physical movements.

Especially when using the most common measurement techniques, such as chronoamperometry, cyclic voltammetry, differential pulse voltammetry, and square wave voltammetry, a battery-less NFC potentiostat offers significant advantages with comparable performance to commercial benchtop potentiostats^{156–158}. These potentiostats are approximately the size of a credit card and are affordable^{156,157}. The wireless power supply operates through inductive coupling between an NFC-capable smartphone and the potentiostat. The primary coil (smartphone) generates a magnetic field, while the secondary coil (potentiostat) receives energy¹⁵⁹. This enables devices to charge or power up without physical connections at distances of up to five centimeters¹⁵⁹. Additionally, communication between the potentiostat and the smartphone is based on electromagnetic induction¹⁵⁹. However, there are limitations in the potential ranges that can be used due to the NFC technology's limited power supply, which can be addressed through sensor miniaturization¹⁵⁶.

1.7.6 Efficiency, cost, and simplicity

Electrochemical sensors play a crucial role in rapid and efficient analyte detection, especially when working with minimal sample volumes. To achieve cost-effectiveness, it is advisable to produce electrodes from inexpensive raw materials, such as polymers or paper, rather than relying on for example commercial screen-printed electrodes as the foundation for the electrode system. This approach not only reduces overall costs but also minimizes dependence on external suppliers.

When designing the production process, consider energy efficiency. Avoid energy-intensive steps (such as heating) and aim for a continuous, streamlined process. As a general guideline, fewer production steps are the key for low-cost sensors. Prioritize simplicity in the overall product design—devices should be user-friendly, effective, and affordable.

Researchers are encouraged to provide detailed cost analyses of electrode materials and production expenses in their sensor publications. For instance, Perju et al. demonstrated a comprehensive breakdown of material costs for their electrode manufacturing in the supplementary information⁷⁸. Additionally, consider estimating the energy consumption associated with power-intensive steps (e.g., using ovens, heat plates, laser scribing, or electrospinning) in kilowatt-hours (kWh). This holistic approach ensures transparency and facilitates informed decision-making.

1.7.7 Practical considerations

Numerous studies investigating new electrode materials utilize chronoamperometry in stirred solutions. However, it is crucial to assess whether this approach aligns with the final intended application. The primary benefit of employing a stirred solution lies in the ability to conduct chronoamperometry until the signal stabilizes. This stabilization leads to improved standard deviation of the blank due to reduced signal fluctuations, resulting in significantly enhanced limits of detection (LODs). Additionally, the

stirred approach permits incremental addition of the analyte, facilitating the construction of a calibration curve on the same electrode within a single measurement. Consequently, this further minimizes standard deviation and enhances LOD. Furthermore, using a stirred measurement approach enhances mass transport, and since we patiently await a stable signal, there are no abrupt charging currents or background current shifts, as seen in non-stirred approaches when initiating a new measurement for each analyte concentration.

However, the stirred approach often proves impractical because customers prefer a simpler method: directly adding the sample onto the electrode and initiating the measurement. Despite its convenience for customers, the non-stirred approach presents challenges. It exhibits charging current at the measurement's outset, and variations in background currents occur from electrode to electrode and measurement to measurement, ultimately leading to an increased LOD. In conclusion, we encourage researchers to directly explore the certainly more challenging, non-stirred approaches. Hereby, alternative strategies are required to address the unique challenges associated with this approach. For example, in our research group, we developed a non-stirred hydrogen peroxide sensor. As part of the pretreatment, we needed to perform ten consecutive measurements in the blank at the same potential as the measurement itself, in order to ensure a stable background current before introducing hydrogen peroxide⁶³. If the resulting LODs of the non-stirred approach are not low enough for the desired application, an implementation of customer-friendly and simple strategies to preconcentrate or purify the samples before measurement could be used¹²⁹.

Another practical consideration for researchers is that some enzyme-free sensors face challenges in oxygen-dissolved solutions, as the presence of dissolved oxygen can interfere with the sensor's performance¹⁶⁰. This problem is often addressed by attempting to remove oxygen by bubbling nitrogen (N₂) through the solution, which is highly impractical for real applications. To address this issue, one potential solution is to incorporate oxygen-scavenging molecules to the sample such as sodium thiosulfate or ascorbic acid, which can remove or neutralize dissolved oxygen. However, these oxygen-scavengers could lead to interfering signals at the electrode (due to the low oxidation potential) or quench analytes such as hydrogen peroxide¹⁶⁰. Additionally, electrochemical filters can be used to remove oxygen¹⁶¹. In this method, a porous electrode is placed on top of the electrochemical sensor, separated by an additional porous layer, allowing for the electrochemically induced oxygen-reduction reaction to remove oxygen¹⁶¹. However, it is important to consider that the electrochemical removal of oxygen may change the local pH near the electrochemical sensor. Another approach could involve the development of sensor materials that are inherently resistant to oxygen interference, ensuring reliable performance even in oxygen-rich environments.

1.8 Conclusion and outlook

The review provided an overview of the advancement in non-enzymatic sensors and their potential applications towards point-of-care (POC) testing. Various strategies including conventional techniques, e.g., screen printing, and emerging strategy, have been employed for generating non-enzymatic electrodes in a mass-producing manner which will ultimately provide POC devices with low cost. In this regard, we evaluate the pros and cons of each technique. Moreover, we also provide characteristics of sample matrices as well as relevant analytes which need to be considered to efficiently apply non-enzymatic sensors raising specific points of concern in sensor development. We lastly give the discussion on other remaining challenges and some published studies as well as our viewpoints, which are promising to tackle such issues. In addition to this, we also want to give our perspective in the light of fabrication to end-users which could make non-enzymatic sensors to be more attractive for POC testing.

Although various kinds of fabrication technology have been proposed for generating non-enzymatic transducers, only some of them possess potential for POC devices considering speed and cost of production. Herein, screen-printing and roll-to-roll (R2R) printing are well established techniques allowing massive production of electrodes within a short time period. However, manufacturers must critically investigate the catalyst-ink formular to ensure its homogeneity and consequently electrode reproducibility. Typically, catalysts need to be blended with other conductive materials, e.g. carbon powder, and binding agent to assist printing and film formation process. This makes the embedded catalyst not useful, raising the concern about their cost-effectiveness, in particular, with costly catalyst materials. Therefore, creating a very thin film or developing the printing of pure catalysts would be favorable. In addition, further studies on adhesion between the formulated ink and various substrates, e.g., paper and textile materials, would allow the applications of non-enzymatic sensors to be expandable.

Apart from the conventional strategies, laser-induced carbon-graphene hybrid technology has emerged and gained popularity nowadays. Unlike thin film electrodes obtained from screen-printing and R2R printing, the laser-based fabrication method provides 3D-porous film with immense surface area which can rationally boost detection sensitivity. Even though the initial investment cost is high, it is considered effective for the long run overall. Nevertheless, laser-scribing technology is at an early stage which requires more development and careful attention. For example, highly porous electrodes, on one hand, are highly sensitive but could, on the other hand, cause poor reproducibility as well. This is because rough surfaces with microstructure typically exhibit hydrophobic properties which hinder inhomogeneous contact between aqueous solutions and electrodes. Thus, high wettability of the entire electrode surface must be ensured. This could be probably done by plasma treatment or chemical treatment. However, in case the problem still exists, variations between electrode-to-electrode may be solved by ratio metric measurements in which internal reference signal is used for normalization. Furthermore, properties of laser-induced non-enzymatic electrodes after production must be carefully

investigated. Based on our experience, the freshly produced electrodes yield high sensitivity, but the performance diminished over time after storage. Studies on storage conditions or development of protective coatings are encouraged to standardize electrode's property.

Various sample matrices constitute not only different levels of analyte but also distinct potential interferences which pose significant challenges in non-enzymatic sensors. Although blood contains a high abundance of analyte and is widely used in clinical diagnostics, other biological fluids which can be accessed non-invasively and contain fewer interfering species are preferential. These fluids include sweat, saliva, urine, and breath. However, the analytes in such biological samples are typically in a low amount. Therefore, highly sensitive non-enzymatic sensors are majorly required. Concerning the lag time, comparison analyte levels between blood and non-invasive biological fluids must be intensively conducted to guarantee reliability of the result. In addition to clinical samples, non-enzymatic sensors possess potential applications in measurement of analyte in water, food and beverages, and cell culture medium in bioprocess. Except water, the non-clinical samples typically contain high amount of analytes and interfering species. Most of reports suppress the interfering effect by diluting samples with measurement buffer. Nevertheless, an extreme dilution could potentially cause errors as analyte concentrations are reduced as well.

Finally, as discussed in the remaining challenges there have been many promising studies which can be exploited to overcome the issues. With these altogether and further developments we strongly believe that non-enzymatic sensors will become a robust and viable tool in POC testing in the future where desired analytical performance can be achieved in an affordable manner which eventually can improve quality of life.

2. Motivation and Structure of the Thesis

Electrochemistry is one of the most promising point-of-care techniques in analyte detection due to its direct on-site data readout, sensitivity, and scalability. These and more advantages, which were discussed in **Chapter 1**, make it a valuable tool. With more complex samples, electrochemical biosensors must become more sophisticated to achieve sensitive and selective detection of specific analytes amidst many interfering substances. This is typically achieved with enzyme-based electrochemical sensors. Currently, three generations of enzyme-based biosensors exist, distinguishable by how the electrode communicates with the enzyme: (i) detecting the co-substrate/-product of the enzyme reaction, (ii) using a synthetic redox mediator, or (iii) enabling direct electron transfer with a nanomaterial-based electrode. Besides their high specificity that also works in complex sample matrices, enzymes have several disadvantages, such as high costs and instability under harsh conditions (e.g., sterilization). Therefore, the 4th generation of electrochemical biosensors, which employs an enzyme-free approach with the analyte reacting directly on the electrode surface, needs to emerge as the future of biosensor technology.

Chapter 1 provides a broad overview of the 4th generation of electrochemical biosensors, i.e., enzyme-free sensors. It begins by highlighting the need for affordable sensors not only in diagnostics but also in environmental monitoring and food safety, which can be fulfilled by enzyme-free electrochemical sensors. Furthermore, it defines “non-enzymatic”, a term ambiguously used in literature, and investigates the non-enzymatic detection mechanism of one of the most widely measured analyte, glucose. The chapter then introduces conventional and emerging fabrication methods for producing non-enzymatic electrochemical sensors and compares them in terms of their practicability for mass production. It also discusses the problems and possibilities of clinical and non-clinical sample matrices, focusing on what to consider when developing an electrochemical sensor for each matrix. The final part of this chapter discusses promising strategies and technologies for addressing remaining challenges, e.g., anti-fouling, biocompatibility, and practical considerations.

In our working group, we developed one of the emerging fabrication methods introduced in **Chapter 1.5**, namely laser scribing of nanofibers, to produce a porous electrode material with embedded nanocatalysts. This method involves a two-step production process: (i) electrospinning a spinning solution of commercially available raw materials (polymer granulate, metal salts, organic solvent) to produce nanofibers, and (ii) laser-scribing these nanofibers with a CO₂ laser to form laser-induced carbon nanofibers (LCNFs) used as an electrode. Both methods are suitable for mass production and can be rapidly adjusted to meet other challenges and applications (e.g., adjusting fiber mat thickness by spinning time, catalyst material by the introduced metal salt, and carbonization of the fiber mat by laser power).

However, in the detection of glucose of a previous LCNF study, despite achieving very low limits of detection, impractical conditions such as a stirred measurement setup and a high pH of the analyte solution (0.5 M NaOH) were used, which strongly deviates from the pH of biological samples. To fit the requirement of electrochemical sensors applicable to real sample matrices, the electrodes need to be

adapted. Therefore, first an in-depth characterization of the electrode material to fully understand the chemistry behind the electrochemical measurement is conducted. The main goal is then to further develop the LCNF electrode material and detection method to ensure practical and user-friendly analyte detection suitable for real-world applications. In the development of the electrode material, pure metal LCNFs (Ni, Pt) are compared with their alloyed LCNFs, as these are known to improve the catalytic behavior.

In **Chapter 3**, pure Pt and Ni LCNFs, as well as Pt-Ni-alloyed LCNFs of various compositions, are investigated for their catalytic behavior towards hydrogen peroxide, an important molecule in many metabolic processes. It shows how metal concentration and composition influences the morphology (investigated by SEM) and the effective surface area (measured electrochemically) of the electrode material. Due to selectivity issues in the presence of ascorbic acid, uric acid, and dopamine, strategies to prevent interferences are tested. Additionally, the recovery of measurements in pure and diluted human serum as well as the impact of thin polymer films added by drop-coating on top of the electrode were examined.

Furthermore, **Chapter 3** contains unpublished results aimed at further solving the selectivity problem in hydrogen peroxide detection. The first approach involved using the same electrode material but at a lower/slightly negative potential. Since no good stabilization of the blank measurement was observed in non-stirred conditions, a new measurement strategy was employed. Here, a blank measurement in PBS was followed by a measurement in a hydrogen peroxide solution, and the difference between both signals was plotted against the hydrogen peroxide concentration as a calibration curve.

The second approach in the unpublished results of **Chapter 3** explores using polyoxometalates (POMs) as catalysts for hydrogen peroxide detection at a slightly negative potential. Initially, POMs were investigated by cyclic voltammetry at various pH conditions for stability and catalytic activity towards hydrogen peroxide reduction. $\text{SiMo}_{12}\text{O}_{40}^{4-}$ (SiMo) emerged as the most promising candidate. Various methods to attach SiMo onto the LCNF surface were explored, such as co-spinning and consecutive laser scribing, drop-coating on untreated LCNF, and drop-coating on PEGylated (Pt-)LCNF.

Chapter 4 contains the most promising results of the thesis and starts with an extensive characterization of the Pt-Ni-alloyed LCNFs using various methods. The formation, structure and composition of the nanoparticles is investigated by transmission electron microscopy coupled with energy-dispersive X-ray spectroscopy (TEM-EDX) and X-ray photoelectron spectroscopy (XPS). The structure and chemistry of the carbon matrix is revealed by small angle X-ray scattering (SAXS) and XPS, respectively. The goal was to enable glucose detection, one of the most important analytes in diagnostics, under physiological conditions. Usually, glucose oxidation on Ni catalysts is only achieved at an alkaline pH. The goal could then be accomplished by *in situ* generating a local high pH electrochemically at the Pt sites of the alloy, prior to the measurement. Hereby, pretreatment and catalyst-cleaning conditions are optimized, and the selectivity of the sensor is investigated. Additionally, the aging of the electrodes is monitored by contact angle measurements and the impact on the overall performance of these electrode

(limit of detection). For future goals such as an application in health diagnostics, the impact of sterilization on the performance of the electrode towards glucose detection is also investigated, as well as the recovery of glucose signal in 20% human serum.

In **Chapter 5**, the previously investigated Ni-LCNFs are applied for non-invasive diagnostics, i.e., detection of glucose in simulated breath. For better applicability, working-, counter- and reference-electrode are laser scribed as a 3-electrode system on the nanofiber mat. In this approach, the porosity of the LCNF electrodes is used to capture glucose from an aerosolized glucose solution. Drying the electrode after the capturing is not only used to concentrate glucose at the electrode surface but also to remove interferent volatile components which could be found in human breath. After drying, a defined amount of 0.1 M NaOH solution is placed on the electrode as an electrolyte and a source of hydroxide ions, needed for a functional nickel catalyst. The challenge in this work is that the electrode can't be calibrated before the measurement since the glucose is already deposited and would be consumed. Furthermore, batch to batch variations are too high to enable a simple current readout. Facing these problems, our approach conducts a simple CV measurement, which contains the oxidation peak and the reduction peak of the Ni-catalyst. Since, at low glucose concentrations, mainly the oxidation peak is increased by the addition of glucose, the reduction peak of the catalyst only reflects the amount of Ni-catalyst in contact with the solution on each individual electrode. By taking the ratio of both peaks, we achieve to have a glucose concentration measurement and an internal calibration just by using one measurement. Furthermore, the correlation between the glucose solution in the nebulizer and the captured solution on the electrode as well as the signal of possible interferents are investigated.

Chapter 6 summarized the overall results and key findings of this thesis. Furthermore, remaining problems and suggestions to solve them as well as future perspectives of LCNFs are discussed.

3. Investigating nanocatalyst-embedding laser-induced carbon nanofibers for non-enzymatic electrochemical sensing of hydrogen peroxide

3.1 Abstract

In this present study, we explored the catalytic behaviors of the in situ generated metal nanoparticles, i.e., Pt/Ni, embedded in laser induced carbon nanofibers (LCNFs) and their potential for H_2O_2 detection under physiological conditions. Furthermore, we demonstrate current limitations of laser-generated nanocatalyst embedded within LCNFs as electrochemical detectors and possible strategies to overcome the issues. Cyclic voltammetry revealed the distinctive electrocatalytic behaviors of carbon nanofibers embedding Pt and Ni in various ratios. With chronoamperometry at +0.5V, it was found that modulation of Pt and Ni content affected only current related to H_2O_2 but not other interfering electroactive substances, i.e., ascorbic acid (AA), uric acid (UA), dopamine (DA), and glucose. This implies that the interferences react to the carbon nanofibers regardless of the presence of metal nanocatalysts. Carbon nanofibers loaded only with Pt and without Ni performed best in H_2O_2 detection in phosphate buffered solution with a limit of detection (LOD) of 1.4 μM , a limit of quantification (LOQ) of 5.7 μM , a linear range from 5-500 μM and a sensitivity of $15 \mu\text{A} \cdot \text{mM}^{-1} \cdot \text{cm}^2$. By increasing Pt loading the interfering signals from UA and DA could be minimized. Furthermore, we found that modification of electrodes with nylon improves the recovery of H_2O_2 spiked in diluted and undiluted human serum. The study is paving the way for the efficient utilization of laser-generated nanocatalyst embedding carbon nanomaterials for non-enzymatic sensors, which ultimately will lead to inexpensive point-of-need devices with favorable analytical performance.

This chapter has been published and formatted to fit this thesis:

Bruckschlegel, C., Schlosser, M. & Wongkaew, N. Investigating nanocatalyst-embedding laser-induced carbon nanofibers for non-enzymatic electrochemical sensing of hydrogen peroxide. *Analytical and Bioanalytical Chemistry* 415.18 (2023): 4487-4499.

3.2 Author contributions

The author and Dr. Nongnoot Wongkaew contributed equally to design of the experiments. The author conducted the experiments and evaluated the data. Dr. Marc Schlosser conducted SEM-EDX measurements shown in Figure 3.2. The author and Dr. Nongnoot Wongkaew wrote the manuscript draft. Dr. Nongnoot Wongkaew led the project administration.

3.3 Graphical abstract

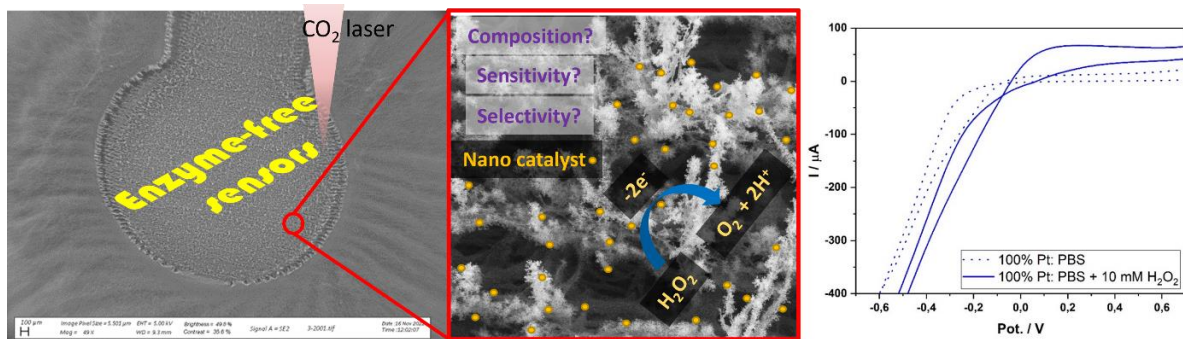


Figure 3. 1: Graphical abstract of chapter 3.

3.4 Introduction

Hydrogen peroxide (H_2O_2) is one of crucial small molecules not only present in living organisms but also in industries and environment as usage agents or contaminants¹⁶². Apart from these, H_2O_2 is formed in catalytic reactions by many oxidases, e.g., glucose oxidase, which are commonly detected or used in many biosensing platforms^{163,164}. Monitoring H_2O_2 both released from cells or inside cellular compartment under physiological conditions is of interest as H_2O_2 plays a crucial role in regulating characteristics of cells. Abnormality in H_2O_2 level in physiological processes can potentially be an indicator of many diseases, including cancer¹⁶⁵. Continuous monitoring of H_2O_2 through wearable devices has recently received much attention. For example, detecting H_2O_2 in wound through a bandage is beneficial for preventing chronic and infectious wounds¹⁶⁶. Furthermore, H_2O_2 in exhaled breath can be a biomarker for asthma, lung cancer, and pulmonary disease¹¹³. Trends in developing H_2O_2 sensors is thus pointed towards onsite and continuous measurement.

Titration¹⁶⁷, spectroscopic^{168,169}, fluorescent¹⁷⁰, and chemiluminescent methods¹⁷¹ have been traditionally employed for detecting H_2O_2 . Nevertheless, the aforementioned techniques are not suitable for onsite monitoring. Instead, with well-established miniaturized readers, electrochemical methods are more attractive and can realize simpler, faster, more sensitive and cost-effective measurements. Electrochemical detection of H_2O_2 using peroxidase, e.g., horseradish peroxidase (HRP), has been widely used due to favorable sensitivity and selectivity¹⁷². Nevertheless, cost and instability of enzyme make enzyme-based biosensors less attractive in practice, in particular in resource-limited areas. Therefore, the development of non-enzymatic electrochemical sensors for H_2O_2 detection has thus caught our attention.

Since Tour's group pioneered the utilization of a CO_2 laser for patterning carbon nanomaterials on commercial plastics, e.g., polyimide (PI) film, a great number of follow-up research has been carried out, which also included the development of smart sensors^{173,174}. Large production capacity, high flexibility in electrode design, cost-effectiveness in terms of materials and instrumentation, and desirable analytical performance of the laser-generated carbon nanoporous materials make the strategy highly attractive to be used in electrochemical sensors, especially towards affordable point-of-need devices.

Furthermore, introducing functional entities into polymeric carbon precursors prior to laser-pyrolysis allows one to create carbon nanomaterial hybrids, which not only further enhance electron transfer but also enable additional capability, e.g., electrocatalytic reaction that cannot be obtained from pristine carbon nanomaterials.

Previous studies have demonstrated incorporation of metal salts into or onto polymeric carbon precursors and the *in situ* generation of metal nanocatalysts embedded within the as-obtained carbon nanomaterials^{58,175–177}. For example, Tour's group prepared PI film containing organic metal salt, e.g., metal complex cobalt(III) acetylacetone, iron(III) acetylacetone, or molybdenyl(VI) acetylacetone, and exposed the film to a CO₂ laser, enabling the formation of nanocrystal metal oxides embedded within laser-induced graphene⁵⁸. The work opens up for a variety of applications not only in energy-related fields, as shown by the authors, but also in non-enzymatic electrochemical sensors. In our group, instead of preparing a polymer film, we used electrospinning technology to obtain a functional 3D-fibrous polymeric carbon precursor. Here, high porosity, immense surface area, and homogeneous dispersion of metal salt realized by electrospinning potentially provide the resulting carbon electrodes with high-performance when compared to that of polymeric films. As an example, in our previous study, the electrodes made from laser-induced carbon nanofibers embedded with Ni (Ni-LCNFs) have enabled the detection of glucose in basic medium at sub-micromolar range with negligible interferences²⁴. As recently demonstrated also by our group, the 3D-porous LCNFs can be further integrated into microfluidic analytical devices, enabling the detection of dopamine in pM range⁷⁸.

Various metals have been in fact successfully incorporated to carbon electrodes for H₂O₂ detection^{13,19}. For example, Mei et al. proposed a construction of PtNi alloy decorated MWCNTs for non-enzymatic electrochemical sensors of H₂O₂ with excellent sensitivity and limit of detection (LOD) in the nanomolar range¹⁴⁵. Additionally, the PtNi alloy offered the possibility to detect glucose under physiological pH, unlike traditional detection strategies where basic solution medium is required²⁴. Recently, Xi et al. reported PtNi nanoparticles with Ni-rich cores and Pt-rich shells that possessed a record high catalytic efficiency with K_{cat} of 10⁷ s⁻¹, which is much more efficient than pure Pt nanoparticles (a well-known type of efficient peroxidase mimics with similar sizes)¹⁴². Therefore, the combination of Pt and Ni within LCNFs is of an interest in this study. In particular, we expected to gain new knowledge on fabricating LCNF electrodes with more than a single metal and their applicability for H₂O₂ sensing.

Herein, we aim to explore the effect of various combinations of Pt and Ni embedded within LCNFs and reveal their electrochemical behaviors towards non-enzymatic detection of H₂O₂. In this study, cyclic voltammetry was used to assess the electrocatalytic behaviors whereas chronoamperometric detection was mainly employed to evaluate the analytical performance. As non-enzymatic electrochemical sensors typically suffer from electroactive interferences, in particular at high applied voltage, we thus thoroughly investigated the effect of each metal composition on selectivity. Furthermore, we investigated some strategies to overcome the signal interferences both in buffer and human serum samples.

3.5 Materials and methods

3.5.1 Preparation of LCNF

Nanofiber mats were prepared by electrospinning of 15% (w/v) Matrimid® 5218 (Huntsman Advanced Materials BVBA, Belgium) and various ratios and amounts of platin(II)-acetylacetone ((97%, Sigma-Aldrich, Germany) and nickel(II)-acetylacetone (95% Sigma-Aldrich, Germany) dissolved in N,N-dimethylacetamide (Merck, Germany) (see supporting information: table S1 and figure S2). All Ni:Pt-ratios are given in mol-percent. The metal-salt percentages refer to the dry mass of the polymer. For nanofibers without any metal, a suspension of laser-induced graphene flakes was added to the spinning solution instead of a metal salt. The spinning solutions were stirred at least overnight for homogeneous distribution of all components. The electrospinning was conducted with a rotary drum, tip-to-collector distance of 15 cm, flow rate of spinning solution (10 μ L/min) and fiber-deposition substrate (indium tin oxide coated poly(ethylene terephthalate); ITO/PET, sheet resistivity 60 Ω /sq, 1 ft \times 1 ft \times 5 mil, Sigma Aldrich, Germany). For the rotary drum, an ITO/PET piece of 10 cm \times 30 cm and two slides of aluminum foil touching both long sides of the ITO/PET were attached to the collector of the rotary drum with adhesive tape to ensure electrical connection between the ITO surface and the grounding. The size of the resulting collecting area was around 9 cm \times 25 cm, the applied voltage was 11-12 kV and the drum rotation speed was set to 150 rpm. The optimized spinning time of the rotary drum was 3h 30 min. The exact temperature and humidity during the spinning is shown in Table S1. The resulting nanofibers were at least dried overnight in the fume hood from organic solvent. The laser-induced carbon nanofibers (LCNFs) were generated by laser-scribing the electro spun fibers with a CO₂-laser (10.6 μ m, VLS 2.30, Universal Laser System, Polytech Systeme GmbH, Germany). The laser settings were set to a lasing speed of 60% (1,270 mm·s⁻¹), an image density of 1,000 DPI and a laser power of 1.5 W. If the laser conditions were adjusted (lower laser power or higher lasing speed; see Table S1), the LCNFs were destroyed (electrode burning) with standard conditions. The reasons of such deviations are (i) the various metal compositions with different resulting heat transfer during laser scribing and (ii) low humidity (< 40%) during electrospinning which usually results in thinner mats. To keep constant laser conditions despite of point (i), the total metal-salt percentages compared to polymer-dry mass were reduced from 25% (LCNFs with 100% Ni) to 15% (LCNFs with 100% Pt).

3.5.2 Morphology characterization

Elemental mapping and energy dispersive X-ray (EDX)-spectra of LCNFs were investigated with scanning electron microscopy-energy dispersive X-ray (SEM-EDX) (Zeiss/EVO MA 5 with Bruker XFlash Detector 630M. The samples were cut with a scissor and not further treated before the measurement.

The morphology of the nanofibers and the various LCNFs were investigated by scanning electron microscopy (SEM, Zeiss/LEO 1530, Germany). The samples were cut with a scissor and platinum-sputtered (1-2 nm layer thickness) before the measurement.

3.5.3 Electrochemical characterization

The MultiPalmSens4® (PalmSens, Netherlands) with a 3-electrode system (working electrode: LCNF, counter electrode: Pt-wire, reference electrode: Ag/AgCl) was used for all electrochemical measurements. The working area of the LCNF had a geometric size of 0.07 cm² and was separated from the contact-part of the LCNF with the potentiostat by candle wax. For both measurements cyclovoltammetry (CV) and chronoamperometry (CA), a drop of the solution (40 µL) was placed on the LCNF while the counter and reference electrodes were reaching into the drop.

CV for effective surface area (ESA) determination was performed from -0.6 to 1.2 V at 25, 50, 75, 100, 150 and 200 mV·s⁻¹ in 1 mM ferri/ferrocyanide (in 0.1 M phosphohate buffer (phosphate buffered saline tablet, Sigma Aldrich, Germany; dissolved in Millipore water; if slight deviations from pH were measured, the solution was adjusted with HCl/ NaOH (1M) to pH= 7.4), 0.1 M KCl).

CVs to see the catalytic effect of the LCNFs were performed from -0.8 V to 0.8 V at 50 mV·s⁻¹ in phosphate buffer (pH= 7.4) and in 10 mM H₂O₂ (Merck, Germany, diluted from a stock solution (CAS-Nr.: 7722-84-1)) in phosphate buffer (pH= 7.4). Firstly, one electrode was measured for 3 cycles in PBS. After that, the same electrode measured a drop of 10 mM H₂O₂ in PBS. For the figures, the 3rd cycle of the PBS measurement (usually slight changes of the CV are observed from cycle 1 to cycle 2. From cycle 2 on, the CV is stable) and the 1st cycle of the measurement with H₂O₂ were used. In the figures which show CVs, the average CV of n electrodes (see 'n' in the figure caption) is shown.

Chronoamperometry (CA) was measured in a non-stirred solution (40 µL placed on the electrode) with a fixed potential of 0.5 V for 100 s. The average signal of the timespan 50-55 s was used as a signal of the CA since this timespan showed low standard-deviation between electrodes. As a pretreatment, CAs in pure PBS of one and the same electrode were measured until the signal was constant (usually 10 measurements). After each CA-measurement, the drop was removed and a fresh one was placed. After that, a dose-response curve for the analyte (H₂O₂) or of a disturbing molecule (ascorbic acid (Merck, Germany), uric acid (Sigma Aldrich, Germany), dopamine Sigma Aldrich, Germany) and glucose (Sigma Aldrich, Germany)) in PBS was measured with the same electrode. Considering LOD-calculation, the last 3 measurements in PBS buffer (the stabilized blank signal) of one electrode were used to calculate the standard deviation of the blank for this electrode. The LOD of a certain LCNF was then calculated by using the average standard deviation of the blank measurement of n electrodes (see 'n' in figure caption) and the average slope of the calibration curve.

To study the impact of sample matrix, CA measurements were initially performed on an electrode 3 times in PBS-buffer to establish a stable background current. Then the buffer was removed. After that, 40 µL of human serum (Sigma Aldrich, H4522) was dropped (either pure or diluted, i.e., 50% human serum + 50% PBS) onto the same electrode for a 4th CA measurement. Hereby, for every H₂O₂ concentration spiked in human serum (0, 50, and 100 µM), a fresh electrode was used. In case of a polymer coating, 1 µL of the respective polymer-solution (5 w% nylon in formic acid) was dropped onto the electrode and evaporated in the fume hood at room temperature for approximately 1h.

3.6 Results and discussion

3.6.1 Characterization of nanocatalyst embedding LCNFs

In a previous study, we found that electrospinning enabled the uniform distributions of Ni throughout the as-spun PI nanofibrous precursor as well as within the LCNF electrodes studied by scanning electron microscopy with energy dispersive X-ray analysis (SEM-EDX)²⁴. Similarly, to ensure no adverse effect resulted from the metal mixture in their distribution, elemental mapping of Ni- and Pt-atoms was performed for the most representative component, i.e., (50% Pt + 50% Ni)- LCNFs. As shown in **Figure 3.2A**, the EDX-signals resulting from Ni and Pt are equally distributed across the whole imaging area. In addition, the intensities of EDX-spectra taken from the selected areas for the various LCNF hybrids are highly correlated with the investigated Pt/Ni compositions (**Figure 3.2B**).

An evaluation and a summary of these EDX-spectra is given in **Table 3.1**. Herein, comparisons between the measured mass concentrations of Pt- and Ni-atoms presented in the as-prepared LCNFs and their original content in the spinning solution were made. It should be noted that even though inductively coupled plasma mass spectrometry (ICP-MS) is known as a more suitable and accurate technique to determine mass concentration of metals the challenges encountered during the sample preparation did not allow us to achieve reliable data with ICP-MS. Therefore, the data from SEM-EDX are provided for the discussion.

As expected, when increasing Pt or Ni in the spinning dope, the mass of metals in the fibers (rel. to total mass of LCNFs) significantly increased. This implies that during laser-scribing, most of the oxygen and nitrogen in acetylacetone and PI nanofibers (or Matrimid[®]) was removed⁶². We observed that LCNFs with higher Ni contents, i.e., (25% Pt + 75% Ni) and (100% Ni), contained more oxygen which suggested that during laser-scribing, not all PI nanofibers were completely converted into LCNFs, which is also in good agreement with the SEM study of various investigated LCNFs (see **Figure S3.1A, B**). This is likely due to the fact that higher thermal conductivity of Ni leads to lower heat localization. In other words, the heat carried by Ni diffuses away faster than that of Pt. The carbon content was nevertheless roughly the same in all investigated LCNFs. In addition to SEM-EDX characterization, electroactive surface area (ESA) was determined for the investigated LCNF hybrids (**Figure S3.2**). As well as the peaks of the ferro/ferricyanide redox couple, another anodic and cathodic peak couple appeared at around +0.7 V and +0.6 V, respectively, when Ni was present in the LCNFs in relatively high amounts, as reported in our previous study²⁴. Such peaks prove the formation of Ni₂[Fe(CN)₆]²⁻, which requires a Ni²⁺-ion, indicating that the nanocatalysts rather consists of NiO than other possible forms, e.g., NiO₂ and Ni₃O₄^{24,178,179}. The incorporation of high Pt content in Pt/Ni-LCNF hybrids tended to reduce ESA, which is likely due to greater heat localization behavior of Pt during the lasing process, causing stronger material ablation and less fiber-like structures on top of the usual grid-pattern of the laser-scriber (see **Figure S3.1A-E**). However, when Pt is present alone within LCNFs, a larger amount of Pt is required to increase ESA (see also **Table S3.1**), caused by an increased amount of very fine structures arising on top of the usual grid pattern (compare **Figure S3.1E** and **S3.1G**). This suggests that

Pt and Ni mutually facilitated the heat localization during laser-carbonization. For LCNFs without any metal, the laser-power had to be reduced to 0.9 W in order to avoid the electrode burning, leading to a LCNF without the typical pattern of the laser scriber (see **Figure S3.1F**) and a subsequent lower ESA (see **Figure S3.2F**). Finally, we have proven that incorporation of metal into PI nanofibers plays a great role in maintaining the integrity of laser-carbonization as the LCNFs without metal possessed approx. 2- to 3-times less surface area in comparison to the others (**Figure S3.1F**).

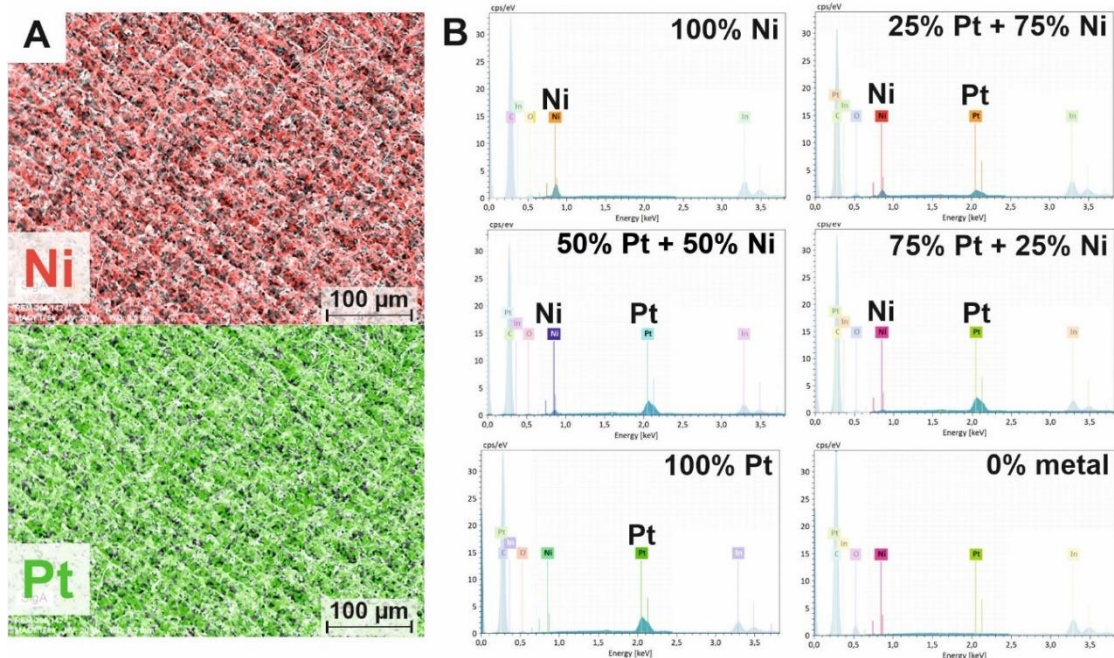


Figure 3.2: (A) Elemental mapping of Ni and Pt for a (50% Pt + 50% Ni)-LCNFs by SEM-EDX. (B) EDX spectra of various LCNF hybrids focused on Ni and Pt for an area with the size of the SEM image shown in (A), i.e., of around 520 μm × 350 μm.

Table 3.1: Summary of the results from EDX-spectra shown in Figure 1B.

Pt content (mol-%)	$\frac{m(Pt(acac))}{m(spinning\ soln.)}$ (% wt)	$\frac{m(Pt)}{m(LCNFs)}$ (% by EDX)	Ni content (mol-%)	$\frac{m(Ni(acac))}{m(spinning\ soln.)}$ (% wt)	$\frac{m(Ni)}{m(LCNFs)}$ (% by EDX)	$\frac{m(O)}{m(LCNFs)}$ (% by EDX)	$\frac{m(C)}{m(LCNFs)}$ (% by EDX)
100	6.45	8.5 ± 0.3	0	0	-	2.9 ± 0.6	70 ± 8
75	6.23	8.1 ± 0.3	25	0.69	0.79 ± 0.06	2.8 ± 0.6	70 ± 8
50	5.37	7.2 ± 0.3	50	1.67	2.00 ± 0.09	2.5 ± 0.5	71 ± 8
25	3.5	2.8 ± 0.1	75	2.96	2.5 ± 0.1	5.7 ± 0.9	60 ± 7
0	0	-	100	4.57	5.3 ± 0.2	6 ± 1	71 ± 8

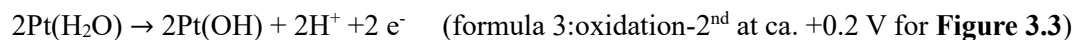
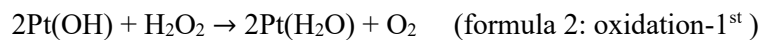
3.6.2 Electrochemical characterization towards H₂O₂

Variation of the metal ratio did not only affect the ESA but also played a significant role in the electrocatalytic reaction for non-enzymatic electrochemical detection of H₂O₂. Therefore, we systematically characterized the LCNFs loaded with Pt and/or Ni by cyclic voltammetry (CV) to see which LCNF hybrid offered the best catalytic effect towards H₂O₂ (**Figure 3.3**). LCNFs containing only Ni nanocatalysts (**Figure 3.3A**) did not show a prominent electrocatalytic activity towards H₂O₂ for both oxidative and reductive regions as expected. However, (25% Pt + 75% Ni)-LCNFs (**Figure 3.3B**) were already sufficient to enable the oxidation and reduction of H₂O₂, exhibiting oxidation and reduction peaks at around +0.2 V and -0.4 V, respectively. The oxidative peak was independent of Pt content when considered within Pt/Ni-LCNF hybrids (**Figure 3.3B to 3.3D**). However, the LCNFs containing only Pt exhibited lower anodic peak intensity as well as an undistinguishable cathodic response from the background (**Figure 3.3E**). The decreased anodic peak could be attributed to a smaller ESA comparing to the others (**Figure S3.1E**). No significant oxidative or reductive action towards H₂O₂ is displayed by the LCNF electrode without any metal (**Figure 3.3F**), which clearly shows that the Pt and/or Ni within LCNF majorly promote electrocatalytic reaction of H₂O₂ while edge/defects of the graphitic sheets play no significant role¹⁸⁰. Finally, increasing the Pt content resulted in a strong reduction of water, i.e., hydrogen evolution reaction¹⁸¹.

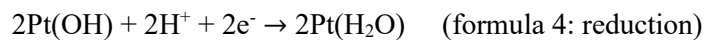
The results shown in **Figure 3.3** indicate that Pt plays a major role in the electrocatalytic activity of H₂O₂. As suggested by the other studies^{182,183}, the oxidation and reduction should start with spontaneous adsorption of H₂O₂ (non-electrochemical process) on the free Pt-surface:



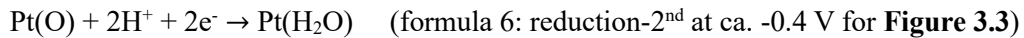
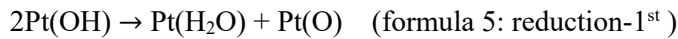
As Katsounaros et al. showed by quantum chemical ab initio calculations, in an oxidation-reaction, another H₂O₂-molecule interacts with the two OH-groups adsorbed on the Pt-surface and is oxidized to oxygen (formula 2: oxidation-1st), whereas the resulting water-molecules are further oxidized by the Pt surface (formula 3: oxidation-2nd)¹⁸², which yields the measurable current at the electrode:



On the other hand, in a reduction-reaction, this OH-group will be spontaneously reduced into water, and free Pt-sites are available for new coming H₂O₂ molecules again¹⁸²:



As reported by Xi et al, a Ni/Pt alloy potentially enhances the catalytic activity towards H_2O_2 because of weaker binding of the products to the alloy surface¹⁴². By density functional theory (DFT) calculations, Xi et al. also showed that the adsorption energy of both the OH-species and the O-species on the Pt surface decreases by incorporation of Ni¹⁴². By considering the intermediate steps of formula 4, both species as following could appear during reduction reaction:



As can be seen from **Figure 3.3B to 3.3E**, no significant difference was observed for the anodic peaks when introducing Ni into the LCNF hybrids in contrast to the cathodic currents. This is likely due to the fact that Ni tended to reduce the adsorption energy of the intermediates only for the reduction reaction¹⁴², thus modulating catalytic behavior for H_2O_2 reduction.

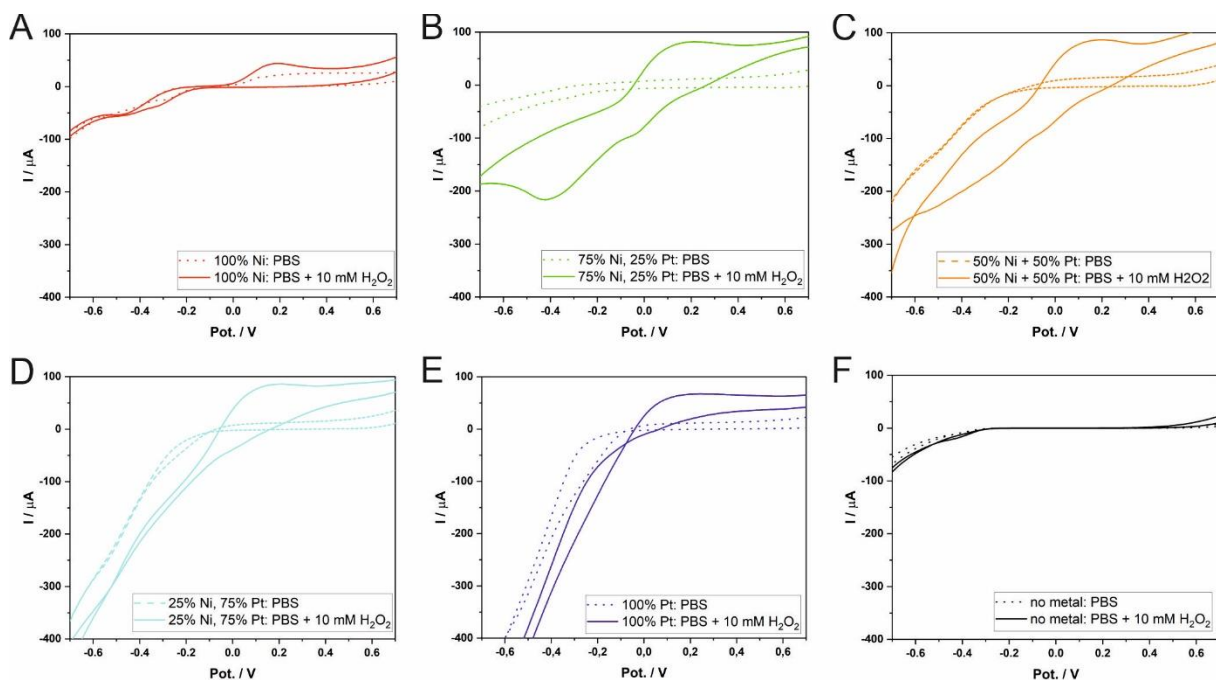


Figure 3.3: Cyclic voltammograms of LCNFs with various metal compositions where A to E are from (100% Ni)-LCNFs, (75% Ni + 25% Pt)-LCNFs, (50% Ni + 50% Pt)-LCNFs, (25% Ni + 75% Pt)-LCNFs, and (100% Pt)-LCNFs, respectively, (mol-% are given). (F) LCNFs without metal. The characterizations were performed in PBS (pH = 7.4) with and without 10 mM H_2O_2 (n=3). The potential (Pot.) is given against Ag/AgCl reference electrode. Scan rate of 50 mV/s was used.

For H_2O_2 detection at constant potential (chronoamperometry, CA), one might want to use the (25% Pt + 75% Ni)-LCNF electrode set to -0.5 V, where a better selectivity towards H_2O_2 can be generally realized¹⁸⁴, judging from the cyclic voltammograms in **Figure 3.3**. However, we chose a potential of +0.5 V instead. This contrary decision can be explained by the fact that, in our experiment, a positive potential usually showed good reproducibility from electrode to electrode, good sensitivity towards

H_2O_2 when using CA, and finally provided a stable signal during CA measurements. On the contrary, the application of -0.5 V mostly gave poor reproducibility and signals uncorrelated with H_2O_2 concentrations (data not shown). It might be possible that during the oxidative scans of CVs shown in **Figure 3.3B**, the embedded nanocatalyst underwent a necessary oxidation prior to being able to reduce H_2O_2 . This encourages further intensive studies, which we unfortunately have not been able to address so far in this investigation.

3.6.3 Influence of various Pt and Ni content on analytical performance

3.6.3.1 Sensitivity and limit of detection

As discussed in section 2, CA at a positive potential (+0.5 V) was performed for all LCNF electrodes with various Pt/Ni content. **Figure 3.4A** shows the average current in the timespan from 50-55s of a chronoamperometric measurement as a function of the H_2O_2 -concentration in PBS solution (pH= 7.4). The slopes of the resulting calibration curves increased with the Pt to Ni ratio. This was particularly obvious when Pt content rose from 0% to 50% in the Pt/Ni-LCNF hybrids. The sensitivity already reached the maximum at 50% Pt content in the mixture. This indicates that Pt majorly controls the electrocatalytic oxidation of H_2O_2 . In addition, the result here may suggest that laser-scribing probably led to the generation of individual Pt- and Ni-oxides rather than the formation of a PtNi alloy, as such an alloy was suspected to improve the catalytic reaction of H_2O_2 , as reported previously^{142,145}.

As a next step, we compared the limit of detection (LOD) of the various LCNFs by using the slopes of the calibration curves in **Figure 3.4A** from a concentration range of 5 – 500 μM H_2O_2 (compare with **Figure S3.3**), which yielded a good linear correlation. As mentioned earlier in the experimental parts, CA was run for ten times in pure PBS before each calibration to ensure a stable background-signal whereas the last three consecutive measurements were used to calculate the standard deviation of the blank within the same electrode (with this standard deviation, a LOQ of 5.7 μM was calculated for the pure Pt-electrodes). Since we repeated such measurements also for several different electrodes of the same material type, a measure of uncertainty can be assigned to the standard deviation of the blank measurement. Hence, both the slope and the standard deviation of the blank measurement have an uncertainty, which leads, of course, to a standard-deviation of the LOD, calculated by the sum of the partial derivatives multiplied with the respective uncertainty. The LODs of the different LCNFs were shown in **Figure 3.4B**. Although the sensitivities were highly comparable for Pt/Ni-LCNFs with Pt content above 50% in the metal mixture, the LOD tends to decrease, reaching the best value of 1.4 ± 0.4 μM for (100% Pt)-LCNF. This can be explained by the fact that the standard deviation of the blank decreases when Pt content increases, i.e., ± 5 nA, ± 1.3 nA, and ± 0.7 nA, for (50% Pt + 50% Ni)-LCNFs, (75% Pt + 25% Ni LCNFs), and (100% Pt)-LCNFs, respectively. This may also imply that addition of Ni causes inhomogeneity of the resultant Pt/Ni-LCNFs hybrids, thus generating higher variation between different electrodes (see also the standard deviations of current response from (75% Ni + 25% Pt)-LCNFs shown in **Figure 3.4A**.

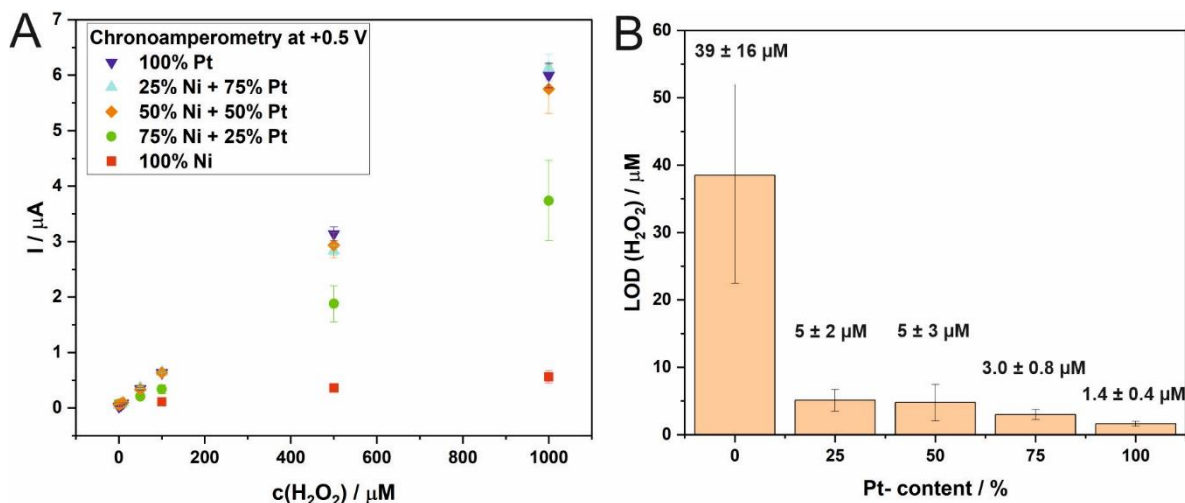


Figure 3.4: Analytical performance of various LCNFs hybrid electrodes. (A) Calibration curves of the various metal LCNFs for the detection of H_2O_2 obtained by non-stirred chronoamperometry at $+0.5\text{ V}$ ($n \geq 6$). (B) Limit of detection for LCNFs with various Pt-ratios.

Overall, the analytical performance obtained in this work is highly competitive to the other studies (**Table 3.2**), especially considering time, cost, and effort in manufacturing process. The estimated total material cost per electrode with the current electrode design is less than 20 euro cent which is highly suitable for single use analysis. Furthermore, the high flexibility of material and detection limit in low micromolar range for monitoring H_2O_2 without the need of stirring make the nanocatalyst-LCNF hybrids attractive for developing wearable devices.

Since Pt has a higher heat localization capability than Ni, we thus had to reduce the total mass of metal-salt added to the spinning solution when increasing Pt-content (**Figure S3.4A**) to keep the same laser scribing conditions for a better comparison. As a result, we could not obviously see the direct impact of the various metal compositions asserted only from **Figure 3.4A**. In addition, the ESA also slightly varied when LCNFs contained different Pt/Ni combinations (**Figure S3.4B**). For a better comparison of the LCNFs, the sensitivities obtained from **Figure 3.4A** were divided by (i) the metal-salt- or the Pt-salt-concentration of the respective spinning solution, and by (ii) their ESA (**Figure S3.2B**). As shown in **Figure 3.5**, by increasing the Pt content, the sensitivity per metal-salt (concentration of both Ni and Pt ions in the spinning solution) is linearly increased from 0% Pt to 100% Pt whereas the sensitivity per Pt-salt (concentration of Pt-ions in the spinning solution) is almost constant with the best performance obtained at 100% Pt. These two observations confirmed that increasing the amount of Pt in the LCNFs improved the detection sensitivity of H_2O_2 in which Pt is mostly responsible for the sensitivity towards H_2O_2 , not from bimetallic Pt/Ni alloy as reported by other studies^{142,145}. Instead, adding Ni to the Pt-LCNF tended to poison the Pt-nanocatalyst, hindering electrocatalytic reaction of H_2O_2 .

Table 3. 2: Comparison of Pt-LCNF with various Pt- and carbon-nanomaterial-based electrodes considering the effort of production, Limit of detection (LOD), measurement conditions, linear range, and applied potential.

Material	Production steps	LOD / μM + measurement condition	Linear range / μM	Pot. vs. Ag/AgCl / V	literature
Pt-LCNF	Electrospinning, Laser-scribing	1.4 ± 0.4 Non-stirred	5-500	+ 0.5	This study
Pt-nanoparticles (NPs)-rGO	rGO ^a , synthesis of Pt-NPs, preparation of Pt-NP-rGO nanocomposite, deposition on glassy carbon electrode (GCE)	0.5 stirred	2-710	0.0	¹⁸⁵
Pt-NPs-multi-walled carbon nanotubes (MWCNT) - rGO	MWCNT was bought and pretreated, preparation of freestanding GO ^a -CNT paper, reduction to rGO ^a -CNT paper, Pt-sputtering	0.01 stirred	Up to 25	- 0.05	¹⁸⁶
Pt-nanoflower – nitrogen doped rGO	Synthesis of N-graphene, electrophoretic deposition of N-graphene-modified ITO, electrochemical deposition of Pt nanoflower	0.34 stirred	1-1000	- 0.4	¹⁸⁷
Pt-NPs-carbon nanofibers (CNF)	Electrospinning, deposition of Pt on NFs, carbonization of NFs, deposition on GCE	1.7 stirred	5-15000	- 0.2	¹⁸⁸
Pt-TiO ₂ -SWCNT	SWCNT was bought, preparation of SWCNT-film, electrochemical deposition of TiO ₂ structures, Photoinduction of platinum nanoparticles	0.73 ± 0.04 stirred	1-1500	+ 0.7	¹⁸⁹
Pt _{0.5} Au _{0.5} @C-GCE	Preparation of PtAu@C catalyst by microwave-assisted polyol process, catalyst in naftion-solution drop-coated on cleaned GCE	2.4 stirred	7-6500	+ 0.3	¹⁹⁰
Pt-MWCNT	screen-printing carbon black ink onto an Ag coated PET plastic film, Pt-MWCNT nanohybrid was prepared based on Watanabe method deposition of Pt-MWCNT on screen printed electrode	Not specified Non-stirred	1000-15000 100-1000 10-100	+ 0.3 (vs. screen printed Ag/AgCl-ink)	¹⁹¹
PtNi-MWCNT	MWCNT was bought and acid-pretreated, Synthesis of PtNi/C nanocomposites, preparation of catalyst-ink and drop-coating on GCE	0.06 stirred	0.2-24600	- 0.4	¹⁴⁵
a) Graphene oxide (GO): was either synthesized or purchased; Reduced graphene oxide (rGO): GO was reduced in a further production step					

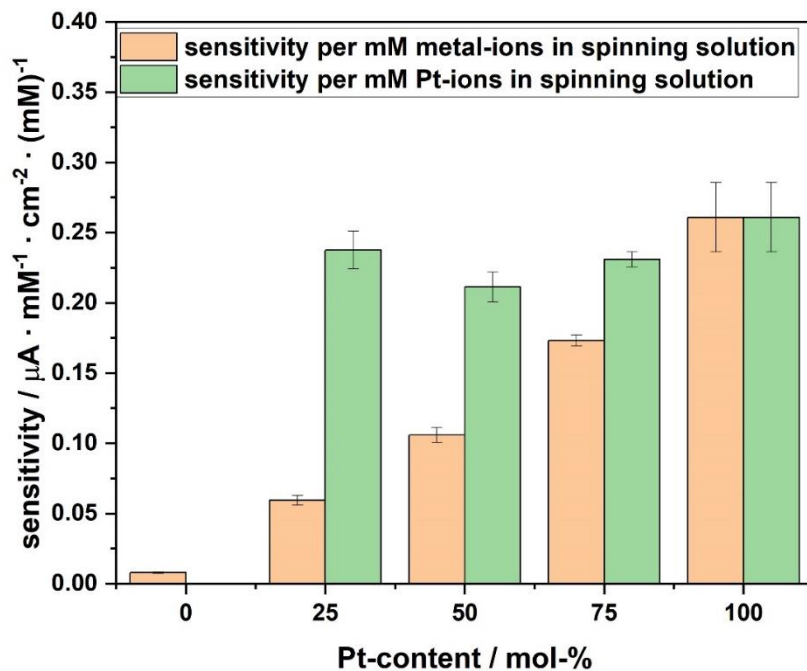


Figure 3. 5: Impact of Pt on the normalized sensitivities shown in Figure 3A of various Pt/Ni-LCNF hybrids.

3.6.3.2 Selectivity

As important as the sensitivity and LOD, the selectivity was studied, especially when applying a high oxidative potential. Therefore, we investigated common electroactive species, which may potentially interfere the detection of H_2O_2 , e.g., ascorbic acid (AA), uric acid (UA), dopamine (DA) and glucose (Glu). As shown in **Figure 3.6A to 3.6E**, the CA signals of 100 μM AA, UA, DA and Glu in PBS seem to be quite similar for all Pt/Ni-LCNF hybrids whereas current responses from H_2O_2 (100 μM in PBS) is highly dependent on Pt content. When using LCNF electrodes without metal (**Figure 3.6F**), the currents from the interferences are prominently seen and approx. 2-times of the signals obtained from LCNFs electrodes which contained metal(s). This is likely due to the fact that edge/defects of the LCNFs are the major cause of poor selectivity where the highly electroactive species, e.g., AA, UA, and DA, can easily oxidize at the sites ¹⁹². These findings emphasize the importance of the exposure of nanocatalyst on the exterior of LCNF surfaces to specifically facilitate electrocatalytic oxidation of H_2O_2 ¹⁹³. In order to achieve such features, core-shell electrospinning, i.e., PI solution and Pt salt solution is, respectively, fed inside and outside a concentric spinneret, could potentially be applied. Alternatively, spraying or applying Pt salt solution on PI nanofibers prior to laser-scribing may efficiently provide nanocatalysts on LCNF surface.

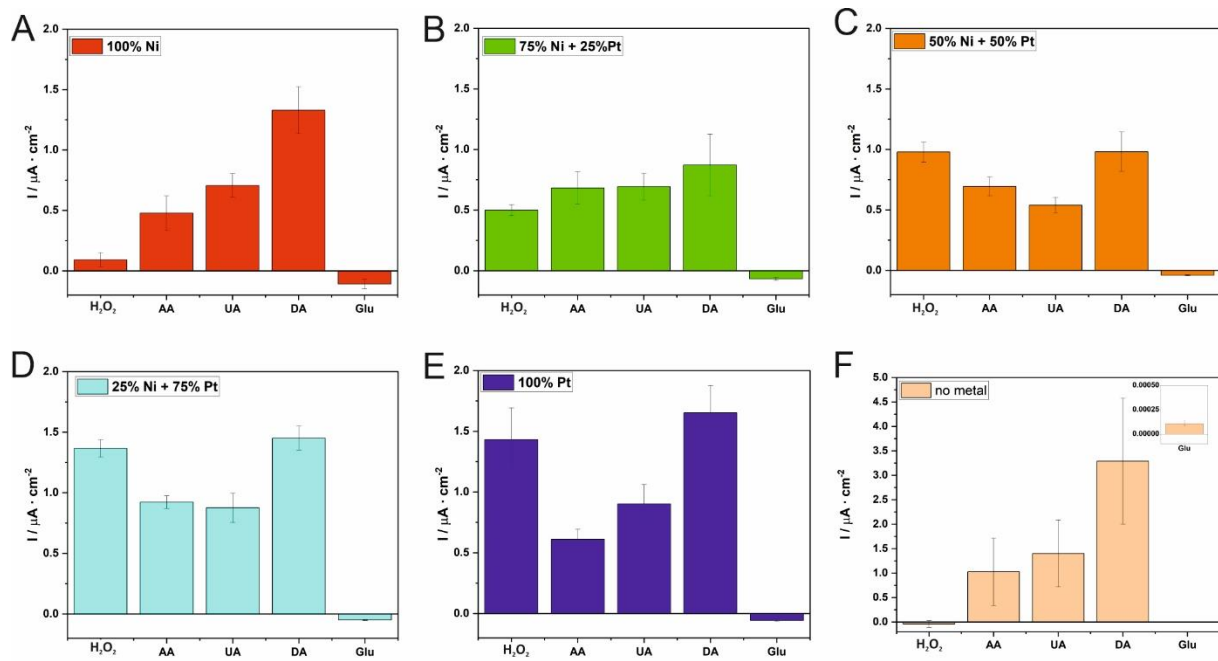


Figure 3.6: Selectivity of LCNFs with various metal compositions (A: 100% Ni, B: 75% Ni + 25% Pt, C: 50% Ni + 50% Pt, D: 25% Ni + 75% Pt, E: 100% Pt, F: no metal) in PBS solution (pH = 7.4) towards H₂O₂, ascorbic acid (AA), uric acid (UA), dopamine (DA) and glucose (Glu) (n=3). The diagrams show the amperometric response of 100 μM substance in PBS from which the signal in pure PBS solution was subtracted.

3.6.4 Investigating strategies for suppressing signals from UA, AA, and DA

In this section, various strategies on suppressing current signals from UA, AA, and DA were mainly investigated as Glu exhibits negligible signal in our current setup. Since the high interfering signals of AA, UA, and DA resulted from the laser-induced graphene itself, one strategy to enhance selectivity is to increase the metal content compared to the dry mass of the PI polymer of the spinning solution. This should principally lead to a higher amount of nanocatalyst present on the LCNF surface while reducing the effect of electrochemical oxidation by the laser-induced graphene. We here continued to investigate the LCNFs containing only Pt as those provided greater analytical performance towards H₂O₂ detection than the others.

Prior to considering the selectivity, we assessed the effect of Pt content on the detection sensitivity of H₂O₂. As shown in **Figure 3.7A**, the increase of Pt content from 15% to 25% slightly improved the detection sensitivity of H₂O₂ which is mainly attributed to the elevated ESA. The currents normalized by their ESAs were similar for both cases. However, at an increased Pt content of 25% the electrodes became more exclusive to UA and DA as indicated by the drop of their signals (relative to that of H₂O₂) comparing to 15% Pt (**Figure 3.7B**). The results suggested that UA and DA are more difficult to be oxidized at 25% Pt-LCNFs when compared to H₂O₂. It should be noted that even though the interfering signal from DA is relatively high, DA is commonly present in real samples at a very low level, i.e., pico- to nanomolar range¹⁹⁴, and should not cause problems during measurements. To further improve the selectivity against UA, increasing Pt content higher than 25% is promising. In contrast to UA and DA,

incorporating more Pt in LCNFs rather facilitated better electron transfer for AA which is known to be an easily oxidizable species¹⁹².

We then further studied different electrode modifications where polymers, i.e., Nafion and nylon, were applied onto the 25% Pt -LCNFs by drop-casting, aiming to suppress the signal interferences from AA. As can be seen in **Figure S3.5**, electrodes coated with either Nafion or nylon yielded poorer current ratios of H₂O₂ to AA in comparison to unmodified electrodes, which is likely due to the blockage of electroactive surfaces by non-conductive polymers. Nevertheless, we found that using the same amount of polymer, nylon is superior to Nafion which is probably attributed by its non-bulky chemical structure as well as intrinsic highly hydrophilic property that provides less hinderance for electron transfer between analytes and the electrodes.

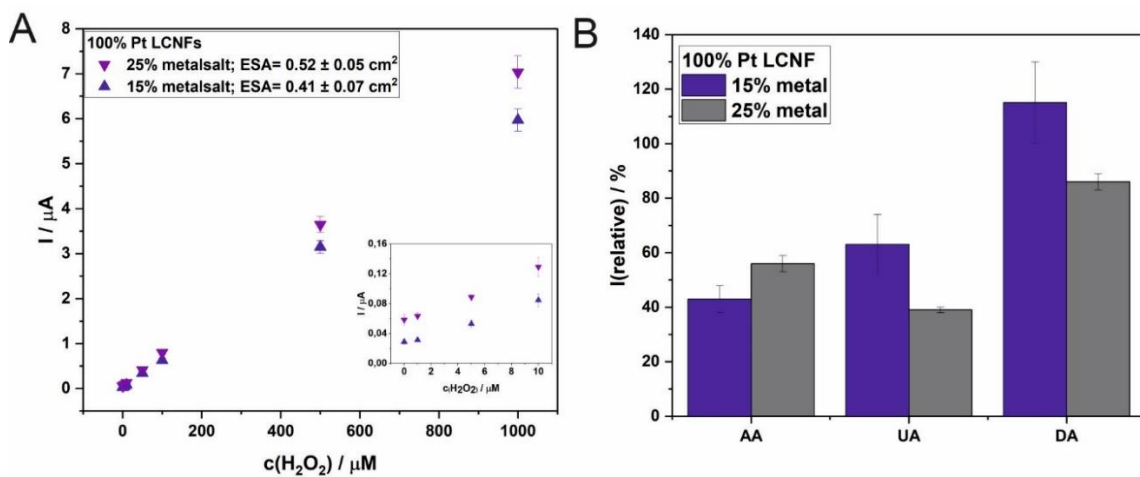


Figure 3.7: (A) Calibration curves of pure Pt-LCNFs with different metal-to-polymer ratios for the detection of H₂O₂ obtained by non-stirred chronoamperometry at +0.5 V (n≥3). (B) The % relative signal (at +0.5V) of AA, UA, and DA (100 μM in PBS) compared to the signal of a 100 μM H₂O₂ solution in PBS for investigated metal ratios (compared to dry mass of the polymer in the spinning solution).

Although, nylon did not exhibit a favorable effect on suppressing signal from AA we found that it improved the recovery of H₂O₂ in a matrix of diluted human serum as can be seen from **Figure 3.8**, which has never before been reported¹⁹⁵. It thus suggests that nylon may be a good candidate as anti-fouling for bioelectronic devices.

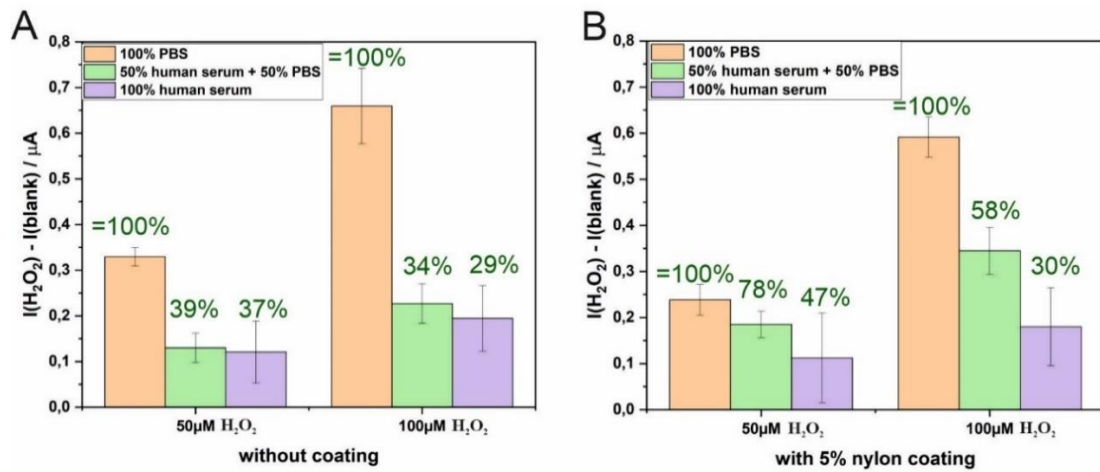


Figure 3.8: The current response of 50 μM and 100 μM of H_2O_2 added to a blank minus the current response of the blank without any H_2O_2 . Hereby, the blank is either pure PBS, a 50:50 mixture of PBS and human serum, or pure human serum for (A) the 25% metal pure Pt- LCNF and for (B) the 25% metal pure Pt-LCNF with a 1 μL of 5 w% Nylon-coating. The green numbers refer to the recovery, whereas current responses in pure PBS solution are defined as 100% ($n \geq 3$).

3.7 Conclusions

Although the laser-induced carbonization strategy has promised the fabrication of non-enzymatic electrochemical transducers, to the best of our knowledge, there have not been systematic studies which addresses the effect of nanocatalyst composition on H_2O_2 sensing with respect to sensitivity and selectivity when measured under physiological conditions. Here, we demonstrated the incorporation of Pt and/or Ni within electrospun polyimide nanofibers and their conversion into nanocatalysts embedded within laser-induced carbon nanofibers by CO_2 laser. The carbon nanofiber hybrids were studied towards their capability in non-enzymatic electrochemical detection of H_2O_2 . Modulation of Pt and Ni content within the nanofiber substrate resulted in distinctive electrocatalytic behavior of H_2O_2 oxidation and reduction as well as the analytical performance with respect to sensitivity and selectivity. The combination between Pt and Ni within the carbon nanofibers did not show superior analytical performance as compared to the present of Pt alone. With the optimal hybrid composition the favorable detection sensitivity and linear range could be attained. However, at the current stage of our development, the hybrid electrodes are not ready for final applications yet as further effort has to be made towards the improvement of selectivity. The results shown in the study suggest further developments on generating electrospun nanofibers where metal salts can be exposed on the exterior to eliminate interfering signal from electroactive species. In addition, to apply other electrochemical detection methods, e.g., differential pulse or square wave voltammetry, may allow distinguishable signals from interfering and H_2O_2 species. Furthermore, electrode modification with cationic nanofibers may be considered as anionic interfering species such as ascorbic and uric acid could be electrostatically trapped to the fibers. These findings will ultimately strengthen research and applications of the laser-generated nanocatalysts for non-enzymatic electrochemical sensors.

3.8 Supporting information

3.8.1 Optimized conditions for preparing LCNFs-embedded with nanocatalysts at various metal compositions

Table S3. 1: Composition of metal precursors, electrospinning conditions, laser settings, and their electroactive surface area determined by Randles–Ševčík equation.

Name of metal composition	Metal salt compared to dry mass of Matrimid / %	Spinning	Humidity / %	Temp. / °C	Laser scribe (power; scribing rate)	ESA / cm ²
100% Ni	25	Rotary drum	59	23	1.5W; 60%	0.52±0.03
100% Ni	25	Rotary drum	37	22	1.5W; 60%	0.54 ± 0.04
75% Ni + 25% Pt	22.5	Rotary drum	42	23	1.2W; 60%	0.53±0.03
50% Ni + 50% Pt	20	Rotary drum	48	22	1.5W; 60%	0.59±0.03
25% Ni + 75% Pt	17.5	Rotary drum	33	22	1.2W; 75%	0.39 ± 0.04
25% Ni + 75% Pt	17.5	Rotary drum	43	22	1.5W; 60%	0.44±0.01
100% Pt	15	Rotary drum	49	26	1.5W; 60%	0.41 ± 0.06
100% Pt	15	Rotary drum	54	23	1.5W; 60%	0.42±0.04
100% Pt	25	Rotary drum	48	22	1.5 W; 60%	0.52 ± 0.05
100% Pt	25	Rotary drum	50 ± 5	22	1.5 W; 60%	0.64 ± 0.04

3.8.2 Morphological characterization of LCNFs by SEM

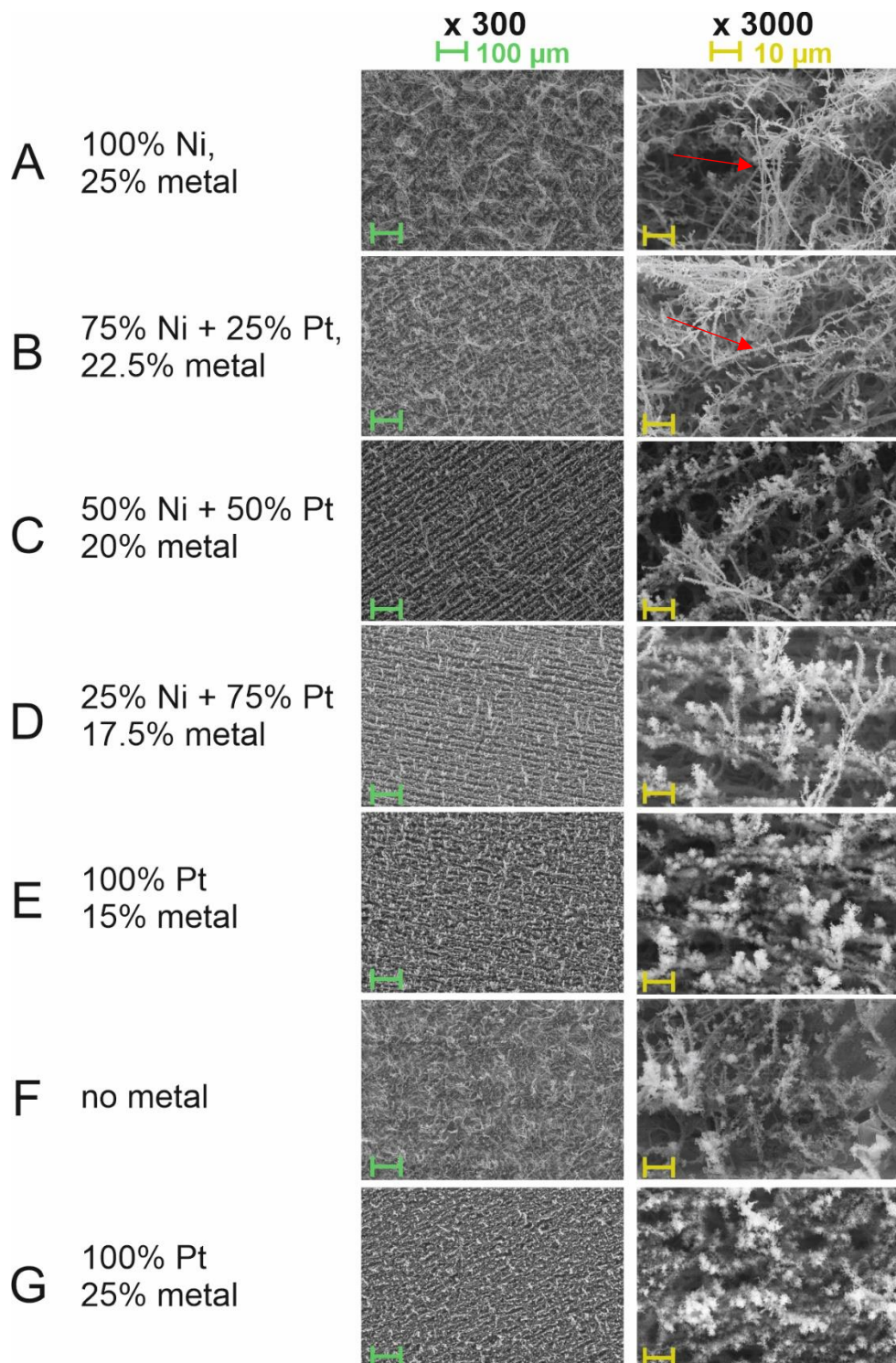


Figure S3. 1: SEM pictures of various LCNFs with a magnification of 300 in the left and 3000 in the right column. The red arrows point at the fibrous samples that may be under carbonized.

3.8.3 Determining electroactive surface area

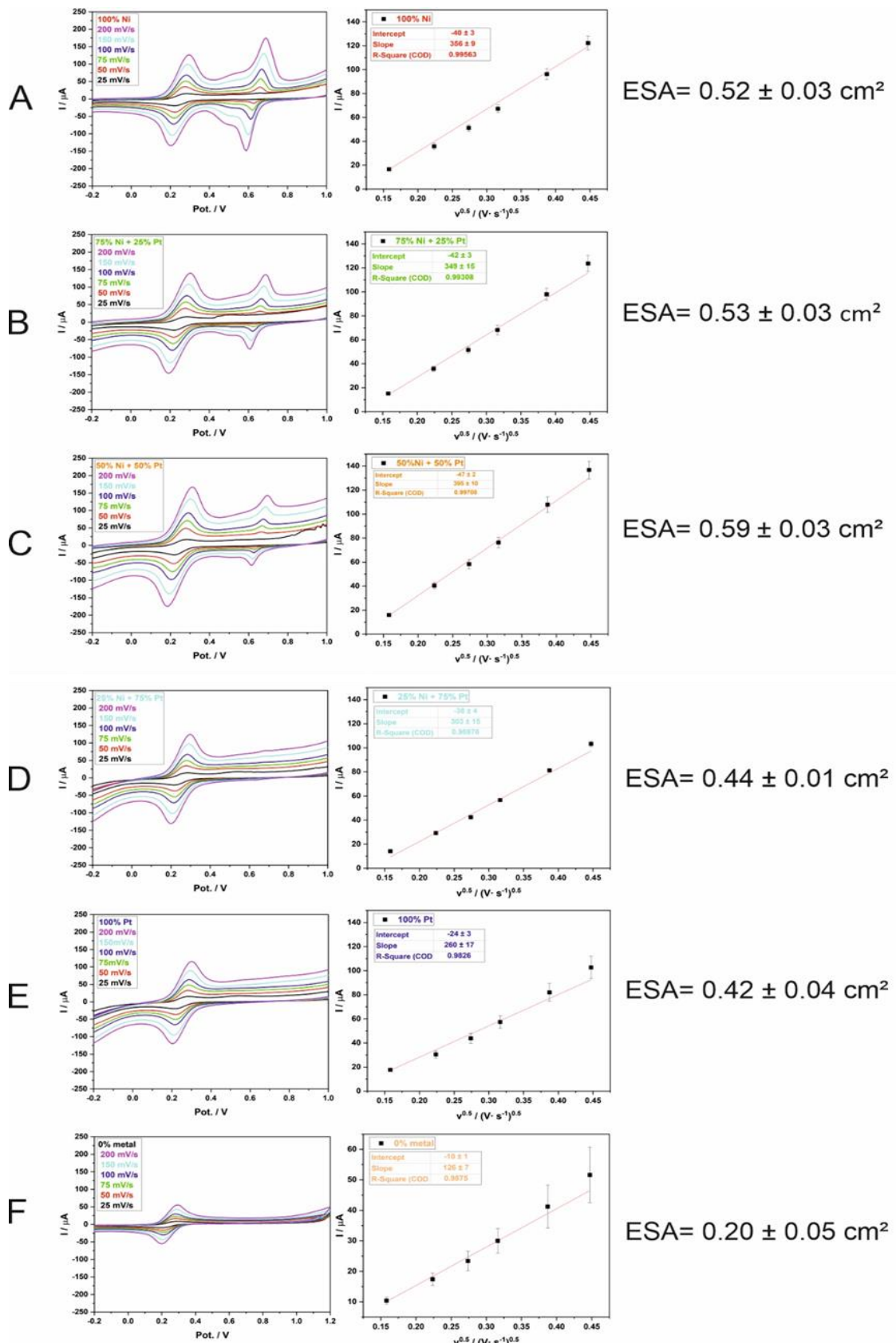
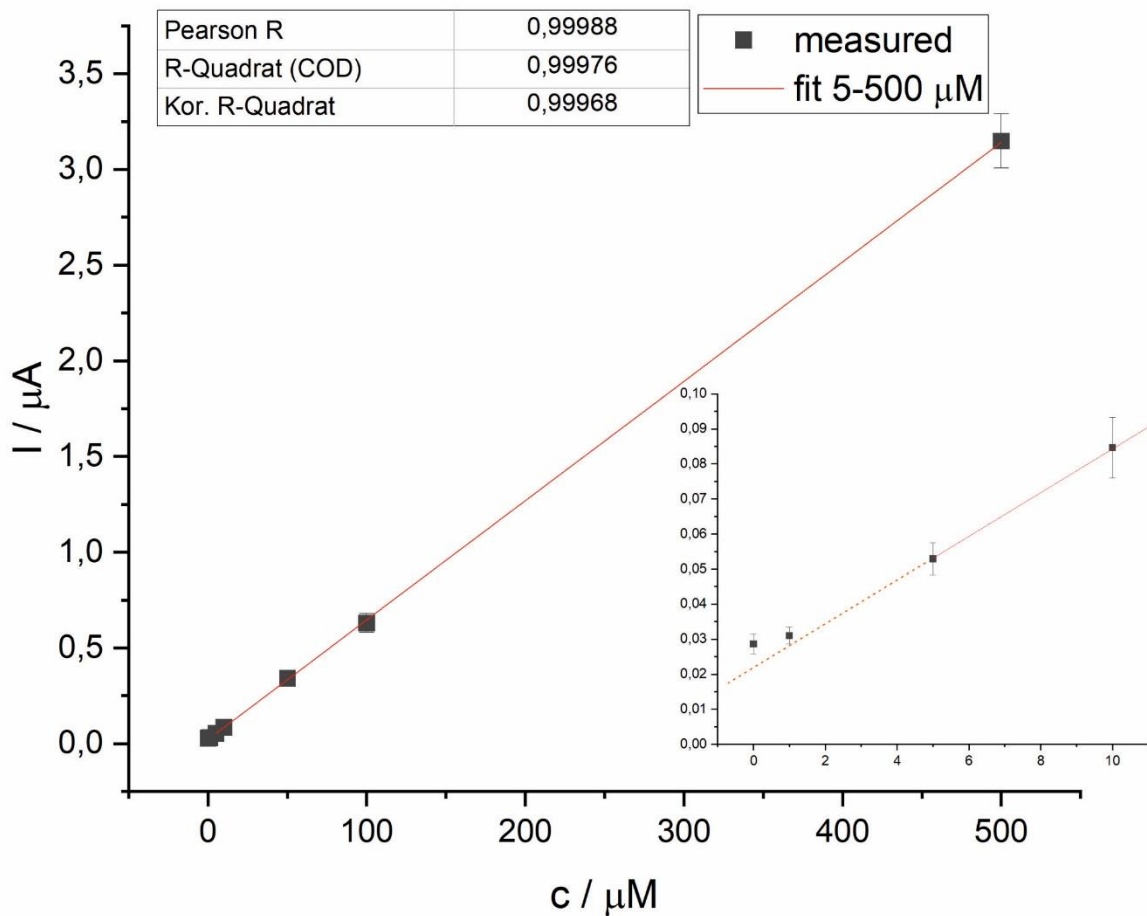


Figure S3.2: Cyclic voltammograms at various scan rates of LCNFs (A: 100% Ni, B: 75% Ni + 25% Pt, C: 50% Ni + 50% Pt, D: 25% Ni + 75% Pt, E: 100% Pt, F: no metal) in 1mM ferri/ferrocyanide in PBS-solution (pH = 7.4) ($n \geq 5$), the respective Randles-Sevcik plot of the ferri/ferrocyanide peak (~ 300 mV, oxidation scan (IUPAC)) and the resulting effective surface area (ESA). The peak couple above $+0.6$ V in A-C (also slightly visible in D) relate to the formation of nickel hexacyanoferrate species.

3.8.4 The linear range of 100% Pt-LCNF



3.8.5 Evaluating impact of Pt at various mol-%

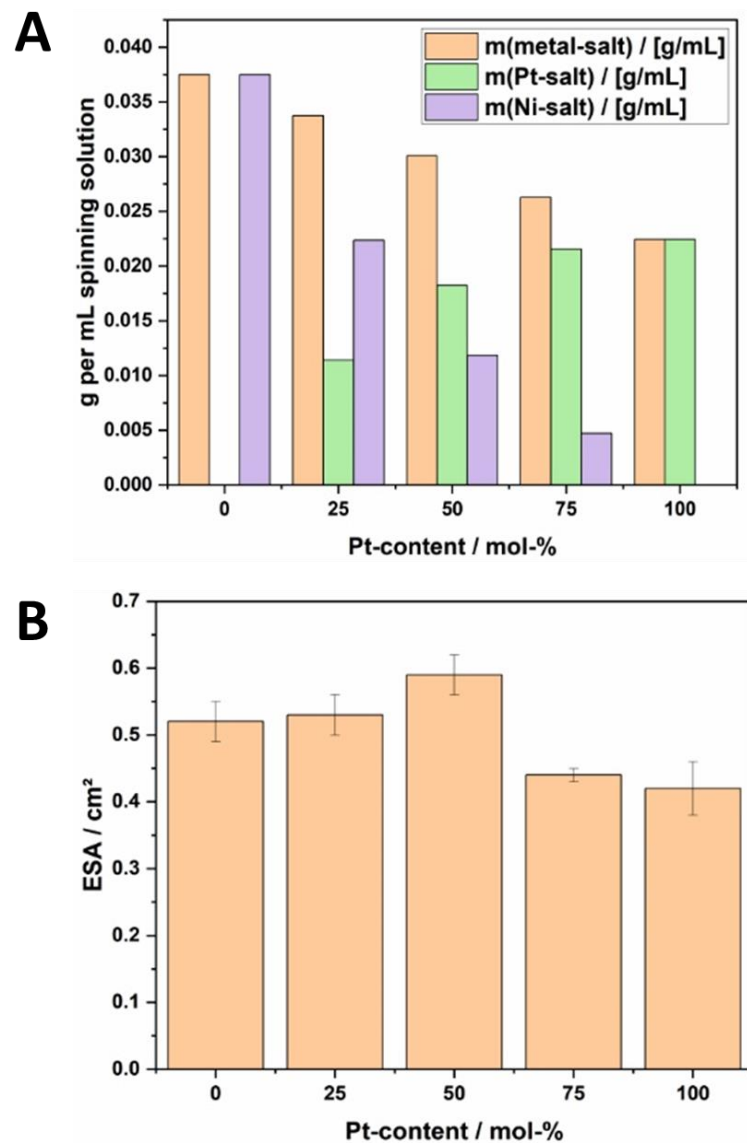


Figure S3. 4: Mass of the Pt- and Ni-salt per mL spinning solution of the investigated LCNFs and the resulting ESAs from Figure S1.

3.8.6 Effect of anionic polymer coating on minimizing signal interference from ascorbic acid (AA)

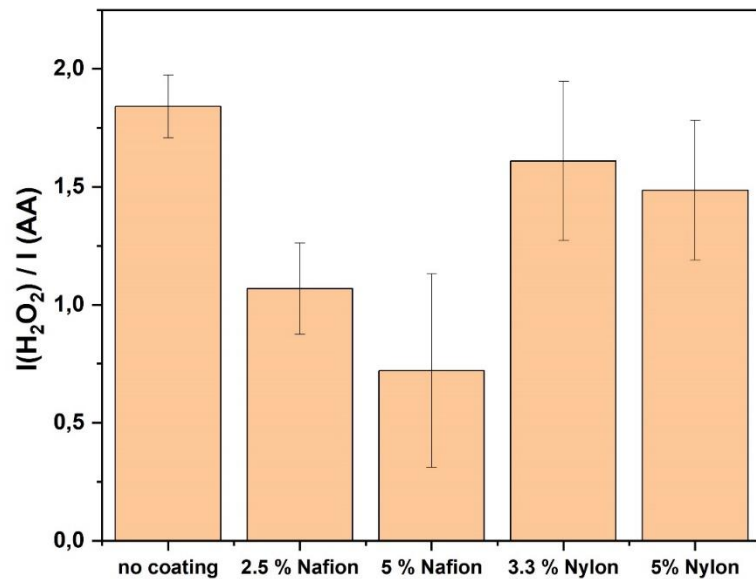


Figure S3. 5: Effect of polymer coatings of 25% Pt-LCNF on the selectivity shown by the signal ratios of H_2O_2 to ascorbic acid (AA). The H_2O_2 and AA concentrations were prepared at 100 μM in PBS (n=3).

3.9 Additional studies towards H₂O₂ detection – lower measurement potential

This chapter has not been published. All experiments were performed by the author.

3.9.1 Motivation and strategy

The published results demonstrated an approach requiring a high voltage of +0.5 V for the electrocatalytic oxidation of H₂O₂⁶³. This method was robust and reproducible, but led to the generation of interfering current signals, particularly from ascorbic acid (AA). Thus, the challenge of selectivity needs to be addressed. To improve selectivity, a potential close to 0 V or even negative potentials would be necessary. However, our previous studies showed that negative potentials did not stabilize even after many consecutive measurements, as described in Chapter 3.6.2. With that, a new measurement approach needs to be applied as well.

In the previous work, the characterization of electrodes by cyclic voltammetry (CV) was performed using an anodic scan from -0.8 V to +0.8 V. This yielded maximum anodic currents around +0.5 V, with currents increasing as Pt content increased. Therefore, LCNFs containing only Pt exhibited the best performance in the previous study, excluding the beneficial feature of the Pt/Ni combination. Unlike our previous study, in this approach, we conducted a cathodic sweep from +0.3 V to -0.3 V to avoid dramatic changes in the properties of the nanocatalysts, such as oxidation or reduction of the catalyst itself, and the effects of water splitting at high and low potentials prior to the electrocatalytic reaction. Additionally, we considered the reduction current of H₂O₂ instead. Considering a new measurement approach, instead of measuring several consecutive times in a buffer until the signal stabilizes (which did not occur at negative potentials even after 10 consecutive measurements), the new approach included one measurement in PBS and a second one in an H₂O₂ solution. Afterwards, the difference between the two measurements was taken into account. This approach helped to limit deviations between electrodes and decreased the measurement time.

3.9.2 Experimental

Cyclic voltammetry (CV) was performed with 3 consecutive scans from +0.3 V to -0.3 V at 50 mV·s⁻¹ in phosphate buffer (1x PBS, pH = 7.4) to ensure a stabilized background current. After that, 10 mM H₂O₂ (Merck, Germany, (CAS-Nr.: 7722-84-1)) in phosphate buffer (1x, pH = 7.4) was used for a consecutive scan to investigate the catalytic behavior of various alloys.

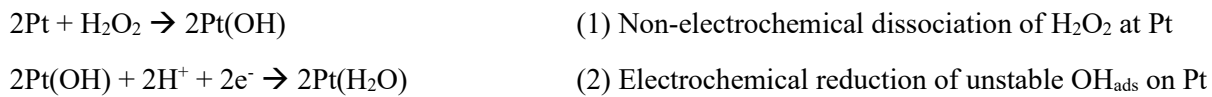
Chronoamperometry (CA) was performed for 50 s in PBS solution at various potentials. After waiting 50 s (and meanwhile removing the drop and placing a new drop of either PBS, 25 µM, 50 µM, 75 µM, 100 µM, 500 µM of hydrogen peroxide in PBS or 100 µM of ascorbic acid in PBS), a second measurement on the same electrode was performed for 50 s at the same potential. For both measurements, the average signal from 45-50 s was used as the signal of the measurement to prevent charging current. After that, the signal of the first measurement was subtracted from the second measurement to remove influences of the background. The difference is called “dI” and will be further

stated in this paper. For every concentration, a fresh electrode was used. Thus, for a dose-response curve with 6 concentrations (0, 25 μ M, 50 μ M, 75 μ M, 100 μ M, 500 μ M) and 6 repetitions (n=6), a total of 36 electrodes were used.

For LOD-calculation, three times the standard deviation of dI (0 μ M H_2O_2 in PBS) was divided by the slope of the dose-response curve in the range of 0-100 μ M.

3.9.3 Results and discussion

Similar to the published study, **Figure S3.6** clearly shows that Pt alone plays a major role in generating either reduction or oxidation current from H_2O_2 which is not the case for Ni. The electrocatalytic reduction signal at around +0.05V should be attributed to the two steps as following.



In contrast, the anodic current at ca. +0.15 V should be ascribed to the reactions shown below.

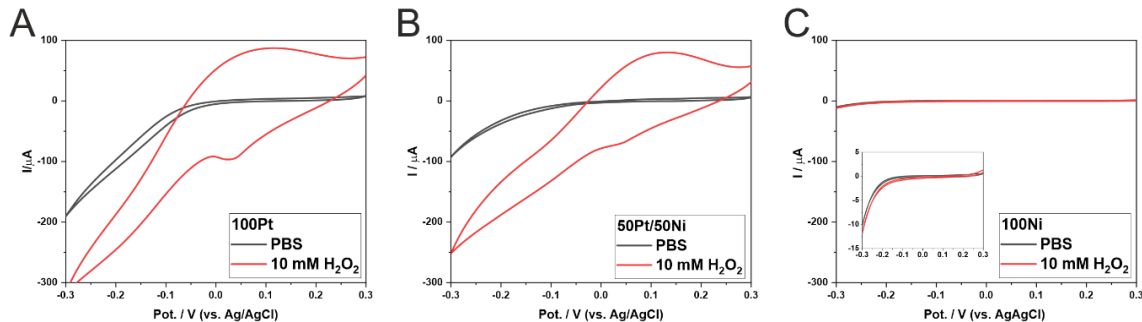
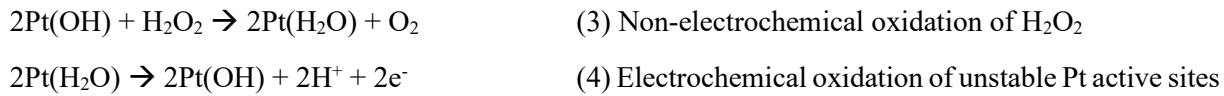


Figure S3.6: Cyclic voltammograms of LCNF electrodes with various Pt and Ni compositions running from +0.3 V to -0.3 V. The characterizations were performed in 40 μ L solution droplet (PBS with and without H_2O_2 , pH = 7.4) using scan rate of 50 mVs⁻¹.

However, it should be noted that the presence of Pt also modulates the potential window when the measurements are carried out in PBS (without oxygen removal). Here, reduction of oxygen ($\text{O}_2 + 4\text{H}^+ + 4\text{e}^- \rightarrow 2\text{H}_2\text{O}$) strongly started at around -0.05 V for 100Pt-LCNF electrode (**Figure S3.6A**)¹⁶⁰, and -0.15 V for 50Pt/50Ni-LCNFs (**Figure S3.6B**) while slightly occurred at ca. -0.2 V for 100Ni-LCNFs (**Figure S3.6C**). The strong current signal from oxygen reduction critically affects the detection sensitivity of H_2O_2 specifically when determined at low concentrations. As can be seen in **Figure S3.7** where the potential at -0.2 V applied to 100Pt-LCNF electrodes did not provide any signal responses that correlated to H_2O_2 concentrations, especially, at the low micromolar ranges, attributed to

the dominant effect of oxygen reduction. With this, we thus chose to investigate the voltages of -0.1 V, 0 V, and +0.1 V for 100Pt-LCNFs, 50Pt/50Ni-LCNFs, and 100Ni-LCNFs electrodes in further chronoamperometric measurements.

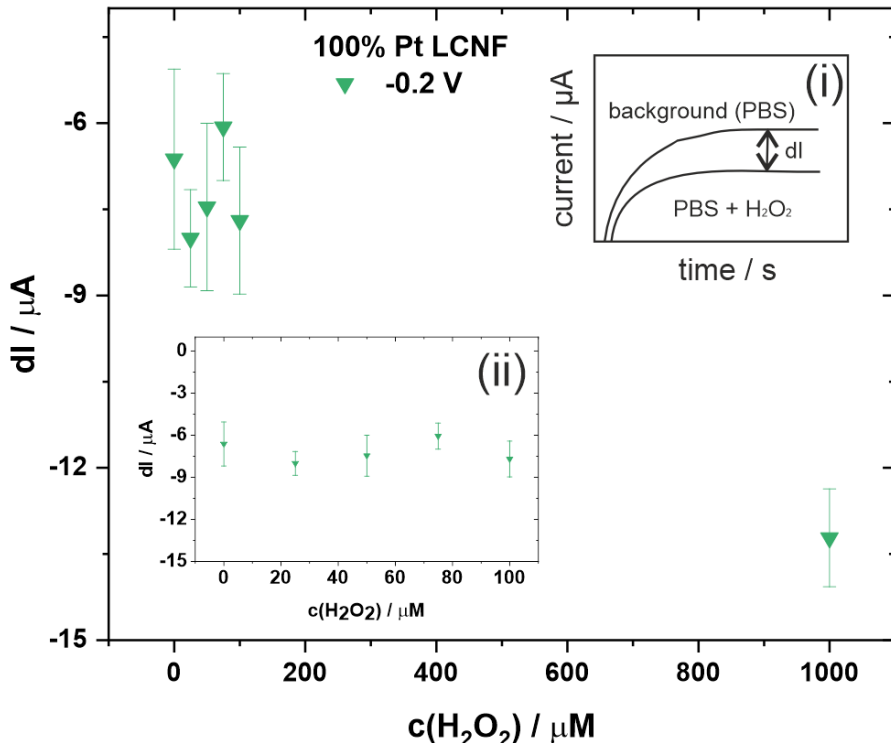


Figure S3.7: Dose response curve of H_2O_2 measured by chronoamperometry at -0.2 V under stagnant condition using 100Pt-LCNF electrodes. H_2O_2 solutions were prepared in PBS buffer (pH 7.4). ($n = 5$) Inset (i) and (ii) represents the exemplary chronoamperograms for data evaluation, and the background-subtracted signals at low H_2O_2 concentrations.

As shown in **Figure S3.8A-i**, application of $+0.1$ V resulted in high fluctuation in cathodic currents for 100Pt-LCNFs and 50Pt/50Ni-LCNFs. This could be attributed to H_2O_2 oxidation concomitantly occurring at this potential (see also the CVs in **Figure S3.6A and S3.6B**). Moving towards the more cathodic potentials (**Figure S3.8A-ii and S3.8A-iii**), i.e., 0.0 V, the current responses against H_2O_2 concentrations were improved and 100Pt-LCNF electrodes performed better than 50Pt/50Ni-LCNFs considering the overall analytical performance. However, by using -0.1 V, the LOD drastically increased for both 100Pt-LCNFs and 50Pt/50Ni-LCNFs due to a less stable background signal.

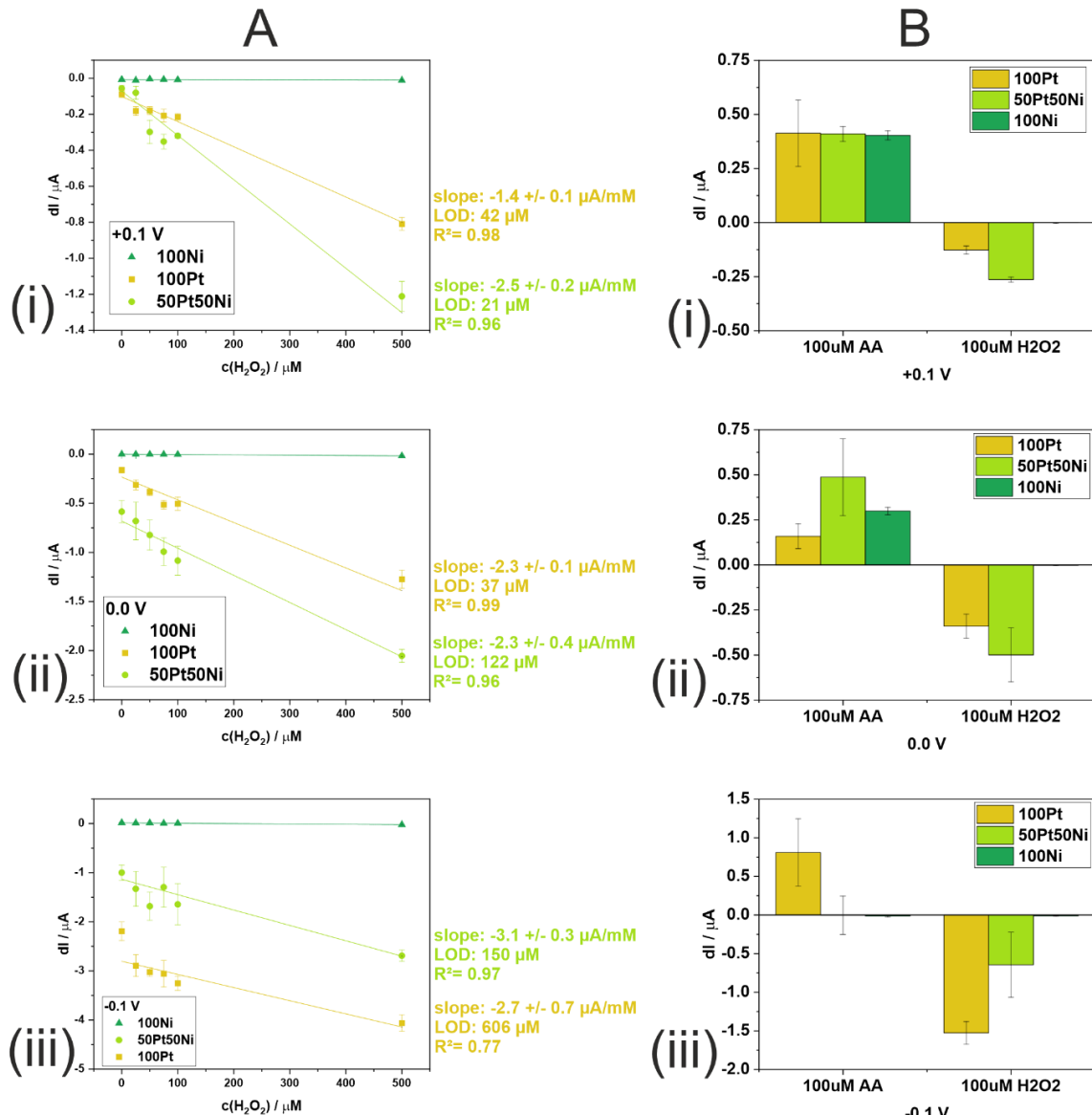


Figure S3.8: Characterization of analytical performance of the electrodes for H_2O_2 detection. (A) Dose response curves obtained from chronoamperometric measurements when applying the potential at (i) $+0.1 \text{ V}$, (ii) 0.0 V , and (iii) -0.1 V ($n=6$). (B) Chronoamperometric signals (blank was subtracted) for selectivity studies against AA performed at (i) $+0.1 \text{ V}$, (ii) 0.0 V , and (iii) -0.1 V ($n=6$).

At first glance, the results shown in **Figure S3.8A** suggested that using 50Pt50Ni-LCNFs and conducting chronoamperometric measurements at $+0.1 \text{ V}$ would be the best option. Nevertheless, it is necessary to perform a parallel experiment to ensure the selectivity of the electrodes, especially against AA. As shown in **Figure S3.8B**, 100Pt-LCNFs at all investigated potentials generated non-negligible anodic currents from AA whereas 100Ni-LCNFs only oxidized AA at 0.0 V and $+0.1 \text{ V}$. Although AA and H_2O_2 undergo different redox reactions when they are co-present in the mixture, the oxidative current can potentially diminish the cathodic current intensities of H_2O_2 . Therefore, suppression of anodic current generated from AA while being able to detect H_2O_2 is much more favorable. Interestingly, 50Pt50Ni-LCNFs could meet such requirements where the others could not consider the measurement at -0.1 V . This may imply that Ni could potentially suppress the reactivity of 50Pt/50Ni-LCNFs towards

oxidation of AA in the cathodic region, i.e. voltages below 0.0 V, while retaining desired activity of Pt nanocatalyst for H_2O_2 reduction. We suggest that the higher amount of negatively charged oxygen groups as observed in XPS spectra repels ascorbic acid when Ni is present (later shown in **Figure S4.2Biii**). Thus, the results highlight the synergistic effect gained from Pt/Ni alloy in improving selectivity of H_2O_2 detection against AA. However, the reproducibility, limit of detection (LOD), and linearity from applying -0.1 V were not satisfactory (**Figure S3.8A-iii**), requiring further improvements. The high variation within 50Pt/50Ni-LCNFs could be ascribed to the fact that the well-maintained fibrous structure of LCNFs containing Ni prevented homogeneous spreading of H_2O_2 solutions on the transducer interface. This could be possibly overcome by hydrophilic treatments of the as-prepared electrodes prior to performing the measurements. Such treatments could further allow the utilization of available active surface area, which subsequently can improve LODs and linearity.

3.9.4 Conclusions

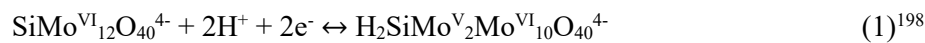
The carbon nanofibers carrying Pt/Ni alloy were employed as enzyme-free electrodes for H_2O_2 detection. The Pt/Ni alloy enhances the selectivity towards H_2O_2 detection against interfering species, i.e., ascorbic acid. However, it was observed that a lower potential (e.g., -0.2 V) is needed to achieve better selectivity (reduce signals from ascorbic acid), which results in worse sensitivity towards H_2O_2 due to the reduction of oxygen. There are strategies to remove oxygen from the analyte solution (chapter 1.7.7), but this would complicate the construction of the sensor or measurement setup.

3.10 Additional studies towards H₂O₂ detection – Polyoxometalates as catalysts

This chapter has not been published. Most experiments were performed by the author. Michael Födlmeier supported experiment implementation during a research lab course.

3.10.1 Motivation and strategy

As we have observed in chapter 3.9, it seems to be not possible to find a potential window to detect H₂O₂ sensitive and selective enough to be competitive with other sensors, just by using Pt/Ni-LCNFs. With that, a new catalyst for hydrogen peroxide reduction needed to be investigated. In this context, Polyoxometalates (POMs) are a very promising candidate due to their excellent redox properties and peroxidase-mimicking activities^{196,197}. For example, the SiW₁₂O₄₀⁴⁻ -ion (SiMo) can be reduced 3 consecutive times as suggested in literature¹⁹⁶:



To show the electrochemical activity and catalyst-behavior of SiMo, CV measurements of laser-induced graphene-LCNFs (LIG-LCNFs; LCNFs without any metal; prepared as described in chapter 3.5.1; electrochemical behavior of LIG-LCNF in PBS shown in **Figure 3.3F**) with SiMo and with SiMo + 10 mM H₂O₂ were performed:

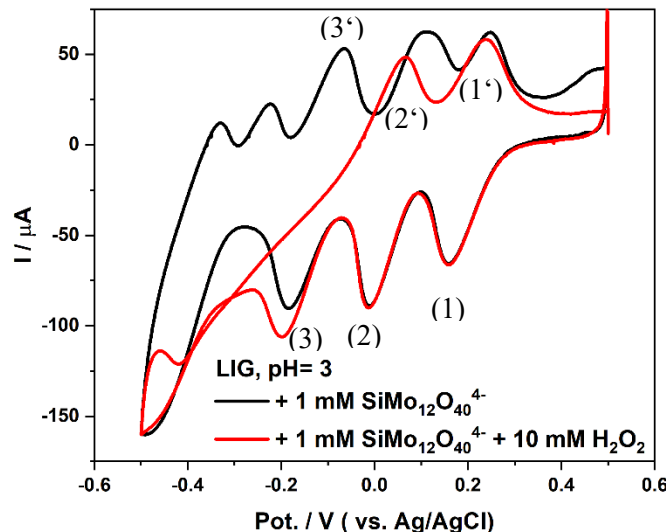


Figure S3. 9: CV scan of laser induced graphene-LCNFs (LIG-LCNF) with 1 mM SiMo in citrate buffered solution (pH= 3) with and without 10 mM H₂O₂. Numbers in brackets refer to reactions shown above.

The first and second reduction peak ((1), (2) in **Figure S3.9**) show no changes after the addition of H_2O_2 . However, the corresponding oxidation peak ((2') in **Figure S3.9**) decreases after the addition of H_2O_2 . This indicates that SiMo, after the second reduction (i.e., $\text{H}_4\text{SiMo}^{\text{V}}_4\text{Mo}^{\text{VI}}_8\text{O}_{40}^{4-}$), is capable of reducing H_2O_2 (a decreased (2') peak means that SiMo is already oxidized by H_2O_2), but at low reaction rates. The more pronounced reduction peak after the addition of H_2O_2 ((3) in **Figure S3.9**) indicates that SiMo, after the third reduction (i.e., $\text{H}_6\text{SiMo}^{\text{V}}_6\text{Mo}^{\text{VI}}_6\text{O}_{40}^{4-}$), is capable of reducing H_2O_2 at -0.2 V. The kinetics of this H_2O_2 reduction reaction are much faster, as evidenced by the increased reduction current at (3) and the absence of the corresponding oxidation current, which means that all of the catalyst is already oxidized by H_2O_2 . It also appears that the reduction of oxygen occurs below -0.3 V. This suggests that SiMo could be a potential catalyst for H_2O_2 reduction within a potential window where ascorbic acid is not oxidized, and only small amounts of oxygen are reduced. However, it is important to note that the stability of polyoxometalates (POMs) is highly sensitive to pH, with optimal stability at low pH values. In this chapter, only measurements with SiMo will be presented. Measurements with other POMs, such as $\text{PMo}_{12}\text{O}_{40}^{3-}$, $\text{SiW}_{12}\text{O}_{40}^{4-}$, and $\text{PW}_{12}\text{O}_{40}^{3-}$, did not show good stability during electrochemical measurements or increased pH values (data not shown), which (stability towards increased pH) is consistent with the literature^{197,199}. The performance and stability of SiMo in different solutions (pH 2 to 7.4) will be investigated, along strategies to deposit it on the electrode surface and prevent leaching.

3.10.2 Experimental

LCNF-preparation:

LIG-LCNFs and Pt-LCNFs were prepared as described in chapter 3.5.1.

POM-co-spun nanofibers:

POM-co-spun nanofiber mats were prepared by electrospinning of 15% (w/v) Matrimid® 5218 (Huntsman Advanced Materials BVBA, Belgium) as described in chapter 3.5.1. To prepare a spinning solution, $\text{SiMo}_{12}\text{O}_{40}^{4-}$ was bought as an aqueous solution from Sigma Aldrich, water was evaporated at room temperature in the fume hood over the weekend, and further dried in a desiccator. For POM-fibers, Matrimid® and dried $\text{H}_4\text{SiMo}_{12}\text{O}_{40}$ powder was weighted in a vial (15 w% compared to polymer dry mass) and dissolved in N,N-dimethylacetamide (Merck, Germany). For POM-Pt- and POM-Ni-fibers, 20 w% (compared to polymer dry mass) of the respective metal salt (Pt(II)-/Ni(II)-acetylacetone), 5 w% (compared to polymer dry mass) of dried $\text{H}_4\text{SiMo}_{12}\text{O}_{40}$ - powder, and Matrimid® was dissolved in N,N-dimethylacetamide.

POM-co-spun LCNFs:

POM-/POM-Pt-/POM-Ni-fibers were laser scribed as described in Chapter 3.5.1, with a laser power ranging from 1.5 to 2.1 W.

Direct drop-coating of POM:

10 μ L of a 10 mM $\text{H}_4\text{SiMo}_{12}\text{O}_{40}$ solution in double-distilled (bidest) water was dropped onto the working area of the LCNF. The electrode was placed in a fume hood for approximately one hour until the solvent evaporated and the electrode was dry again. Afterwards, the electrode was washed three times with bidest water to remove weakly attached POM. In this approach, POMs are expected to adsorb due to electrostatic interactions with π -electrons of the graphene like structure²⁰⁰.

Drop-coating of POM on hydrophilic monolayers:

PEGylation of Pt-nanoparticles of Pt-LCNFs:

Pt-sites of 100% Pt-LCNF (15 wt% metal) were PEGylated with 10 μ L of an aqueous 50 mM PEG-thiol solution [poly(ethylene glycol) methyl ether thiol (M_{average} = 800 g/mol)] for 1 hour in a closed petri dish (to prevent evaporation of the water). The thiol group of the PEG-thiol is expected to build covalent bonds with Pt-atoms on the surface of the electrode. After that, the remaining drop was removed, and the PEGylated electrode was washed three times with bidest water. This procedure was followed by POM drop-coating as described above. In this approach, POMs are expected to adsorb on the hydrophilic PEG-groups due to the superchaotropic effect²⁰¹.

Ethomeen C/25 coating on LIG-LCNF:

LIG-LCNFs were treated with O_2 plasma at 100 W for 5 minutes to increase the amount of oxygen-containing, negatively charged groups on the electrode surface^{202,203}. 1.5 μ L of a 10 mM aqueous Ethomeen C/25 (tertiary amine ethoxylatebased; M= 861 g/mol; Akzo Nobel company) solution was dropped onto the electrode. The surfactant is expected to interact strongly with the negatively charged groups on the electrode surface due to the positively charged $\text{R}_3(\text{NH})^+$. After washing, the procedure was followed by POM drop-coating as described above. In this approach, POMs are expected to adsorb on the hydrophilic groups of the surfactant due to the superchaotropic effect²⁰¹.

Small Angle X-Ray Scattering (SAXS)

SAXS measurements were performed as described in chapter 4.5.2.

3.10.3 Results and discussion

As a first step, the pH stability of SiMo was investigated using cyclic voltammetry (CV) measurements of LIG-LCNF electrodes of 1 mM SiMo, dissolved in either 10 mM phosphate-buffered or 10 mM citrate-buffered solutions. The exact pH was adjusted from the initial citrate buffer (pH 3) or phosphate buffer (pH 7.4) by adding HCl or NaOH. The presence of the well-defined reduction peaks of SiMo at approximately +0.15 V, -0.05 V, and -0.2 V were used to predict if SiMo remained sufficiently stable within roughly 30 minutes (the time between solution preparation and the end of measurement), which would be adequate for a later application in a sensor. From **Figure S3.10**, it can be observed that only a pH of 7 and above leads to the direct decomposition of SiMo, and a pH of 6 already shows a smaller reduction peak at -0.2 V, indicating stability issues with the polyoxometalate. For a pH of 5 and below, SiMo seems to be sufficiently stable. Considering the catalytic activity towards H₂O₂ reduction, focusing on the reduction peak at -0.2 V, H₂O₂ reduction improves as the pH decreases from 7 to 5, reaching its optimum between pH 5 and 3, and then decreases at pH 2.

Examining the corresponding oxidation peak located between -0.1 and -0.2 V (H₆SiMo^V₆Mo^{VI}₆O₄₀⁴⁻ → H₄SiMo^V₄Mo^{VI}₈O₄₀⁴⁻ + 2H⁺ + 2e⁻), it is evident that at pH 3, the oxidation peak is mostly absent. This indicates that all the H₆SiMo^V₆Mo^{VI}₆O₄₀⁴⁻ was already oxidized by H₂O₂, whereas there is still H₆SiMo^V₆Mo^{VI}₆O₄₀⁴⁻ present at other pH values. In conclusion, the best catalytic behavior was observed at pH 3, while the optimal pH for biomedical applications would be pH 7.4.

In the next step, various strategies to deposit SiMo on the electrode surface were investigated (instead of having SiMo in the solution). The two pH values of 3 and 7.4 were compared, as the electrode matrix could potentially protect SiMo from the solution, thereby stabilizing it at higher pH levels.

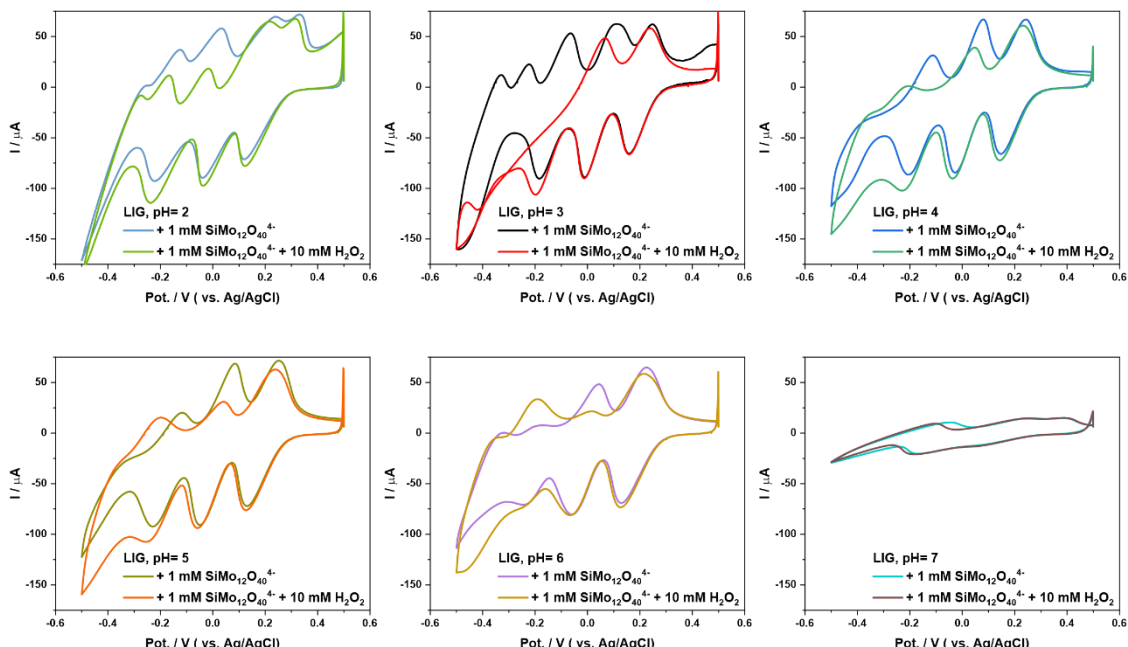


Figure S3. 10: CVs (50 mV/s) of 1 mM SiMo in solutions with various pH-values on LIG-LCNFs with and without 10 mM H₂O₂.

The first strategy to deposit the polyoxometalate (POM) was co-spinning. The major advantage of this method is that it requires no additional production steps, as POMs are dissolved directly in the spinning solution. Three approaches were investigated: 15 w% POM @ Matrimid® fibers, 5 w% POM + 20 w% Ni @ Matrimid® fibers, and 5 w% POM + 20 w% Pt @ Matrimid® fibers. The rationale behind the hybrid POM-metal material was to test whether the presence of a metal salt during laser scribing influences the stability of POM and leads to a stable metal-nanoparticle-POM composite.

However, neither the POM-LCNF alone nor the POM co-spun LCNF with metal salts exhibited typical SiMo peaks during CV measurements in citrated buffered solution (**Figure S3.11i**) or phosphate buffered solution (**Figure S3.12i**) after laser scribing the electro spun fibers. Additionally, no catalytic activity towards hydrogen peroxide reduction at around -0.2 V was observed (**Figures S3.11ii** and **S3.12ii**). Only a slightly increased reduction current at -0.2 V was noted when Pt was co-spun for both pH values, which can be attributed to the catalytic activity of platinum rather than SiMo. Furthermore, the redox couple at -0.6 V could be attributed to cycling Pt species (**Figures S3.11Cii**), as it only occurs at pH 3 when Pt is present. When Ni was present, an additional oxidation peak at +0.3 V was observed at both pH 3 and 7.4 (**Figures S3.11Bii** and **S3.12Bii**).

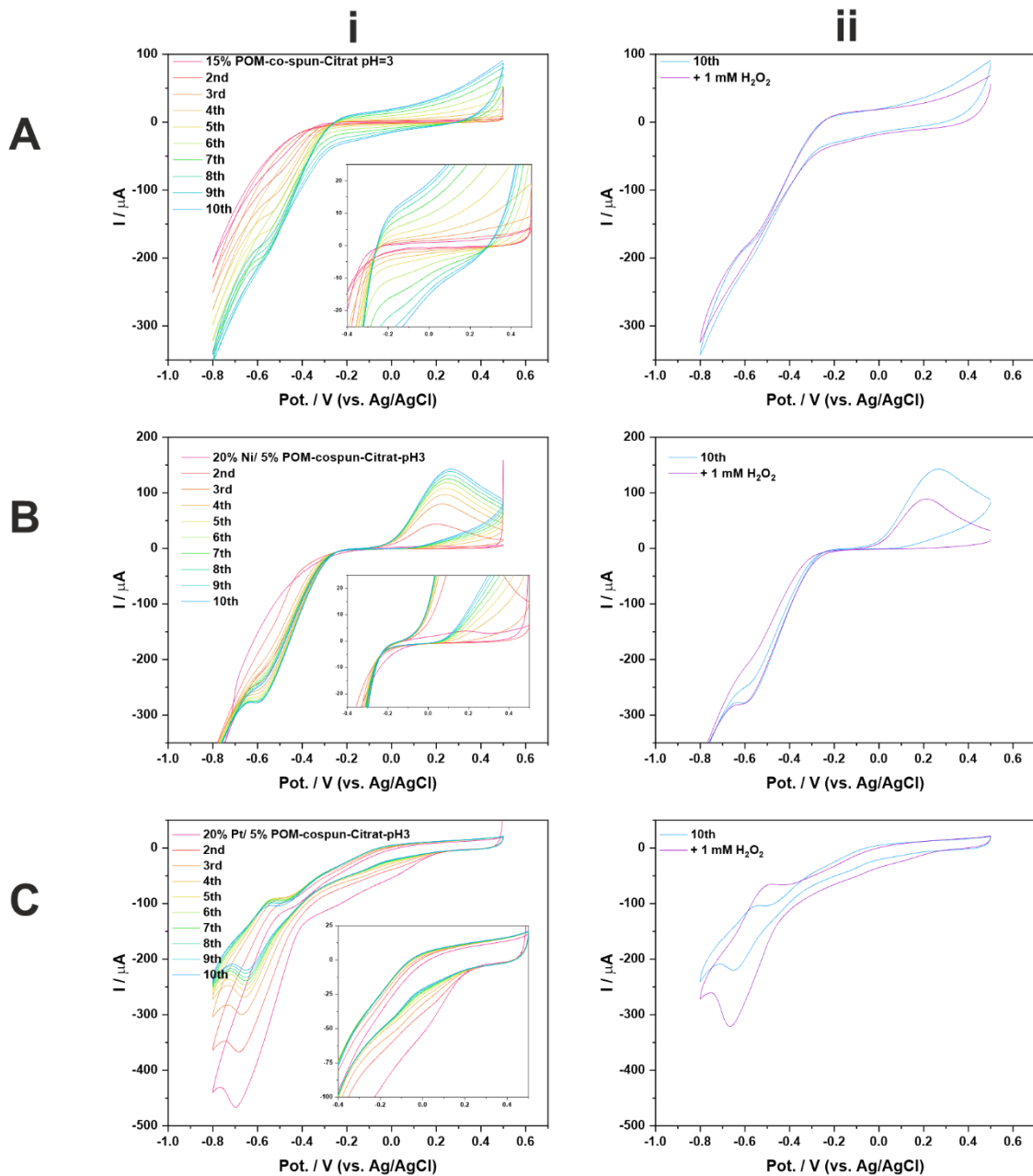


Figure S3.11: CV measurements of SiMo-co-spun LCNF (i) for ten consecutive times in citrate buffered solution (pH= 3) and (ii) the 10th scan in buffer versus an additional scan in citrate buffered solution with 1 mM H₂O₂. For (A), 15 w% POM @ Matrimid® fibers, for (B), 5 w% POM + 20 w% Ni @ Matrimid® fibers, and, for (C), 5 w% POM + 20 w% Pt @ Matrimid® fibers were used.

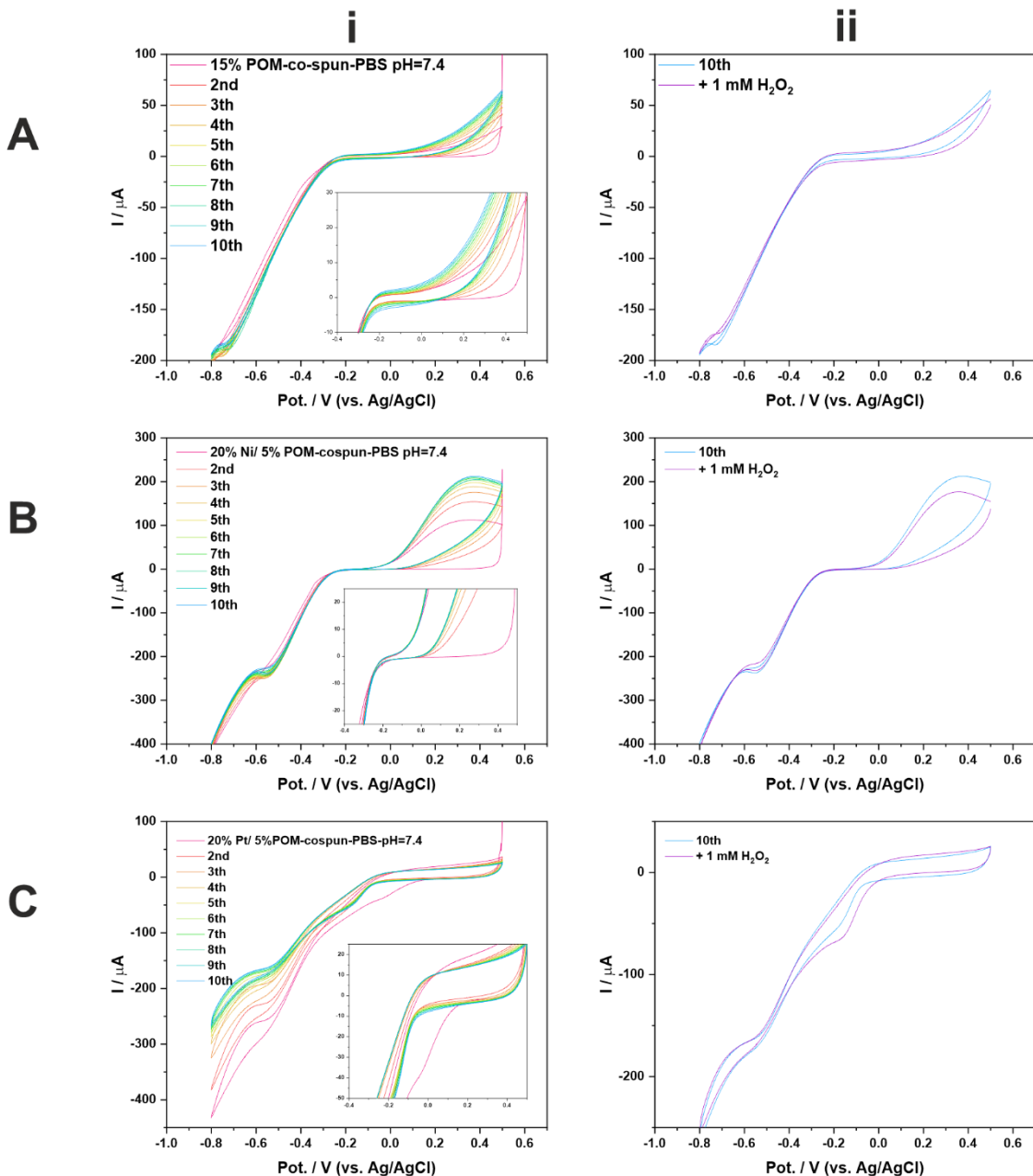


Figure S3. 12: CV measurements of SiMo-co-spun LCNF (i) for ten consecutive times in phosphate buffered solution (pH=7.4) and (ii) the 10th scan in buffer versus an additional scan in phosphate buffered solution with 1 mM H₂O₂. For (A), 15 w% POM @ Matrimid® fibers, for (B), 5 w% POM + 20 w% Ni @ Matrimid® fibers, and, for (C), 5 w% POM + 20 w% Pt @ Matrimid® fibers were used.

To determine whether POMs are destroyed in the spinning solution, during electrospinning, or -most likely- during laser exposure, small-angle X-ray scattering (SAXS) was used to check if POMs retained their well-defined spherical shape in the co-spun nanofibers before and after laser exposure. Therefore, concentrations ranging from 1.5 mM to 150 mM SiMo in water were investigated using SAXS (**Figure S3.13**) to understand which signal comes from SiMo when measuring the solid samples. A very defined scattering from 1 to 10 nm⁻¹ can be observed for both raw spectra and spectra after the subtraction of water. The size of SiMo was further determined by fitting the spectra of the 1.5 mM SiMo solution (**Figure S3.14**) with a simple sphere model ($r= 0.456$ nm) by using the program SASfit.

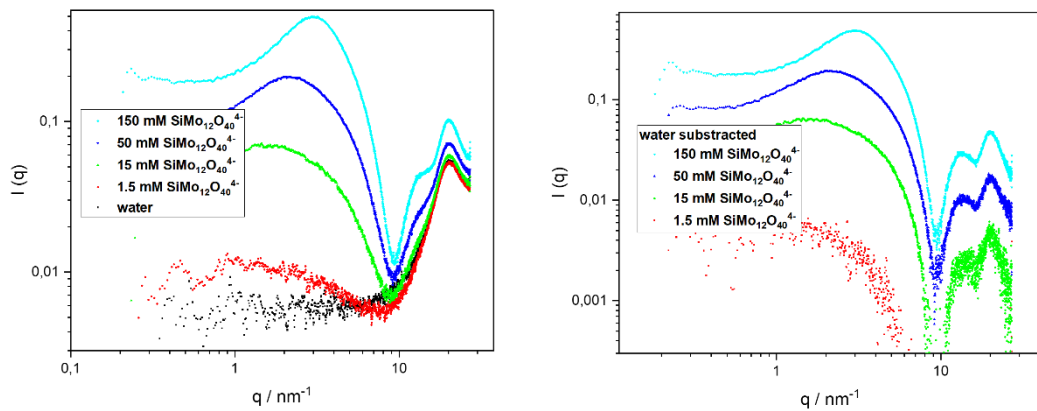


Figure S3.13: SAXS spectra of aqueous SiMo samples (0, 1.5, 15, 50, 150 mM)(left) and the spectra after subtraction of scattering from water (right).

According to SAXS measurements, SiMo is still present in the electrospun nanofibers, as indicated by the scattering similar to the scattering of SiMo (**S3.15A**), which is absent in the SAXS spectra of, for example, Pt-nanofibers (**Figure S3.15B**). Furthermore, a reflex at $q = 6 \text{ nm}^{-1}$ is present in POM-co-spun nanofibers (**Figure S3.15A**), corresponding to a repetitive distance between two objects of $(2 \cdot \pi/q = 1.05 \text{ nm})$. This could be interpreted as the POM-POM distance on the nanofibers, suggesting that POMs are very close to each other, considering that the diameter of SiMo is 0.91 nm (**Figure S3.14**). POMs were added to these fibers at 15 wt% compared to the dry mass of the polymer, so it is indeed possible that there are regions within the nanofiber matrix where these distances are prevalent. However, after laser scribing, the contribution of POM to the SAXS spectra almost disappeared (**Figure S3.16**), although it is still present when comparing the spectra with Pt-LCNFs, which do not contain any POMs. In conclusion, according to SAXS, POMs are not harmed during electrospinning, but POMs are almost completely destroyed after laser scribing. This raises the question of whether the remaining POM is even present on the surface of the LCNF and thus accessible to the solution, or within the LCNF matrix, making it undetectable on the electrode. This would explain the recoded CV spectra in **Figure S3.11** and **Figure S3.12**.

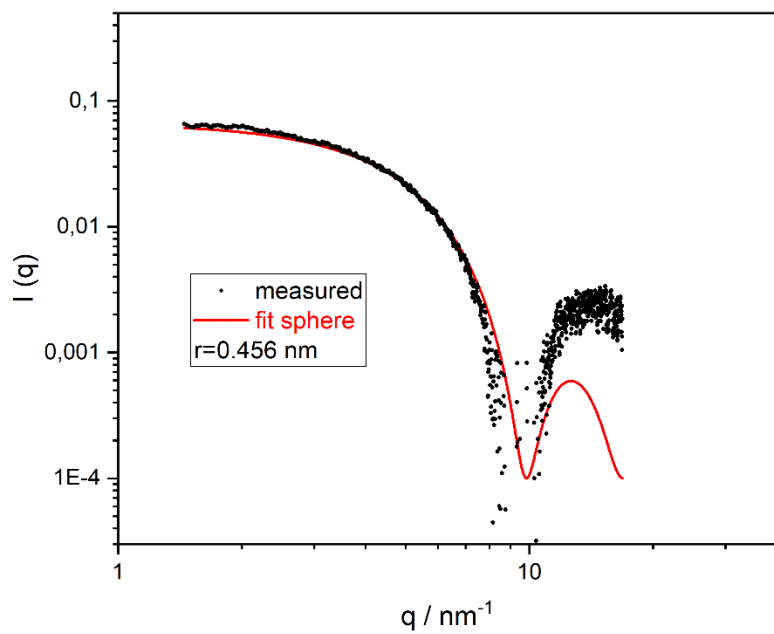


Figure S3. 14: SAXS spectra of 1.5 mM SiMo (water subtracted) and a fit by using a monodisperse sphere-model ($r = 0.456 \text{ nm}$; SASfit).

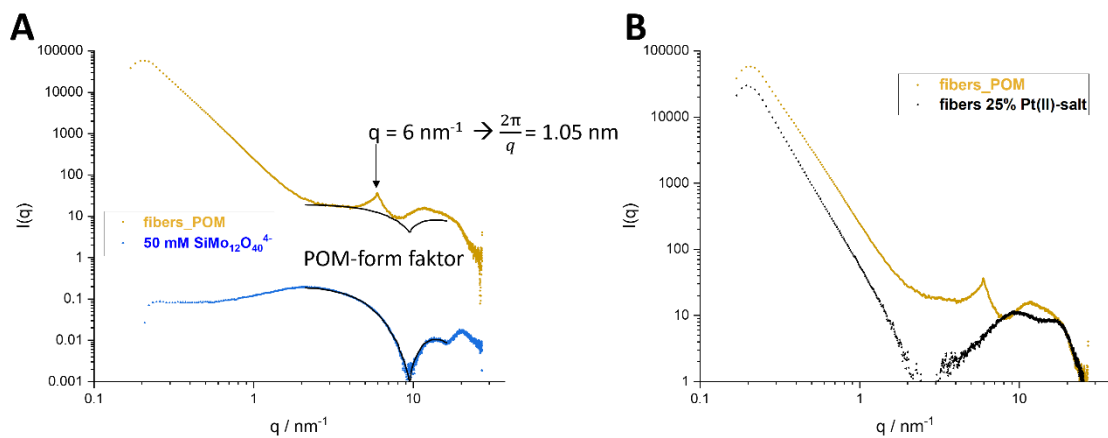


Figure S3. 15: SAXS spectra of (A) SiMo in aqueous solution (50 mM) and Matrimid-nanofibers with SiMo embedded (co-spun) and (B) Matrimid-nanofibers with and without SiMo embedded.

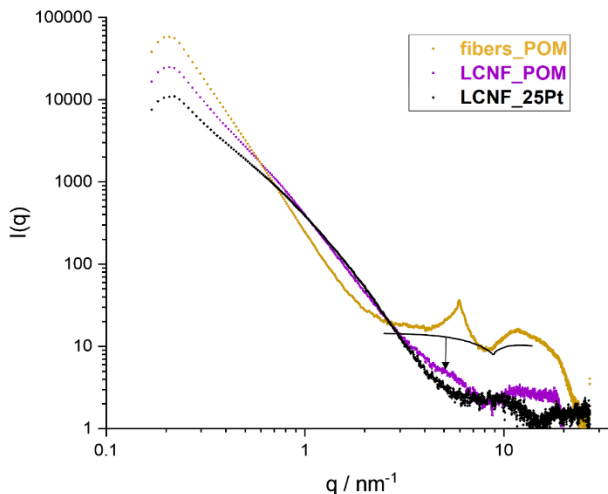


Figure S3. 16: SAXS spectra of Matrimid-nanofibers with SiMo embedded before (fibers_POM) and after (LCNF_POM) laser scribing and in comparison, a laser scribed LCNF without POMs (LCNF_25Pt). The form factor of SiMo present in LCNF_POM is implied by the black arrow.

Since co-spinning of POMs did not result in sufficient amounts of working catalyst at the electrode surface, drop-coating of POM with consecutive drying of the electrode was investigated. However, drop-coating SiMo onto untreated LIG-LCNFs did not lead to stable attachment due to electrostatic interactions between POM and LCNF²⁰⁰. This was evidenced by the reduced CV signals after exchanging the drop and starting a second measurement (**Figure S3.17**).

As a result, a second strategy to attach POMs on the LCNF surface was explored: the adsorption of polyoxometalates onto hydrophilic surfaces, with the dehydration of POMs serving as an enthalpic driving force (superchaotropic effect)^{201,204}. Note that the adsorption behavior of ions can be linked to their charge density, with superchaotropic ions to be expected between 6 and 12 charges per nm³²⁰¹. Due to their charge density, these ions can't build as much hydrogen bonds with water as water does in its bulk^{205,206}. In conclusion, the enthalpic gain during the adsorption of superchaotropic ions is achieved by the formation of additional hydrogen bonds when water is released in its bulk. With a size of 0.38 nm³ ($V = \frac{4 \cdot \pi}{3} \cdot (0.45 \text{ nm})^3 = 0.38 \text{ nm}^3$) and 4 charges, SiMo has a charge density of 10.5 charges per nm³ and can be classified as superchaotropic. To achieve a superchaotropic adsorption, a hydrophilic surface of the electrode is required. In conclusion, a Pegylation of the surface is promising²⁰¹. For a PEGylation, nanoparticles of Pt-LCNF were functionalized by incubating the Pt-LCNF in a PEG-thiol solution²⁰⁷. The PEG-thiol is expected to covalently bind to the Pt nanoparticles by a Pt-S bond. After functionalization with PEG, drop-coating of the POM indeed led to more stable attachment of POMs (**Figure S3.18Bi**: (pH=3), **Figure S3.19Bi**: pH=7.4) compared to untreated Pt-LCNF (**Figure S3.18Ai**: (pH=3), **Figure S3.19Ai**: pH=7.4). Additionally, for both pH=3 and pH=7.4, the catalytic reduction of H₂O₂ between -0.2 V and -0.6 V was significantly improved for PEGylated Pt-LCNF compared to untreated Pt-LCNF (**Figure S3.18Bii** vs. **Figure S3.18Aii**; **Figure S3.19Bii** vs. **Figure S3.19Aii**).

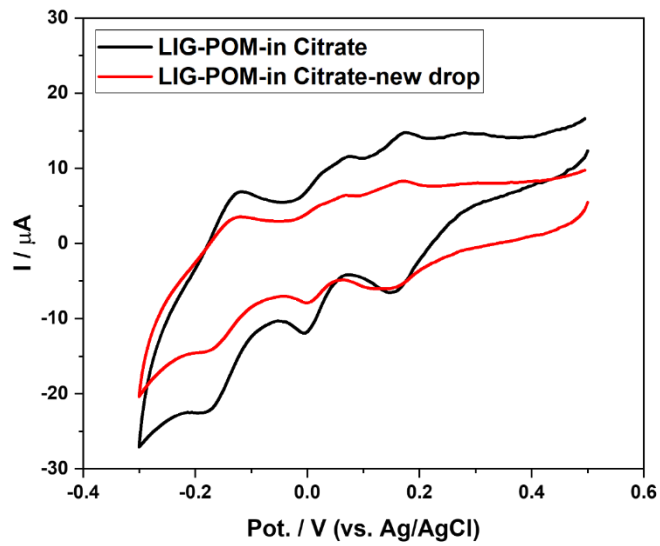


Figure S3.17: Two consecutive measurements of POM deposited on LIG-LCNF by dropcoating in citrate buffered solution.

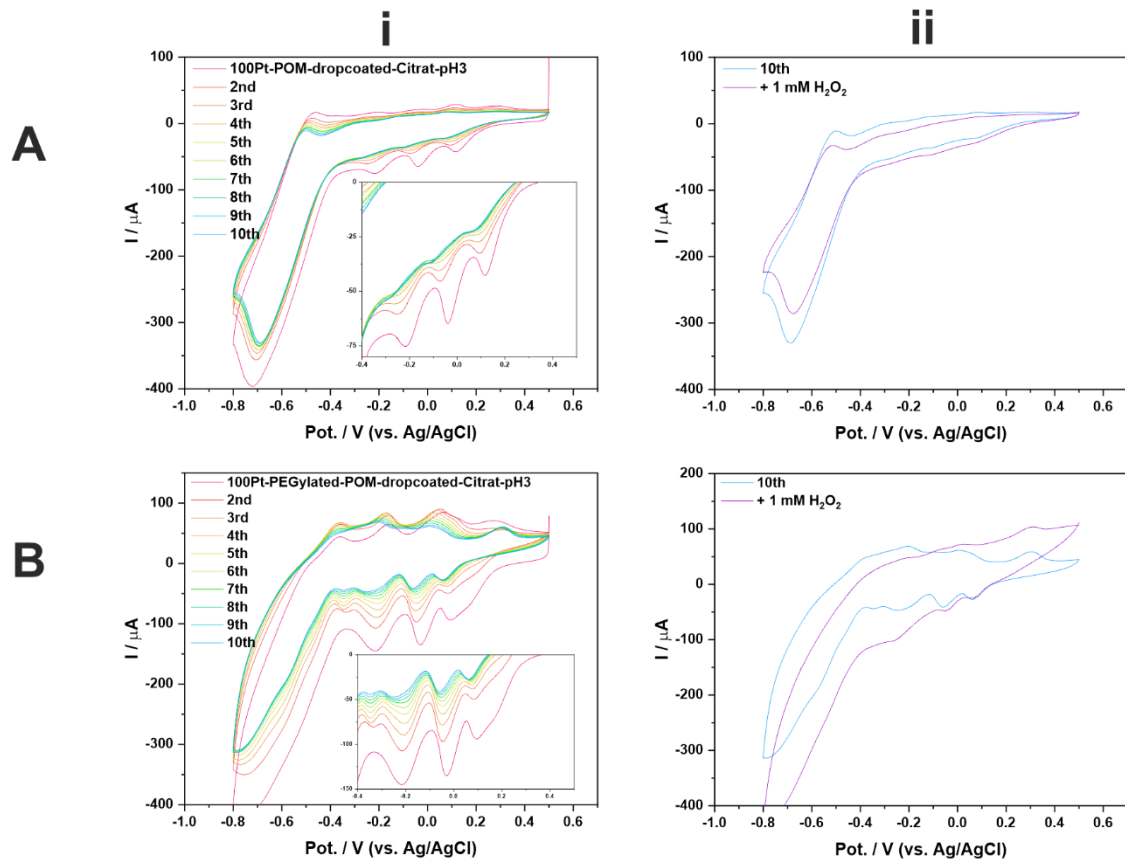


Figure S3.18: CV measurements of SiMo dropcoated on (A) Pt-LCNF and on (B) PEGylated Pt-LCNF (i) for ten consecutive times in citrate buffered solution (pH= 3), and (ii) the 10th scan in buffer versus an additional scan in citrate buffered solution with 1 mM H₂O₂.

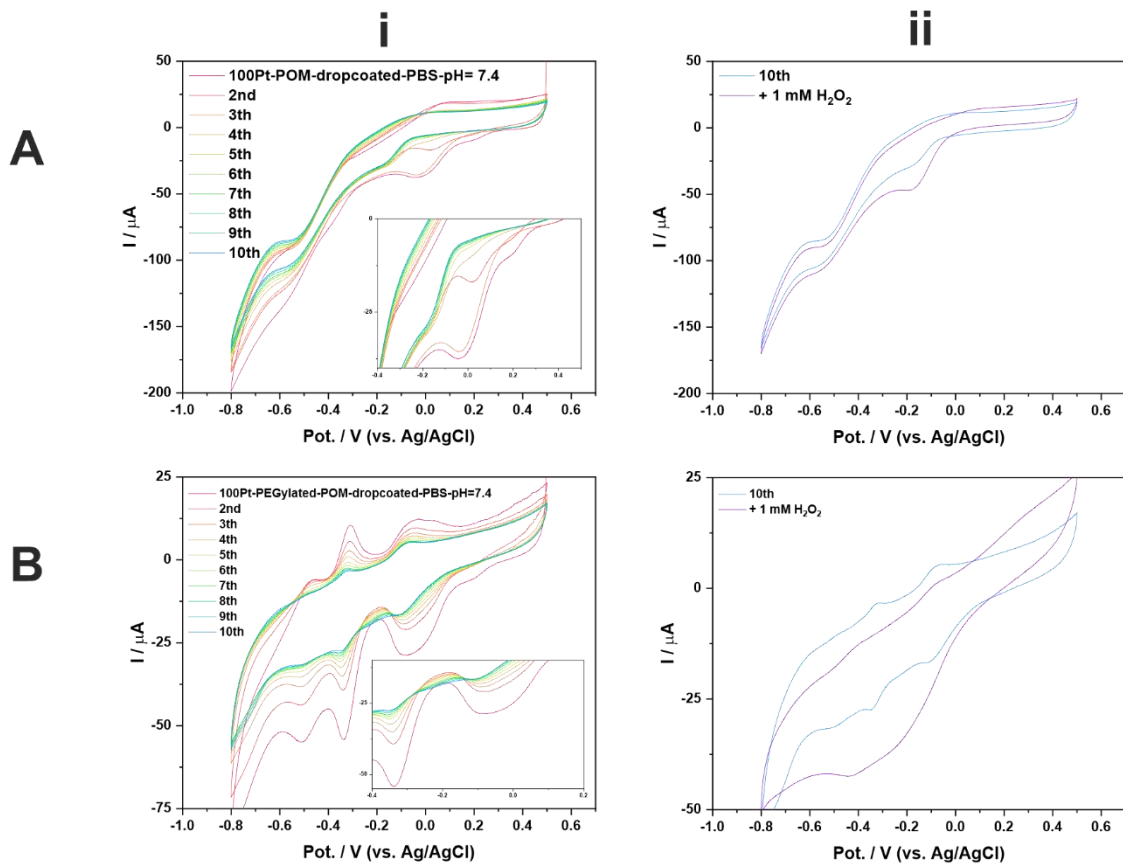


Figure S3.19: CV measurements of SiMo dropcoated on (A) Pt-LCNF and on (B) PEGylated Pt-LCNF (i) for ten consecutive times in phosphate buffered solution (pH= 7.4), and (ii) the 10th scan in buffer versus an additional scan in phosphate buffered solution with 1 mM H₂O₂.

As the scan ranges in previous measurements were chosen to reflect harsh conditions to induce detachment of POMs (scan range from -0.8 V to +0.6 V), the POM-drop-coated PEGylated Pt-LCNF was again investigated within a range where the third reduction of SiMo was just about to occur (+0.5 V to -0.3 V; **Figure S3.20**). However, even with PEG-coating, SiMo is much better stabilized at pH 3 (**Figure S3.20A**) compared to pH 7.4 (**Figure S3.20B**).

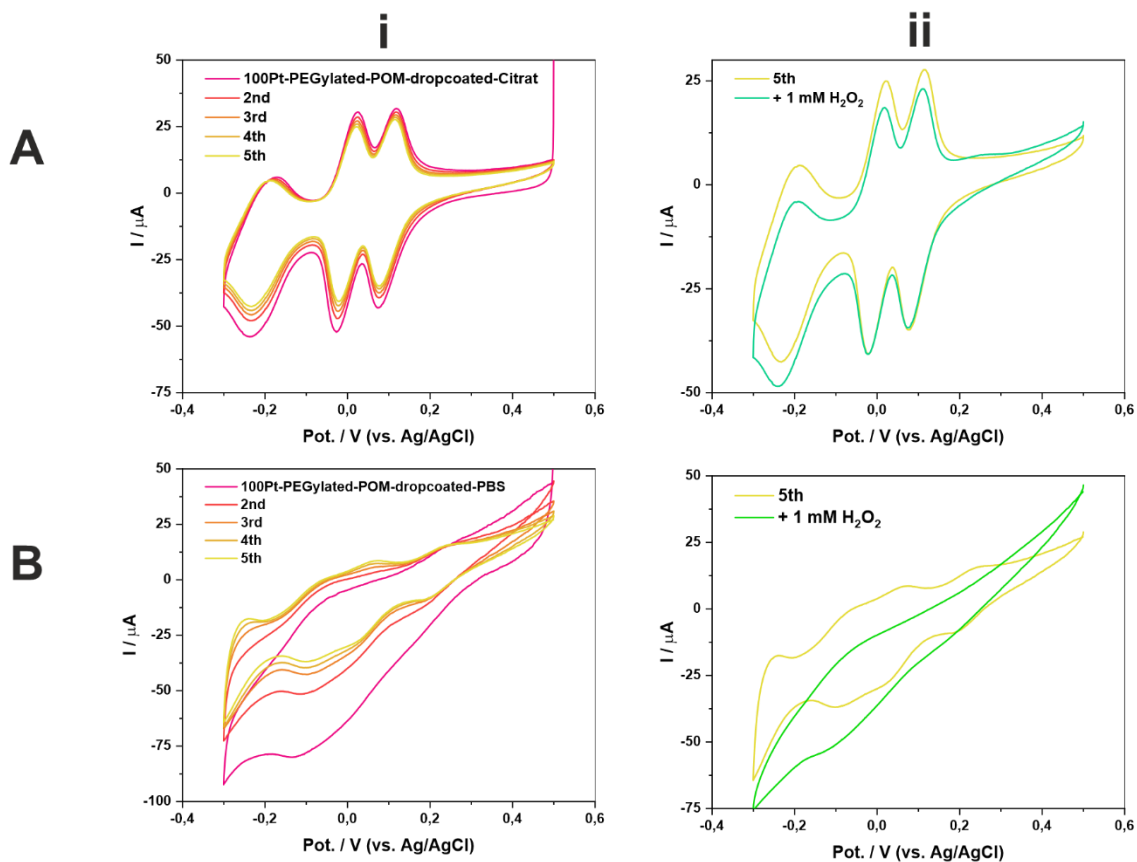


Figure S3.20: CV measurements with a smaller scan range of SiMo dropcoated on PEGylated Pt-LCNF in (A) citrate buffer (pH= 3) and (B) phosphate buffer (pH= 7.4), (i) for ten consecutive times in buffered solution, and (ii) the 10th scan in buffer versus an additional scan in buffered solution with 1 mM H₂O₂.

Additionally, a cheaper approach to PEGylate LCNFs than with Pt-LCNFs and a PEG-thiol was investigated. This approach involved adding negative charges to the LIG-LCNF (metal-free) surface with an oxygen plasma treatment²⁰³, followed by drop-coating the positively charged surfactant Ethomeen C/25²⁰⁸. The plasma treatment should enhance the electrostatic interactions between the LCNF and the surfactant. This PEGylation also led to stable attachment of POM in citrate buffer (**Figure S3.21D**). Note that the oxygen plasma treatment increased the effective surface area of the electrode because of the increased hydrophilicity (higher signal of the first scan), but the negative charges of the added oxygen groups repelled the negatively charged SiMo, which led to a weaker attachment (faster decay of signal in consecutive scans, **Figure S3.21A, B**). Furthermore, without the negative charges due to the oxygen plasma²⁰³, the positively charged surfactant seems to be weaker bound to the LCNF, which can be seen the drop of signal after washing the electrode (**Figure S3.21C**). However, only a slight catalytic effect towards reduction of hydrogen peroxide was observed for the plasma treated LCNF and the plasma treated Ethomeen-coated LCNF (compare blue (H₂O₂) vs. orange (10th scan) lines at -0.2 V in **Figure S3.21**).

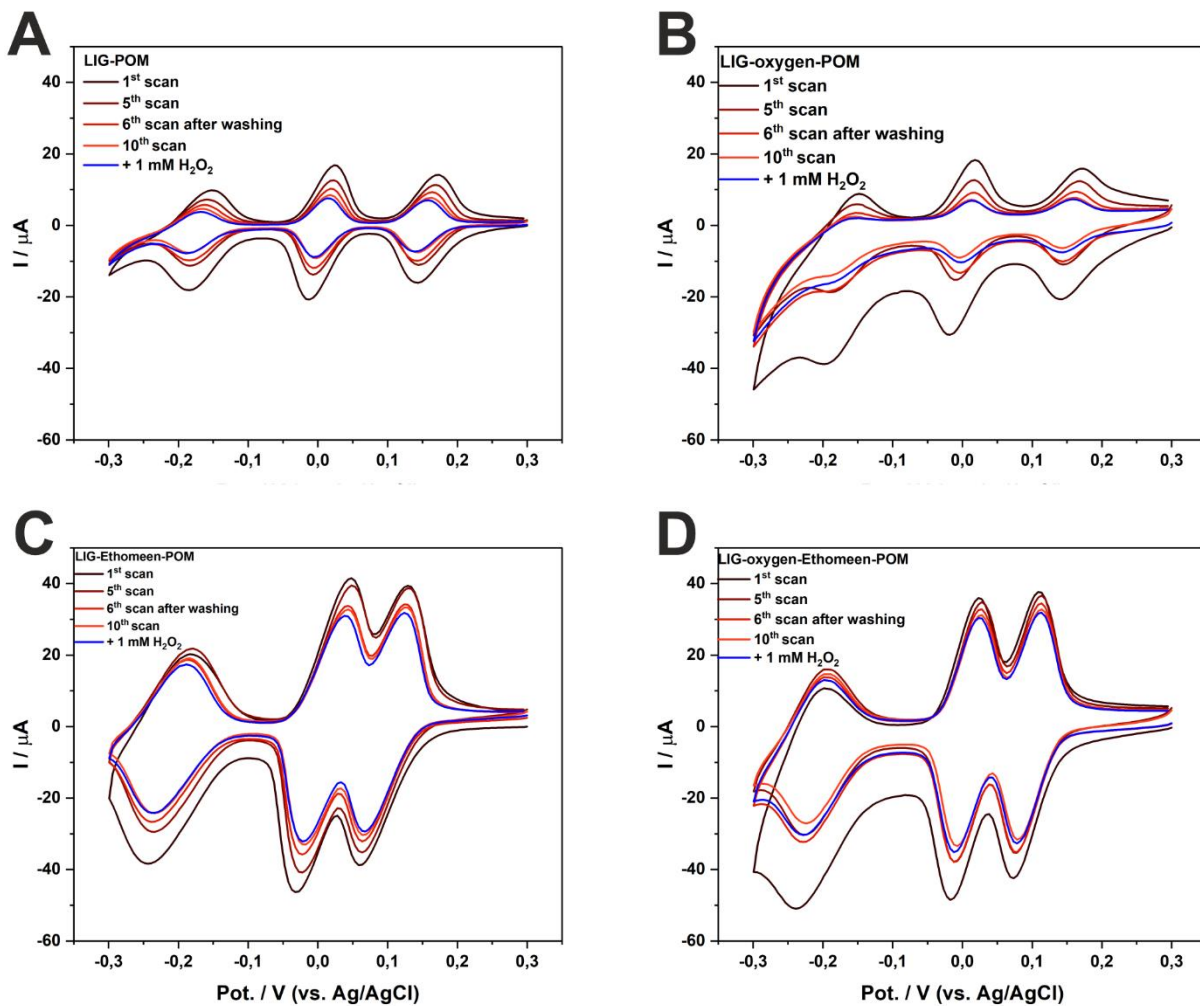


Figure S3.21: CV measurements of SiMo dropcoated on (A) laser induced graphene (LIG) LCNF, (B) oxygen-plasma treated LIG LCNF, (C) Ethomeen C/25 dropcoated LIG-LCNF, and (D) oxygen-plasma treated, Ethomeen C/25 dropcoated LIG-LCNF in citrate buffered solution (pH= 3). CV measurements show the first and the fifth scan in one solution. The sixth and the tenth scan of a consecutive measurement after washing the electrode are shown as well. After that, a scan in 1 mM H_2O_2 was recorded.

As indicated in **Figure S3.22**, Pt-LCNF alone also catalyzes H_2O_2 reduction in both the phosphate and citrated buffered solutions. Various experiments (CV-ratiometric approaches, stirred and unstirred chronoamperometric approaches, both PEGylation strategies; data not shown) did not lead to a better or similar sensitivity towards hydrogen peroxide detection when using SiMo. The problem was the high reduction current of the catalyst itself, which was only slightly increased by adding 1 mM of hydrogen peroxide, meaning that the catalyst is not fast enough at low analyte concentrations. Another problem was, similar to the approaches with Pt-LCNF, that no good stabilization of the blank measurement was achieved for non-stirred measurement setups. This is probably due to the fact that reduced forms of POMs can get oxidized by dissolved oxygen²⁰⁹, leading to the same problem as observed with Pt-LCNFs.

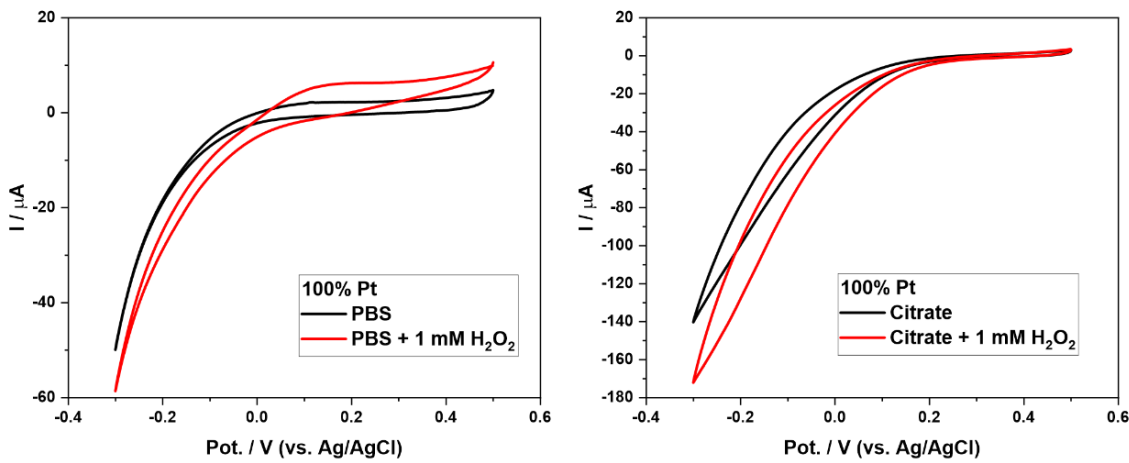


Figure S3. 22: CV measurement of pure Pt-LCNF (15 w%) in phosphate and citrate buffered solution with and without 1 mM H_2O_2 .

3.10.4 Conclusions

In this chapter, polyoxometalates were successfully attached to PEGylated LCNFs. This was achieved in two ways: (i) by a PEG-thiol forming covalent bonds with the Pt-nanoparticles of Pt-LCNF, and (ii) by electrostatic interactions of the negatively charged, oxygen-plasma treated LCNF and the positively charged surfactant Ethomeen C/25. Unfortunately, sensitive detection of H_2O_2 was not achieved in either citrated buffered solution or phosphate buffered solution. Nevertheless, it was shown how to deposit POMs onto LCNFs. Due to the low prices of both LCNFs and POMs, this system could be applied in catalysis, because various POMs have shown to catalyze many different reactions, like for example water splitting^{209–211}.

4. Laser generated Pt/Ni nanocatalysts-carbon nanofibers enabling ratiometric enzyme-free glucose detection at physiological pH

4.1 Abstract

We propose a bimetallic alloy composed of Pt and Ni embedded within laser-induced carbon nanofibers (Pt/Ni-LCNFs) as enzyme-free transducer for detection of glucose under physiological pH. Laser-exposure on electrospun polyimide nanofibers, embedded with Pt and Ni precursors, facilitated not only the formation of LCNFs but also the generation of Pt/Ni nanoparticles with a radius of approximately 2 nm and a distinctive crystalline structure. X-ray photoelectron spectroscopy revealed the oxidation states of the laser generated Pt/Ni and confirmed the formation of the Pt/Ni alloy nanocatalysts. Additionally, small-angle X-ray scattering has shown that the graphitic structures of the LCNFs strongly depend on the metal salts concentrations and molar ratio. Pt/Ni-LCNFs were exploited as enzyme-free electrodes for glucose sensing at physiological pH. The presence of Pt in the alloy enabled a low potential (-0.9 V for 20 s) *in situ* generation of highly localized OH⁻ which facilitated glucose electrooxidation by Ni. Under optimized conditions, Pt/Ni-LCNFs achieved reliable glucose detection in physiological conditions (pH 7.4), with detection limit of 0.3 mM, linearity from 0.1 mM - 4 mM, and minimal interference from other electroactive species. Ratiometric data acquisition strategy provided an excellent recovery rate (95 ± 10 %) in diluted human serum. Furthermore, unlike enzyme-based sensors, the catalytic activity of Pt/Ni LCNFs was maintained after sterilization, highlighting their robustness and potential in biomedical applications and bioprocess monitoring.

This chapter has been submitted as an original research article in Sensors and Actuators B and was formatted to fit for this thesis.

4.2 Author contribution

The author contributed to the conceptualization, design of the study, experimental investigation, data acquisition, interpretation of the data, and writing original draft. Vivien Fleischmann supported the experimental investigation. Dr. Aladin Ullrich conducted the TEM-EDX measurements and contributed to Figure 4.2 and its interpretation. Prof. Luc Girard supported us with XPS measurements, interpretation of the data and reviewing. Dr. Pierre Bauduin contributed with project administration, funding acquisition, supervision, writing – review & editing, Prof. Antje Bäumner contributed with project administration, funding acquisition, reviewing and supervision. Dr. Nongnoot Wongkaew led the conceptualization, project administration, funding acquisition, supervision, and writing of the original draft.

4.3 Graphical abstract

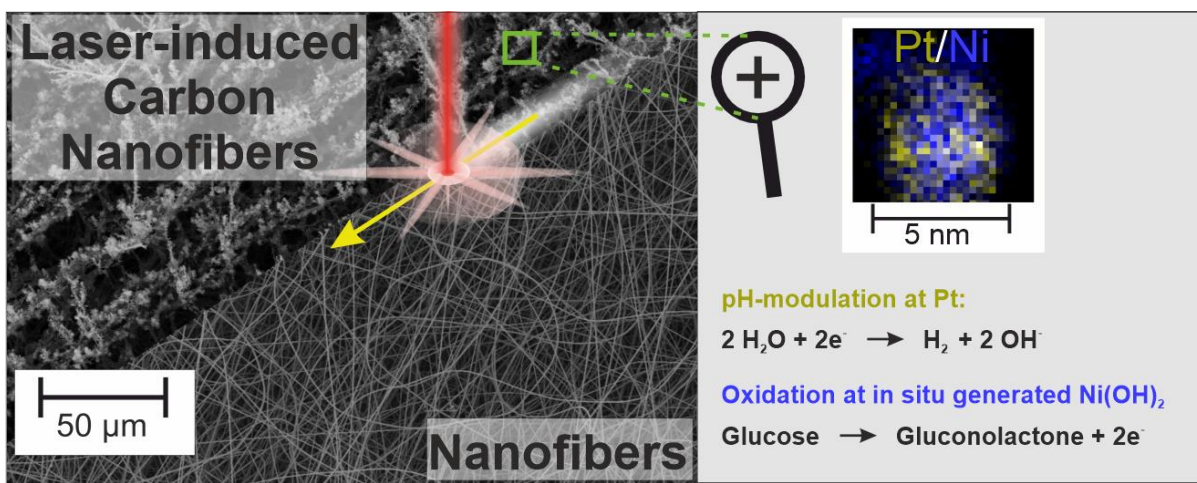


Figure 4. 1: Graphical abstract of chapter 4.

4.4 Introduction

Electrochemical sensors-based enzyme-free approaches have shown superior features in terms of cost and stability when compared to conventional enzyme-based sensing strategies. Various kinds of metal and metal oxide nanomaterials have been proposed as useful nanocatalysts in this endeavor, but bimetallic ones have gained significant interest nowadays because they offer synergistic effects that typically make the electrocatalytic reaction better than their monometallic counterparts²¹². In particular, Pt/Ni nanocatalysts have received a lot of attention in the development of enzyme-free sensors. For example, Pt/Ni nanocatalysts are highly attractive for glucose sensing, as seen from previous studies that demonstrated superior analytical performance for glucose detection at either alkaline or physiological pH^{213–215}. When using Pt alone, the sensors typically suffer from surface poisoning of the nanocatalyst due to dehydrogenated intermediates during the electrooxidation of glucose. The addition of a non-noble metal to the nanocatalyst can potentially remove the poisonous intermediates and thus promote electron-transfer reactions, rendering a desirable catalytic effect when compared to monometallic Pt nanoparticles²¹⁶. Pt/Ni alloys decorated multi-walled carbon nanotubes (MWCNT) have been successfully employed for glucose detection at physiological pH¹⁴⁵. Herein, the amperometric measurements at +0.1 V were applied to electrocatalyze glucose oxidation. The Pt/Ni alloys have also been proven to be biocompatible^{217,218}, making them highly attractive for biomedical applications.

Various approaches have been reported for synthesis of Pt/Ni alloys or with carbon hybrids and have been successfully applied to enzyme-free sensors. These include chemical reduction^{142,145}, electrodeposition^{213,219}, and thermal treatment²²⁰. Despite the great success of the previous reports on synthesis and using Pt/Ni nanocatalysts in enzyme-free sensors, their utility in point-of-care (POC) testing is yet to be achieved. This is mainly because the proposed fabrication techniques are sophisticated, and incompatible for scaling up, and rather costly. Moreover, the measurements mostly require laboratory equipment, e.g. a stirrer, to achieve the greatest analytical performance.

Carbon nanomaterials and their functional hybrids fabricated by laser-writing hold great promise in addressing the aforementioned challenges¹⁹. Here, the mixture of carbon and metal nanocatalyst precursors can be facilely and economically converted into nanocatalyst-carbon hybrids via CO₂ laser exposure, as shown in the pioneered work by Tour's group, in which the as-generated electrodes were mainly used for the oxygen reduction reaction applicable in energy conversion and storage.⁵⁸ Nevertheless, their proposed strategy inevitably requires annealing of the precursor substrate prior to the laser exposure. Also, the formation of mixed metal precursors has not yet been investigated.⁵⁸ These issues leave room for further studies, in particular towards the manufacturing of enzyme-free sensors in which mass-production capability, arbitrary electrode designs, and low overall cost are advantageous. Moreover, the strategy offers a highly controllable manner and needs only simple instrumentation without expensive cleanroom facilities.

Our group has employed laser pyrolysis technology to generate 3D-porous carbon electrodes from electrospun polyimide (PI) nanofiber substrates, termed laser-induced carbon nanofibers (LCNFs). Here, unlike the polyamic acid (PAA) which was used by Tour's group⁵⁸, a solvent-soluble PI, Matrimid®5218, has been employed. This thus eliminates the need for an imidization process, i.e., PAA being converted into PI prior to annealing and laser-pyrolysis. Upon optimization of fabrication process parameters as reported earlier⁶², the LCNFs exhibit 3D-porous structures and superior analytical performance for common redox markers in comparison to commercially available screen-printed electrodes. We later demonstrated the integration of the LCNF electrodes within miniaturized analytical systems where the devices were able to detect dopamine⁷⁸, and DNA targets in pM range²²¹. This is clearly attributed to the presence of a 3D-porous nanostructure within the microfluidic analytical system. This development thus opens many promising future prospects, especially in the area of POC testing where high detection sensitivity is required.

Furthermore, we have proven that metal salt precursors, e.g., Ni acetylacetone, doped within electrospun PI nanofibers can be *in situ* converted into Ni nanocatalysts embedded within the LCNFs²⁴. The as-generated Ni-LCNFs have been successfully applied for glucose detection under alkaline conditions, providing a limit of detection (LOD) in the sub μ M range. We also proved that the stability of the Ni nanocatalysts embedded within LCNFs under stirred solution for a long period is much greater than that of electrodeposited Ni onto LCNFs. To take a step further, we recently attempted to fabricate bimetallic Pt/Ni alloys embedded within LCNFs where optimization of fabrication processes and electrochemical performance were assessed for H₂O₂ as a model analyte⁶³. However, the studies mostly focused on analytical aspects where in-depth investigations on the Pt/Ni-LCNFs have not yet explored. In addition, unlike Ni-LCNFs that require alkaline detection medium for the measurement²⁴, the Pt/Ni-LCNFs are highly promising for glucose detection under physiological pH. Here, nobel metals such as Au, Pd, and Pt have been exploited for *in situ* generation of OH⁻ via electrochemical reduction of proton (water splitting), subsequently promoting electrocatalytic oxidation of glucose by the catalyst itself¹⁴⁸ or the added active one, e.g., Co or Ni^{148,222}. Despite their excellent analytical performance and potential

for integration into wearable glucose sensing devices, the studies still presented some shortcomings. These include the need for complex fabrication systems and high reduction potentials in OH⁻ generation^{147,222}. Moreover, the nanocatalysts must be coated with a polymer layer to ensure mechanical stability after electrodeposition²²², which could diminish their electrocatalytic activity and possibly explain the need for higher reduction potential. Taken together, the beneficial features of Pt/Ni-LCNFs could help address these issues, ultimately leading to highly practical and efficient sensors at lower cost. In the present work, we thus aimed to fabricate Pt/Ni-LCNFs and perform in-depth studies focused on material characterizations and their associated electroanalytical performance in order to exploit the electrodes for enzyme-free glucose detection at physiological pH. Herein, we characterized the materials by transmission electron microscopy (TEM) and high spatial resolution TEM (HRTEM) to explore the sizes and crystallinity of the nanocatalysts, respectively. In addition, we elucidated the Pt/Ni alloyed structure via scanning TEM coupled with energy-dispersive X-ray spectrometry (STEM-EDS). We also revealed the influence of Pt and/or Ni on the resulting graphite/graphene oxide structure, i.e. arrangement of graphene sheets and defects, of LCNFs and the oxidation states of added metal(s) via X-ray photoelectron spectroscopy (XPS). Additionally, small-angle X-ray scattering (SAXS) was used to characterize the graphitic structure of the LCNFs, specifically the stacking of graphene sheets and their interlamellar distance. The capability of Pt/Ni nanocatalysts to generate local OH⁻ and subsequently oxidize glucose, as well as the influence of their composition, were carefully examined. Two distinct measurement approaches were explored: 1) single measurement, and 2) multiple measurements performed on each electrode, in which their detection sensitivity and selectivity were compared and discussed. Furthermore, we also investigated the effects of electrode ageing and sterilization to access the remaining electrocatalytic activity of Pt/Ni nanocatalysts.

4.5 Materials and methods

4.5.1 Fabrication of laser-induced carbon nanofibers

For electrospinning, a polymer solution containing 15% (w/v) Matrimid® 5218 (Huntsman Advanced Materials BVBA, Belgium) in N,N-dimethylacetamide (Merck, Germany) was prepared. Additionally, 25% w/w metal salt (based on the dry mass of the polymer) was added, specifically platinum(II)-acetylacetone (97%, Sigma-Aldrich, Germany) and nickel(II)-acetylacetone (95%, Sigma-Aldrich, Germany), in various molar ratios (1:0, 3:1, 1:1, 1:3, 0:1). These mixtures were called 100Pt, 75Pt/25Ni, 50Pt/50Ni, 25Pt/75Ni, and 100Ni, respectively. The resulting solutions were stirred overnight. Electrospinning was performed following a method similar to that in a previous publication.⁶³ Specifically, a rotary drum collector with a rotation speed of 150 rpm and a 15 cm distance between the needle (20 G) and collector was used. The applied potential during electrospinning ranged between 12 and 13 kV, at a flow rate of the spinning solution of 10 µL/min. As an additional substrate for collecting nanofibers, an indium tin oxide-coated poly(ethylene terephthalate) sheet (ITO/PET) with a sheet resistivity of 60 Ω/sq (1 ft × 1 ft × 5 mil, Sigma Aldrich, Germany) was employed. The substrate, cut into pieces of 10 x 30 cm, was attached to the collector of the rotary drum, with the non-conductive side touching the collector. Grounding of the conductive side of the substrate was achieved using aluminum foil, which made contact with both the substrate and the rotary drum collector. The spinning time was set to 3 hours, and the temperature ranged between 22 and 28 degrees Celsius, with humidity maintained between 30% and 50%. After spinning, nanofiber mats were dried at room temperature overnight in a fume hood to remove any organic solvent residues.

Laser-induced carbon nanofibers (LCNFs) were generated using a CO₂ laser (10.6 µm, VLS 2.30, Universal Laser System, Polytech Systeme GmbH, Germany). The lasing speed was maintained at 60% (1,270 mm·s⁻¹), the image density was set to 1,000 DPI, and optimal reproducibility was achieved with a laser power of 2.4 W.

The price per electrode, depending on the metal composition, was estimated in **Figure S4.1A** for an electrode size shown in Figure **S4.1B**. Hereby, one fiber mat was electrospun within 3 h and 228 electrodes could be laser-scribed (a row of electrodes was scribed at the same time) at on one mat within approximately 45 minutes.

4.5.2 Characterization methods

The TEM analysis was performed at a JEOL NEOARM F200 instrument, equipped with a JEOL EDS detector, at 200kV beam energy. The samples were prepared by scratching LCNFs off the ITO/PET substrate. The resulting powder was suspended in ethanol and ultrasonicated for 1 minute. After waiting for 10 minutes so that the bigger particles would settle, 10 µL of the supernatant solution was deposited on a TEM grid (carbon film on 400 squares copper grid mesh). The grid was dried at room temperature. No further treatment like plasma cleaning was applied.

For SEM, samples were PdAu-sputtered (2.45 kV, 22 mA, 20 s) before the measurement (SEM, Zeiss/LEO 1530, Germany).

The surface composition was monitored by X-ray photoelectron spectroscopy (XPS) on an ESCALAB 250 (Thermo Electron). The X-ray excitation was provided by a monochromatic Al $\text{K}\alpha$ (1486.6 eV) source. Analyzed surface has a 500 μm diameter. The background signal was removed using the Shirley method²²³. The surface atomic concentrations were determined from photoelectron peaks areas using the atomic sensitivity factors reported by Scofield²²⁴. Binding energies (BE) of all core levels were referred to the C-C of C1s carbon at 284.8 eV.

SAXS measurements were performed on a bench built by XENOCS with Mo radiation ($\lambda = 0.071$ nm). A q -range from 0.2 to 35 nm^{-1} was recorded on an online scanner detector from MAR Research (diameter: 345 mm). Data analysis was performed with pySAXS. As the sample holder, a self-made powder holder was used (a tube with a diameter of roughly 0.5 cm, closed on both sides with Kapton foil. For background correction, the empty holder with Kapton foil on both sides was subtracted. Silver behenate in a 2 mm quartz capillary was used for scattering vector calibration. For sample preparation, untreated LCNF electrodes were scratched off the ITO/PET substrate and directly filled into the sample holder.

4.5.3 Electrochemical measurements

As a potentiostat, the MultiPalmSens4® (PalmSens, Netherlands) was used. All measurements were performed with a 3-electrode system, i.e., LCNF as a working electrode, a Pt-wire as a counter electrode, and an Ag/AgCl electrode as reference electrode for all electrochemical measurements. The geometric size of the LCNF was 0.07 cm^2 , isolated from the contact part of the electrode by candle wax. All measurements were conducted non-stirred with a 40 μL drop of the solution placed on the LCNF, with the Pt-wire and Ag/AgCl electrode dipping into the drop. All electrodes were used (if not stated otherwise) without any pretreatment on the same day they were laser-scribed (usually 1-6 h after scribing).

Glucose measurements:

To investigate the impact of pH on alloyed LCNFs, NaOH (Sigma-Aldrich, Germany) was added to a 1x PBS solution (Merck, Germany, initial pH = 7.4, 10 mM phosphate buffer, 2.7 mM KCl, 137 mM NaCl) until reaching pH values of 7.7, 11.8, 12.6, or 12.9. Subsequently, these solutions were used to perform three cyclic voltammetry (CV) scans on untreated, fresh LCNF electrodes (scan range from -0.1 V to +0.9 V). Additionally, a fourth CV scan was conducted on the same electrode using the same PBS+NaOH solution containing 10 mM glucose.

For investigating pH modulation, LCNFs in a 1x PBS solution (pH = 7.4) were employed. Prior to the CV scan, electrochemical pretreatments (20 s at -0.8 V, 20 s at -0.9 V, and 40 s at -0.8 V) were applied

directly before the CV scan (ranging from -0.1 V to +0.9 V). Notably, a pretreatment at -0.7 V did not enable glucose detectability.

For the single measurement performed on each electrode (used in the calibration curve and aging study), pristine Pt/Ni-LCNF electrode was immersed in a 1× PBS solution (pH = 7.4, 10 mM phosphate buffer, 2.7 mM KCl, 137 mM NaCl) containing glucose concentration of interest. Following a pretreatment at -0.9 V for 20 s, a CV scan was performed from 0.0 V to +0.8 V. Contact angles in the aging study were determined on untreated electrodes. For a pretreatment with Tween to enhance wettability of 20-day-old electrodes, a 0.05 w% Tween in PBS solution was placed on the electrode. After 10 s, the drop was removed and washed 3 times with PBS buffer.

For multiple measurements on the same electrode the following procedure was sequentially carried out: 1) pretreatment at -0.9 V for 20s (unless stated otherwise) in PBS; 2) a CV scan from 0.0 V to +0.8 V; 3) electrode cleaning by application of -0.2 V for 60s (unless stated otherwise); and 4) repeating steps 1) to 3) for five times in the new PBS solution for every CV to establish stable background signal; and 5) repeating steps 1) to 3) again for new analyte solution. The sequential electrochemical measurement steps were computed by using a script in the software MultiTrace 4.5 from PalmSense. The script was constructed in the following sequence:

{

-Measurement (Cyclic Voltammetry (pretreatment setting: E deposition: -0.9 V; t deposition: 20 s; Cyclic voltammetry settings: t equilibrium: 0 s, E begin: 0.0 V, E vertex1: +0.8 V, E vertex 2: 0.0 V, E step: 0.001 V, Scan rate: 0.05 V/s);

-Wait (Wait for 10 seconds)

-Chronoamperometry (Chronoamperometry settings: t equilibrium: 0 s, E dc -0.2 V, t interval: 0.1 s, t run: 60 s).

}

In the recovery study, human serum was bought from Sigma-Aldrich (H4522) and either used pure or diluted by 1:5 in PBS.

4.6 Results and discussion

4.6.1 Structural and composition analysis

We investigated LCNF without metal (**Figure 4.2Ai**), 100Pt-LCNF (**Figure 4.2Aii**), 50Pt/50Ni-LCNF (**Figure 4.2Aiii**), and 100Ni-LCNF (**Figure 4.2Aiv**) using transmission electron microscopy (TEM). The average radii of the nanoparticles investigated are as follows: 1.4 ± 0.6 nm for 100Pt, 1.1 ± 0.7 nm for 50Pt/50Ni, and 2 ± 1 nm for 100Ni. **Figure 4.2A** also provides a detailed size distribution of the radii for each metal composition.

Furthermore, high-resolution TEM (HRTEM) was employed to investigate the crystal structure. Specifically, we examined (i) the graphite-like structure of LCNF and (ii) the metal nanoparticles (**Figure 4.2B**). In **Figure 4.2Bi**, we observed various (001)-d-spacings of the graphite-like carbon matrix, ranging from 0.71 nm to 0.75 nm. For comparison, pure graphite would exhibit a (001)-d-spacing of 0.672 nm.²²⁵ This result suggests that LCNFs contain several functional oxygen groups, which increase the distance between stacked graphene sheets. An irregular occurrence of these functional groups likely contributes to the varying distances between the sheets. Consequently, we can infer that the carbon matrix is similar to graphene oxide (GO) or reduced graphene oxide (rGO).

Regarding the nanoparticles in 100Pt-LCNF and 50Pt/50Ni-LCNF (**Figure 4.2Bii+iii**), both exhibit similar (111)- and (100)-d-spacings. These values align with literature data: (111)-d-spacing of 0.226 nm/0.236 nm vs. 0.227 nm for pure Pt²²⁶ and 0.225 nm for PtNi alloy²²⁷; (100)-d-spacing of 0.398 nm/0.396 nm vs. 0.392 nm for pure Pt²²⁶ and 0.389 nm for PtNi alloy²²⁷. The measured angle between the (111) and (100) planes of 55° matches perfectly with the theoretical value of 54.7° for a cubic system.

Figure 4.2Biv shows that 100Ni particles have a (111)-d-spacing of 0.246 nm and a (100)-d-spacing of 0.429 nm. Comparing these values to XRD measurements in literature²²⁸, we find that they are closer to a NiO lattice rather than a Ni lattice (2θ of (111) equals 37.26° for NiO and 44.50° for pure Ni, resulting in a (111)-d-spacing of 0.24 nm and 0.20 nm, respectively. Furthermore, 2θ of (200) equals 43.29° for NiO and 51.86° for Ni, giving a (100)-d-spacing of 0.42 nm and 0.36 nm, respectively).

Finally, STEM-EDX analysis of different 50Pt/50Ni particles revealed that out of 10 investigated particles, 70% of them are nanoparticles with a Ni-rich core and a Pt-rich shell as shown in **Figures 4.2 Ci-iv**, and 30% of the investigated nanoparticles have an equal distribution of both elements (**Figure 4.2 Di-iv**). The results suggested that synthesis of nanoparticles during laser scribing tends to be rather random, with a general preference of Ni-atoms to be located inside the particles. However, when the nanoparticles contain higher amounts of Ni, there is a greater likelihood that Ni will be also present on the surface.

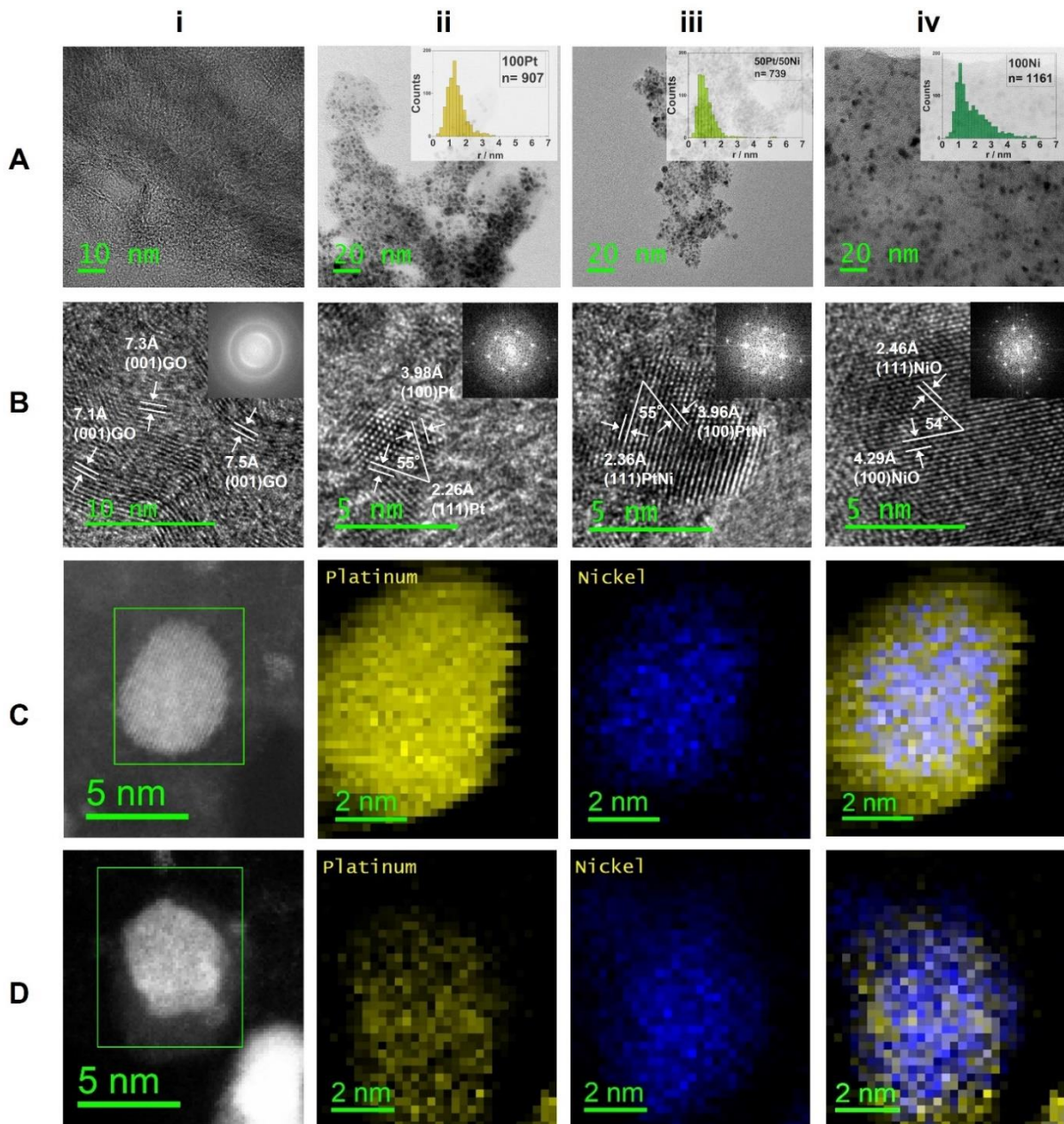


Figure 4. 2: Structural and composition analysis of the laser-generated LCNFs with various Pt and Ni content. (A) An overview of TEM images and the respective size distribution (radius of nanoparticles) of (i) LCNFs, (ii) 100Pt-LCNFs, (iii) 50Pt/50Ni-LCNFs, and (iv) 100Ni-LCNFs. (B) The crystalline structure of (i) LCNFs, (ii) 100Pt-LCNFs, (iii) 50Pt/50Ni-LCNFs, and (iv) 100Ni-LCNFs revealed by HRTEM. (C) STEM-EDS image showing (i) the mapping area of 50Pt/50Ni alloy core-shell nanoparticle focused on (ii) Pt, (iii) Ni, and (iv) Pt-Ni overlay. (D) STEM-EDS image showing (i) the mapping area of 50Pt/50Ni alloy non-core-shell nanoparticle focused on (ii) Pt, (iii) Ni, and (iv) Pt-Ni overlay.

The correlation between morphological structures and the metal compositions of Pt/Ni-LCNFs were thoroughly characterized using scanning electron microscopy (SEM) in a previous work⁶³. Thus, we only provided the exemplary SEM images of 50Pt/50Ni-LCNFs in the current study (**Figure S4.1C**). The distorted fibrous structure can be expected due to harsh conditions of the single laser exposure process. However, the resulting edges and defects are likely to be beneficial as they may serve as active sites and enhance the accessibility of analytes to the embedded nanocatalysts. For further detail on the

microstructures of LCNFs with other metal combinations, the authors guided readers to our previous study⁶³.

In the previous study, we also performed SEM-EDX analysis to reveal global information on the distribution of nanoparticles over the chosen electrode area and the percentage of Pt, Ni, O, and C found within the Pt and/or Ni-LCNFs. However, as the surface chemistry of Pt and/or Ni-LCNFs play a pivotal role in electrocatalytic reactions of enzyme-free sensors the SEM-EDX data in the previous study are insufficient. Therefore, want to further explore these aspects in more detail using X-ray photoelectron spectroscopy (XPS).

To reveal the impact of Pt and/or Ni on the graphitic characteristics of LCNFs, the deconvoluted XPS spectrum of C1s orbitals for each type of electrode was divided into four peaks (**Figure S4.2A**). These peaks were assigned to different carbon environments, i.e., C (sp²) at 284.3 eV, C(sp³) at 284.7 eV, C-O at 285.7 eV, C=O / O-C=O at 288.3 eV²²⁹⁻²³¹. The quantitative evaluation of XPS data shown in **Figure 4.3A** demonstrated that the 100Pt-LCNFs possessed a greater amount of graphite, indicated by C(sp²) peak, than 100Ni-LCNFs. When combining the two metals (50Pt/50Ni-LCNFs), Ni induced a stronger impact than Pt in the formation of sp² hybrid as indicated by the reduction of C(sp²) peak by 12% (compared to 100Pt-LCNFs). Considering the presence of edges/defects where oxygenated functional groups are present, 100Ni-LCNFs exhibited O-C=O and C=O contents higher than those of 100Pt-LCNFs. 50Pt/50Ni LCNFs possessed O-C=O and C=O contents similar to those of 100Pt-LCNFs, which may imply that Pt plays a major role in removing these functional groups. This could be due to the lower intrinsic thermal conductivity of Pt that allows better heat localization within PI nanofibers during laser exposure, thus facilitating more complete thermal reduction processes. In contrast Ni, with its higher thermal conductivity, enables faster heat dissipation along the PI nanofibers, leading to less generation of rGO in comparison to 100Pt-LCNFs. For 50Pt/50Ni-LCNFs, Ni seemed to play an essential role in the heat dissipation process as seen from the similar rGO content obtained when compared to 100Ni-LCNFs. Nevertheless, the combination of 50Pt/50Ni promoted the presence of C-O, which is still unclear to us. Overall, it could be concluded that Ni induced the generation of oxygenated groups on LCNFs more than Pt. The data from the C1s orbital (**Figure 4.3A**) are consistent with those observed for the O1s orbital (**Figure S4.2B**).

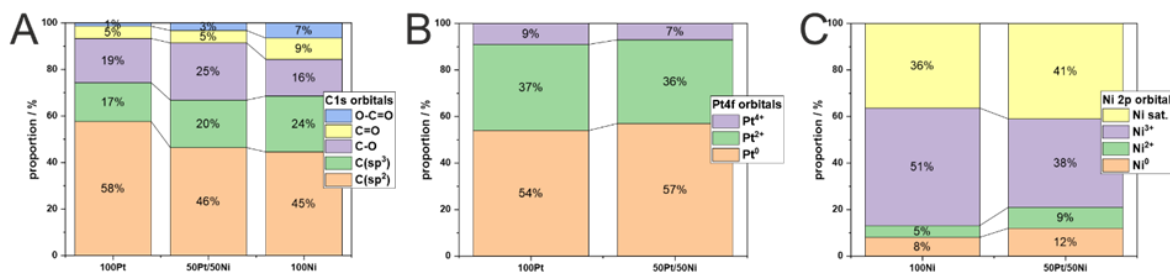


Figure 4.3: XPS analysis of surface chemistries at (A) C1s orbitals, (B) Pt4f orbitals (Pt⁰ and Pt²⁺ and their satellites are combined), and (C) Ni2p orbitals (Ni³⁺ and its satellite are combined).

Considering the XPS spectra of the Pt4f orbital for the 100Pt- and 50Pt/50Ni-LCNFs, the deconvolution of the spectra resulted in five peaks, which corresponded to various oxidation states, i.e., Pt⁰ (at 70.9 and 74.3 eV), Pt²⁺ (at 72.2 and 75.7 eV), and Pt⁴⁺ (at 77.2 eV) (see also **Figure S4.3A**)²³². Here, Pt⁰ is the dominant species among the others (**Figure 4.3B**), and has commonly been employed for electrocatalytic reactions in enzyme-free electrochemical sensors. The obtained three valence states of Pt in our study are in accordance with the study in which Pt nanoparticles decorated carbon nanotubes in aqueous solution were generated via femtosecond laser²³³. This work employed potassium hexachloroplatinate (IV) (K₂PtCl₆) as the precursor, which is different from ours where platinum(II) acetylacetone is used. Nevertheless, Liu et al. and co-worker reported the presence of Pt²⁺ and Pt⁴⁺ when used ultraviolet (355 nm) picosecond laser to convert platinum(II) acetylacetone mixed with polybenzimidazole (instead of PI) into Pt nanoparticles embedded in graphene films.²³⁴ However, in the work reported by Scroccarello et al.⁶⁴, the major valence state of Pt nanoparticles generated by using CO₂ laser exposure on the film made from GO and K₂PtCl₄ was Pt⁰. These could suggest that the valence states of laser-generated Pt nanoparticles are affected by various factors, i.e., lasing environment including matrices and other compositions where Pt precursor is embedded, type of Pt precursor (counter ion), and type of laser. However, it should be noted that introducing Ni did not significantly alter the content of valence states for Pt (**Figure 4.3B**). This may be due to its inherent characteristics as a noble metal.

The deconvoluted XPS spectra for Ni2p orbitals of 100Ni- and 50Pt/50Ni-LCNFs displayed in **Figure S4.3B** revealed the presence of Ni⁰, Ni²⁺, and Ni³⁺ within 100Ni-LCNFs and 50Pt/50Ni-LCNFs. However, unlike Pt shown in **Figure 4.3B**, **Figure 4.3C** illustrated the notable difference in the proportions of the valence states when compared between 100Ni-LCNFs and 50Pt/50Ni-LCNFs. Here, Ni³⁺ was the prominent valence state within 100Ni-LCNFs while Ni⁰ and Ni²⁺ were majorly present in 50Pt/50Ni-LCNFs. The decrease of Ni³⁺ and the increase of Ni⁰ and Ni²⁺ in 50Pt/50Ni-LCNFs may be attributed to the intrinsic low heat conduction of Pt that allows more efficient heat localization. In agreement with C1s orbitals, less heat hinders generation of reduced GO (lower rGO:GO ratio), where Ni could serve as a reduction agent. The observation of Ni⁰, Ni²⁺, and Ni³⁺ in our study was consistent with the work reported by Jiménez-Pérez et al. where Pt/Ni electrocatalysts were synthesized via electrodeposition of K₂PtCl₆ and Ni(CH₃CO₂)₂ on screen-printed electrodes²³⁵. It is interesting to point out that the proposed electrodeposition strategy by Jiménez-Pérez et al. also enabled the valence states of Pt⁰, Pt²⁺, and Pt⁴⁺. The as-developed Pt/Ni porous nanoarchitectures on screen-printed carbon electrodes exhibited superior electrocatalytic activity for H₂O₂ detection in the aerosol phase.

Furthermore, according to XPS spectra of Pt⁰ for 50Pt/50Ni-LCNFs (**Figure S4.3A-ii**), the slight shifts to higher binding energy in comparison to that of 100Pt-LCNFs (**Figure S4.3A-i**) suggested Pt/Ni alloy formation^{142,220}. However, it is worth mentioning that in the previous report²²⁰, negative shifts of Pt4f were observed in contrast to our case. This might be caused by the difference in the synthesis atmosphere where the Pt/Ni alloy synthesis shown in the literature²²⁰, proceeded under inert gas while ours was

performed under an ambient environment. The evidence of alloy formation was also supported by the shifts of Ni^{3+} and Ni^0 towards lower binding energies (**Figure S4.3B**). To our knowledge, this is the first report elucidating the potential of CO_2 laser for *in situ* generation of Pt/Ni alloy embedded within carbon nanomaterial matrices, carried out in one-step.^{219,220,236}.

Small-angle X-ray scattering (SAXS) is a useful technique for assessing structural information of carbon nanomaterials²³⁷. To our knowledge, SAXS has never been used for characterization of laser-induced carbon nanomaterials and their hybrids. A typical SAXS spectrum, which plots the scattered intensity, $I(q)$, against the scattering vector, q , on a logarithmic scale, is shown in **Figure S4.4**. This figure presents the spectra of 100Pt-LCNFs, 100Ni-LCNFs, and 50Pt/50Ni-LCNFs. Interestingly, only the 100Pt-LCNFs sample exhibits a q^2 dependency in the low q region (0.2 to 0.6 nm^{-1}), indicating the presence of flat surface structures. These structures, ranging in size from approximately 10 up to at least 30 nm (calculated as $(2\pi)/q$), reflect the size of reduced graphene oxide (rGO) or graphene oxide (GO) sheets. However, this scattering is largely overshadowed by a q^3 dependency, which suggests the presence of undefined structural arrangement of the graphitic sheets within the LCNFs.

To eliminate this overshadowing scattering, we used an $I(q) \cdot q^3$ vs. q plot shown in **Figure 4.4**. **Figure 4.4** displays the scattering from LCNFs containing various metal compositions and metal concentrations. Interestingly, a broad reflex at 18.7 nm^{-1} emerges with both increasing Ni content (Pt < PtNi < Ni) and increasing overall metal content (15 wt% < 20 wt% < 25 wt%). It is also possible to compare this reflex with X-Ray Diffraction (XRD) data. Here, we converted the q -vector of 18.7 nm^{-1} to its corresponding 2θ angle for copper radiation ($\lambda = 0.154 \text{ nm}$), resulting in $2\theta = 26.5^\circ$. According to the literature^{238,239}, this angle corresponds to the interlayer distance between two graphene layers, C (002) in crystal structure; a distance of 0.335 nm.

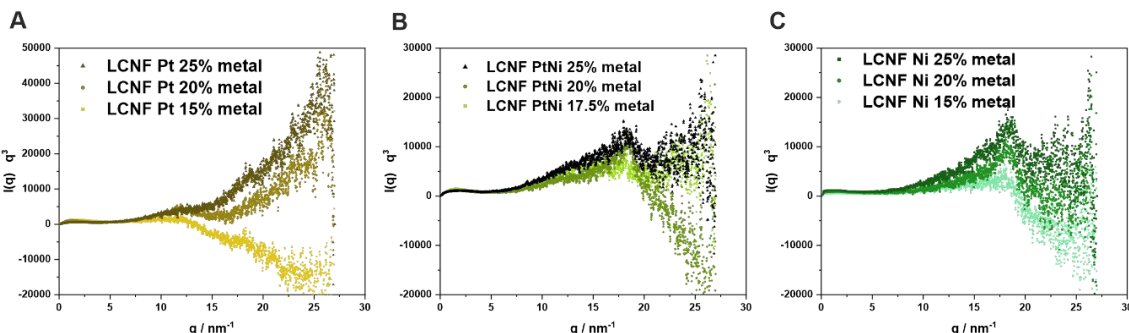


Figure 4.4: $I(q) \cdot q^3$ vs. q plot of 100Pt-LCNFs (A), 50Pt/50Ni-LCNFs (B) and 100Ni-LCNFs with various metal concentrations.

For pure graphite, the reflex at 18.7 nm^{-1} is typically sharp and pronounced due to graphite's well-defined crystal structure²³⁸. However, for less defined structures like reduced graphene oxide (rGO), as observed in TEM images in **Figure 4.2Ai**, a broad reflex similar to the SAXS ($I(q) \cdot q^3$ vs. q) plot in **Figure 4.4B and 4.4C** is present²³⁹. Therefore, we propose that the more pronounced peak indicates an increasing formation of consistently stacked rGO-like layers. When oxygen-containing groups within

the graphite layers are unevenly distributed, the uniform layering structure breaks down, resulting in the disappearance of the reflex at 18.7 nm^{-1} . The results presented in **Figure 4.4** suggest that the type and amount of metal (Ni or Pt) play critical roles in the uniform conversion of Matrimid to rGO. Specifically, Ni appears to be more effective than Pt in such a conversion process. Notably, 100Ni-LCNFs exhibit a greater degree of uniform stacking of rGO, particularly at elevated Ni content, which is not observed in the case of 100Pt-LCNFs. A comparison to HRTEM pictures of rGO structures in 100Ni and 100Pt LCNFs shown in **Figure S4.5** is in agreement with this observation.

In conclusion, we can propose/hypothesize that the enhanced heat conduction of Ni facilitates fast heat dissipation along the nanofiber precursor, promoting the uniform generation of stacked rGO sheets. In contrast, Pt leads to greater heat localization, resulting in intense local and unevenly distributed heat spots within 100Pt-LCNFs. These heat spots disrupt the uniform stacking, affecting the distribution of oxygenated groups. Hence, SAXS is here a powerful method for elucidating the graphitic structure of LCNFs.

4.6.2 Pt/Ni-LCNFs for glucose detection – single measurement per electrode

4.6.2.1 Pt/Ni alloy in LCNFs enabled the detection of glucose present in physiological pH

Originally, we aimed to introduce Pt and Ni into LCNFs to enable the detection of glucose under physiological pH as previously reported by other studies^{145,240}. However, the laser-generated Pt/Ni embedded LCNFs did not provide the result as expected. None of the metal combinations yielded any useful signal for glucose detection at pH 7.7 (**Figure S4.6**). This is likely due to the difference in preparation method of Pt/Ni alloy and how Pt/Ni are organized within the carbon nanomaterial matrix, which critically affects the electrocatalytic ability. As shown by Mei et al.¹⁴⁵ PtNi nanoparticles were able to oxidize glucose at physiological pH when attached to multi-walled carbon nanotubes (MWCNTs). However, no catalytic activity was observed when pristine carbon black was used as the matrix.

The electrocatalytic reaction of our LCNF electrodes can be seen only when Ni is present in high contents, and the measurement is performed at basic pHs. This might be explained by the formation of core-shell structure rather than random distribution of Pt and Ni atoms on the nanocatalyst's surface (see also **Figure 4.2C**) which may hinder the mutual benefit of Pt and Ni in enabling electrocatalytic reaction of glucose at neutral pHs. **Figure 4.5A** depicted the linear correlation between detection sensitivity of glucose per pH and Ni content (from 25% -100%) evaluated from **Figure S4.6**, suggesting the important role of Ni and OH^- for glucose oxidation, as generally known in the following reactions:



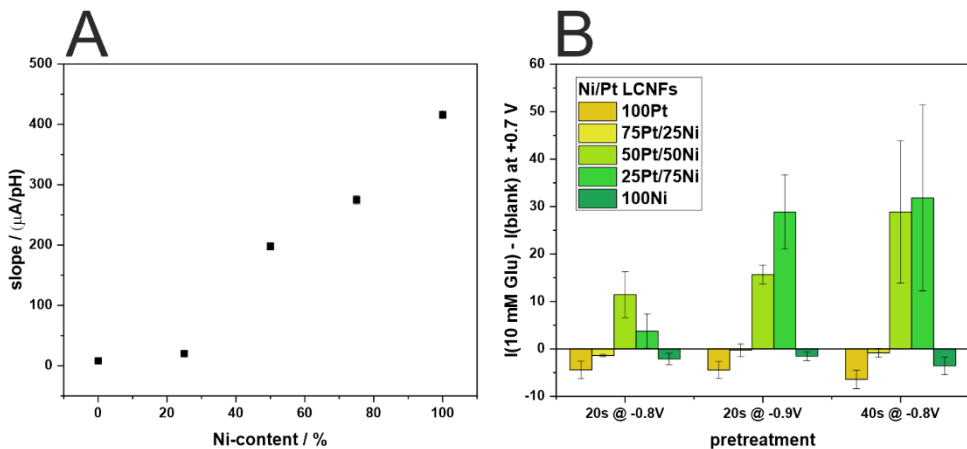


Figure 4.5: Electrochemical characterizations of electrodes for glucose detection. (A) Impact of Ni content on the sensitivity of glucose considering the anodic currents at +0.7 V and a pH above 11.5 (Figure S4.5). (B) Optimization of electrochemical pretreatment conditions for increasing pH locally (n=3).

As it is important to provide OH^- to allow the electrocatalytic reaction of glucose to be possible under physiological pH, *in situ* electrochemically generation of OH^- at the Pt vicinity through the water splitting reaction ($4 \text{H}_2\text{O} + 4\text{e}^- \rightarrow 2 \text{H}_2 + 4 \text{OH}^-$) prior to glucose measurement by CV was thus studied. Hereby, the LCNF electrodes containing either Pt or Ni alone did not result in any promising anodic peak from glucose oxidation under the investigated pretreatment conditions (Figure S4.7). In contrast, the electrodes with Pt/Ni alloy exhibited the expected outcome. Nevertheless, it is necessary to modulate Pt and Ni composition as well as the pretreatment conditions, i.e., voltage and time, to enable efficient *in situ* generation of OH^- and electrocatalytic oxidation of glucose (Figure 4.5B). The ratio of Pt and Ni can greatly affect the electrocatalytic oxidation. As the core (Ni)-shell (Pt) structure is formed (Figure 4.2C-iv) in this case, a small amount of Ni is unfavorable. This can be clearly supported by the inability of 75Pt/25Ni-LCNFs to promote electrocatalytic oxidation of glucose even when the electrodes were pretreated prior to glucose measurement (Figure S4.7). The pretreatment at greater negative voltages and longer times generates higher glucose responses as expected. Here, the 25Pt/75Ni-LCNFs pretreated at -0.9 V for 20s were selected due to their greatest sensitivity, favorable reproducibility, short pretreatment time, and lower cost (less use of Pt). It should be noted that increasing the voltage of pretreatment, e.g., up to -1 V, adversely resulted in poorer signal reproducibility. Some other previous studies have employed much higher voltages: -1.5 V for OH^- generation and +1.0 V for 2 s for electrode cleaning²²², and multiple potential steps including -2.0 V for 20 s to provide the alkaline condition, 0.2 V for 5 s to oxidize glucose, and 1.0 V for 2 s to clean the electrode surface¹⁴⁸. The lower potential used in our study underscores the efficiency of the bimetallic catalysts and allows the use of more affordable potentiostats that are not capable of applying high potentials, further reducing the overall cost of the setup.

In order to prove whether the glucose properly undergoes electrocatalytic reaction as commonly achieved from basic solution, we performed CVs that compared the signals of the glucose measurements in PBS buffer with adjusted pH of 11.8 and with electrochemically generated OH^- prior to the CV measurements (Figure 4.6A). The region from +0.6 V to +0.9 V, where electrocatalytic reaction of

glucose occurs, is still similar to the case of PBS buffer at pH 11.8 (absence of glucose), indicating the formation of Ni(OH)_2 species which gets oxidized to NiO(OH) (see **Figure S4.6 and reaction 2**)²⁴. Additionally, the proper increase of anodic current at around +0.7 V when glucose is present thus confirmed that *in situ* generation of OH^- assisted by Pt allows glucose measurement even if it is originally present at physiological pH. Furthermore, the intensity of anodic current at around +0.7 V is proportional to glucose concentration (**Figure 4.6B-ii**) but suffers from undesirable reproducibility (5-16% RSD). However, for freshly used electrodes, the pretreatment produces a non-negligible peak at around +0.15 V, which is absent when performing CV in PBS buffer pH 11.8. Although we are not clear yet about the source of the peak, the intensity of the peak at +0.15 V correlates with the peak intensity at +0.7 V and provides additional information on the activity of the individual electrode. With this, normalization of the signals at +0.7 V with the maximum peaks at around +0.15 V enabled the generation of greater reproducible signals with variations at only 2 – 8% RSD when using a new electrode for each measurement (**Figure 4.6B-iii**).

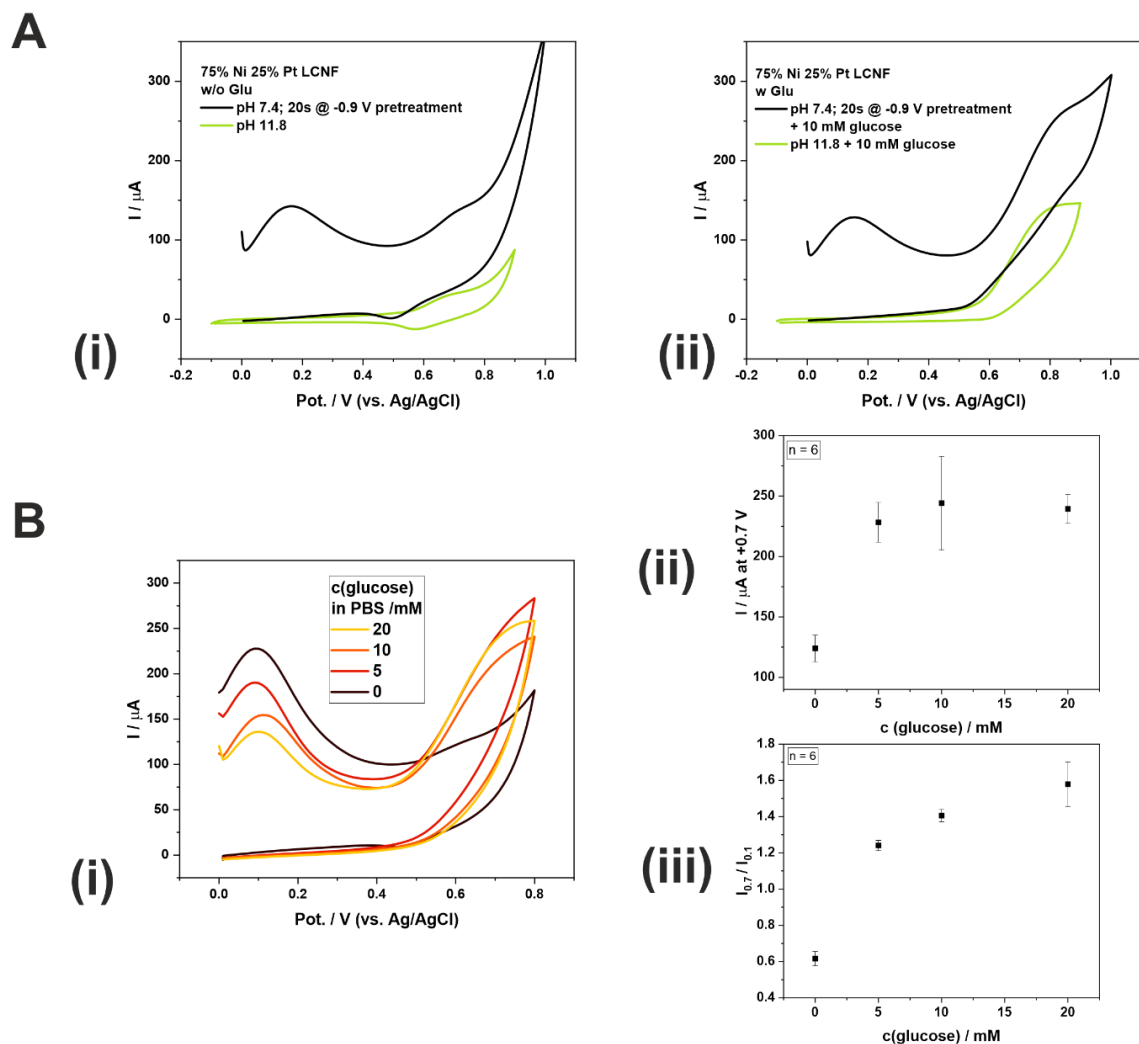


Figure 4. 6: Electrochemical detection of glucose using *in situ* generation of OH^- strategy prior to CV measurement. (A) Proof-of-principle of electrocatalytic reaction (i) without and (ii) with glucose characterized by CV. (B) (i) Exemplary CVs at various concentrations of glucose using pretreatment strategy (-0.9 V for 20s), and (ii and iii) improving reliability of data acquisition (n= 6). The CV measurement was conducted using a 50 mVs⁻¹ scan rate.

4.6.2.2 Effect of electrode ageing and sterilization on electrocatalytic activity for glucose

In general, it is known that electrodes with high surface activity show ageing effects over time when stored under ambient conditions. It was also shown here that storage affected electroanalytical performance and wettability (**Figure 4.7** and **Figure S4.8**). In general, high signals were obtained for fresh electrodes resulting though also in high standard deviations and hence worse limit of detection (LOD) than those aged for a few days under ambient conditions. Furthermore, the increase of water contact angle from ca. 100° to ca. 120° well supports the diminishing performance of the sensor with age. Herein, the increase in electrodes' hydrophobicity prevents homogeneous contact between the analyte solution and the electrode's surface. This problem can be circumvented by, for example, the addition of a surfactant, e.g., Tween. Here, the dramatic increase in linear correlation and approximately 5-fold improvement in LOD after addition of Tween emphasize the necessity of wettability when using 3D-porous carbon nanofiber electrodes (**Figure 4.7D to 4.7F**).

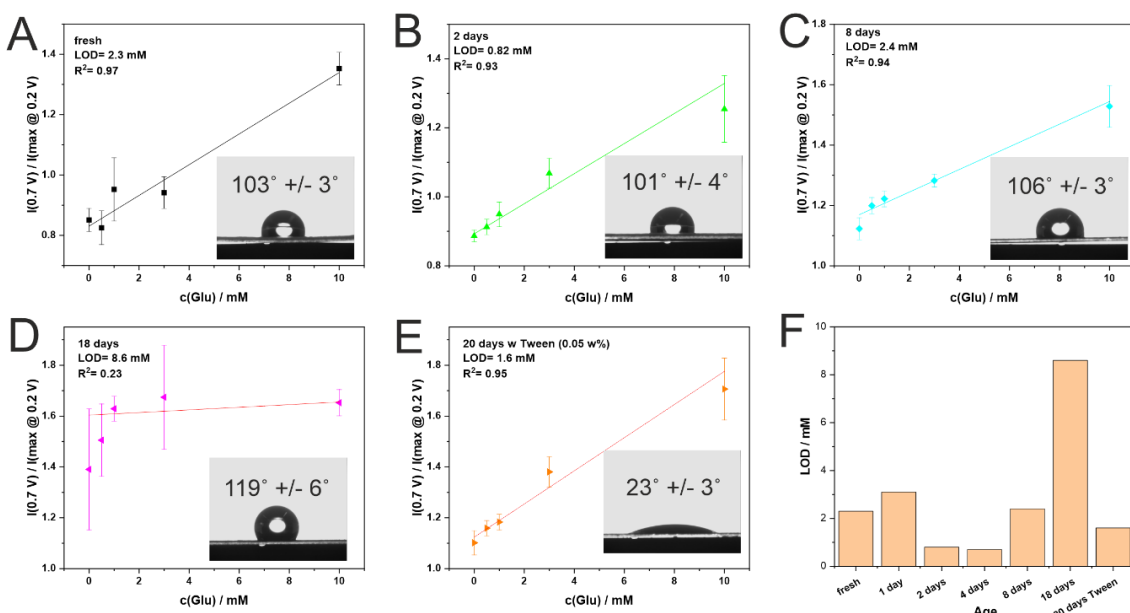


Figure 4.7: Effect of electrode ageing on the detection sensitivity of glucose when electrodes were stored under ambient conditions for 0, 2, 8, and 18 days (A-D, respectively), where the insets display water contact angles for each case. (E) Improvement of analytical performance of 20-day old electrodes by the addition of Tween-20 to the measurement solution (n=5). (F) Summary of LODs from A-E.

The best analytical performance using the single measurement per electrode approach was achieved from electrodes aged for two days, resulting in a limit of detection (LOD) of 0.82 mM (S/N = 3), a sensitivity of 0.06 mM⁻¹, and a linear range from 0 mM – 10 mM ($R^2 = 0.93$).

Bioanalytical applications in general can require the use of electrodes under sterile conditions, which is a major hurdle for enzyme-based biosensors, as the proteins seldomly withstand required sterilization procedures. This opens a unique application field for nanzyme sensors. Therefore, we investigated the effect of sterilization using two common techniques, i.e., heat steam (autoclaved) and 70% alcohol

solution. Both sterilization techniques did not result in any obvious change of signal in comparison to non-sterilized electrodes (**Figure S4.9**), paving the way for their usability in these areas.

4.6.3 Pt/Ni-LCNFs for glucose detection – multiple measurements per electrode

Even though the single measurement approach shown in **section 4.6.2** offers acceptable detection sensitivity, we still aim to further enhance the analytical performance. The poor wettability and microstructures with rough surface topography of pristine Pt/Ni LCNF electrodes could be a limiting factor for detection ability in the single measurement approach described in **section 4.6.2** (**Figure S4.1C**). In this case, the glucose solution may primarily react with the surface, rather than penetrating deeper into the porous structure. As a result, we attempted to measure the glucose solution using the same electrodes over multiple runs, which could improve surface wettability. However, it is crucial to ensure that the signal from each subsequent measurement remains unaffected by the previous one. Initially, we performed multiple measurements of 10 mM glucose on the same electrode, applying a pretreatment at -0.9 V for 20 seconds prior to each CV scan. However, the oxidation current significantly decreased over successive scans (**Figure S4.10A**), likely due to electrode fouling from adsorbed reaction products. To address this, we tested an electrochemical cleaning procedure by applying potentials of -0.2 V, 0.0 V, or +0.2 V for 60 seconds after each CV scan, prior to replacing the old drop with a new drop of glucose solution (**Figure S4.10B**). We found that a slightly negative potential (-0.2 V) was optimal, while potentials of 0.0 V and +0.2 V worsened the reusability of the electrode. Since the reaction product of glucose oxidation is gluconolactone, which further reacts with water in a hydrolysis reaction to gluconic acid⁵, we assume that deprotonated gluconic acid interacts with Ni sites in higher oxidation states (**Figure 4.3**). Gluconic acid can be removed from the catalyst surface through a slightly negative electrochemical cleaning step. Without such a cleaning step, the harsh pretreatment at -0.9 V for 20 seconds might induce further reactions with gluconic acid, rather than simply removing it from the catalyst surface.

In addition, we hypothesized that the detection sensitivity is mainly hindered by the large capacitive background current after OH⁻ generation (**Figure 4.6**). To address this issue, we implemented an electrochemical stabilization procedure to achieve lower background CV signal. Specifically, five CV scans were performed repeatedly in PBS, with a fresh drop introduced for each measurement scan on the same electrode (see **section 4.5.3** for details). Clearly, the stabilization step reduced the capacitive current over the course of the five CV scans. The unknown anodic peaks at around +0.15 V disappeared, while the peak couples at ca. +0.7 V and +0.5 V (corresponding to **reaction 2**) became more prominent in the later scans (**Figure 4.8A**). We assumed that the repeated CV scans in PBS helped remove edges/defects of LCNFs, thereby exposing more catalytic sites through electrochemical etching.

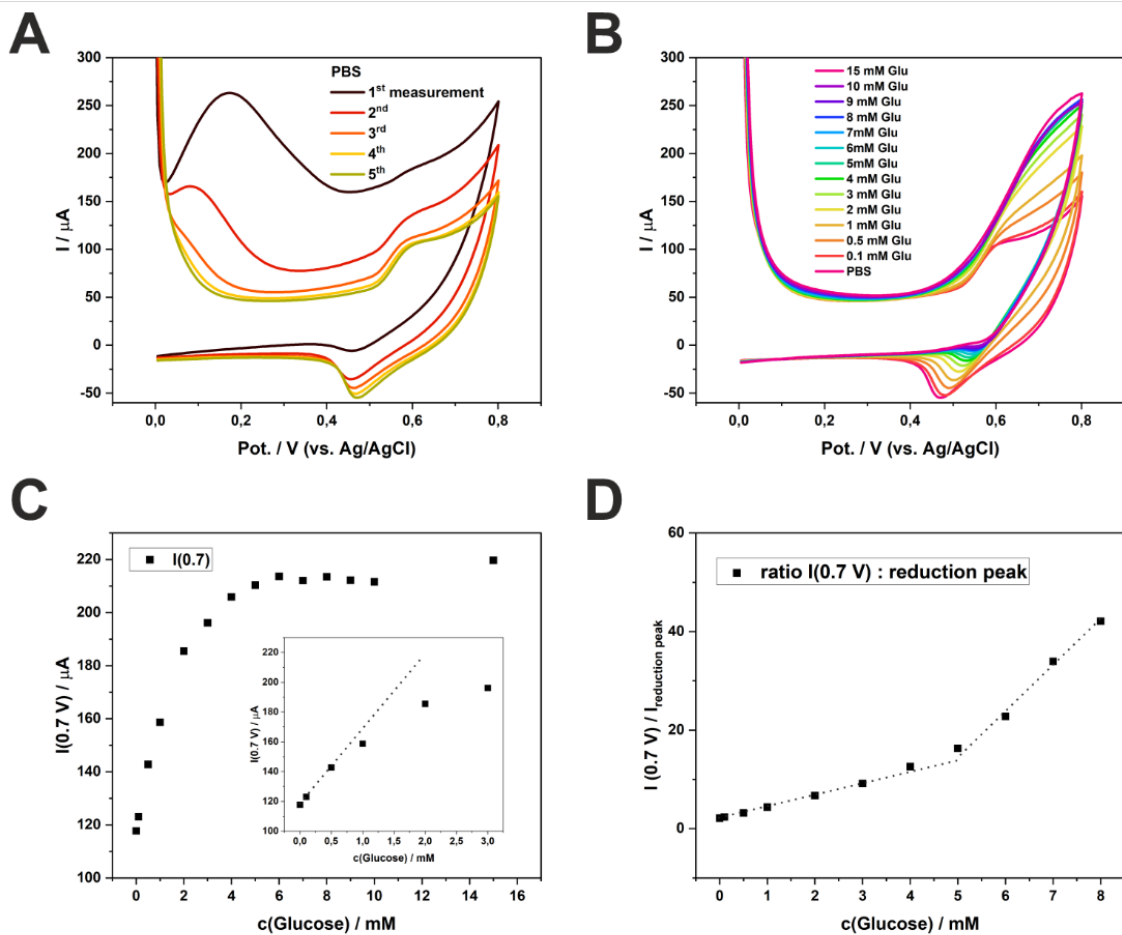


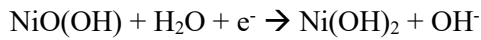
Figure 4.8: Continuous measurements of glucose on one electrode. A pretreatment of -0.9 V before each CV measurement was conducted for 20 s. (A) Stabilization of signal and diminishment of background current after 5 CV measurements in PBS. (B) CVs of various glucose concentrations measured consecutively. The CV of PBS is the same CV as the 5th measurement in (A). (C) Dose-response curve considering the anodic current at +0.7 V. (D) Dose response curve considering the ratio between the current at +0.7 V and the reduction peak at +0.5 V. Since the ratio is a negative value, the absolute value was plotted.

As expected, the consecutive CV signals show a strong proportional relationship with the introduced glucose concentrations (**Figure 4.8B**). The anodic current at +0.7 V was taken as the signal response (**Figure 4.8C**), exhibiting Michaelis-Menten behavior with $K_m = 1.3 \text{ mM}$ and $V_{max} = 112 \mu\text{A}$. These values were calculated using the equation $I = \frac{V_{max} \cdot c(\text{Glu})}{K_m + c(\text{Glu})} + I(c(\text{Glu}) = 0 \text{ mM})$. The K_m value suggests, that at a glucose concentration of 1.3 mM, half of the available catalyst actively undergoes reactions with glucose at a potential of +0.7 V. The linearity of the curve was observed in the range of 0.1 mM – 0.5 mM ($R^2 = 0.999$; considering the data points at 0 mM, 0.1 mM and 0.5 mM), resulting in the LOD of $0.06 \pm 0.04 \text{ mM}$ ($S/N = 3$) and a sensitivity of $50 \mu\text{A}/\text{mM}$.

As an alternative to direct data readout of the anodic peak at +0.7 V (**Figure 4.8C**), we found that taking the ratio between the anodic current (around +0.7 V) and the cathodic current (around +0.5 V) extended the linear range (**Figure 4.8D**). This approach revealed two distinct linear correlations: one between 0.1 mM and 4 mM ($R^2 = 0.994$) and another between 5 mM and 8 mM ($(R^2 = 0.992)$, with a LOD of $0.3 \pm 0.1 \text{ mM}$ ($S/N = 3$). Compared to **Figure 4.8C**, this data acquisition strategy expanded the linear range

by a factor of 8. We hypothesize this following discussion to support why taking the ratio can expand the linear range.

Compared to using the oxidation peak at +0.7 V for ratiometric data analysis, we understand the meaning of the reduction peak (at around +0.5 V), which corresponds to the reduction of the catalyst that did not react with glucose:



At concentrations of 0.5 mM and above, sufficient glucose is present to significantly reduce the catalyst during the entire scan. Consequently, even though the catalyst is saturated during the anodic scan, a lower cathodic current corresponding to the reduction peak of the catalyst is additionally observed, further increasing the ratio at higher glucose concentrations. This straightforward approach extends the linear range from 0.1 mM – 0.5 mM (**Figure 4.8C**) to 0.1 mM – 4 mM (**Figure 4.8D**), as we are no longer only dependent on the maximal reaction rate at +0.7 V in the anodic scan.

4.6.4 Selectivity study

Like other enzyme-free electrodes, electroactive interfering species can be problematic, requiring careful investigation. To address this, we examine the effect of interfering species commonly found in blood by adding them to the 1 mM glucose in PBS solution at their relevant clinical concentrations,⁵ i.e., 0.4 mM uric acid (UA), 125 mM NaCl (nearly double the NaCl concentration in PBS), 0.1 mM ascorbic acid (AA), 0.02 mM cysteine, and a mixture of all of these species.

Initially, we assessed the selectivity of these interfering species for the single measurement per electrode approach (see also **section 4.6.2**). Unfortunately, species such as UA, NaCl, and AA interfered with the glucose measurements (**Figure 4.9A**). This could be due to the high number of edges/defects the pristine Pt/Ni-LCNFs, which may provide favorable site for electroactive interfering species.²⁴¹ Additionally, in comparison to our previous study where glucose was measured on Ni-LCNF electrodes in alkaline medium, NaCl at 250 mM showed negligible interference.²⁴ This suggests that the high background current in the single measurement approach, used to calculate the ratiometric signal, can be easily influenced by interfering species. However, in practical applications involving complex samples like blood, food, and beverage, dilution is commonly performed, which could help mitigate interference effects.

Alternatively, when we conducted the selectivity study using the multiple measurements per electrode approach (see **section 4.6.3**), we observed that this strategy showed high selectivity for glucose, as indicated by the slight deviations in the signal when comparing glucose in PBS with and without interfering species (**Figure 4.9B**). This favorable selectivity could be attributed to the electrochemical etching that occurs during stabilization process (five consecutive CV scans in PBS). This procedure not only eliminates edges and defects where electroactive species such as AA and UA prefer to react, but also exposes more active catalytic sites for glucose, allowing for a more selective reaction. Furthermore, because CV is used, fast reacting species react at lower potentials, reducing their concentrations during

the glucose oxidation. The most prominent interfering signal arose from UA, as evidenced by the oxidation peak at around +0.3 V (**Figure 4.9B i**). Additionally, consecutive measurements on the same electrode with and without glucose exhibited the high reliability of this approach (**Figure 4.9B ii**). Finally, apart from the superior selectivity, the multiple measurement per electrode approach obviously enables a large discrimination between glucose and background signal (see also **Figure 4.9A-ii** and **4.9B-ii**).

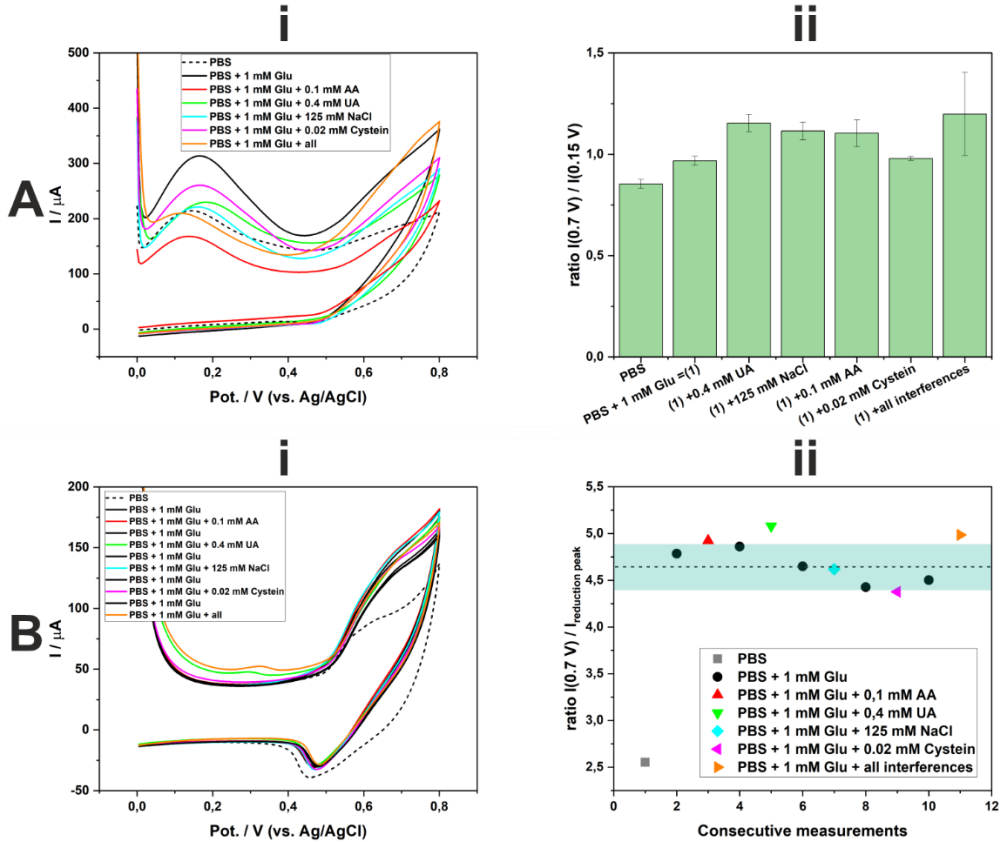


Figure 4. 9: Selectivity study. (A) single measurement per electrode approach: (i) the exemplary CVs randomly chosen from all measurements, and (ii) the corresponding ratiometric signals ($n \geq 3$). (B) multiple measurements per electrode approach: (i) CVs and (ii) the corresponding ratiometric signals ($n=1$) where the dash line indicated the mean value of PBS + 1 Glu mM and the highlight indicated its error range.

4.6.5 Recovery study

As a final step, we assessed the performance of the sensor in human serum using the multiple measurements per electrode approach. The human serum contained $4.8 \text{ mM} \pm 0.1 \text{ mM}$ ($n = 3$) glucose, according to measurements made with the commercially available Roche Accu-Chek®. However, we still faced challenges due to the matrix effect when measuring glucose in the human serum without dilution. Specifically, the pure human serum caused a significant reduction in the peaks associated with Ni(OH)_2 (**Figure S4.11A**), resulting in a ratiometric signal of 5.4, which corresponds to approximately 1 mM glucose (compared to **Figure 4.8D**). From the shift of the Ni peaks to higher potentials, we concluded that it was not possible to achieve the same local pH increase in undiluted human serum as was achieved with PBS solution. Attempts to increase the pretreatment time (up to 40 s) and apply a

more negative potential (up to -1.8 V) (**Figure S4.11B**) did not yield favorable results. We hypothesize that the proteins in human serum predominantly blocked the catalyst on the electrode, thereby hindering the performance of the sensor.

As an alternative approach, we conducted measurements in diluted serum (20% human serum, 80% PBS; resulting glucose concentration: 0.96 mM). We initially recorded a calibration curve (0 mM, 0.1 mM, 0.5 mM, 0.8 mM, 1.0 mM, 1.2 mM glucose in PBS) and then measured either the diluted human serum (20% human serum in PBS; 0.96 mM glucose) or the same solution spiked with 0.25 mM glucose (20% human serum in PBS; 1.21 mM glucose) (**Figure 4.10**). Since good linearity was achieved within the calibration curve (**Figure 4.10 B**), we reduced the number of calibration points to a single glucose concentration (**Figure S4.12**, electrode 5,6) after the stabilization in PBS (5 measurements). Despite the catalyst being blocked by proteins, the ratiometric approach enabled to achieve a good recovery for diluted serum ($99 \pm 10\%$), and spiked diluted serum ($91 \pm 12\%$) (**Table 4.1**). This could be attributed to the self-correction of the CV signal, where both oxidation and reduction currents decreased concomitantly with catalyst blocking. Overall, the recovery for both the spiked and non-spiked measurements was $95 \pm 10\%$ ($n = 6$).

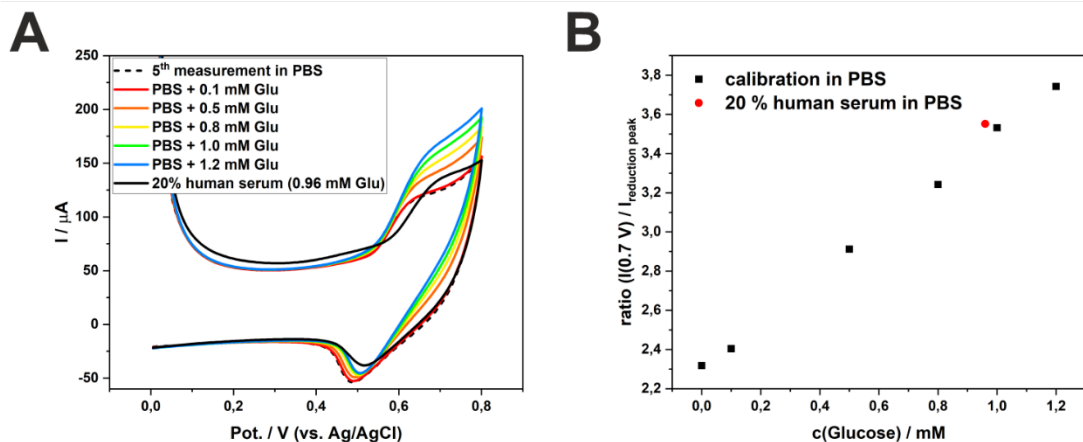


Figure 4. 10: Measurement in 20% human serum. (A) CVs of calibration in PBS solution and consecutive measurement in diluted human serum. (B) Respective ratios of (A).

Table 4. 1: Measurement in undiluted and diluted (20%) human serum. Concentrations are calculated from data shown in **Figure S4.12** (n=3).

sample	c(Roche AccuChek®)	c(measured)	Recovery
Undiluted serum	4.8 \pm 0.1 mM	-	-
20% serum 80% PBS	0.96 \pm 0.02 mM ¹	0.95 \pm 0.08 mM	99 \pm 10 %
20% serum 80% PBS, spiked	1.21 \pm 0.02 mM ¹	1.1 \pm 0.1 mM	91 \pm 12 %

¹ calculated from measurement in undiluted serum

4.7 Conclusions

We demonstrated the *in situ* generation of Pt/Ni alloy embedded within carbon nanofibers by CO₂ laser writing. Through extensive characterization techniques (HR)TEM, STEM-EDS, XPS, and SAXS, we gained valuable insights into the chemistry and structural morphologies of Pt/Ni alloy embedded within carbon nanofibers, shedding light on the effects of the added metals on the materials' properties. These Pt/Ni alloy embedded in carbon nanofibers were then employed as enzyme-free electrodes for glucose detection, specifically at physiological pH. The beneficial role of Pt/Ni alloy was realized in its ability to efficiently facilitate local OH⁻ generation at Pt sites, which is critical for the electrocatalytic oxidation of glucose by Ni. Consequently, these electrodes offer promising potential for glucose detection under physiological conditions, paving the way for wearable sensor development.

Moreover, we highlighted the significant impact of electrode ageing on performance and reproducibility, an area that requires further investigation. Nevertheless, our study emphasized the high stability of these nanocatalysts, even under harsh sterilized conditions, showcasing their potential for bioprocess monitoring and biomedical applications. The simplicity of electrode fabrication, combined with their favorable electrocatalytic properties, straightforward data analysis, and durability, makes the laser-generated Pt/Ni carbon nanofibers highly attractive for point-of-care testing applications.

4.8 Supporting information

4.8.1 Price per electrode

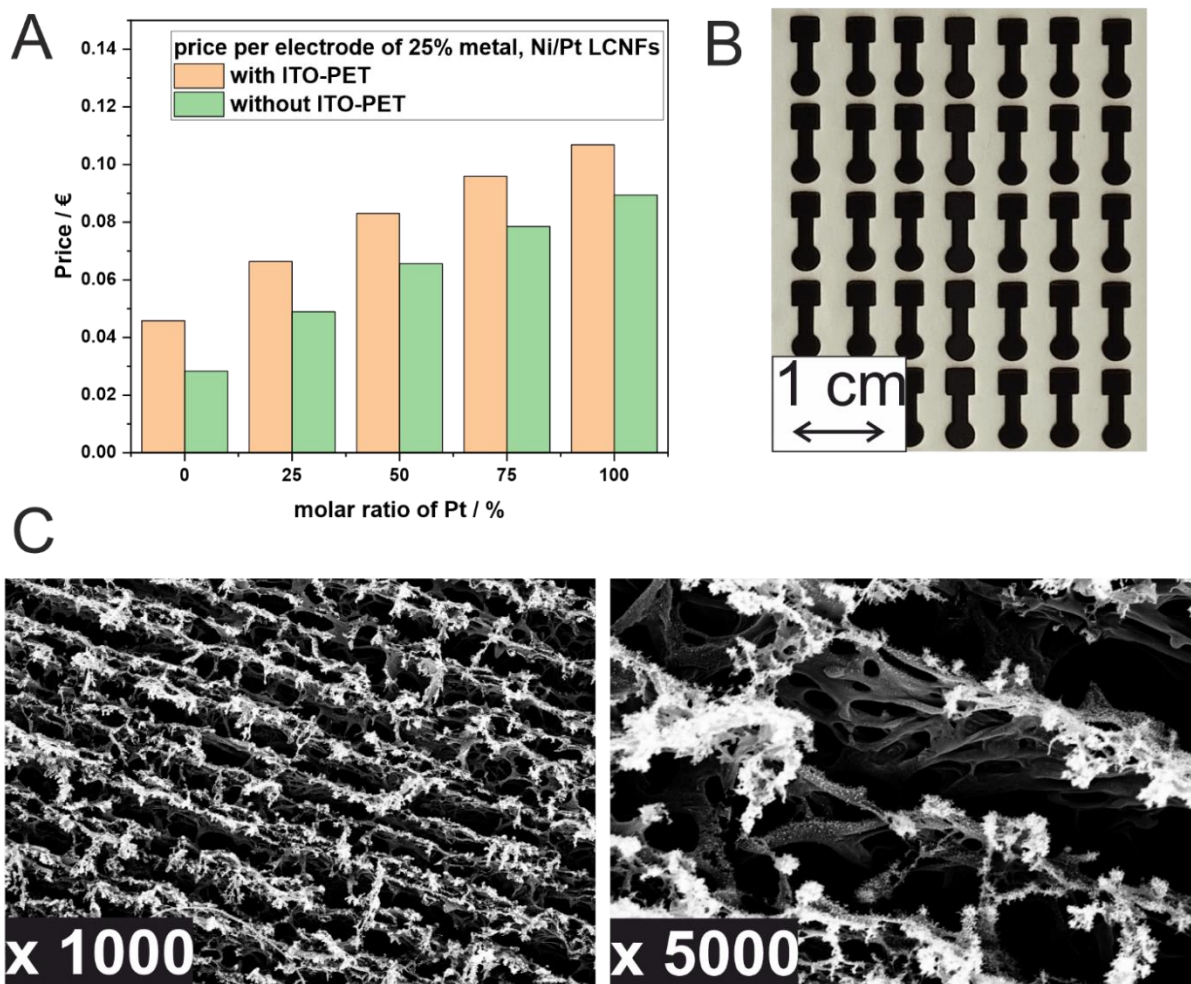


Figure S4. 1: Price estimation per electrode when using the scribing pattern shown in (B). (C) SEM pictures of the produced electrode material (LCNF) with a 1000- and 5000-fold magnification.

Price estimation of the electrode is shown in **Figure S1A** for a scribing pattern shown in **Figure S1B**. We estimated the price per electrode for two different supports (PET/ITO as used in this publication and filter paper, which could be used to further decrease cost). For calculations, a price of 27.2 € per 30 cm x 30 cm ITO/PET sheet, 0.042 € per mL DMAc, 212 € per g Pt(II) acetylacetone, 5.74 € per g Ni(II)acetylacetone, 0.5 € per g Matrimid was used. Furthermore, we estimated that a nanofiber mat (place for 228 electrodes) should consume at the current manufacturing state (stirring overnight, electrospinning for 3h, laser scribing the whole mat) less than 2 kWh, resulting in an additional cost of 0.5 € (assuming a price of 0.25 € per kWh).

4.8.2 Characterization of surface chemistry focusing on carbon and oxygen

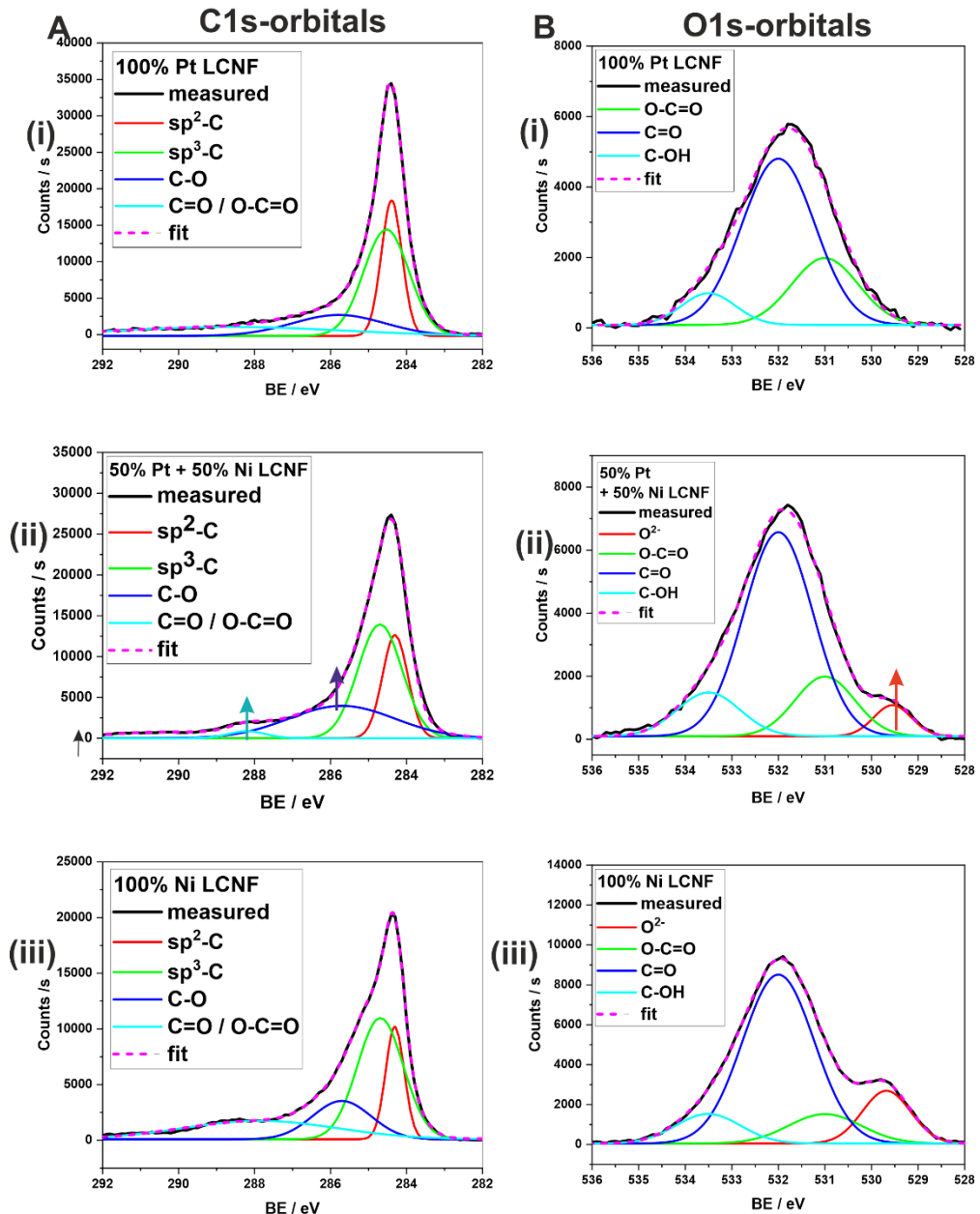


Figure S4. 2: Deconvoluted XPS spectra with background subtracted of (A) C1S orbitals, and (B) O1s orbitals for (i) 100Pt-LCNFs, (ii) 50Pt/50Ni-LCNFs, and (iii) 100Ni-LCNFs. Blue- and purple-colored arrows indicate an increase of oxygen-containing groups with increasing Ni-content. The red arrow highlights an increasing appearance of O²⁻ with increasing Ni-content, arising from Ni-oxide species.

4.8.3 Characterization of surface chemistry focusing on Pt and Ni

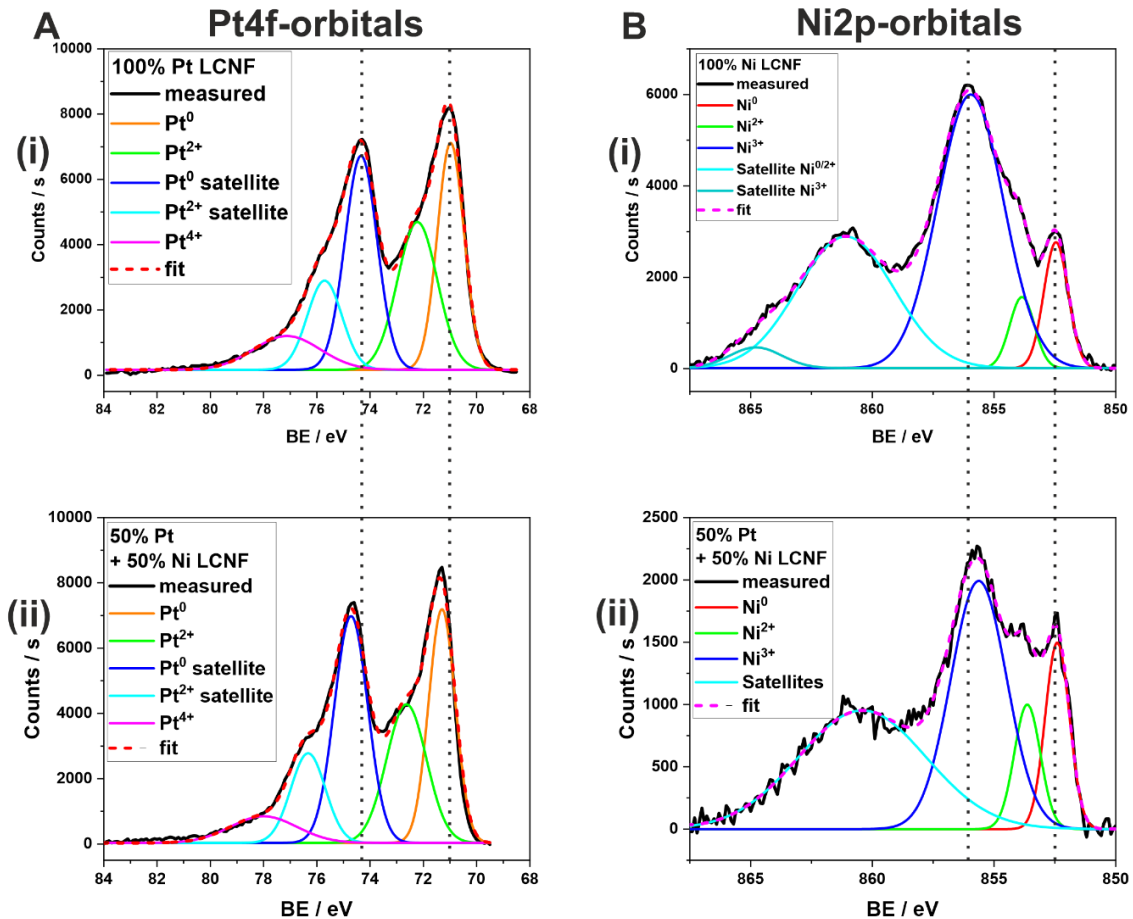


Figure S4. 3: Deconvoluted XPS spectra with background subtracted of (A) Pt4f orbitals, and (B) Ni2p orbitals for (i) individual metal either 100Pt-LCNFs or 100Ni-LCNFs, and (ii) 50Pt/50Ni-LCNFs.

4.8.4 Small Angle X-ray Scattering (SAXS) analysis

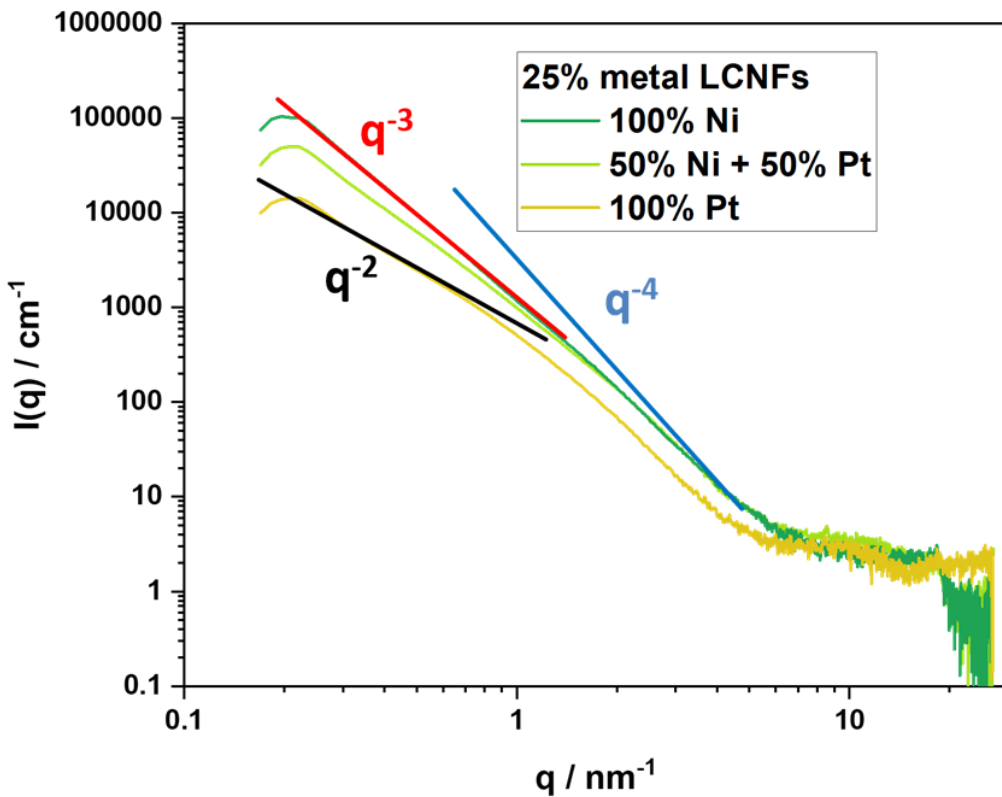


Figure S4. 4: Full range SAXS spectra and fitted patterns of the as-generated materials.

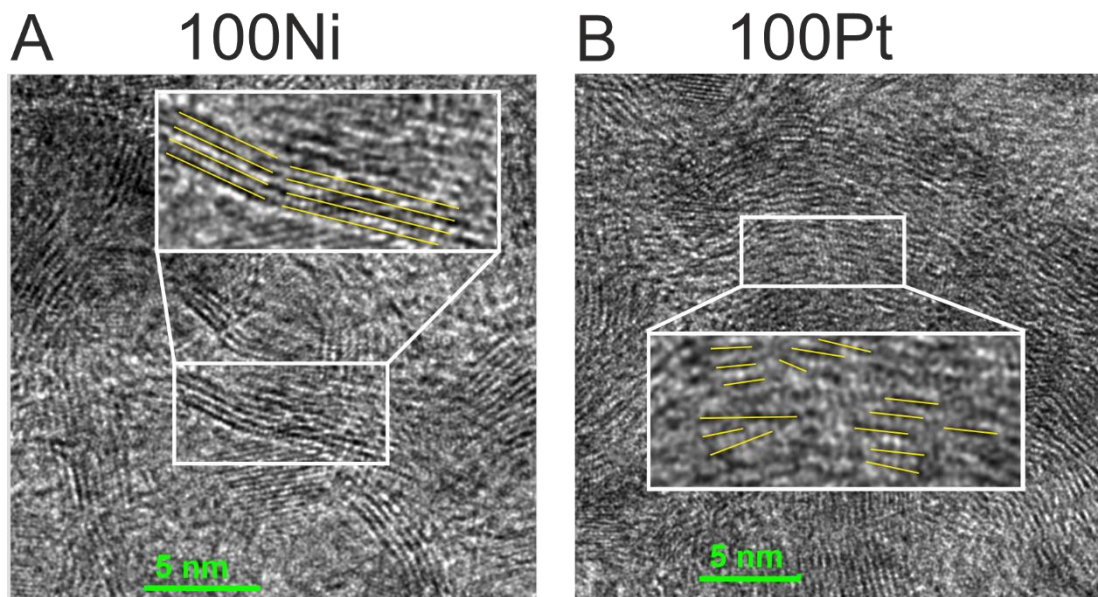


Figure S4. 5: HRTEM of (A) 100Ni and (B) 100Pt LCNFs focusing on rGO structure. An additional zoom highlights the more ordered structure within 100Ni-LCNFs, explaining the appearance of the 18.6 nm^{-1} reflex in SAXS spectra of 100Ni-LCNFs.

4.8.5 Electrocatalytic oxidation of glucose at various pHs and metal compositions

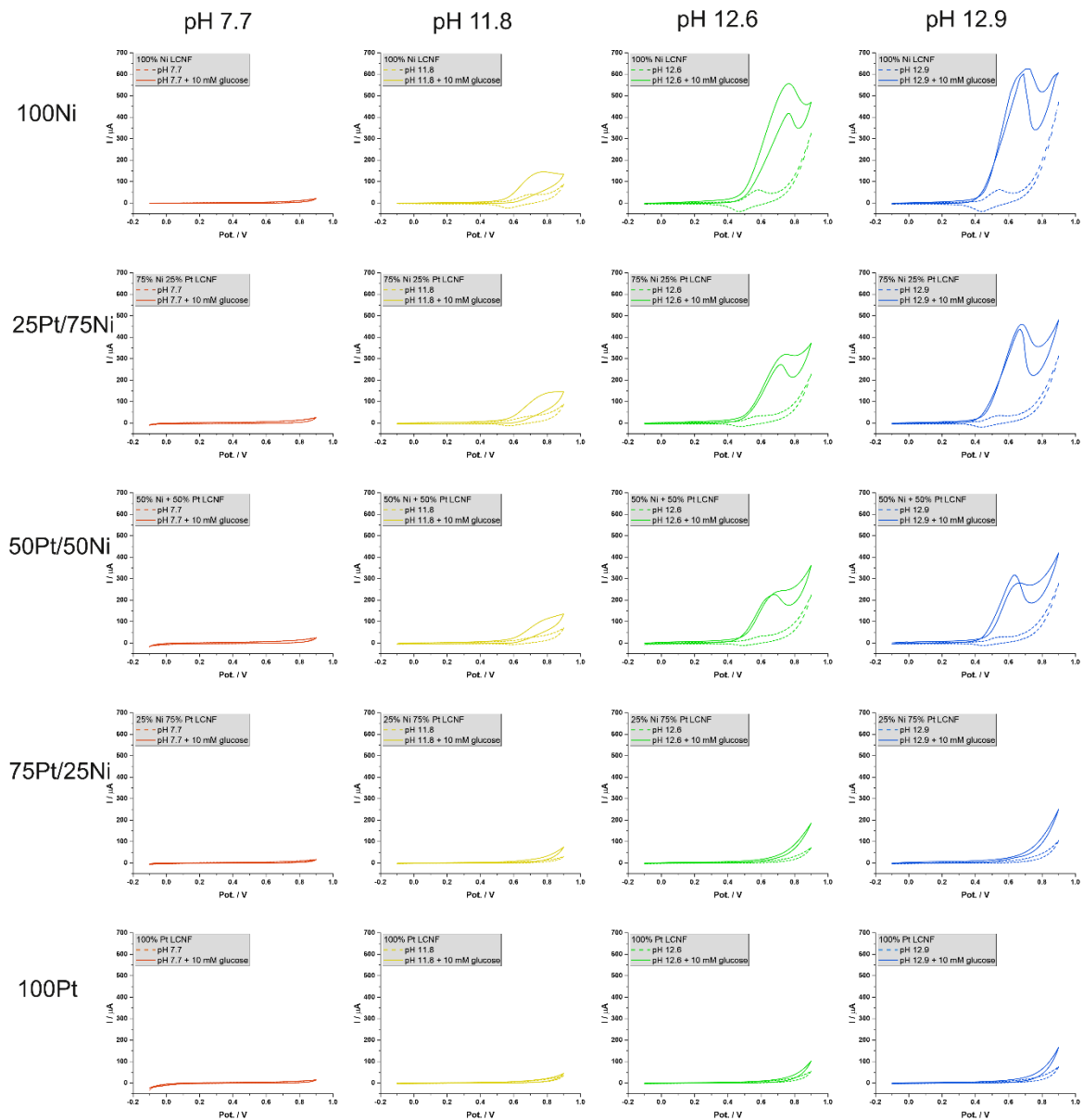


Figure S4. 6: Cyclic voltammograms (CVs) of 10 mM glucose (solid line) compared with 0 mM glucose (dash line) from LCNF electrodes contained various metal compositions measured under different pHs. Glucose solutions were prepared in PBS buffer adjusted to the desired pHs by NaOH (1 M). CV was performed using scan rate of 0.05 V/s. Each CV was from the averaged current obtained from individual triplicate measurements.

4.8.6 Optimization of pretreatment conditions for electrocatalytic oxidation of glucose present in physiological pH

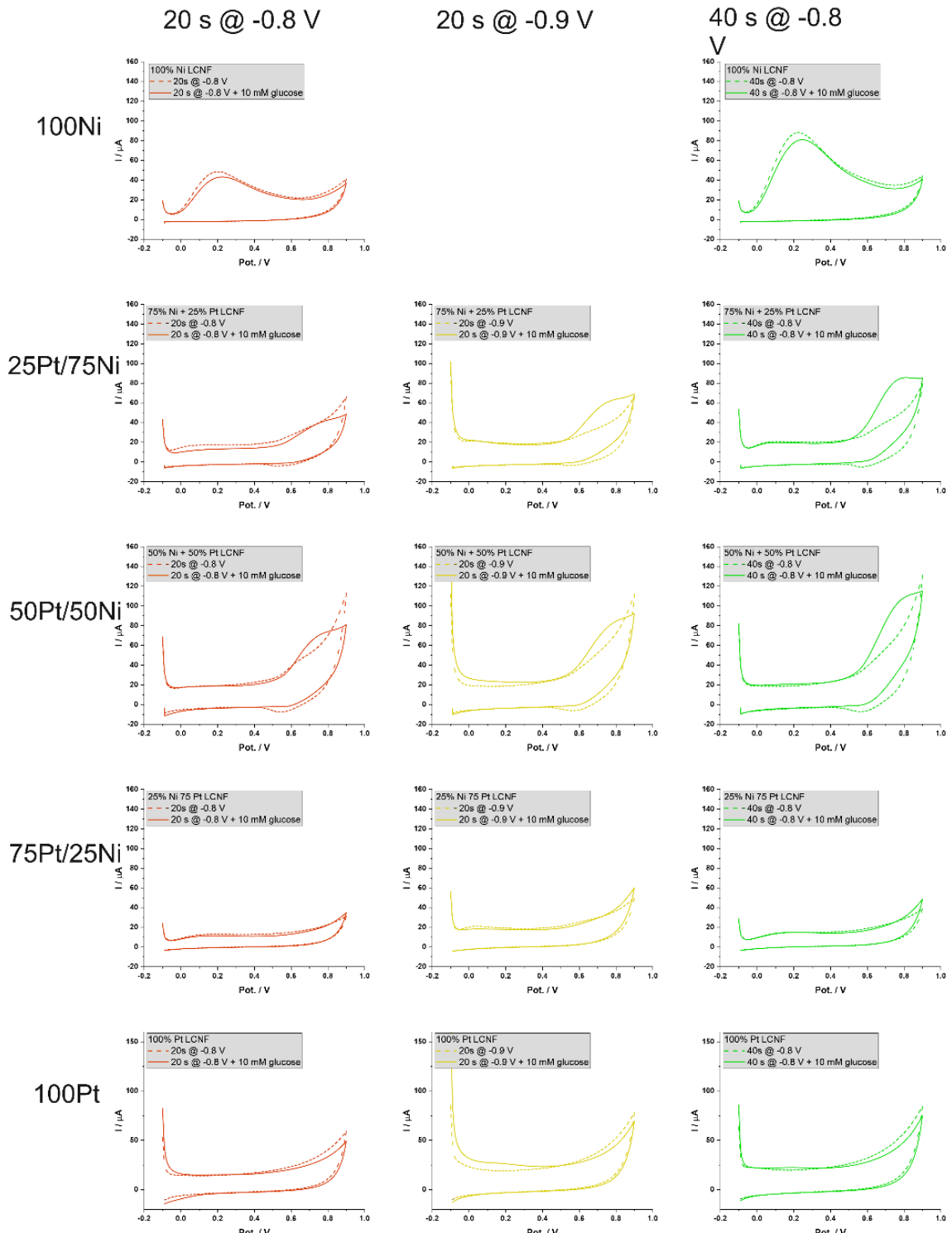


Figure S4.7: CVs of 10 mM glucose (solid line) compared with 0 mM glucose (dash line) from LCNF electrodes contained various metal compositions after pretreatment at various times and applied voltages. Here, the pretreatment condition was applied directly before the respective CV scan, either in the absence or presence of glucose. Glucose solution was prepared in PBS buffer (pH 7.4). The absence of the oxidation peak at around 0.15 V is due to the fact that the electrodes were no fresh electrodes and already performed measurements for **Figure S4.6**.

4.8.7 Effect of electrode ageing

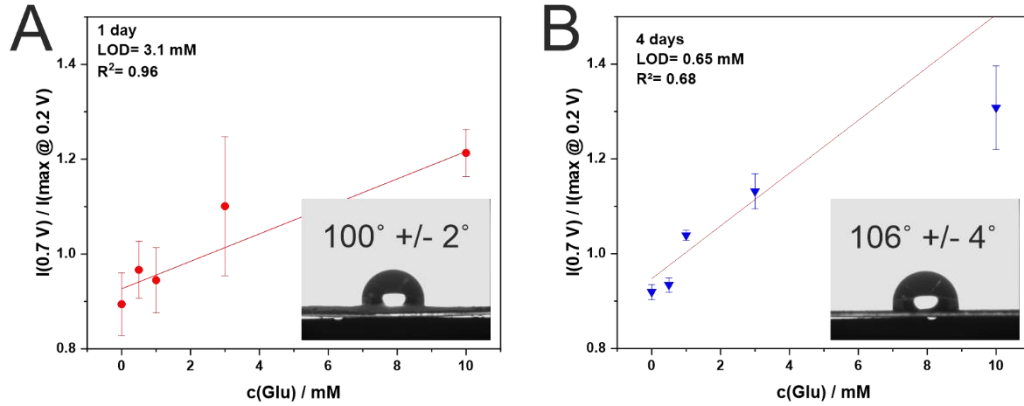


Figure S4. 8: Effect of electrode ageing on detection sensitivity of glucose when electrodes were stored under ambient conditions for (A) 1 day, and (B) 4 days.) where the insets display water contact angle for each case. ($n = 5$)

4.8.8 Effect of sterilizations

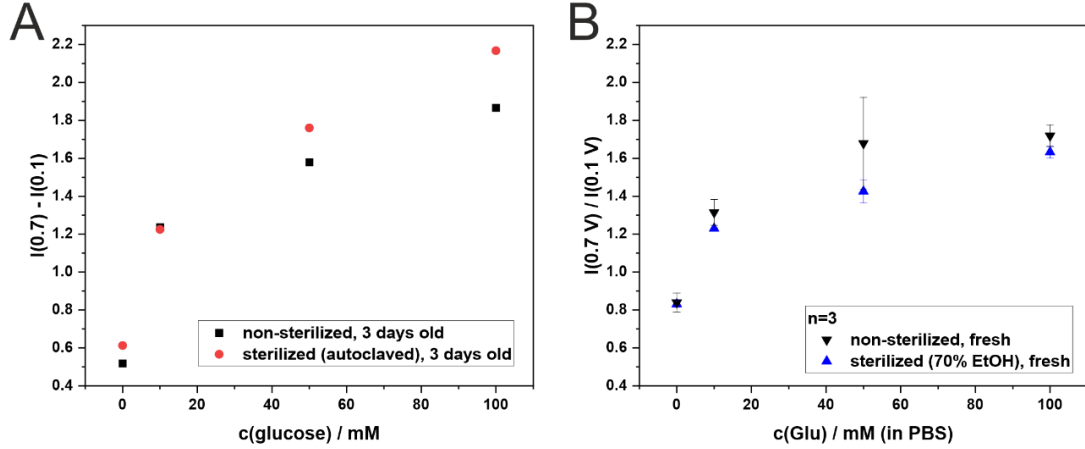


Figure S4. 9: Comparison of the glucose signals obtained from electrodes without and with sterilization by (A) autoclaved at 121°C for 15 min, and (B) exposed to 70% ethanol for 10 min. For both conditions, electrodes were dried prior to the measurements.

4.8.9 Reusability of electrodes

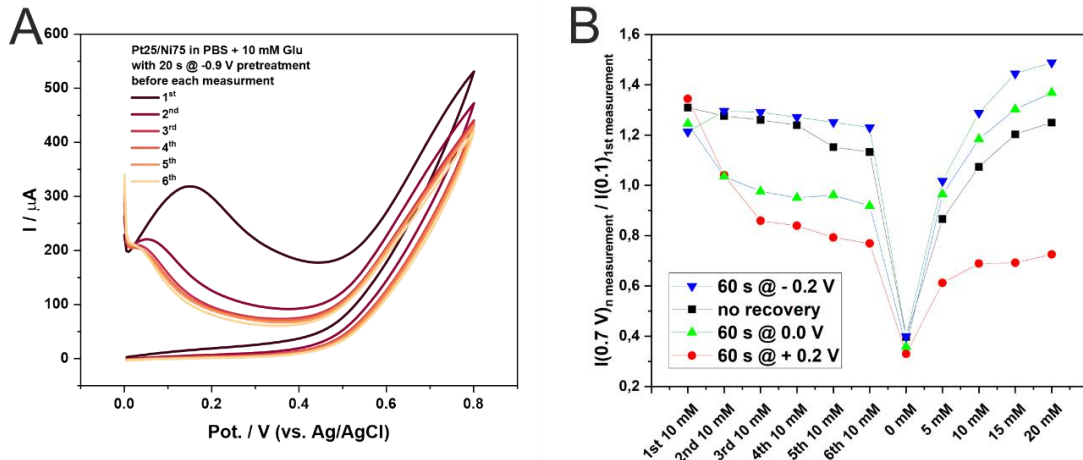


Figure S4. 10: (A) Reusing an electrode for several consecutive measurements in PBS + 10 mM glucose solution. After each CV measurement, a fresh drop of solution was placed. (B) Impact of an electrode cleaning. The procedure was: pretreatment (-0.9 V for 20 s) - measurement (CV) - recovery treatment (-0.2/0.0/+0.2 V for 60 s) – place fresh drop on electrode. After 6 consecutive measurements in 10 mM glucose solution, a 0 mM, 5 mM, 10 mM, 15 mM, and 20 mM glucose in PBS was measured. For a better comparison between the electrodes, the ratio $I(0.7 V)_n / I(0.1 V)_1$ of first measurement was used.

4.8.10 Measurement in undiluted and diluted human serum

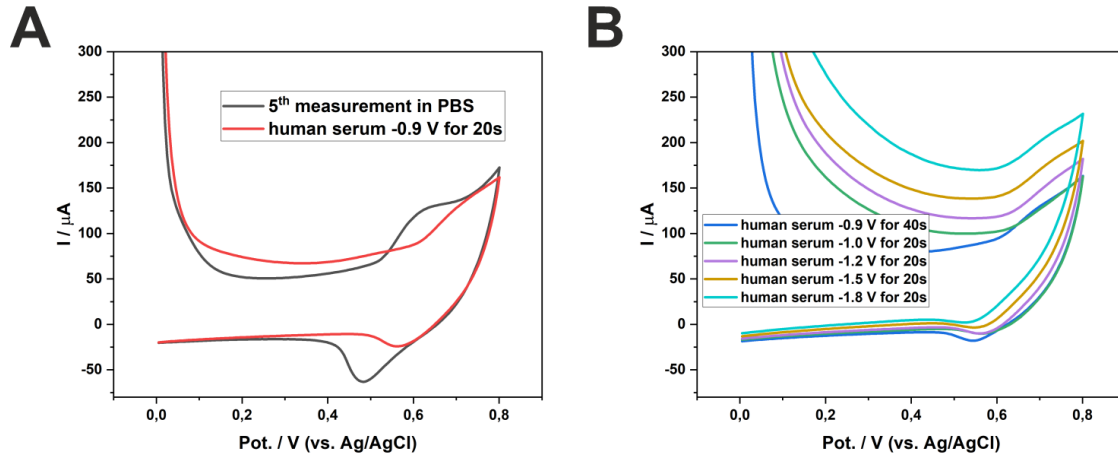


Figure S4. 11: (A) The stabilized, 5th measurement in PBS and a consecutive measurement in undiluted human serum. (B) CVs with various pretreatments in undiluted human serum.

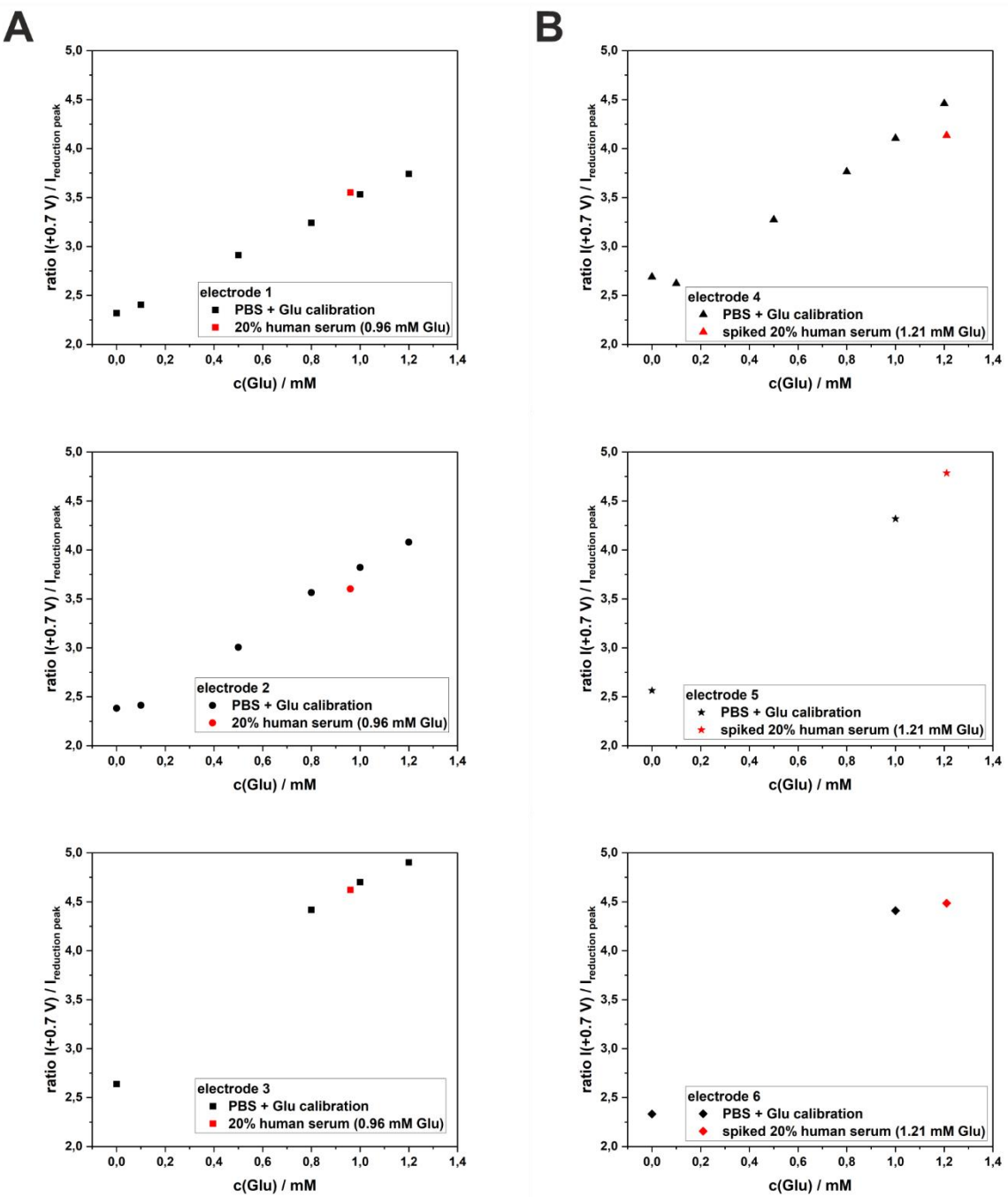


Figure S4. 12: Calibration and measurements of (A) 20 % human serum (0.96 mM glucose according to Roche AccuChec) and (B) 20% human serum spiked with 0.25 mM glucose (in total 1.21 mM glucose. Due to good linearity of electrodes 1, 2 and 4, calibration measurements were reduced for electrodes 3, 5 and 6.

5. Laser-induced Carbon Nanofibers as Permeable Non-enzymatic sensor for Biomarker Detection in Breath Aerosol

5.1 Abstract

Detection of biomarkers in breath aerosol has become an attractive tool for non-invasive diagnostics. Herein, a novel breathable electrochemical enzyme-free sensor made from laser-induced carbon nanofibers embedding Ni nanocatalysts (Ni-LCNFs) is proposed. The porous sensing film was generated via an instantaneous LCNF formation with concomitant reduction of Ni cations. Unlike traditional non-breathable sensors, the 3D porous Ni-LCNF electrode allows efficient capture and straightforward sensitive detection of aerosolized glucose, which were enabled through its permeability, large surface area, and nano-Ni catalytic ability. The sensor potentiality was proved by measuring aerosolized glucose as a model analyte and its integration onto a breathing mask. The detection mode is based on the electrocatalytic oxidation of glucose mediated by the nano-Ni catalysts where reproducible and accurate data can be easily and reliably obtained using the oxidation/reduction peak ratio as analytical signal. The final device configuration shows a limit of detection of $0.7 \mu\text{M}$ with high selectivity toward potential interferents commonly present in breath. The Ni-LCNF sensors were able to determine simulated aerosols containing clinically relevant glucose levels. Although in-vivo validation studies must be conducted in future work, the proposed device results in a captivating point-of-care device integrable in breathing masks and breath analysis devices.

This chapter will be further used as a manuscript that is intended to be submitted to Analytical Chemistry as a technical note article.

5.2 Author distribution

The author and Selene Fiori contributed equally to conceptualization, design of the study, experimental investigation, data acquisition, interpretation of the data, and writing original draft. Katharina Weiß, Keyu Su, and Michael Födlmeier helped during initial experimental investigations. Prof. Flavio Della Pelle, Dr. Annalisa Scroccharello, and Prof. Dario Compagnone revised the original draft and contributed to funding acquisition and supervision. Prof. Antje J. Bäumner contributed to project administration and supervision. Dr. Nongnoot Wongkaew lead conceptualization, project administration, funding acquisition, supervision, and writing of the original draft.

5.3 Graphical abstract

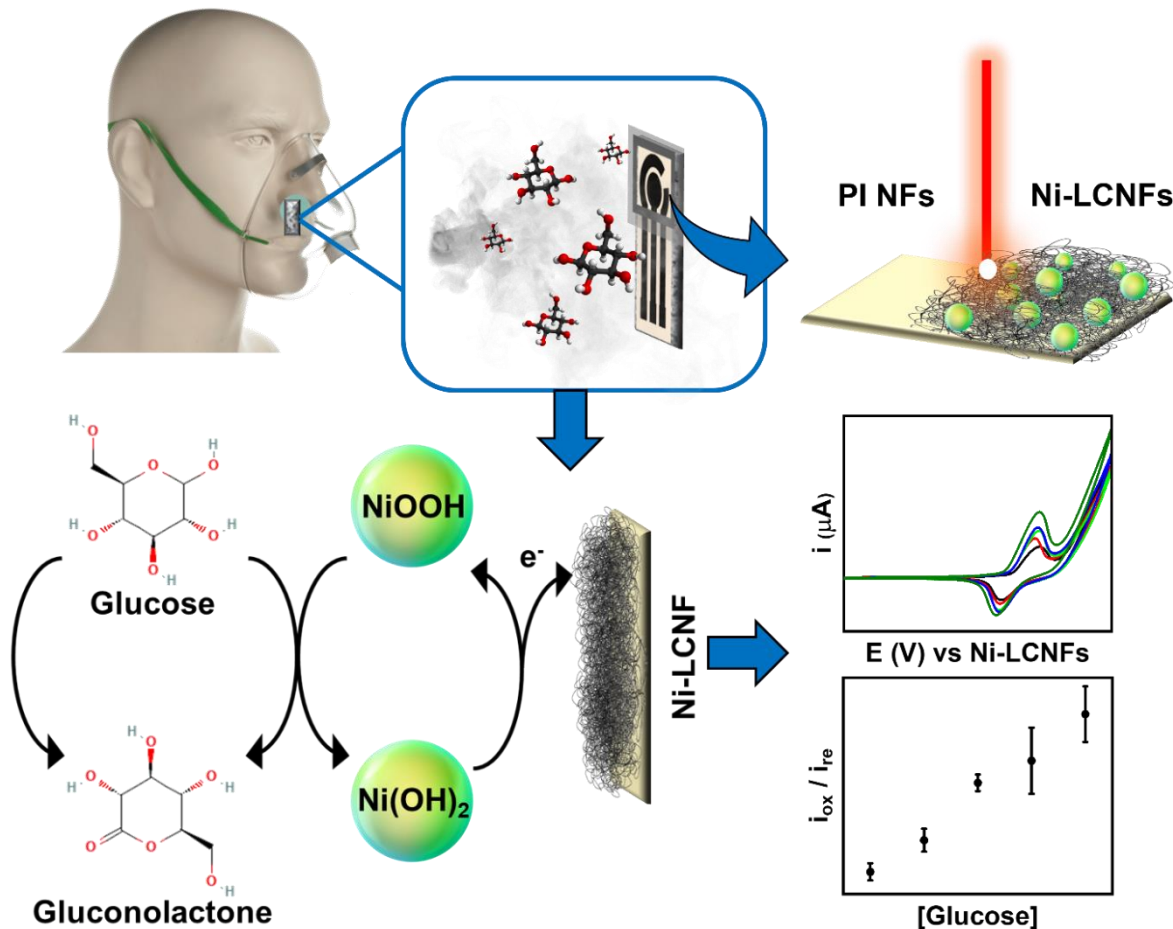


Figure 5. 1: Graphical abstract of chapter 5.

5.4 Introduction

In the diagnostics field, the detection of biological biomarkers via non-invasive methods has received increasing attention, since they offer simple sampling and a more extensive screening capacity, avoiding injury due to the insertion of tools inside the body or skin puncture^{242,243}. Alternative to conventional biological fluids, i.e., saliva, urine, tears, sweat, plasma, blood, etc., breath has become a captivating sample for non-invasive analysis²⁴³. Indeed, breath can be easily collected in the form of aerosol and contains diagnostically important markers whose concentration is related to their content in blood²⁴⁴. Nevertheless, the main problem with the analysis of exhaled breath aerosol is the concentration of the biomarkers, significantly lower than blood. Among others, glucose, a relevant biomarker for several diseases and chronic health problems, has an average concentration of 4.8 mM in blood in healthy people, while in respiratory fluids it is present in about 10-fold less amount¹¹⁴. The glucose undergoes a further dilution during the condensation of exhaled breath aerosol, necessitating the use of a proper 'breath collection' strategy associated with adequate detection methods²⁴⁵.

Several analytical approaches are currently used for analysis of breath condensate such as gas chromatography, mass spectrometry, and laser spectroscopy^{242,246}. In this framework, electrochemical sensors are emerging as easy-to-use and low-cost analytical devices for clinical diagnostic¹⁴⁶. Electrochemical sensors include enzyme-based and enzyme-free detection strategies¹⁸. The former has the advantage of high selectivity and sensitivity, nevertheless, it requires a dedicated enzyme immobilization process, needs controlled temperature, humidity, and pH, and often shows poor stability/storability²⁴⁷. These drawbacks make enzyme-free sensors attractive, considering their facile preparation, low-cost, and suitability for mass production^{146,248}.

Carbon nanofibers (CNFs) are useful sensing materials for electrochemical sensors, particularly appealing for breath analysis. CNF films, properly manufactured/used, possess a 3D porous structure with high surface and electron-transfer capability²⁴⁹. Noteworthy, thanks to their structure, CNF porous films enable effective permeation of gaseous phases, potentially allowing capturing/concentrating biomarkers in breath aerosol²⁴⁹.

CNFs are usually obtained via a two-step manufacturing process, including the production of nanofibers precursor and consecutive carbonization. Several methods have been proposed for the production of nanofibers, among these, electrospinning turns out to be simple, versatile, and prone to large-scale production^{247,250}. Briefly, a polymer solution is subjected to a high voltage, and, when the repulsive forces on the charged polymer exceed the surface tension of the formed droplet, a jet of the polymer is obtained, enabling nanofiber formation onto the collector¹⁹. Subsequent carbonization is usually conducted at extremely high temperatures under inert gas²⁴⁷. However, conventional carbonization approaches are not very suitable for direct electrode patterning and integration in sensors/devices, making them unfavorable for mass production.

On-site direct laser-induced fiber pyrolysis can effectively resolve the aforementioned issues. Indeed, CO₂-laser treatment can straightforwardly convert electrospun polyimide (PI) nanofibers into laser-induced carbon nanofibers (LCNFs), allowing the formation of conductive porous films with on-demand shape and design⁶². Moreover, simply adding a metal precursor into the PI spinning solution, LCNFs decorated with nanoparticles/nanostructures can be produced, improving the electron transfer ability and/or inducing additional catalytic features at the sensing film⁶³. This co-synthesis using CO₂ laser approach has proven to be efficient and practical for other materials such as graphene and conductive carbon inks where the as-developed sensors were successfully applied for H₂O₂, neurotransmitters and flavonoids determination^{64,251-254}.

Our group has previously generated Ni-LCNF working electrodes demonstrating their ability in the non-enzymatic detection of glucose in basic environment²⁴. The Ni-LCNF electrodes were fabricated on conductive indium tin oxide (ITO) coated polyethylene terephthalate (PET) support. In this pioneering work, even though the electrodes provided a favorable analytical performance, the carbon nanofibrous sensing film does not provide permeability to gases and the measurement setup necessitates the use of external reference (RE) and counter (CE) electrodes. These unfavorable features thus limit their

applicability for breath sensor development. In another study by our group, we developed a manufacturing process where LCNF electrodes can be fabricated without ITO/PET support⁷⁸. Herein, Fe-LCNF electrodes were generated and employed as working, reference, and counter electrodes within a sensing device. The use of Fe-LCNFs as a RE has proven to be reliable and stable for electrochemical measurements.

In this work, a permeable Ni-LCNF integrated sensor for breath analysis was developed and its exploitability proved by using aerosolized glucose as model analyte. The sensor allows a direct measurement of glucose from 'the captured glucose aerosol'. The sensor design and catalytic features were optimized, together with the breath capture and measurement set-up. Moreover, the effect of sensor storage conditions and interferent studies were also investigated. Eventually, we demonstrated the sensors' capability to detect glucose at clinically relevant levels when integrated into medical breathing masks.

5.5 Materials and methods

5.5.1 Chemicals and materials

Solvent soluble PI Matrimid 5218 was purchased from Huntsman Corporation (The Woodlands, Texas, U.S.). Nickel (II) acetylacetone, sodium hydroxide, D-glucose monohydrate, hydrogen peroxide, nickel (II) nitrate hexahydrate, potassium chloride, acetone ($\geq 99.5\%$ purity), ethanol ($\geq 99.8\%$ purity), ammonia and sodium L-lactate were purchased from Sigma Aldrich (St Louis, MO, USA). Dimethylacetamide (DMAc) was purchased from Acros Organics (Thermo Fisher Scientific Inc., Geel, Belgium). Screen-printed carbon electrodes were purchased from Metrohm DropSens (Llanera, Asturias, Spain). 100 mM stock solution of glucose was prepared in 0.1 M NaOH aqueous solution and stored at 4 °C.

5.5.2 Apparatus

Electrospinning was performed using a Starter Kit-Aligned 40kV (Linari Engineering srl, Pisa, Italy) with a rotating aluminum collector cylinder (diameter of 80 mm and length of 120 mm), equipped with a 5 mL glass syringe with a 20G needle. A CO₂ laser (VLS 2.30 system, 30W) from Universal Laser System Inc. (Scottsdale, Arizona, USA) with a 2.0'-lens in focus was used for laser scribing of nanofibers. To increase the hydrophilicity of Ni-LCNF film a UV-ozone cleaner from Jelight Co. Inc., model n° 42-220 (Irvine, California, USA) was employed, with a power of 200-240 V and frequency of 50 Hz. A wax printer (ColorQube 8880DN, Xerox Corporation, USA) was used to print hydrophobic regions onto polyester plastic foils (Overhead transparencies, thickness 0.10 mm, Avery Zweckform, Code: 3560) to define the working area and insulate the back of the sensors. Designs for the laser and wax printer were realized using CorelDRAW 2022 software. Electrochemical measurements were conducted using a multichannel potentiostat (MultiPalmSens4) from PalmSens (Palm Instruments BV,

Houten, Netherlands). Breath simulation process was performed by nebulizing glucose solutions using an Inhalator from Medisana (Neuss, Germany), power 60 W, nebulization speed of 0.2 mL min^{-1} .

5.5.3 Sensor manufacturing

The main manufacturing steps of Ni-LCNFs based sensor are illustrated in **Figure 5.2 A-H**.

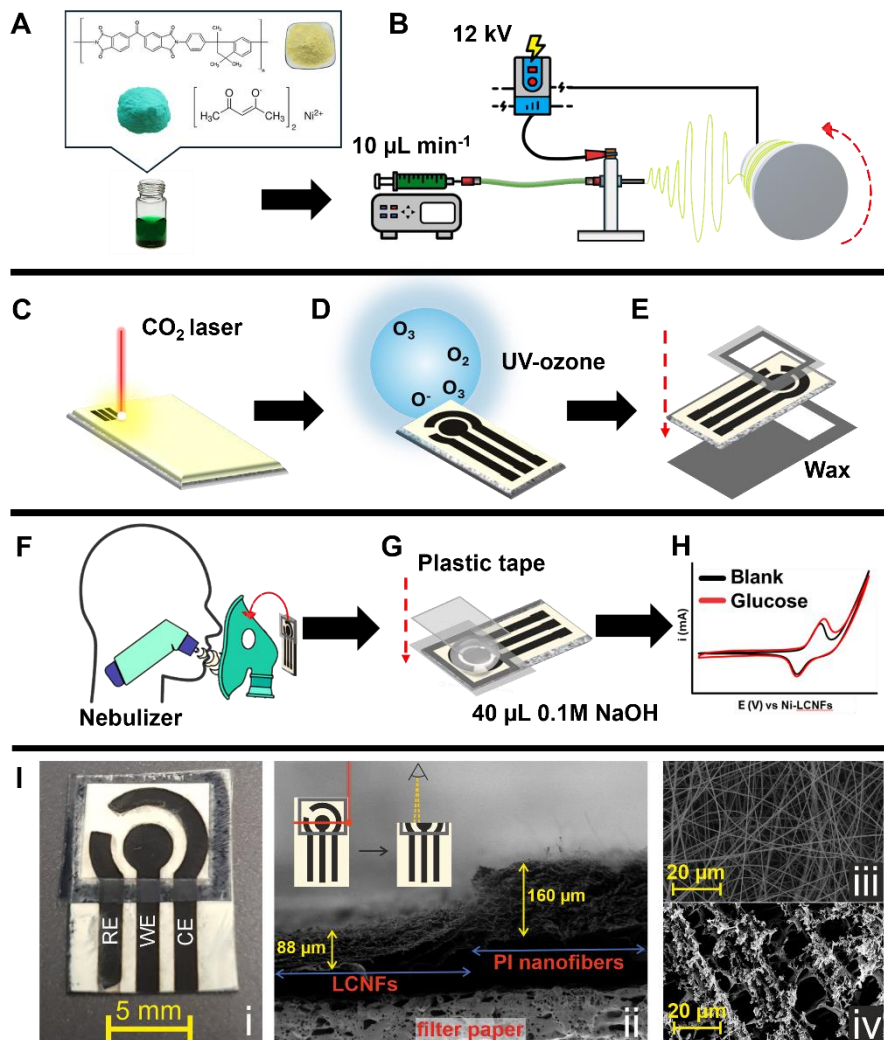


Figure 5.2: Schematic representation of sensor fabrication and measurement procedure. (A) Preparation of the spinning solution. (B) Electrospraying set-up to produce a nanofiber mat on filter paper. (C) Laser-induced carbon nanofibers (LCNFs) embedding Ni nanocatalysts generation using CO_2 laser. (D) UV-Ozone treatment for enhancing the hydrophilicity of sensors' surface. (E) Wax transferring to confine the sensor working area. (F) Experimental set-up to test the potentiality of the sensor when integrated into a breathing mask. (G) Electrochemical measurement set-up for determining the glucose aerosol after capturing in a closed configuration. (H) Example of cyclic voltammograms in absence and presence of glucose. (I) Picture of the Ni-LCNFs device (i). SEM micrograph of the sensor's side-view (ii). Micrograph of the as-spun nanofibers (iii) and the Ni-LCNFs after device assembly (iv).

In brief, a spinning solution containing 0.6 g of Matrimid and 0.15 g of Ni (II) acetylacetone was prepared in a total volume of 4 mL of DMAc (**Figure 5.2A**). The solution was stirred overnight and subjected to the electrospraying process (**Figure 5.2B**). The electrospraying was conducted at a voltage of 12 kV with a flow rate of $10 \mu\text{L min}^{-1}$ for 5 h. The nanofibers were collected onto a chromatography filter paper (Whatman 1 CHR, 0.18 mm, 87 g m^{-2}) fixed around a drum rotating at 150 rpm. A tip-to-

collector distance was maintained at 15 cm. The conditions of the spinning chamber were settled at 24 ± 1 °C and 34 ± 9 % of humidity. After leaving the nanofibers drying overnight under room conditions, they were subjected to a CO₂ laser scribing process to obtain in one step laser-induced carbon nanofibers decorated with Ni-nanoparticles (Ni-LCNFs) (**Figure 5.2C**). CO₂ laser conditions employed: 2.55 W laser power, 76.2 cm s⁻¹ laser speed 76.2 cm s⁻¹, and 1000 DPI (dots per inch) image density resolution. For each nanofibers mat (size of 26 cm × 10 cm) 120 complete Ni-LCNF sensors are obtained; each sensor includes a working electrode (WE; d = 3 mm), reference electrode (RE), and counter electrode (CE), including the respective contacts (1 mm x 1 cm long). To improve the hydrophilicity of the sensing surface, sensors were treated with a UV-ozone cleaner for 5 min (**Figure 5.2D**). Afterward, to delimitate the sensors' working area and insulate the back side, hydrophobic wax barriers were employed. The wax was initially printed on two plastic foils according to **Figure 5.2E**, then the sensor was sandwiched between them employing two glass slides held together by paper clips. Eventually, the wax was transferred into the sensor via melting in the oven (100 °C, 15 min), resulting in its transfer and percolation among nanofibers and paper pores (**Figure 5.2E**). Finally, the glass slides were disassembled, and the plastic foils removed.

5.5.4 Measurement setup

Electrochemical measurements for glucose detection optimization were conducted by dropping 40 µL of the working solution onto the sensor working area; these measurements were performed without placing the plastic cover on top of the sensor, configuration named “*open device*” (**Figure 5.2E**).

Figure 5.2F illustrates the setup for measuring glucose in nebulized samples (breath simulation). To simulate the generation of breath aerosol, a plastic breathing mask with two lateral holes was placed onto a 3D-printed head model with an opening hole at the mouth in which the nebulizer was positioned. The sensor was placed on the external side of the mask, positioning the sensor working area correspondingly to a mask lateral hole (the other hole was plugged) (**Figure 5.2F**). Aqueous glucose solutions were nebulized for 5 min and the generated aerosol was collected on the sensor. After drying for 20 min at room temperature, 40 µL of 0.1 M NaOH was dropped on the working area of the sensor and a plastic tape was placed to close the working area (**Figure 5.2G**). This configuration, named “*closed device*”, forces the aerosol to penetrate the nanofibers enhancing the detection sensitivity. Eventually, the measurement was performed via cyclic voltammetry (CV) in the potential range of window 0.0 - 1.0 V, using a scan rate of 50 mV s⁻¹ and E step of 0.001 V; Ni-LCNF was used as RE. (**Figure 5.2H**).

5.5.5 Morphological characterization

Scanning electron microscope (Zeiss/LEO 1530, Germany) was used to characterize micro/nanostructure of the Ni-LCNFs film (**Figure 5.2I, i-iv**); micrographs acquisition was done after Au-Pd sputtering. Sensor side-view micrograph (**Figure 5.2I-ii**) was obtained by cutting the sensor with the CO₂ laser in the cutting mode (laser power: 30W; laser speed: 50.8 cm s⁻¹).

5.6 Results and discussion

5.6.1 Sensor fabrication

In a previous study of our group, a sensor prototype constituted of Fe-LCNFs as WE, RE, and CE was proposed; the manufacturing approach, based on a static nanofibers collector, enabled the fabrication of 12 sensors per batch⁷⁸. While, in this study, PI nanofibers were collected on a larger rotating drum, allowing to obtain ca. 120 complete sensors per batch. The strategic use of the rotating drum nanofibers collector returns a nanofiber mat with random orientation (**Figure 5.2I-iii**), with an average diameter of ca. 300 nm. The longer collection time per collecting area in this study 52 cm²/h (vs. 32 cm²/h)⁷⁸ made the fiber mat thicker (ca. 1.5-times) (**Figure 5.2I-ii**), thus necessitates stronger laser power to sufficiently carbonize the entire nanofiber mat in vertical direction. Eventually, when subjected to laser treatment the nanofibers results in a conductive 3D-porous structure (**Figure 5.2I-iv**). The complete device fabrication process is detailed in section "Sensor manufacturing".

5.6.2 Measuring glucose by direct detection mode

Initially, to understand the ability of the Ni-LCNF sensors to directly determine glucose, cyclic voltammetry (CV) was run using the sensor in the configuration "open device".

Figure 5.3A shows CVs performed in 0.1 M NaOH at three different Ni-LCNF sensors.

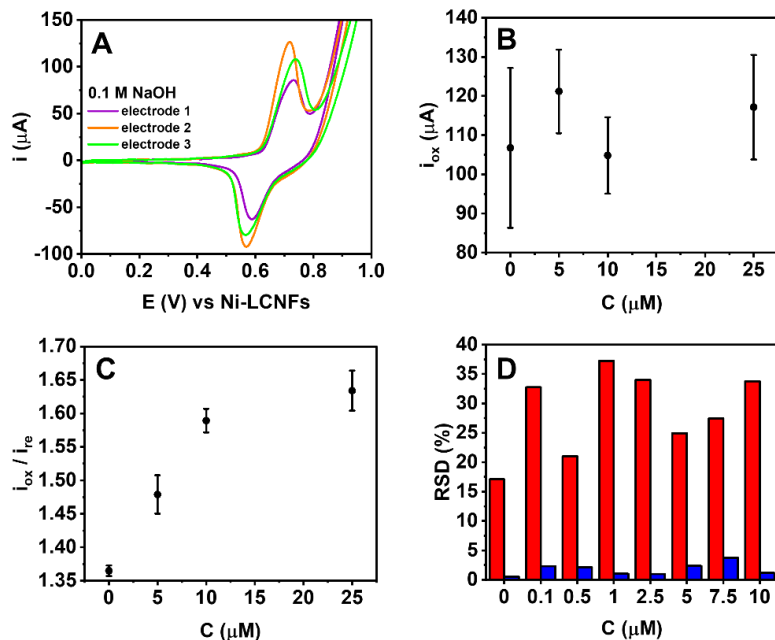
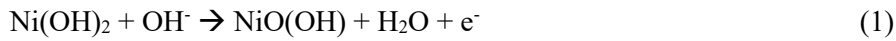


Figure 5. 3: (A) High signal variations of CVs obtained from three different Ni-LCNF sensors performed in 0.1 M NaOH without glucose. (B) Anodic peak current (i_{ox}) obtained with glucose 5, 10 and 25 μM . (C) Peak intensity ratio (i_{ox}/ire) determined at glucose 5, 10 and 25 μM . The data in B and C were extrapolated from the same CVs. (D) Comparison of relative standard deviation (RSD) calculated from anodic peak current (red) and i_{ox}/ire (blue) evaluated at concentrations of glucose enclosed between 0.1 and 10 μM . All data were obtained using the individual sensors (open device configuration) ($n=3$).

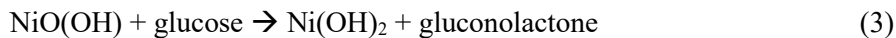
Ni-LCNF sensors, in an alkaline environment, give rise to characteristic peaks; these peaks are attributable to the nano-Ni redox chemistry^{24,255}. In particular, Ni(OH)₂ is oxidized during the anodic scan at around +0.7 V, following the reaction reported below.



In the reverse scan (cathodic scan) the Ni(O)OH is reduced at around +0.55 V, according to the reaction reported below.



It is well known that, the NiO(OH) enables the electrocatalytic oxidation of glucose to gluconolactone following this reaction^{24,255}.



Therefore, the presence of glucose can lead to a concentration-proportional increase in oxidation currents, which can be employed as analytical signals.

The sensor was then tested in the presence of increasing concentrations of glucose; the obtained CVs are reported in **Figure S5.1**. In the presence of glucose, the redox behavior changes, and the oxidation reaction results in a more pronounced anodic peak. Unfortunately, the peak current obtained does not give rise to proper dose-response behaviour and the reproducibility of the signals is rather poor (RSD \leq 31%, n=3) (**Figure 5.3B**). This can be attributed to the high heterogeneity between device-to-device, which makes absolute oxidation currents not reproducible. To overcome this issue, the ratio between anodic and cathodic peak current ($I_{\text{ox}}/I_{\text{re}}$) was employed to evaluate the glucose response. While the oxidation peak accounts for the active Ni(OH)₂ sites on the electrode and the glucose concentration in the solution (see also reaction 1 and 3), the reduction peak well reflects the amount of as-generated NiO(OH) species in the electrocatalytic system (see also reaction 2) which can be varied from electrode-to-electrode. Therefore, the cathodic peak current resulting from NiO(OH) species can be rationally served as an internal signal reference, indicating actual functional sites available on each electrode. As a result, this ratiometric data analysis facilitates the drastic improvement in signal reproducibility (**Figure 5.3C and 5.3D**).

In addition, the greater dose-response curve behaviour (**Figure 5.3B**) can be also achieved because elevating glucose concentration not only enables an increase in oxidation peak but also a decrease in the reduction peak as demonstrated in our previous study²⁴. Consequently, a greater discrimination among various glucose concentrations can be obtained. The decrease in reduction peak at higher glucose concentrations is attributed to the lower amount of NiO(OH)₂ during cathodic scan, i.e., higher number of NiO(OH)₂ are spent for electrocatalytic oxidation of glucose. The reduction in cathodic peak intensity when increased glucose concentration cannot be seen clearly in the present study (**Figure S5.1**) owing to high variations between device-to-device.

In comparison to the widely used amperometric signal, the intrinsic self-correcting factors offered by the CV signal make our evaluation method more reliable, specifically for 3D-porous electrodes that

possess high heterogeneity²⁵⁶⁻²⁶¹. In addition, unlike amperometric signals, the potential shifts from electrode-to-electrode that may occur do not significantly affect the ratiometric analytical signal.

5.6.3 Optimization of sensor production

To achieve the best analytical performance, different parameters were optimized during the sensor fabrication process, whose main steps are resumed in **Figure 5.2**. In this phase, the measurements were simply performed by dropping the NaOH solution containing glucose onto the working area (*open device* configuration).

Since the surface of pristine LCNFs is typically highly hydrophobic, a hydrophilic treatment to enhance their wettability is required. Therefore, two different strategies, i.e., oxygen plasma treatment and UV-Ozone treatment, were initially investigated. Both techniques induce the formation of -OH and other oxygen-containing groups on the LCNFs surface, improving in this way the hydrophilicity of the sensors^{202,203}. Hydrophilic treatments were carried out after laser-scribing Ni-LCNF film formation. The hydrophilic treatments greatly reduced the electrode variability, making the response of the sensor more reproducible ($\text{RSD}_{\text{non-treated}} \leq 75\%$; $\text{RSD}_{\text{plasma}} \leq 22\%$; $\text{RSD}_{\text{UV-Ozone}} \leq 5\%$; $n=3$). Owing to the greatest reproducibility, the UV-ozone treatment was chosen for further studies. The UV-Ozone treatment did not significantly affect the LCNF referencing system, as can be seen from the slight peak potential shift in **Figure S5.2A** (approx. 30 mV - 25 mV vs. the untreated sensor). Afterward, the UV-Ozone treatment time was further optimized (**Figure S5.2B**); 10 min-treatment was too aggressive and thus returned poor reproducible signals ($\text{RSD} \leq 22\%$, $n=3$). Even though treatment times of 3 and 5 min provided highly comparable performance, 5 min was chosen for further studies considering the greater signal reproducibility ($\text{RSD}_{3\text{min}} \leq 4\%$ vs. $\text{RSD}_{5\text{min}} \leq 2\%$, $n=3$).

Eventually, the laser power (LP) was optimized, attempting Ni-LCNFs synthesis applying a power enclosed to 2.25 and 3.00 W (**Figure S5.3**). The calculated LOD tends to improve up to an LP of 2.55 W, after which it is drastically worsened. This can be due to the excessive power that can destroy the nanofibers. On the other hand, too low LP is not energetic enough to effectively induce the carbonization of the nanofibers and the formation of nickel nanoparticles. According to the results, a laser power of 2.55 W was selected.

5.6.4 Sensor electroanalytical performance

As already demonstrated in our previous study, the performance of LCNF-based sensors can be improved using a closed working chamber⁷⁸. This approach is easily applicable by closing the working area with a plastic foil after the deposition of the working solution (**Figure 5.2G**); this gives rise to a homogeneous spreading of the solution. In addition, the pressure exercised from the closing foil forces the solution to percolate the 3D-porous structure of LCNFs. As expected, the closed device remarkably enhanced the analytical performance as seen from the improvements in sensitivity (11.5-times) and LOD (50-times) in comparison to the *open device* (**Figure S5.4**). The extremely low LOD (0.71 μM) obtained

confirms that the closed system approach is highly efficient in boosting the sensitivity of the Ni-LCNF sensors and was therefore used for the following nebulization experiment (**Figure 5.4**).

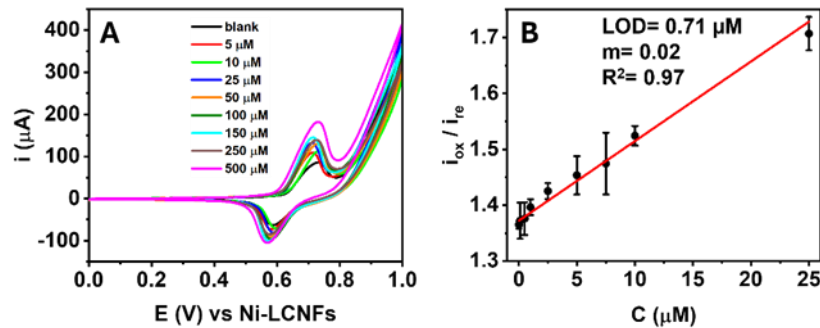


Figure 5.4: (A) Exemplary CVs obtained with increasing concentrations of glucose using the closed device configuration. (B) Calibration curve obtained with the closed device configuration ($n=3$). Linear fit equation $y=0.0161[\pm 0.0011]x + 1.3701 [\pm 0.0038]$, $R^2=0.9709$.

5.6.5 Capturing and measurement of aerosolized glucose

The permeability to aerosol phases of our sensing devices makes them highly attractive for capturing analytes present in breath. Nevertheless, owing to the limitation of facility, real-breath testing has not been yet performed in this study but it will be conducted in the future. Instead, to simulate breath analysis the sensor was integrated into a plastic breathing mask and placed on a 3D-printed head model as described in section "Measurement set-up"; the measurement was performed in the "*closed device*" configuration after capturing (**Figure 5.2F-G**).

Aerosolized glucose generated by the nebulizer was employed to demonstrate the proof-of-concept and investigate the capability of the sensor to capture and determine an analyte in an aerosol phase. At first, to maximize the capture efficiency of glucose, the sensor was vertically placed over the nebulizer outlet in which the aerosol collection time (**Figure 5.5A**) and the distance between the nebulizer outlet and the sensor (**Figure 5.5B**) were investigated. In this phase, the 3D-printed head model was not used.

The aerosol collection time was initially studied using a distance of 0 cm (meaning the sensor was placed directly at the nebulizer outlet). A glucose concentration of 0.4 mM was selected for the nebulizer because this concentration mirrors the glucose level found in healthy lung fluid. This is based on the typical ratio of glucose concentration in lung fluid to that in blood, which is approximately 1:12¹¹⁴. After glucose aerosol capturing, the sensor was dried for 20 min and measured according to section "Measurement setup". **Figure 5.5A** reports the glucose concentration measured; the amount of glucose determined increased up to 3 min while extending the collection time did not significantly increase glucose capturing ability. Instead, too long collection time (30 min) negatively affects the measurement probably because the collected drops become larger and fall off the sensor. A collection time of 5 min was selected as the best compromise between signal intensity and reproducibility. Nevertheless, as a nebulizer generates aerosolized glucose much more efficiently and intensely than the real breathing

system, the proper collection time can take longer. Therefore, it is mandatory to study in real-world applications, particularly when considering the additional breathing-in process.

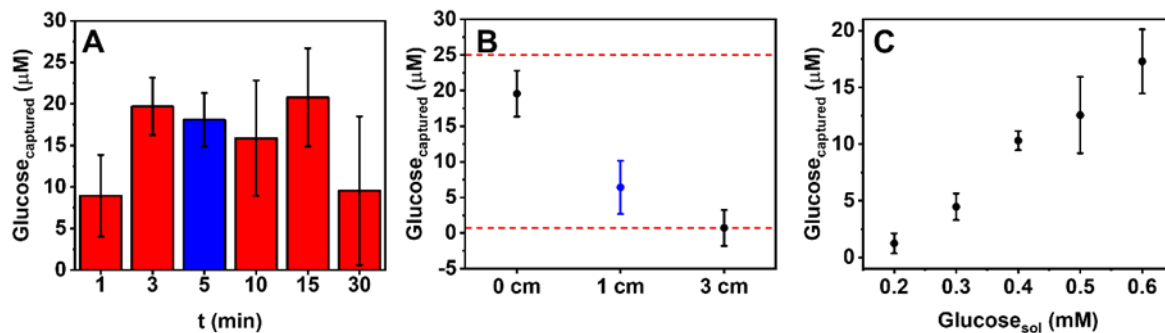


Figure 5.5: (A) The concentration of glucose measured with the close device configuration after nebulization of 0.4 mM glucose solution at different times. (B) Optimization of the distance between sensor surface and nebulization source. Graph reports the glucose concentrations obtained from nebulizing 0.4 mM glucose for 5 min, placing the sensor at 0, 1 and 3 cm of distance from the nebulizer. Red dashed lines represent the LOD and the superior limit of linear range. (C) Correlation between concentrations of glucose in the nebulized solutions and the captured glucose measured with the device (n=3).

Subsequently, the distance between the nebulization source and the sensor was investigated (**Figure 5.5B**). The distance of 0 cm was discarded since it was practically inapplicable in real situations and too close to the linear range limit. Therefore, as compromise, a practical distance of 1 cm (in blue in **Figure 5.5B**) was selected, since it can be used in real breath analysis allowing glucose level oscillation. Therefore, using the optimized parameters, the impact of nebulizer solution concentration was studied, simulating physiological changes in lung fluid concentration. Glucose concentration was studied from 0.2 to 0.6 mM, corresponding to blood concentrations ranging from 2.4 mM to 7.2 mM (healthy individuals typically have about 5 mM glucose)¹¹⁴. The obtained cyclic voltammograms are reported in **Figure S5.5**.

Figure 5.5C proves the nice correlation ($r = 0.9761$) between the glucose present in the nebulization solution and the sensor-captured glucose, moreover, the sensor yields reproducible data ($\text{RSD} \leq 12\%$, $n=3$).

In order to highlight the beneficial features of the proposed permeable sensors over traditional screen-printed carbon electrodes (SPEs) for capturing and detecting aerosolized glucose, their electrochemical performances were compared (**Figure S5.6**). A commercial SPE was modified via electrodeposition of a 10 mM solution of $\text{Ni}(\text{NO}_3)_2$ in 0.1 M KCl, carried out by CV in the potential range 0.0 / -1.5 V for 3 consecutive scans^{262,263}. The presence of an oxidation peak at 0.55 V and a reduction peak at 0.15 V in alkaline conditions (**Figure S5.6A**), which are not present in the CVs of unmodified SPE (**Figure S5.6A** black lines and inset), confirms successful nickel deposition (note that the silver ink reference electrode shifts the peak potential compared to the Ni-LCNF reference electrode). Afterward, the Ni-modified SPE was tested to capture glucose under the conditions reported in section “Measurement setup”. The Ni-modified SPE allows glucose detection at 0.4 mM only when a drop of the solution is deposited onto the sensor surface, while it is unable to detect glucose from the nebulized solution (**Figure S5.6A** and

S5.6B). This result greatly emphasizes the advantages of the proposed sensors over conventional SPEs in capturing and detecting aerosolized analytes.

Eventually, the sensor stability over time was studied in closed (petri dish) and unprotected ambient conditions (**Figure 5.6A**). As expected, after 2h the signal from the unprotected sensor significantly decreased, compared to the freshly UV-Ozone-treated electrode; subsequently, the sensor response further decreased over time. On the other hand, by shielding the sensors from the air, the sensors' response is less affected over time.

Interferent studies were finally conducted. Overall, breath aerosol is considered a 'clean' sample matrix, majorly constituted of water. However, some potential interferent species, including lactate, acetone, ethanol, ammonia, and H_2O_2 , can be co-present with glucose in the breath aerosol. **Figure 5.6B** greatly demonstrates the high selectivity of the proposed sensor toward glucose detection even in the presence of electroactive or potential interfering compounds present at glucose-equimolar level.

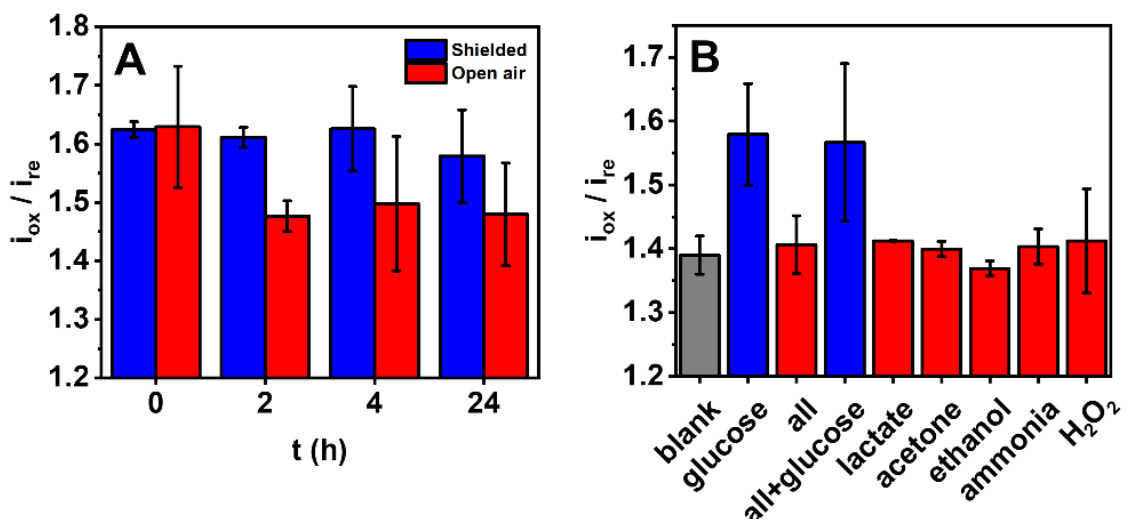


Figure 5.6: (A) Stability of the sensor of the complete devices shown in **Figure 5.2E**. Graph reports the electrochemical response from nebulized glucose solution at 0.4 mM. (B) Selectivity study for potential interference found in breath. Glucose and interfering species at concentration of 0.4 mM were used in nebulized solutions.

5.7 Conclusions

Fabrication of laser-induced carbon nanofiber-embedded with nickel nanoparticles (Ni-LCNFs) transducer and its use as a permeable enzyme-free electrochemical transducer for capturing and detecting aerosolized glucose have been demonstrated. The three-electrode system made from Ni-LCNF electrodes enabled reliable cyclic voltammetric signals resulted from electrocatalytic oxidation of glucose by Ni nanocatalysts. Unlike conventional amperometry, taking the ratio of anodic to cathodic current (internal reference signal) in cyclic voltammetry can significantly overcome the high variation between device-to-device. Upon optimization of sensor manufacturing and electrochemical measurement procedure, detection of glucose at sub-micro molar concentrations was feasible without the need of solution stirring. When we further applied the sensors for capturing and detecting glucose in aerosol form, the high surface area and breathability of Ni-LCNF electrodes unsurprisingly exhibited superior analytical performance, especially comparing to non-permeable electrodes. The drying step of captured aerosol prior detection was also believed to play a key role in enhancing detection sensitivity, i.e. strengthen adhesion between analyte and electrode surface, and selectivity, i.e., removal of volatile and labile interfering compounds. The analytical performance of the sensors can be maintained with closed environment, shielding from the ambient air. In the future work, the analytical performance and practicality of the sensors for *in vivo* measurements will be investigated. Furthermore, as the fabrication strategy is highly versatile, i.e., types of nanocatalysts can be changed into others such as platinum, extension to other breath analytes, e.g., H₂O₂, can be foreseen. Thus, the as-developed permeable enzyme-free electrochemical sensors are highly attractive for developing breath analysis in which not only low-cost manufacturing cost, but also high analytical performance can be achieved.

5.8 Supporting information

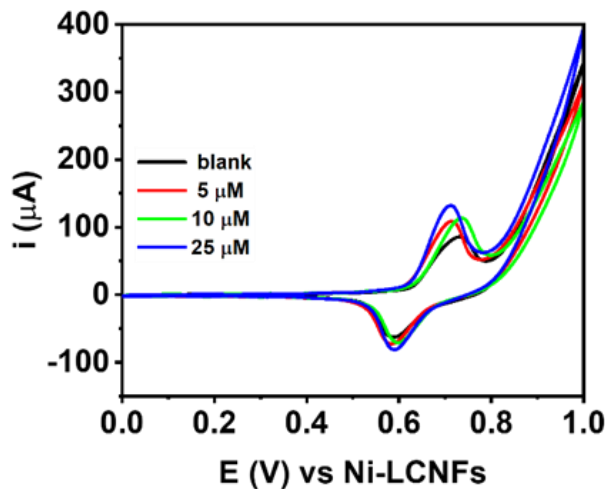


Figure S5. 1: Cyclic voltammograms obtained in presence of different amount of glucose. CVs obtained from Ni-LCNF sensor performed in 0.1 M NaOH (blank) and with 5, 10 and 25 μ M of glucose.

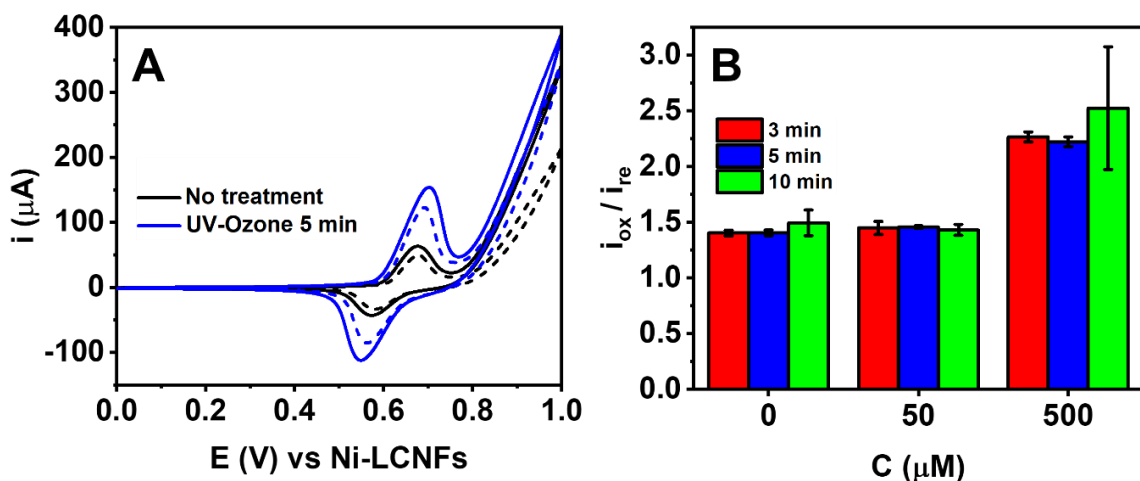


Figure S5. 2: Effect of UV-ozone treatment. (A) Cyclic voltammograms obtained from Ni-LCNF sensor untreated and treated with UV-ozone (5 min, and 0.5 L min⁻¹ O₂ flow rate). Measurements were performed in 40 μ L of 0.1 M NaOH without (dashed lines) and with 50 μ M glucose (continuous lines). (B) Comparison of signal ratio obtained in presence of different amount of glucose, after UV-ozone treatment performed with different duration.

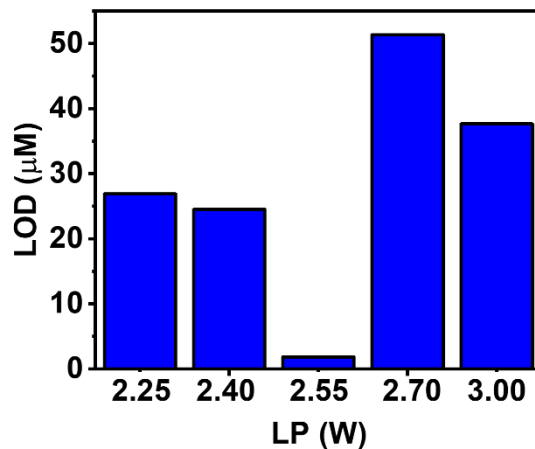


Figure S5. 3: Influence of laser power on the limit of detection. Limit of detections calculated from the dose response curve (glucose concentration range 0-500 μM in 0.1 M NaOH). The measurements were performed using the open device configuration with triplicate measurement.

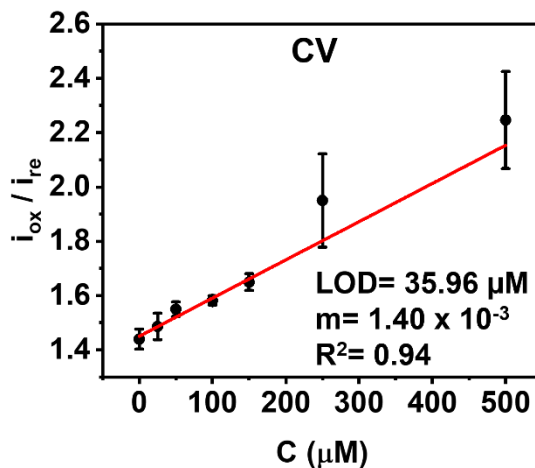


Figure S5. 4: Dose response curve obtained from open device configuration. Linear fit of the data extrapolated from CV in the range 0-500 μM of glucose in 0.1 M NaOH. Equation: $y=0.0014 [\pm 1.6422 \times 10^{-4}] x + 1.4503 [\pm 0.0165]$, $R^2=0.9362$ ($n=3$).

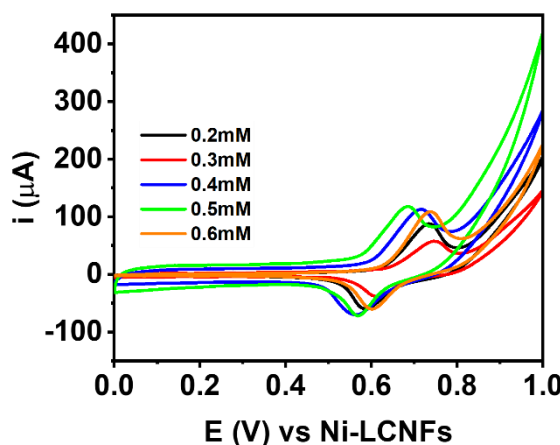


Figure S5. 5: Cyclic voltammograms obtained from different glucose concentrations nebulized.

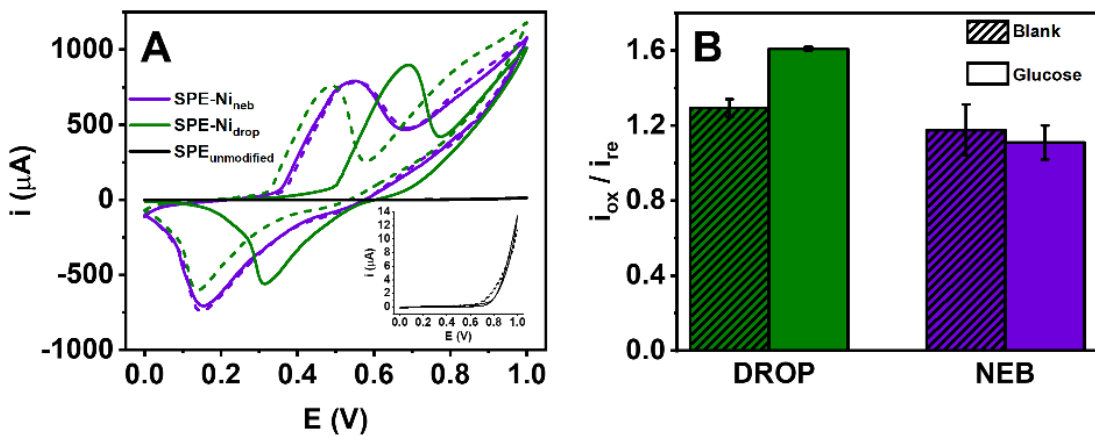


Figure S5.6: Glucose measurement using Ni-modified commercial screen-printed electrodes (A) Electrochemical behavior of SPEs with and without electrodeposited Ni. The inset reports the zoomed signal of the unmodified SPE. The CVs of SPE-Ni_{drop} were obtained from drop-testing for 0.1 M NaOH (dashed line) and 0.4 mM of glucose (solid line). The CVs of SPE-Ni_{neb} were obtained after capturing nebulized glucose using 0 mM (dashed line) or 0.4 mM (solid line). (B) Comparison of the I_{ox}/I_{re} with (0.4 mM glucose) and without glucose for drop and aerosol measurements using SPE-Ni electrodes.

6. Conclusion and Future Perspectives

This thesis discusses the need for enzyme-free electrochemical sensors due to their numerous advantages, such as capability of miniaturization, immediate data readout, sensitivity, low cost, scalability, and portability, which make them suitable for point-of-care applications. Nowadays, often enzymes are used to enhance the selectivity of the electrochemical sensors¹⁵. However, enzyme-based sensors do have some drawbacks such as high cost and stability issues, which underlines the need of an enzyme-free alternative^{6-8,15}.

Non-enzymatic sensors consist of a conductive material that enables an electrocatalytic reaction with an analyte, typically involving metals, metal oxides, and/or graphene and its derivatives^{15,19}. There are many ways to fabricate non-enzymatic electrochemical sensors, either by modifying already conductive material with the functional catalyst material (drop casting, dip coating, electrodeposition, electroless deposition)^{26,34,35} or by producing the catalyst material and the conductive support in one step (screen-, inkjet-, 3D-, Roll-to-roll-printing, laser-induced carbonization)^{37,44,52,53,62}. Each of these techniques has its own strengths, weaknesses, and potential for mass production.

Among these, the emerging technology of laser-induced carbonization is very promising due to its simplicity, adaptability, minimal production steps from raw materials to complete electrode, and extremely low production cost after the initial invest in a laser engraver. There are many strategies to fabricate laser-induced functional hybrid electrodes⁵⁸⁻⁶⁴, however, in terms of production cost, reproducibility, and porosity (which increases the accessibility of catalyst material), electrospinning to produce the precursor material seems most promising and was used in this thesis. In this process, precursor materials (polymer, metal salts) are dissolved in an organic solvent (spinning solution), electro spun, and laser scribed, all without the need for energy-consuming heating steps^{24,62,63}.

In the first project of this thesis, spinning solutions containing Matrimid® (polyimide) and various amounts of Pt(II)- and Ni(II)-acetylacetone were electro spun on conductive ITO-coated PET sheets (ITO-PET) at around 12 kV to produce a nanofiber mat. Both metals were chosen because of the well-known catalytic properties of their alloys towards hydrogen peroxide reaction^{142,145}. LCNFs were produced by laser scribing these fibers with a CO₂-laser engraver. The aforementioned Pt-Ni-alloys are expected to form when laser scribing a fiber mat that contains both metal salts. SEM-EDX measurements revealed the metal-, carbon- and oxygen composition of the surface of the LCNFs. A higher amount of nickel increased the oxygen content from $2.9 \pm 0.6\%$ to $6 \pm 1\%$, which implies that not all of the nanofibers were converted into LCNFs. This was also confirmed by SEM measurements (fiber fragments within the LCNFs) and is probably caused by the higher thermal conductivity of nickel, which leads to a lower local heat during the laser treatment. Elemental mapping showed a very homogeneous distribution of the metals, meaning an equal distribution of the catalyst. The catalyst behavior was investigated by cyclic voltammetry of hydrogen peroxide solutions and showed that platinum is mainly responsible for the catalytic reaction. Especially the oxidation of hydrogen peroxide was not improved by increasing the nickel content of the alloyed LCNF. In contrast, hydrogen peroxide reduction was

strongly enhanced by the addition of nickel, likely because Pt-Ni-alloy decreases the adsorption energy of reduction reaction intermediates compared to pure Pt¹⁴². However, applying a negative potential caused stabilization issues of blank measurements in unstirred conditions probably due to oxygen reduction reaction of dissolved oxygen. In conclusion, a positive potential was chosen to sensitively oxidize hydrogen peroxide. For pure Pt, a LOD of $1.4 \pm 0.4 \mu\text{M}$ with a linear range from 5-500 μM was achieved (chronoamperometry; potential: +0.5 V vs. Ag/AgCl), which worsened with increasing Ni content. The drawback of the high oxidation potential is the low selectivity because electroactive molecules such as ascorbic acid, uric acid, or dopamine can be oxidized at the graphene oxide/reduced graphene oxide sites of the electrode. This is evident not only from the fact that signals from these interferences appeared even with LIG-LCNFs (metal-free), but also because increasing the metal content of the electrode improved selectivity. Anionic polymer coatings of the electrode consisting of Nafion® worsened selectivity, whereas a Nylon coating did not change it. However, by using Nylon as an antifouling-coating, the recovery of spiked real sample measurements in pure and diluted human serum was significantly enhanced.

To further improve selectivity towards hydrogen peroxide, a new measurement approach was used. Even though the blank measurements of potentials used for hydrogen peroxide reduction did not stabilize, the potentials -0.1 V, 0 V, and +0.1 V (vs. Ag/AgCl) were investigated to prevent oxidation of interfering molecules. In this approach, instead of waiting for a stabilization of the signal, one electrode was used for exactly two chronoamperometry measurements, i.e. (i) a blank measurement in PBS and (ii) a measurement in PBS spiked with hydrogen peroxide. This procedure was repeated for various hydrogen peroxide concentrations and the difference in current, ΔI , between the spiked and the blank measurement was used versus the spiked concentration as a calibration curve. The best LOD (21 μM) was achieved by using the 50% Ni + 50% Pt LCNF at +0.1 V, but with ascorbic acid being oxidized in a large manner. The best selectivity was achieved by using 50% Ni + 50% Pt LCNF at -0.1 V but led to an insufficient LOD of 150 μM . Future research in this direction could investigate strategies to remove dissolved oxygen such as the incorporation of oxygen-scavenging molecules as discussed in Chapter 1.7.7. This approach could lead to a better limit of detection at negative potentials due to lower background current. In a next step, a catalyst that allows hydrogen peroxide reduction at potentials equal to or below -0.1 V (vs. Ag/AgCl) without leading to oxygen reduction reaction was needed. Therefore, the polyoxometalate (POM) $\text{H}_4\text{SiMo}_{12}\text{O}_{40}$ (SiMo) was a promising candidate due to its catalytic activity towards hydrogen peroxide reduction¹⁹⁶ and its (at least short-term) stability in almost neutral pH¹⁹⁹. An initial study showed that SiMo is stable during the time of a measurement in solutions of a pH ranging up to 6. Furthermore, catalysis of hydrogen peroxide reduction started at -0.2 V and was most active at a pH of 3. Various approaches to attach POM to the LCNF were tested such as co-spinning with consecutive laser scribing and drop-coating. While laser-scribing of POM-co-spun fibers destroyed most of the catalyst (detected by small-angle X-ray scattering (SAXS)), drop-coating on untreated LCNF (attachment due to electrostatic interactions)²⁰⁰ led to significant loss of signal due to leaching during

measurement. The next approach was to PEGylate Pt-LCNF with poly(ethylene glycol)-methyl-ether-thiol (PEG-thiol) to provide a hydrophilic surface. With an enthalpic gain due to the recovery of hydrogen bonds between water molecules by dehydration of both the hydrophilic surface and the POMs, SiMo adsorbed much more stable onto the LCNF due to the so-called superchaotropic effect²⁰¹. The same effect was later achieved by attaching the cationic surfactant Ethomeen C/25 onto UV-ozone-treated LCNF. The ozone treatment was used to increase negatively charged groups on the LCNF surface which enhanced electrostatic interactions with the positively charged surfactant. However, no satisfactory results for sensitive hydrogen peroxide detection were achieved in non-stirred measurement. Nevertheless, it was shown how to efficiently deposit POMs onto LCNFs, offering a great potential since this could be used for various catalyst materials in many applications, e.g. water splitting^{209–211,264}.

In the second project, the Pt-Ni-alloyed LCNFs were tested for the detection of glucose in physiological conditions, due to promising results of this alloy in literature¹⁴⁵. First, an in-depth characterization of the LCNFs was performed by using high resolution TEM, STEM-EDX, XPS, and SAXS. High-resolution TEM of LCNFs revealed a metal nanoparticle radius of roughly 2 nm. Nanoparticles in Pt- and Pt-Ni-alloyed LCNFs have similar d-spacings like pure Pt and Pt-Ni-alloys found in literature^{226,227}. The d-spacings found in Ni-nanoparticles of Ni-LCNFs seemed to be closer to NiO species than pure Ni²²⁸. STEM-EDX measurements of nanoparticles in the 50% Ni + 50% Pt LCNFs revealed that both Ni-core-Pt-shell as well as homogeneous particles exist. Furthermore, the XPS data confirmed the observation of SEM-EDX data in the previous chapter, that Ni-LCNF indeed lead to a higher oxygen content in the carbon matrix of the LCNF. In addition, the formation of Ni-Pt-alloy in 50% Ni + 50% Pt LCNFs was confirmed. SAXS data showed that nickel, probably due to its better heat conductivity, lead to a more consistently stacking of reduced graphene oxide/ graphene oxide layers, which was observed in high-resolution TEM pictures as well.

An electrochemical investigation by cyclovoltammetry showed that none of the prepared LCNFs showed any catalytic behavior towards glucose oxidation at physiological pH at all. Since it is known that Ni-LCNFs can catalyze glucose oxidation at alkaline conditions¹⁹, an electrochemical pretreatment which should locally increases the pH was investigated for various LCNFs, with both pure Pt- and Ni-LCNFs as well as alloys of them. In terms of signal and standard deviation, 25% Pt + 75% Ni LCNFs and a treatment of -0.9 V for 20 s was most promising. Note that neither pure Pt- nor pure Ni-LCNF led to a promising signal after the electrochemical pretreatment, which suggests that the role of platinum is to efficiently increase the local pH, whereas the *in situ* generated Ni(OH)₂ species catalyzes the oxidation of glucose. In order to enhance the overall performance, electrodes were used for multiple consecutive measurements which reduced the background current caused by the pretreatment. However, the multiple measurements lead to a poisoning of the catalyst, and an electrochemical catalyst cleaning step, i.e. -0.2 V for 60 s, was performed after each measurement. A ratiometric data readout further improved the overall performance of the sensor and lead to a selective detection of glucose with two linear ranges

(0.1 mM – 4 mM and 5 mM – 8 mM) and a LOD of 0.3 ± 0.1 mM. A prominent problem with laser-induced carbon electrodes is the increasing hydrophobicity during aging, which leads to less contact between the sample and the electrode and worsens the overall performance¹⁵⁴. This issue could be solved by a simple 10 s incubation of the LCNF with a 0.05 w% Tween in PBS solution. To proof applicability of the LCNFs in medical diagnostics, sterilization of the electrodes was tested and did not harm their performance. Lastly, a recovery of $95 \pm 10\%$ was achieved in spiked and non-spiked diluted human serum (20% human serum in PBS).

To enhance practicability, future research could use the developed fibers to laser scribe not only the working electrode but also counter- and reference electrodes and investigate the effect towards the pretreatment caused by these changes. Furthermore, strategies to prevent electrode fouling when performing measurement in undiluted blood or human serum should be explored. Due to the fact that simple drop-coating of polymer solutions on top of the electrode harmed the pretreatment, other strategies should be tried. Perhaps electrospinning nanofibers on top of the LCNFs as a filtration system could be a promising solution.

In the last project, Ni-nanofibers were used to produce a LCNF-based 3-electrode system used in a mask to capture artificial breath and consequently detect glucose under alkaline conditions. Nanofibers were collected on filter paper instead of the conductive ITO-PET to prevent a short-circuit during the measurement since electrodes are laser-scribed next to each other. Cyclovoltammetry and a ratiometric data-readout was chosen to enable sensitive detection of glucose in a measurement that does not require a calibration of the electrode before the measurement. The laser power of the scribing process was optimized and hydrophilic treatments to increase the penetration depth of the solution into the LCNF nanostructure, i.e. oxygen plasma and UV-ozone, were investigated to further improve the sensitivity and linear range of the measurement. A laser power of 2.55 W and a UV-ozone treatment of 5 min led to the best signal and reproducibility. After adding the measurement solution (glucose in 0.1 M NaOH), closing the 3-electrode system by a plastic foil on top of the sensor further improved the performance⁷⁸. The pressure originated from the foil is expected to force the solution deeper into the nanostructures of the LCNF. The linear range of the optimized sensor was between 0 - 25 μ M with a LOD of 0.7 μ M. With the optimized measurement setup, the capturing of glucose from artificial breath was investigated. In this approach, a nebulizer was used to produce the artificial breath by nebulizing a glucose solution with a concentration that is present in lung fluids (0.4 mM)¹¹⁴. The optimized capturing resulted in a time of 5 min and a distance between the outlet of the nebulizer and the electrode of 1 cm. The final approach was to place the electrode-system in a mask, collect the simulated breath for 5 min, dry the electrode, and measure. Overall, it was possible to differentiate various nebulized glucose solutions (0.2 mM; 0.3 mM; 0.4 mM; 0.5 mM; 0.6 mM), reflecting blood glucose levels ranging from 2.4 mM to 7.2 mM¹¹⁴. Note that a typical blood glucose level of a healthy individuum is around 5 mM¹¹⁴. A selectivity study showed perfect selectivity towards glucose when interferents expected in breath were present. Further studies in this direction could use a better simulation of the breath, e.g. by using in- and exhaling phases.

Furthermore, glucose levels of real breath before and 1 h after a meal could be investigated and compared to respective blood sugar levels as a final proof of concept.

Overall, in this thesis, the LCNF material was extensively characterized by using various methods to thoroughly understand the surface chemistry of the electrodes. The lightweight nature of the nanofibers and the resulting nanostructured LCNFs led to a material cost below €0.10 per electrode, even when 25 wt% platinum salt relative to the dry mass of the polymer was used. This makes the electrode material a very promising candidate for point-of-care (POC) testing, considering the early stage of development. Although sensitive and selective detection of hydrogen peroxide was not achieved, the results for glucose detection in both physiological conditions and simulated breath are very promising. Even though it was possible to grow cells on laser-scribed graphene²⁶⁵, toxicity of Pt-Ni-LCNFs need to be tested in future research as well. Further studies, as mentioned in this chapter, could ultimately lead to the commercialization of LCNFs in the diagnostics market as non-enzymatic electrochemical sensors. In the context of physiological conditions, implementation of a miniaturized LCNF-based 3-electrode system into a multiple-use test stripe of a glucose meter (blood test) seems to be most-promising. Considering breath analysis, a reusable and washable LCNF system to detect glucose in a mask would make glucose testing for patients much more convenient. Apart from electrochemistry, obtaining approval from the European Medicines Agency (EMA) or the Food and Drug Administration (FDA), as well as developing and producing an affordable home-use potentiostat, are an additional challenging entry barrier into the market.

7. Summary

Electrochemical sensors are ideal candidates for point-of-care diagnostics due to their low cost, sensitivity, and direct data readout. Nowadays, enzyme-based sensors dominate the electrochemical diagnostics market due to their outstanding selectivity. However, there are some drawbacks related to the use of enzyme like stability issues or high manufacturing costs. This thesis highlights the need for enzyme-free alternatives and provides a comprehensive overview of non-enzymatic sensors and their development. The definition, principles, and typical detection mechanisms of electrochemical sensing are explained. Various conventional strategies for fabricating enzyme-free electrochemical sensors, such as drop-casting, dip-coating, electro- and electroless deposition, screen/inkjet/3D-/roll-to-roll printing, and the emerging technology of laser scribing, are introduced and compared in terms of cost, complexity, mass production capability, and their individual pros and cons. Additionally, considerations regarding selectivity, sensitivity, and biofouling when applying these sensors to different matrices, such as clinical samples (blood, dermal interstitial fluid, sweat, saliva, urine, breath) and non-clinical samples (water from rivers, lakes, seas, food and beverages, cell culture media), are presented. Other challenges and potential solutions related to electrode fouling, measurements under physiological conditions, biocompatibility, long-term stability, storage, practical issues, and efficiency are also discussed.

In this thesis, a non-enzymatic electrochemical sensor based on laser-induced carbon nanofibers (LCNFs) for detecting hydrogen peroxide was developed. The working electrode was laser-scribed on polyimide nanofibers produced by electrospinning. These fibers contained either one or a mixture of both metal salts Pt(II)- and Ni(II)-acetylacetone, which were converted to nanoparticles embedded within the LCNF during the laser treatment. The resulting nanoparticles consisted either of Pt- or Ni-metals and their oxides, or Pt-Ni-alloyed metal and its oxide in the case of a mixture. In the measurement setup, a Pt-wire and an Ag/AgCl electrode were used as the counter and reference electrodes, respectively, to investigate hydrogen peroxide detection. LCNFs with various compositions of the metal salts were tested towards the catalytic behavior to hydrogen peroxide and their selectivity. The best sensitivity (with a limit of detection (LOD) of $1.4 \pm 0.4 \mu\text{M}$) in an un-stirred approach was achieved by oxidizing hydrogen peroxide on a pure Pt-LCNF, but this led to unsatisfactory selectivity. Strategies such as increasing the metal content or using polymer coatings were applied to improve selectivity. Drop-coating the electrode with nylon also improved the recovery of hydrogen peroxide spiked in real matrices (undiluted and diluted human serum). Selectivity was further improved by reducing the measurement potential and switching from oxidation to reduction of hydrogen peroxide, although this came at the cost of sensitivity. Additionally, strategies to attach polyoxometalates as alternative catalysts onto the LCNF surface were explored but did not result in sensitive hydrogen peroxide detection.

A second project in this thesis focused on the non-enzymatic electrochemical detection of glucose under physiological conditions. It is well-known that glucose oxidation is catalyzed on Ni-surfaces at an alkaline pH. Therefore, the Pt/Ni-alloyed LCNF described in the previous project was used to efficiently generate a high local pH by an electrochemical pretreatment (-0.9 V for 20 s) on the Pt-sites of the

LCNF, enabling glucose measurement on the Ni-sites of the alloy in a consecutive cyclovoltammetry measurement, even though the initial pH of the solution was 7.4. To enable long-term measurements, an electrochemical treatment after each measurement was introduced to clean the catalyst surface. After optimizing (i) the pretreatment, (ii) the catalyst cleaning, (iii) the measurement conditions, and (iv) the data treatment, glucose could be selectively detected in physiologically relevant concentrations with a LOD of 0.3 ± 0.1 mM. Furthermore, the aging of the electrode was investigated, where hydrophobicity is increasing with time, leading to a reduced contact between electrode and solution. To resolve this, a simple Tween-20 incubation was applied prior to measurement. Finally, the electrode performance was not affected after sterilization, and a recovery of $95 \pm 10\%$ in spiked, diluted human serum was achieved. In the last project, pure Ni-LCNF were laser-scribed as a 3-electrode system (LCNF was used as the working, counter, and reference electrode) and used to detect glucose in simulated breath. Glucose solutions with concentrations similar to those present in lung fluids were nebulized, captured on the porous LCNFs, and electrochemically measured in NaOH solution. With optimized manufacturing, glucose-capturing, and measurement parameters, glucose was detected selectively using cyclovoltammetry and a ratiometric data readout. To simulate variations in lung fluid concentration (reflecting blood sugar level variations), various glucose concentrations of the nebulized solutions were captured, measured, and could be distinguished from each other.

8. Zusammenfassung

Elektrochemische Sensoren erweisen sich durch ihre Zuverlässigkeit, Beständigkeit, geringen Kosten, Sensitivität sowie der Möglichkeit, direkt vor Ort ausgelesen zu werden, als ideale Kandidaten der Vor-Ort-Diagnostik. Heutzutage dominieren vor allem auf Enzym basierende Sensoren den elektrochemischen Diagnostikmarkt, da diese äußerst selektiv sind. Jedoch haben Enzyme durchaus Nachteil bezüglich ihrer Stabilität und Fabrikationskosten. In dieser Arbeit wird die Wichtigkeit nichtenzymatischer Sensoren als Alternative hervorgehoben. Des Weiteren wird ein umfangreicher Überblick nicht-enzymatischer elektrochemischer Sensoren und deren Entwicklung gegeben, welche mit der allgemeinen Definition, dem Messprinzip und einem beispielhaften Reaktionsmechanismus beginnt. Verschiedene etablierte und neue Herstellungsmethoden der nichtenzymatischen Sensoren werden vorgestellt und miteinander in den Punkten Kosten, Komplexität, Umsetzbarkeit in die Massenproduktion und individueller Vor- und Nachteile verglichen. Unter den diskutierten Methoden sind Beschichten durch Auftröpfen, Tauchbeschichten, galvanische und stromlose Abscheidung, Sieb-/Tintenstrahl-/3D-/Rollen-Druck und das Karbonisieren mit Hilfe eines Lasers. Zudem wird darauf hingewiesen, welcher Fokus (auf zum Beispiel Sensitivität, Selektivität oder Ablagerungen auf der Elektrode) bei den jeweiligen realen Probenmatrices gesetzt werden sollte. Diese beinhalten sowohl klinische (Blut, Interstitialflüssigkeit, Schweiß, Speichel, Urin, Atem) also auch nicht-klinische Matrices (Fluss-/See-/Meer-Wasser, Essen und Getränke, Zellkulturmedium). Weitere Herausforderungen und potenzielle Lösungen während der Sensorentwicklung, wie Ablagerungen auf der Elektrode während der Messung, die Messung unter physiologischen Bedingungen, Biokompatibilität, die Stabilität während Langzeit-Messungen, Lagerung, praktische Abwägungen und die Effizienz werden diskutiert.

In dieser Arbeit wurde ein nicht-enzymatischer elektrochemischer Sensor auf Basis von Laser-induzierten Kohlenstoffnanofasern zur Detektion von Wasserstoffperoxid entwickelt. Die Arbeitselektrode wurde mittels Laser auf Polyimid-Nanofasern geschrieben, nachdem diese durch Elektrospinnen hergestellt wurden. Diese Fasern enthielten entweder eines der beiden oder beide Metallsalze Pt(II)- und Ni(II)-acetylacetonat, die während der Laserbehandlung in Nanopartikel umgewandelt und in die Kohlenstoffnanofasern eingebettet wurden. Die entstandenen Nanopartikel bestanden entweder aus Platin- oder Nickelmetall und deren Oxide oder einer Platin-Nickel Legierung zusammen mit dem entsprechenden Oxid im Falle einer Salzmischung. Um Wasserstoffperoxid zu detektieren, wurde als Gegen- bzw. Referenzelektroden ein Platin Draht und eine Silber/Silberchlorid-Elektrode verwendet. Kohlenstoffnanofasern mit verschiedenen Zusammensetzungen der Metallsalze wurden auf das katalytische Verhalten gegenüber Wasserstoffperoxid und deren Selektivität getestet. Die beste Sensitivität in einem nicht gerührten Ansatz wurde mit einer Nachweigrenze von $1,4 \pm 0,4 \mu\text{M}$ durch das Oxidieren von Wasserstoffperoxid an einer Platin-Kohlenstoffnanofasern-Elektrode erreicht, was jedoch zu einer unbefriedigenden Selektivität führte. Strategien, wie die Erhöhung des Metallgehalts der Elektrode oder die Verwendung von Polymerbeschichtungen wurden verwendet, um

die Selektivität zu verbessern. Eine Nylon-Beschichtung verbesserte die Signalausbeute von Wasserstoffperoxid, welches in realen Matrices (unverdünntes und verdünntes menschliches Serum) hinzugefügt wurde. Die Selektivität wurde weiter verbessert, indem das Messpotential reduziert und somit statt der Oxidation eine Reduktion von Wasserstoffperoxid durchgeführt wurde, was aber auf Kosten der Sensitivität ging. Darüber hinaus wurden Strategien zur Anbringung von Polyoxometallaten als alternative Katalysatoren auf der Oberfläche der Kohlenstoffnanofasern untersucht, was jedoch nicht zu einer sensitiven Wasserstoffperoxid-Detektion führte.

Ein zweites Projekt dieser Arbeit konzentrierte sich auf die nicht-enzymatische elektrochemische Detektion von Glucose unter physiologischen Bedingungen. Es ist bekannt, dass die Glucose-Oxidation auf Nickel-Oberflächen bei alkalischem pH-Wert katalysiert wird. Daher wurden die im vorherigen Projekt beschriebenen Pt/Ni-legierten Kohlenstoffnanofasern verwendet, um effizient mit Hilfe einer elektrochemischen Vorbehandlung (-0,9 V für 20 s) einen hohen lokalen pH-Wert an den Platin-Atomen der Legierung zu erzeugen, wodurch die Glucose-Detektion an den Nickel-Atomen der Legierung in einer darauffolgenden Cyclo Voltammetrie-Messung ermöglicht wurde, obwohl der anfängliche pH-Wert der Lösung 7,4 betrug. Um eine Langzeitmessung zu ermöglichen, wurde eine elektrochemische Reinigung der Katalysatoroberfläche nach jeder Messung eingeführt. Nach der Optimierung (i) der lokalen pH-Vorbehandlung, (ii) der Katalysatorreinigung, (iii) der eigentlichen Messungsparameter und (iv) der Datenauswertung konnte Glucose selektiv in physiologisch relevanten Konzentrationen und mit einer Nachweisgrenze von $0,3 \pm 0,1$ mM bestimmt werden. Darüber hinaus wurde die Alterung der Elektroden untersucht, bei der mit voranschreitender Zeit die Hydrophobie zunimmt, welche den Kontakt zwischen Elektrode und Lösung verschlechtert. Diese Problematik wurde mit einer einfachen Inkubation einer Tween-20-Lösung vor der Messung behoben. Außerdem wurde die Leistung der Elektrode nach einer Sterilisation nicht beeinträchtigt und es wurde eine Signalausbeute der Glucose von 95 ± 10 % in verdünntem (20 % in PBS) menschlichen Serum erreicht.

Zuletzt wurden Nickel enthaltende Laser-induzierte Kohlenstoffnanofasern als 3-Elektrodensystem hergestellt (Kohlenstoffnanofasern wurden als Arbeits-, Gegen- und Referenzelektrode verwendet) und zur Detektion von Glukose in simuliertem Atem verwendet. Glukoselösungen mit Konzentrationen ähnlich denen in der Lungenflüssigkeit wurden mit Hilfe eines Inhalators vernebelt, auf den porösen Kohlenstoffnanofaser-Elektroden aufgefangen und elektrochemisch in einer NaOH-Lösung vermessen. Mit optimierten Herstellungs-, Glukosefang- und Messparametern wurde Glukose selektiv mithilfe von Cyclo Voltammetrie und einer ratiometrischen Datenauswertung detektiert. Um Schwankungen in der Lungenflüssigkeitskonzentration (die die Schwankungen des Blutzuckerspiegels widerspiegeln) zu simulieren, wurden Änderungen in der Konzentration der Inhalator-Lösung vorgenommen, welche nach auffangen und vermessen durch den Sensor unterschieden werden konnten.

9. References

- (1) Wild, S.; Roglic, G.; Green, A.; Sicree, R.; King, H. Global prevalence of diabetes: estimates for the year 2000 and projections for 2030. *Diabetes care* **2004**, *27* (5), 1047–1053. DOI: 10.2337/diacare.27.5.1047.
- (2) International Diabetes Federation. *Facts & figures*. <https://idf.org/about-diabetes/diabetes-facts-figures/> (accessed 2024-11-07).
- (3) Grand View Research. *Point Of Care Diagnostics Market Size, Share & Trends Analysis Report By Product (Infectious Diseases, Glucose Testing, Cardiac Markers), By End-use (Clinics, Home, Hospitals), By Region, And Segment Forecasts, 2024 - 2030*. <https://www.grandviewresearch.com/industry-analysis/point-of-care-poc-diagnostics-industry> (accessed 2024-11-07).
- (4) Liu, Y.; Luo, X.; Yu, Q.; Le Ye; Yang, L.; Cui, Y. Review of point-of-care platforms for diabetes: (1) sensing. *Sensors and Actuators Reports* **2022**, *4*, 100113. DOI: 10.1016/j.snr.2022.100113.
- (5) Toghill, K. E.; Compton, R. G. Electrochemical Non-enzymatic Glucose Sensors: A Perspective and an Evaluation. *International Journal of Electrochemical Science* **2010**, *5* (9), 1246–1301. DOI: 10.1016/S1452-3981(23)15359-4.
- (6) He, W.; Huang, Y.; Wu, J. Enzyme-Free Glucose Biosensors Based on MoS₂ Nanocomposites. *Nanoscale research letters* **2020**, *15* (1), 60. DOI: 10.1186/s11671-020-3285-3. Published Online: Mar. 12, 2020.
- (7) Lu, L.-M.; Li, H.-B.; Qu, F.; Zhang, X.-B.; Shen, G.-L.; Yu, R.-Q. In situ synthesis of palladium nanoparticle-graphene nanohybrids and their application in nonenzymatic glucose biosensors. *Biosensors & bioelectronics* **2011**, *26* (8), 3500–3504. DOI: 10.1016/j.bios.2011.01.033. Published Online: Feb. 2, 2011.
- (8) Zhang, Y.; Xiao, X.; Sun, Y.; Shi, Y.; Dai, H.; Ni, P.; Hu, J.; Li, Z.; Song, Y.; Wang, L. Electrochemical Deposition of Nickel Nanoparticles on Reduced Graphene Oxide Film for Nonenzymatic Glucose Sensing. *Electroanalysis* **2013**, *25* (4), 959–966. DOI: 10.1002/elan.201200479.
- (9) Kilic, N. M.; Singh, S.; Keles, G.; Cinti, S.; Kurbanoglu, S.; Odaci, D. Novel Approaches to Enzyme-Based Electrochemical Nanobiosensors. *Biosensors* **2023**, *13* (6). DOI: 10.3390/bios13060622. Published Online: Jun. 5, 2023.
- (10) Raziq, A.; Tariq, M.; Hussain, R.; Mehmood, M. H.; Khan, M. S.; Hassan, A. Electrochemical Investigation of Glucose Oxidation on a Glassy Carbon Electrode Using Voltammetric, Amperometric, and Digital Simulation Methods. *ChemistrySelect* **2017**, *2* (30), 9711–9717. DOI: 10.1002/slct.201701193.
- (11) Si, P.; Huang, Y.; Wang, T.; Ma, J. Nanomaterials for electrochemical non-enzymatic glucose biosensors. *RSC Adv.* **2013**, *3* (11), 3487. DOI: 10.1039/C2RA22360K.

(12) Zhou, C.; Feng, J.; Tian, Y.; Wu, Y.; He, Q.; Li, G.; Liu, J. Non-enzymatic electrochemical sensors based on nanomaterials for detection of organophosphorus pesticide residues. *Environ. Sci.: Adv.* **2023**, *2* (7), 933–956. DOI: 10.1039/D3VA00045A.

(13) Thatikayala, D.; Ponnamma, D.; Sadasivuni, K. K.; Cabibihan, J.-J.; Al-Ali, A. K.; Malik, R. A.; Min, B. Progress of Advanced Nanomaterials in the Non-Enzymatic Electrochemical Sensing of Glucose and H₂O₂. *Biosensors* **2020**, *10* (11). DOI: 10.3390/bios10110151. Published Online: Oct. 22, 2020.

(14) He, J.; Xu, X.; Li, M.; Zhou, S.; Zhou, W. Recent advances in perovskite oxides for non-enzymatic electrochemical sensors: A review. *Analytica chimica acta* **2023**, *1251*, 341007. DOI: 10.1016/j.aca.2023.341007. Published Online: Feb. 25, 2023.

(15) Govindaraj, M.; Srivastava, A.; Muthukumaran, M. K.; Tsai, P.-C.; Lin, Y.-C.; Raja, B. K.; Rajendran, J.; Ponnusamy, V. K.; Arockia Selvi, J. Current advancements and prospects of enzymatic and non-enzymatic electrochemical glucose sensors. *International journal of biological macromolecules* **2023**, *253* (Pt 2), 126680. DOI: 10.1016/j.ijbiomac.2023.126680. Published Online: Sep. 4, 2023.

(16) Panahi, Z.; Custer, L.; Halpern, J. M. Recent advances in non-enzymatic electrochemical detection of hydrophobic metabolites in biofluids. *Sensors and Actuators Reports* **2021**, *3*, 100051. DOI: 10.1016/j.snr.2021.100051.

(17) Liu, Y.; Liu, T.; Jiang, D. Non-enzymatic electrochemical sensor for wearable monitoring of sweat biomarkers: A mini-review. *Current Research in Biotechnology* **2023**, *6*, 100143. DOI: 10.1016/j.crbiot.2023.100143.

(18) Hassan, M. H.; Vyas, C.; Grieve, B.; Bartolo, P. Recent Advances in Enzymatic and Non-Enzymatic Electrochemical Glucose Sensing. *Sensors (Basel, Switzerland)* **2021**, *21* (14). DOI: 10.3390/s21144672. Published Online: Jul. 8, 2021.

(19) Simsek, M.; Wongkaew, N. Carbon nanomaterial hybrids via laser writing for high-performance non-enzymatic electrochemical sensors: a critical review. *Analytical and bioanalytical chemistry* **2021**, *413* (24), 6079–6099. DOI: 10.1007/s00216-021-03382-9. Published Online: May. 12, 2021.

(20) González Fá, A. J.; Orazi, V.; González, E. A.; Juan, A.; López-Corral, I. DFT study of β-d-glucose adsorption on single-walled carbon nanotubes decorated with platinum. A bonding analysis. *Applied Surface Science* **2017**, *423*, 542–548. DOI: 10.1016/j.apsusc.2017.05.227.

(21) Wang, S.-S.; Qiu, W.-J.; Wang, T.-P.; Lee, C.-L. Tuning structures of Pt shells on Pd nanocubes as neutral glucose oxidation catalysts and sensors. *Applied Surface Science* **2022**, *605*, 154670. DOI: 10.1016/j.apsusc.2022.154670.

(22) Burke, L. D. Premonolayer oxidation and its role in electrocatalysis. *Electrochimica Acta* **1994**, *39* (11-12), 1841–1848. DOI: 10.1016/0013-4686(94)85173-5.

(23) Pletcher, D. Electrocatalysis: present and future. *J Appl Electrochem* **1984**, *14* (4), 403–415. DOI: 10.1007/BF00610805.

(24) Simsek, M.; Hoecherl, K.; Schlosser, M.; Baeumner, A. J.; Wongkaew, N. Printable 3D Carbon Nanofiber Networks with Embedded Metal Nanocatalysts. *ACS applied materials & interfaces* **2020**, *12* (35), 39533–39540. DOI: 10.1021/acsami.0c08926. Published Online: Aug. 19, 2020.

(25) Shi, Y.; Ma, Z.-R.; Xiao, Y.-Y.; Yin, Y.-C.; Huang, W.-M.; Huang, Z.-C.; Zheng, Y.-Z.; Mu, F.-Y.; Huang, R.; Shi, G.-Y.; Sun, Y.-Y.; Xia, X.-H.; Chen, W. Electronic metal-support interaction modulates single-atom platinum catalysis for hydrogen evolution reaction. *Nature communications* **2021**, *12* (1), 3021. DOI: 10.1038/s41467-021-23306-6. Published Online: May. 21, 2021.

(26) Kaliyaraj Selva Kumar, A.; Zhang, Y.; Li, D.; Compton, R. G. A mini-review: How reliable is the drop casting technique? *Electrochemistry Communications* **2020**, *121*, 106867. DOI: 10.1016/j.elecom.2020.106867.

(27) Yu, X.; Xing, R.; Peng, Z.; Lin, Y.; Du, Z.; Ding, J.; Wang, L.; Han, Y. To inhibit coffee ring effect in inkjet printing of light-emitting polymer films by decreasing capillary force. *Chinese Chemical Letters* **2019**, *30* (1), 135–138. DOI: 10.1016/j.cclet.2018.09.007.

(28) *Inkjet Printing of Well-Defined Polymer Dots and Arrays*. DOI: 10.1021/la049469o.s001.

(29) Ko, H.-Y.; Park, J.; Shin, H.; Moon, J. Rapid Self-Assembly of Monodisperse Colloidal Spheres in an Ink-Jet Printed Droplet. *Chem. Mater.* **2004**, *16* (22), 4212–4215. DOI: 10.1021/cm035256t.

(30) Eral, H. B.; Augustine, D. M.; Duits, M. H. G.; Mugele, F. Suppressing the coffee stain effect: how to control colloidal self-assembly in evaporating drops using electrowetting. *Soft Matter* **2011**, *7* (10), 4954. DOI: 10.1039/C1SM05183K.

(31) Yunker, P. J.; Still, T.; Lohr, M. A.; Yodh, A. G. Suppression of the coffee-ring effect by shape-dependent capillary interactions. *Nature* **2011**, *476* (7360), 308–311. DOI: 10.1038/nature10344. Published Online: Aug. 17, 2011.

(32) Mampallil, D.; Reboud, J.; Wilson, R.; Wylie, D.; Klug, D. R.; Cooper, J. M. Acoustic suppression of the coffee-ring effect. *Soft Matter* **2015**, *11* (36), 7207–7213. DOI: 10.1039/C5SM01196E. Published Online: Aug. 12, 2015.

(33) Hu, H.; Larson, R. G. Marangoni effect reverses coffee-ring depositions. *The journal of physical chemistry. B* **2006**, *110* (14), 7090–7094. DOI: 10.1021/jp0609232.

(34) Kawakami, H.; Ito, Y.; Chien, Y.-A.; Chen, C.-Y.; Chiu, W.-T.; Chakraborty, P.; Nakamoto, T.; Sone, M.; Chang, T.-F. M. Development of polypyrrole/nano-gold composite for non-enzymatic glucose sensors. *Micro and Nano Engineering* **2022**, *14*, 100109. DOI: 10.1016/j.mne.2022.100109.

(35) Shu, H.; Cao, L.; Chang, G.; He, H.; Zhang, Y.; He, Y. Direct Electrodeposition of Gold Nanostructures onto Glassy Carbon Electrodes for Non-enzymatic Detection of Glucose. *Electrochimica Acta* **2014**, *132*, 524–532. DOI: 10.1016/j.electacta.2014.04.031.

(36) Viswanathan, P.; Kim, J. W.; Manivannan, S.; Kim, K. Methionine-assisted electrodeposition of porous copper cobalt bi-metallic hetero-nanostructures on an indium tin oxide electrode: a disposable and stable electrode for non-enzymatic glucose sensing. *J. Mater. Chem. C* **2024**, *12* (21), 7673–7683. DOI: 10.1039/d4tc00079j.

(37) Suresh, R. R.; Lakshmanakumar, M.; Arockia Jayalatha, J. B. B.; Rajan, K. S.; Sethuraman, S.; Krishnan, U. M.; Rayappan, J. B. B. Fabrication of screen-printed electrodes: opportunities and challenges. *J Mater Sci* **2021**, *56* (15), 8951–9006. DOI: 10.1007/s10853-020-05499-1.

(38) Su, W.-Y.; Wang, S.-M.; Cheng, S.-H. Electrochemically pretreated screen-printed carbon electrodes for the simultaneous determination of aminophenol isomers. *Journal of Electroanalytical Chemistry* **2011**, *651* (2), 166–172. DOI: 10.1016/j.jelechem.2010.11.028.

(39) Antuña-Jiménez, D.; González-García, M. B.; Hernández-Santos, D.; Fanjul-Bolado, P. Screen-Printed Electrodes Modified with Metal Nanoparticles for Small Molecule Sensing. *Biosensors* **2020**, *10* (2). DOI: 10.3390/bios10020009. Published Online: Feb. 1, 2020.

(40) Chu, Z.; Peng, J.; Jin, W. Advanced nanomaterial inks for screen-printed chemical sensors. *Sensors and Actuators B: Chemical* **2017**, *243*, 919–926. DOI: 10.1016/j.snb.2016.12.022.

(41) Yin, W.; Lee, D.-H.; Choi, J.; Park, C.; Cho, S. M. Screen printing of silver nanoparticle suspension for metal interconnects. *Korean J. Chem. Eng.* **2008**, *25* (6), 1358–1361. DOI: 10.1007/s11814-008-0223-y.

(42) Abdolhosseinzadeh, S.; Schneider, R.; Verma, A.; Heier, J.; Nüesch, F.; Zhang, C. J. Turning Trash into Treasure: Additive Free MXene Sediment Inks for Screen-Printed Micro-Supercapacitors. *Advanced materials (Deerfield Beach, Fla.)* **2020**, *32* (17), e2000716. DOI: 10.1002/adma.202000716. Published Online: Mar. 20, 2020.

(43) Romeo, A.; Moya, A.; Leung, T. S.; Gabriel, G.; Villa, R.; Sánchez, S. Inkjet printed flexible non-enzymatic glucose sensor for tear fluid analysis. *Applied Materials Today* **2018**, *10*, 133–141. DOI: 10.1016/j.apmt.2017.12.016.

(44) Sundriyal, P.; Bhattacharya, S. Inkjet-Printed Electrodes on A4 Paper Substrates for Low-Cost, Disposable, and Flexible Asymmetric Supercapacitors. *ACS applied materials & interfaces* **2017**, *9* (44), 38507–38521. DOI: 10.1021/acsami.7b11262. Published Online: Oct. 24, 2017.

(45) Hussain, A.; Abbas, N.; Ali, A. Inkjet Printing: A Viable Technology for Biosensor Fabrication. *Chemosensors* **2022**, *10* (3), 103. DOI: 10.3390/chemosensors10030103.

(46) Ooi, Y.; Hanasaki, I.; Mizumura, D.; Matsuda, Y. Suppressing the coffee-ring effect of colloidal droplets by dispersed cellulose nanofibers. *Science and technology of advanced materials* **2017**, *18* (1), 316–324. DOI: 10.1080/14686996.2017.1314776. Published Online: May. 9, 2017.

(47) Zhao, B.; Lu, M.; Wang, Z.; Jiao, Z.; Hu, P.; Gao, Q.; Jiang, Y.; Cheng, L. Self-assembly of ultrathin MnO₂/graphene with three-dimension hierarchical structure by ultrasonic-assisted co-precipitation method. *Journal of Alloys and Compounds* **2016**, *663*, 180–186. DOI: 10.1016/j.jallcom.2015.12.018.

(48) Shamkhalichenar, H.; Choi, J.-W. An Inkjet-Printed Non-Enzymatic Hydrogen Peroxide Sensor on Paper. *J. Electrochem. Soc.* **2017**, *164* (5), B3101-B3106. DOI: 10.1149/2.0161705jes.

(49) Ahmad, R.; Vaseem, M.; Tripathy, N.; Hahn, Y.-B. Wide linear-range detecting nonenzymatic glucose biosensor based on CuO nanoparticles inkjet-printed on electrodes. *Anal. Chem.* **2013**, *85* (21), 10448–10454. DOI: 10.1021/ac402925r. Published Online: Oct. 10, 2013.

(50) Uzun, S.; Schelling, M.; Hantanasirisakul, K.; Mathis, T. S.; Askeland, R.; Dion, G.; Gogotsi, Y. Additive-Free Aqueous MXene Inks for Thermal Inkjet Printing on Textiles. *Small* **2021**, *17* (1). DOI: 10.1002/smll.202006376.

(51) Pradela-Filho, L. A.; Araújo, D. A. G.; Ataide, V. N.; Meloni, G. N.; Paixão, T. R. L. C. Challenges faced with 3D-printed electrochemical sensors in analytical applications. *Analytical and bioanalytical chemistry* **2024**, *416* (21), 4679–4690. DOI: 10.1007/s00216-024-05308-7. Published Online: Apr. 26, 2024.

(52) Rocha, R. G.; Cardoso, R. M.; Zambiasi, P. J.; Castro, S. V. F.; Ferraz, T. V. B.; Aparecido, G. d. O.; Bonacin, J. A.; Munoz, R. A. A.; Richter, E. M. Production of 3D-printed disposable electrochemical sensors for glucose detection using a conductive filament modified with nickel microparticles. *Analytica chimica acta* **2020**, *1132*, 1–9. DOI: 10.1016/j.aca.2020.07.028. Published Online: Jul. 30, 2020.

(53) Bariya, M.; Shahpar, Z.; Park, H.; Sun, J.; Jung, Y.; Gao, W.; Nyein, H. Y. Y.; Liaw, T. S.; Tai, L.-C.; Ngo, Q. P.; Chao, M.; Zhao, Y.; Hettick, M.; Cho, G.; Javey, A. Roll-to-Roll Gravure Printed Electrochemical Sensors for Wearable and Medical Devices. *ACS nano* **2018**, *12* (7), 6978–6987. DOI: 10.1021/acsnano.8b02505. Published Online: Jun. 25, 2018.

(54) Cagnani, G. R.; Ibáñez-Redín, G.; Tirich, B.; Gonçalves, D.; Balogh, D. T.; Oliveira, O. N. Fully-printed electrochemical sensors made with flexible screen-printed electrodes modified by roll-to-roll slot-die coating. *Biosensors & bioelectronics* **2020**, *165*, 112428. DOI: 10.1016/j.bios.2020.112428. Published Online: Jul. 4, 2020.

(55) Ibáñez-Redín, G.; Rosso Cagnani, G.; O Gomes, N.; Raymundo-Pereira, P. A.; S Machado, S. A.; Gutierrez, M. A.; Krieger, J. E.; Oliveira, O. N. Wearable potentiometric biosensor for analysis of urea in sweat. *Biosensors & bioelectronics* **2023**, *223*, 114994. DOI: 10.1016/j.bios.2022.114994. Published Online: Dec. 15, 2022.

(56) Chawang, K.; Bing, S.; Chiao, J.-C. Printable and Flexible Iridium Oxide-Based pH Sensor by a Roll-to-Roll Process. *Chemosensors* **2023**, *11* (5), 267. DOI: 10.3390/chemosensors11050267.

(57) Fung, C. M.; Lloyd, J. S.; Samavat, S.; Deganello, D.; Teng, K. S. Facile fabrication of electrochemical ZnO nanowire glucose biosensor using roll to roll printing technique. *Sensors and Actuators B: Chemical* **2017**, *247*, 807–813. DOI: 10.1016/j.snb.2017.03.105.

(58) Ye, R.; Peng, Z.; Wang, T.; Xu, Y.; Zhang, J.; Li, Y.; Nilewski, L. G.; Lin, J.; Tour, J. M. In Situ Formation of Metal Oxide Nanocrystals Embedded in Laser-Induced Graphene. *ACS nano* **2015**, *9* (9), 9244–9251. DOI: 10.1021/acsnano.5b04138. Published Online: Aug. 25, 2015.

(59) Fan, L.; Wu, R.; Patel, V.; Huang, J. J.; Selvaganapathy, P. R. Solid-state, reagent-free and one-step laser-induced synthesis of graphene-supported metal nanocomposites from metal leaves and

application to glucose sensing. *Analytica chimica acta* **2023**, *1264*, 341248. DOI: 10.1016/j.aca.2023.341248. Published Online: Apr. 22, 2023.

(60) Zhang, Y.; Zhang, C.; Chen, W.; Liu, Z. One-step laser-induced Cu-embedded graphene for non-enzymatic glucose sensing in beverages. *Journal of Alloys and Compounds* **2024**, *992*, 174563. DOI: 10.1016/j.jallcom.2024.174563.

(61) Zhao, J.; Zheng, C.; Gao, J.; Gui, J.; Deng, L.; Wang, Y.; Xu, R. Co₃O₄ nanoparticles embedded in laser-induced graphene for a flexible and highly sensitive enzyme-free glucose biosensor. *Sensors and Actuators B: Chemical* **2021**, *347*, 130653. DOI: 10.1016/j.snb.2021.130653.

(62) Wongkaew, N.; Simsek, M.; Arumugam, P.; Behrent, A.; Berchmans, S.; Baeumner, A. J. A Robust strategy enabling addressable porous 3D carbon-based functional nanomaterials in miniaturized systems. *Nanoscale* **2019**, *11* (8), 3674–3680. DOI: 10.1039/C8NR09232J.

(63) Bruckschlegel, C.; Schlosser, M.; Wongkaew, N. Investigating nanocatalyst-embedding laser-induced carbon nanofibers for non-enzymatic electrochemical sensing of hydrogen peroxide. *Analytical and bioanalytical chemistry* **2023**, *415* (18), 4487–4499. DOI: 10.1007/s00216-023-04640-8. Published Online: Mar. 18, 2023.

(64) Scroccarello, A.; Álvarez-Diduk, R.; Della Pelle, F.; Carvalho Castro E Silva, C. de; Idili, A.; Parolo, C.; Compagnone, D.; Merkoçi, A. One-Step Laser Nanostructuration of Reduced Graphene Oxide Films Embedding Metal Nanoparticles for Sensing Applications. *ACS sensors* **2023**, *8* (2), 598–609. DOI: 10.1021/acssensors.2c01782. Published Online: Feb. 3, 2023.

(65) Leanne Riley. *Mean fasting blood glucose*. <https://www.who.int/data/gho/indicator-metadata-registry/imr-details/2380> (accessed 2024-11-09).

(66) Patel, B. A. *Electrochemistry for Bioanalysis*; Elsevier, 2021.

(67) Mackay, E. M.; Mackay, L. L. THE CONCENTRATION OF UREA IN THE BLOOD OF NORMAL INDIVIDUALS. *The Journal of clinical investigation* **1927**, *4* (2), 295–306. DOI: 10.1172/JCI100124.

(68) Labib, M.; Sargent, E. H.; Kelley, S. O. Electrochemical Methods for the Analysis of Clinically Relevant Biomolecules. *Chemical reviews* **2016**, *116* (16), 9001–9090. DOI: 10.1021/acs.chemrev.6b00220. Published Online: Jul. 18, 2016.

(69) Ma, Y.; Ma, C.; Wang, Y.; Wang, K. Advanced Nickel-Based Catalysts for Urea Oxidation Reaction: Challenges and Developments. *Catalysts* **2022**, *12* (3), 337. DOI: 10.3390/catal12030337.

(70) Kim, S.; Kim, K.; Kim, H.-J.; Lee, H.-N.; Park, T. J.; Park, Y. M. Non-enzymatic electrochemical lactate sensing by NiO and Ni(OH)₂ electrodes: A mechanistic investigation. *Electrochimica Acta* **2018**, *276*, 240–246. DOI: 10.1016/j.electacta.2018.04.172.

(71) Glynn, R. J.; Campion, E. W.; Silbert, J. E. Trends in serum uric acid levels 1961--1980. *Arthritis and rheumatism* **1983**, *26* (1), 87–93. DOI: 10.1002/art.1780260115.

(72) Butler, A. M.; Cushman, M. DISTRIBUTION OF ASCORBIC ACID IN THE BLOOD AND ITS NUTRITIONAL SIGNIFICANCE. *The Journal of clinical investigation* **1940**, *19* (3), 459–467. DOI: 10.1172/JCI101147.

(73) Lindblad, M.; Tveden-Nyborg, P.; Lykkesfeldt, J. Regulation of vitamin C homeostasis during deficiency. *Nutrients* **2013**, *5* (8), 2860–2879. DOI: 10.3390/nu5082860. Published Online: Jul. 25, 2013.

(74) Moran, J. P.; Cohen, L.; Greene, J. M.; Xu, G.; Feldman, E. B.; Hames, C. G.; Feldman, D. S. Plasma ascorbic acid concentrations relate inversely to blood pressure in human subjects. *The American journal of clinical nutrition* **1993**, *57* (2), 213–217. DOI: 10.1093/ajcn/57.2.213.

(75) Seki, M. Biological significance and development of practical synthesis of biotin. *Medicinal research reviews* **2006**, *26* (4), 434–482. DOI: 10.1002/med.20058.

(76) Weinstein, S. J., Hartman, T. J., Stolzenberg-Solomon, R., Pietinen, P., Barrett, M. J., Taylor, P. R., Virtamo, J., & Albanes, D. Null Association between Prostate Cancer and Serum Folate, Vitamin B 6, Vitamin B12, and Homocysteine **2003** (12(11 II)), 1271–1272.

(77) Revin, S. B.; John, S. A. Simultaneous determination of vitamins B2, B9 and C using a heterocyclic conducting polymer modified electrode. *Electrochimica Acta* **2012**, *75*, 35–41. DOI: 10.1016/j.electacta.2012.04.056.

(78) Perju, A.; Baeumner, A. J.; Wongkaew, N. Freestanding 3D-interconnected carbon nanofibers as high-performance transducers in miniaturized electrochemical sensors. *Mikrochimica acta* **2022**, *189* (11), 424. DOI: 10.1007/s00604-022-05492-2. Published Online: Oct. 18, 2022.

(79) Baldrich, E.; Muñoz, F. X. Carbon nanotube wiring: a tool for straightforward electrochemical biosensing at magnetic particles. *Anal. Chem.* **2011**, *83* (24), 9244–9250. DOI: 10.1021/ac201137q. Published Online: Nov. 11, 2011.

(80) Lin, S.; Liu, C.-C.; Chou, T.-C. Amperometric acetylcholine sensor catalyzed by nickel anode electrode. *Biosensors & bioelectronics* **2004**, *20* (1), 9–14. DOI: 10.1016/j.bios.2004.01.018.

(81) Peaston, R. T.; Weinkove, C. Measurement of catecholamines and their metabolites. *Annals of clinical biochemistry* **2004**, *41* (Pt 1), 17–38. DOI: 10.1258/000456304322664663.

(82) Eidenschink, J.; Bagherimetkazini, S.; Matysik, F.-M. Investigation of the electrochemical behavior of cysteine by hyphenation of electrochemistry and mass spectrometry. *Monatsh Chem* **2022**, *153* (9), 775–780. DOI: 10.1007/s00706-022-02943-7.

(83) McMENAMY, R. H.; LUND, C. C.; ONCLEY, J. L. Unbound amino acid concentrations in human blood plasmas. *The Journal of clinical investigation* **1957**, *36* (12), 1672–1679. DOI: 10.1172/JCI103568.

(84) Calabresi, L.; Gomaraschi, M.; Simonelli, S.; Bernini, F.; Franceschini, G. HDL and atherosclerosis: Insights from inherited HDL disorders. *Biochimica et biophysica acta* **2015**, *1851* (1), 13–18. DOI: 10.1016/j.bbapap.2014.07.015. Published Online: Jul. 25, 2014.

(85) Heikenfeld, J.; Jajack, A.; Feldman, B.; Granger, S. W.; Gaitonde, S.; Begtrup, G.; Katchman, B. A. Accessing analytes in biofluids for peripheral biochemical monitoring. *Nature biotechnology* **2019**, *37* (4), 407–419. DOI: 10.1038/s41587-019-0040-3. Published Online: Feb. 25, 2019.

(86) Scuffi, C. Interstitium versus Blood Equilibrium in Glucose Concentration and its Impact on Subcutaneous Continuous Glucose Monitoring Systems. *European endocrinology* **2014**, *10* (1), 36–42. DOI: 10.17925/EE.2014.10.01.36. Published Online: Feb. 28, 2014.

(87) Madden, J.; O'Mahony, C.; Thompson, M.; O'Riordan, A.; Galvin, P. Biosensing in dermal interstitial fluid using microneedle based electrochemical devices. *Sensing and Bio-Sensing Research* **2020**, *29*, 100348. DOI: 10.1016/j.sbsr.2020.100348.

(88) Patterson, M. J.; Galloway, S. D.; Nimmo, M. A. Variations in regional sweat composition in normal human males. *Experimental physiology* **2000**, *85* (6), 869–875. DOI: 10.1111/j.1469-445x.2000.02058.x.

(89) ROBINSON, S.; ROBINSON, A. H. Chemical composition of sweat. *Physiological reviews* **1954**, *34* (2), 202–220. DOI: 10.1152/physrev.1954.34.2.202.

(90) Hauke, A.; Simmers, P.; Ojha, Y. R.; Cameron, B. D.; Ballweg, R.; Zhang, T.; Twine, N.; Brothers, M.; Gomez, E.; Heikenfeld, J. Complete validation of a continuous and blood-correlated sweat biosensing device with integrated sweat stimulation. *Lab on a chip* **2018**, *18* (24), 3750–3759. DOI: 10.1039/c8lc01082j.

(91) La Count, T. D.; Jajack, A.; Heikenfeld, J.; Kasting, G. B. Modeling Glucose Transport From Systemic Circulation to Sweat. *Journal of pharmaceutical sciences* **2019**, *108* (1), 364–371. DOI: 10.1016/j.xphs.2018.09.026. Published Online: Sep. 28, 2018.

(92) Moyer, J.; Wilson, D.; Finkelshtein, I.; Wong, B.; Potts, R. Correlation between sweat glucose and blood glucose in subjects with diabetes. *Diabetes technology & therapeutics* **2012**, *14* (5), 398–402. DOI: 10.1089/dia.2011.0262. Published Online: Feb. 29, 2012.

(93) Zafar, H.; Channa, A.; Jeoti, V.; Stojanović, G. M. Comprehensive Review on Wearable Sweat-Glucose Sensors for Continuous Glucose Monitoring. *Sensors (Basel, Switzerland)* **2022**, *22* (2). DOI: 10.3390/s22020638. Published Online: Jan. 14, 2022.

(94) Lee, H.; Hong, Y. J.; Baik, S.; Hyeon, T.; Kim, D.-H. Enzyme-Based Glucose Sensor: From Invasive to Wearable Device. *Advanced healthcare materials* **2018**, *7* (8), e1701150. DOI: 10.1002/adhm.201701150. Published Online: Jan. 15, 2018.

(95) Baker, L. B.; Wolfe, A. S. Physiological mechanisms determining eccrine sweat composition. *European journal of applied physiology* **2020**, *120* (4), 719–752. DOI: 10.1007/s00421-020-04323-7. Published Online: Mar. 2, 2020.

(96) Zhang, L.; Xie, S.; Gu, J.; Wang, X. Fabrication of core–shell Pt–Ni(OH)₂ nanosheets on Ni foam and investigation on its detection performance of ammonia–nitrogen in lake and sea water. *J Mater Sci: Mater Electron* **2023**, *34* (11). DOI: 10.1007/s10854-023-10386-x.

(97) Huang, C. T.; Chen, M. L.; Huang, L. L.; & Mao, I. F. Uric acid and urea in human sweat. *Chinese Journal of Physiology* **2002**, *45*(3), 109–116.

(98) García-Carmona, L.; Martín, A.; Sempionatto, J. R.; Moreto, J. R.; González, M. C.; Wang, J.; Escarpa, A. Pacifier Biosensor: Toward Noninvasive Saliva Biomarker Monitoring. *Anal. Chem.* **2019**, *91* (21), 13883–13891. DOI: 10.1021/acs.analchem.9b03379. Published Online: Oct. 14, 2019.

(99) Arakawa, T.; Kuroki, Y.; Nitta, H.; Chouhan, P.; Toma, K.; Sawada, S.-I.; Takeuchi, S.; Sekita, T.; Akiyoshi, K.; Minakuchi, S.; Mitsubayashi, K. Mouthguard biosensor with telemetry system for monitoring of saliva glucose: A novel cavitas sensor. *Biosensors & bioelectronics* **2016**, *84*, 106–111. DOI: 10.1016/j.bios.2015.12.014. Published Online: Dec. 11, 2015.

(100) Gupta, S.; Nayak, M. T.; Sunitha, J. D.; Dawar, G.; Sinha, N.; Rallan, N. S. Correlation of salivary glucose level with blood glucose level in diabetes mellitus. *Journal of oral and maxillofacial pathology : JOMFP* **2017**, *21* (3), 334–339. DOI: 10.4103/jomfp.JOMFP_222_15.

(101) Dhanya, M.; Hegde, S. Salivary glucose as a diagnostic tool in Type II diabetes mellitus: A case-control study. *Nigerian journal of clinical practice* **2016**, *19* (4), 486–490. DOI: 10.4103/1119-3077.183314.

(102) Zhang, W.; Du, Y.; Wang, M. L. On-chip highly sensitive saliva glucose sensing using multilayer films composed of single-walled carbon nanotubes, gold nanoparticles, and glucose oxidase. *Sensing and Bio-Sensing Research* **2015**, *4*, 96–102. DOI: 10.1016/j.sbsr.2015.04.006.

(103) Jaiswal, A.; Madaan, S.; Acharya, N.; Kumar, S.; Talwar, D.; Dewani, D. Salivary Uric Acid: A Noninvasive Wonder for Clinicians? *Cureus* **2021**, *13* (11), e19649. DOI: 10.7759/cureus.19649. Published Online: Nov. 16, 2021.

(104) Temilola, D. O.; Bezuidenhout, K.; Erasmus, R. T.; Stephen, L.; Davids, M. R.; Holmes, H. Salivary creatinine as a diagnostic tool for evaluating patients with chronic kidney disease. *BMC nephrology* **2019**, *20* (1), 387. DOI: 10.1186/s12882-019-1546-0. Published Online: Oct. 29, 2019.

(105) Eom, K. S.; Lee, Y. J.; Seo, H. W.; Kang, J. Y.; Shim, J. S.; Lee, S. H. Sensitive and non-invasive cholesterol determination in saliva via optimization of enzyme loading and platinum nano-cluster composition. *The Analyst* **2020**, *145* (3), 908–916. DOI: 10.1039/C9AN01679A.

(106) Shruthi, D. K.; Channabasappa, S. M.; Mithun, K. M.; Suresh, B. S.; Tegginamani, A. S.; Smitha, T. The Role of Salivary Lactate Levels in assessing the Severity of Septic Shock. *Journal of oral and maxillofacial pathology : JOMFP* **2021**, *25* (3), 437–440. DOI: 10.4103/jomfp.jomfp_199_21. Published Online: Jan. 11, 2022.

(107) Cardoso, A. G.; Viltres, H.; Ortega, G. A.; Phung, V.; Grewal, R.; Mozaffari, H.; Ahmed, S. R.; Rajabzadeh, A. R.; Srinivasan, S. Electrochemical sensing of analytes in saliva: Challenges, progress, and perspectives. *TrAC Trends in Analytical Chemistry* **2023**, *160*, 116965. DOI: 10.1016/j.trac.2023.116965.

(108) Adeniyi, O.; Nwahara, N.; Mwanza, D.; Nyokong, T.; Mashazi, P. Nanohybrid electrocatalyst based on cobalt phthalocyanine–carbon nanotube-reduced graphene oxide for ultrasensitive detection

of glucose in human saliva. *Sensors and Actuators B: Chemical* **2021**, *348*, 130723. DOI: 10.1016/j.snb.2021.130723.

(109) Li, X.; Zhan, C.; Huang, Q.; He, M.; Yang, C.; Yang, C.; Huang, X.; Chen, M.; Xie, X.; Chen, H.-J. Smart Diaper Based on Integrated Multiplex Carbon Nanotube-Coated Electrode Array Sensors for In Situ Urine Monitoring. *ACS Appl. Nano Mater.* **2022**, *5* (4), 4767–4778. DOI: 10.1021/acsanm.1c04220.

(110) Sarigul, N.; Korkmaz, F.; Kurultak, İ. A New Artificial Urine Protocol to Better Imitate Human Urine. *Scientific reports* **2019**, *9* (1), 20159. DOI: 10.1038/s41598-019-56693-4. Published Online: Dec. 27, 2019.

(111) Chen, J.-C.; Kumar, A. S.; Chung, H.-H.; Chien, S.-H.; Kuo, M.-C.; Zen, J.-M. An enzymeless electrochemical sensor for the selective determination of creatinine in human urine. *Sensors and Actuators B: Chemical* **2006**, *115* (1), 473–480. DOI: 10.1016/j.snb.2005.10.015.

(112) Das, S.; Pal, M. Review—Non-Invasive Monitoring of Human Health by Exhaled Breath Analysis: A Comprehensive Review. *J. Electrochem. Soc.* **2020**, *167* (3), 37562. DOI: 10.1149/1945-7111/ab67a6.

(113) Maier, D.; Laubender, E.; Basavanna, A.; Schumann, S.; Güder, F.; Urban, G. A.; Dincer, C. Toward Continuous Monitoring of Breath Biochemistry: A Paper-Based Wearable Sensor for Real-Time Hydrogen Peroxide Measurement in Simulated Breath. *ACS sensors* **2019**, *4* (11), 2945–2951. DOI: 10.1021/acssensors.9b01403. Published Online: Oct. 25, 2019.

(114) Tankasala, D.; Linnes, J. C. Noninvasive glucose detection in exhaled breath condensate. *Translational research : the journal of laboratory and clinical medicine* **2019**, *213*, 1–22. DOI: 10.1016/j.trsl.2019.05.006. Published Online: May. 30, 2019.

(115) Sakumura, Y.; Koyama, Y.; Tokutake, H.; Hida, T.; Sato, K.; Itoh, T.; Akamatsu, T.; Shin, W. Diagnosis by Volatile Organic Compounds in Exhaled Breath from Lung Cancer Patients Using Support Vector Machine Algorithm. *Sensors (Basel, Switzerland)* **2017**, *17* (2). DOI: 10.3390/s17020287. Published Online: Feb. 4, 2017.

(116) Bloemen, K.; Lissens, G.; Desager, K.; Schoeters, G. Determinants of variability of protein content, volume and pH of exhaled breath condensate. *Respiratory medicine* **2007**, *101* (6), 1331–1337. DOI: 10.1016/j.rmed.2006.10.008. Published Online: Nov. 27, 2006.

(117) Hayes, S. A.; Haefliger, S.; Harris, B.; Pavlakis, N.; Clarke, S. J.; Molloy, M. P.; Howell, V. M. Exhaled breath condensate for lung cancer protein analysis: a review of methods and biomarkers. *Journal of breath research* **2016**, *10* (3), 34001. DOI: 10.1088/1752-7155/10/3/034001. Published Online: Jul. 5, 2016.

(118) European Environment Agency. *Industrial pollutant releases to water in Europe*. <https://www.eea.europa.eu/en/analysis/indicators/industrial-pollutant-releases-to-water?activeAccordion=546a7c35-9188-4d23-94ee-005d97c26f2b> (accessed 2024-11-10).

(119) Ilurdoz, M. S. de; Sadhwani, J. J.; Reboso, J. V. Antibiotic removal processes from water & wastewater for the protection of the aquatic environment - a review. *Journal of Water Process Engineering* **2022**, *45*, 102474. DOI: 10.1016/j.jwpe.2021.102474.

(120) Karthik, V.; Selvakumar, P.; Senthil Kumar, P.; Satheeskumar, V.; Godwin Vijaysunder, M.; Hariharan, S.; Antony, K. Recent advances in electrochemical sensor developments for detecting emerging pollutant in water environment. *Chemosphere* **2022**, *304*, 135331. DOI: 10.1016/j.chemosphere.2022.135331. Published Online: Jun. 13, 2022.

(121) Liu, Y.; Xue, Q.; Chang, C.; Wang, R.; Liu, Z.; He, L. Recent progress regarding electrochemical sensors for the detection of typical pollutants in water environments. *Analytical sciences : the international journal of the Japan Society for Analytical Chemistry* **2022**, *38* (1), 55–70. DOI: 10.2116/analsci.21SAR12. Published Online: Feb. 28, 2022.

(122) Cho, G.; Azzouzi, S.; Zucchi, G.; Lebental, B. Electrical and Electrochemical Sensors Based on Carbon Nanotubes for the Monitoring of Chemicals in Water-A Review. *Sensors (Basel, Switzerland)* **2021**, *22* (1). DOI: 10.3390/s22010218. Published Online: Dec. 29, 2021.

(123) Goodman, K. E.; Hua, T.; Sang, Q.-X. A. Effects of Polystyrene Microplastics on Human Kidney and Liver Cell Morphology, Cellular Proliferation, and Metabolism. *ACS omega* **2022**, *7* (38), 34136–34153. DOI: 10.1021/acsomega.2c03453. Published Online: Sep. 19, 2022.

(124) Altahan, M. F.; Ali, A. G.; Hathoot, A. A.; Azzem, M. A. Modified electrode decorated with silver as a novel non-enzymatic sensor for the determination of ammonium in water. *Scientific reports* **2023**, *13* (1), 16861. DOI: 10.1038/s41598-023-43616-7. Published Online: Oct. 6, 2023.

(125) Hossain, M. I.; Hasnat, M. A. Recent advancements in non-enzymatic electrochemical sensor development for the detection of organophosphorus pesticides in food and environment. *Helijon* **2023**, *9* (9), e19299. DOI: 10.1016/j.heliyon.2023.e19299. Published Online: Aug. 22, 2023.

(126) Manikandan, V. S.; Adhikari, B.; Chen, A. Nanomaterial based electrochemical sensors for the safety and quality control of food and beverages. *The Analyst* **2018**, *143* (19), 4537–4554. DOI: 10.1039/C8AN00497H.

(127) Capoferra, D.; Della Pelle, F.; Del Carlo, M.; Compagnone, D. Affinity Sensing Strategies for the Detection of Pesticides in Food. *Foods (Basel, Switzerland)* **2018**, *7* (9). DOI: 10.3390/foods7090148. Published Online: Sep. 5, 2018.

(128) Ferrari, A. G.-M.; Crapnell, R. D.; Banks, C. E. Electroanalytical Overview: Electrochemical Sensing Platforms for Food and Drink Safety. *Biosensors* **2021**, *11* (8). DOI: 10.3390/bios11080291. Published Online: Aug. 23, 2021.

(129) Fiori, S.; Scroccharello, A.; Della Pelle, F.; Del Carlo, M.; Compagnone, D. Integrated paper/graphene 3D pop-up device for the quantitative sensing of carbaryl. *Sensors and Actuators B: Chemical* **2024**, *399*, 134768. DOI: 10.1016/j.snb.2023.134768.

(130) Reardon, K. F. Practical monitoring technologies for cells and substrates in biomanufacturing. *Current opinion in biotechnology* **2021**, *71*, 225–230. DOI: 10.1016/j.copbio.2021.08.006. Published Online: Sep. 2, 2021.

(131) Eisenbrand, G., Ed. *Römpf-Lexikon Lebensmittelchemie*, 2., völlig überarb. und erw. Aufl.; Thieme, 2006.

(132) Campuzano, S.; Pedrero, M.; Yáñez-Sedeño, P.; Pingarrón, J. M. Antifouling (Bio)materials for Electrochemical (Bio)sensing. *International journal of molecular sciences* **2019**, *20* (2). DOI: 10.3390/ijms20020423. Published Online: Jan. 19, 2019.

(133) Lin, P.-H.; Li, B.-R. Antifouling strategies in advanced electrochemical sensors and biosensors. *The Analyst* **2020**, *145* (4), 1110–1120. DOI: 10.1039/c9an02017a.

(134) Saxena, S.; Sen, P.; Soleymani, L.; Hoare, T. Anti-Fouling Polymer or Peptide-Modified Electrochemical Biosensors for Improved Biosensing in Complex Media. *Advanced Sensor Research* **2024**, *3* (5). DOI: 10.1002/adsr.202300170.

(135) Song, G.; Han, H.; Ma, Z. Anti-Fouling Strategies of Electrochemical Sensors for Tumor Markers. *Sensors (Basel, Switzerland)* **2023**, *23* (11). DOI: 10.3390/s23115202. Published Online: May. 30, 2023.

(136) Zhou, L.; Li, X.; Zhu, B.; Su, B. An Overview of Antifouling Strategies for Electrochemical Analysis. *Electroanalysis* **2022**, *34* (6), 966–975. DOI: 10.1002/elan.202100406.

(137) Russo, M. J.; Han, M.; Desroches, P. E.; Manasa, C. S.; Dennaoui, J.; Quigley, A. F.; Kapsa, R. M. I.; Moulton, S. E.; Guijt, R. M.; Greene, G. W.; Silva, S. M. Antifouling Strategies for Electrochemical Biosensing: Mechanisms and Performance toward Point of Care Based Diagnostic Applications. *ACS sensors* **2021**, *6* (4), 1482–1507. DOI: 10.1021/acssensors.1c00390. Published Online: Mar. 25, 2021.

(138) Choi, Y.; Tran, H.-V.; Lee, T. R. Self-Assembled Monolayer Coatings on Gold and Silica Surfaces for Antifouling Applications: A Review. *Coatings* **2022**, *12* (10), 1462. DOI: 10.3390/coatings12101462.

(139) Moonla, C.; Reynoso, M.; Casanova, A.; Chang, A.-Y.; Djassemi, O.; Balaje, A.; Abbas, A.; Li, Z.; Mahato, K.; Wang, J. Continuous Ketone Monitoring via Wearable Microneedle Patch Platform. *ACS sensors* **2024**, *9* (2), 1004–1013. DOI: 10.1021/acssensors.3c02677. Published Online: Feb. 1, 2024.

(140) Shin, D.-S.; Matharu, Z.; You, J.; Siltanen, C.; Vu, T.; Raghunathan, V. K.; Stybayeva, G.; Hill, A. E.; Revzin, A. Sensing Conductive Hydrogels for Rapid Detection of Cytokines in Blood. *Advanced healthcare materials* **2016**, *5* (6), 659-64, 627. DOI: 10.1002/adhm.201500571. Published Online: Jan. 22, 2016.

(141) Zhu, X.; Zhai, Y.; Qin, X.; Ding, Y.; Wang, Y. An antifouling coating that enables electrochemical biosensing of MecA gene in complex samples. *Chemical Engineering Journal* **2024**, *483*, 148975. DOI: 10.1016/j.cej.2024.148975.

(142) Xi, Z.; Wei, K.; Wang, Q.; Kim, M. J.; Sun, S.; Fung, V.; Xia, X. Nickel-Platinum Nanoparticles as Peroxidase Mimics with a Record High Catalytic Efficiency. *Journal of the American Chemical Society* **2021**, *143* (7), 2660–2664. DOI: 10.1021/jacs.0c12605. Published Online: Jan. 27, 2021.

(143) Adeel, M.; Rahman, M. M.; Caligiuri, I.; Canzonieri, V.; Rizzolio, F.; Daniele, S. Recent advances of electrochemical and optical enzyme-free glucose sensors operating at physiological conditions. *Biosensors & bioelectronics* **2020**, *165*, 112331. DOI: 10.1016/j.bios.2020.112331. Published Online: May. 26, 2020.

(144) Shim, K.; Lee, W.-C.; Park, M.-S.; Shahabuddin, M.; Yamauchi, Y.; Hossain, M. S. A.; Shim, Y.-B.; Kim, J. H. Au decorated core-shell structured Au@Pt for the glucose oxidation reaction. *Sensors and Actuators B: Chemical* **2019**, *278*, 88–96. DOI: 10.1016/j.snb.2018.09.048.

(145) Mei, H.; Wu, H.; Wu, W.; Wang, S.; Xia, Q. Ultrasensitive electrochemical assay of hydrogen peroxide and glucose based on PtNi alloy decorated MWCNTs. *RSC Adv.* **2015**, *5* (124), 102877–102884. DOI: 10.1039/C5RA17410D.

(146) Zhu, J.; Liu, S.; Hu, Z.; Zhang, X.; Yi, N.; Tang, K.; Dexheimer, M. G.; Lian, X.; Wang, Q.; Yang, J.; Gray, J.; Cheng, H. Laser-induced graphene non-enzymatic glucose sensors for on-body measurements. *Biosensors & bioelectronics* **2021**, *193*, 113606. DOI: 10.1016/j.bios.2021.113606. Published Online: Sep. 1, 2021.

(147) Strakosas, X.; Selberg, J.; Pansodtee, P.; Yonas, N.; Manapongpun, P.; Teodorescu, M.; Rolandi, M. A non-enzymatic glucose sensor enabled by bioelectronic pH control. *Scientific reports* **2019**, *9* (1), 10844. DOI: 10.1038/s41598-019-46302-9. Published Online: Jul. 26, 2019.

(148) Zhu, X.; Ju, Y.; Chen, J.; Liu, D.; Liu, H. Nonenzymatic Wearable Sensor for Electrochemical Analysis of Perspiration Glucose. *ACS sensors* **2018**, *3* (6), 1135–1141. DOI: 10.1021/acssensors.8b00168. Published Online: May. 25, 2018.

(149) Dang, Y.; Guan, X.; Zhou, Y.; Hao, C.; Zhang, Y.; Chen, S.; Ma, Y.; Bai, Y.; Gong, Y.; Gao, Y. Biocompatible PB/Ti3C2 hybrid nanocomposites for the non-enzymatic electrochemical detection of H₂O₂ released from living cells. *Sensors and Actuators B: Chemical* **2020**, *319*, 128259. DOI: 10.1016/j.snb.2020.128259.

(150) Mosmann, T. Rapid colorimetric assay for cellular growth and survival: application to proliferation and cytotoxicity assays. *Journal of immunological methods* **1983**, *65* (1-2), 55–63. DOI: 10.1016/0022-1759(83)90303-4.

(151) Chen, Y.; Sun, Y.; Li, Y.; Wen, Z.; Peng, X.; He, Y.; Hou, Y.; Fan, J.; Zang, G.; Zhang, Y. A wearable non-enzymatic sensor for continuous monitoring of glucose in human sweat. *Talanta* **2024**, *278*, 126499. DOI: 10.1016/j.talanta.2024.126499. Published Online: Jul. 1, 2024.

(152) Fan, R.; Andrew, T. L. Perspective—Challenges in Developing Wearable Electrochemical Sensors for Longitudinal Health Monitoring. *J. Electrochem. Soc.* **2020**, *167* (3), 37542. DOI: 10.1149/1945-7111/ab67b0.

(153) Li, Z.; Wang, Y.; Kozbial, A.; Shenoy, G.; Zhou, F.; McGinley, R.; Ireland, P.; Morganstein, B.; Kunkel, A.; Surwade, S. P.; Li, L.; Liu, H. Effect of airborne contaminants on the wettability of supported graphene and graphite. *Nature materials* **2013**, *12* (10), 925–931. DOI: 10.1038/NMAT3709. Published Online: Jul. 21, 2013.

(154) Behrent, A.; Borggraef, V.; Baeumner, A. J. Laser-induced graphene trending in biosensors: understanding electrode shelf-life of this highly porous material. *Analytical and bioanalytical chemistry* **2024**, *416* (9), 2097–2106. DOI: 10.1007/s00216-023-05082-y. Published Online: Dec. 12, 2023.

(155) Zhang, L.; Wang, L.; Li, J.; Cui, C.; Zhou, Z.; Wen, L. Surface Engineering of Laser-Induced Graphene Enables Long-Term Monitoring of On-Body Uric Acid and pH Simultaneously. *Nano letters* **2022**, *22* (13), 5451–5458. DOI: 10.1021/acs.nanolett.2c01500. Published Online: Jun. 22, 2022.

(156) Beck, J. J.; Alenicheva, V.; Rahn, K. L.; Russo, M. J.; Baldo, T. A.; Henry, C. S. Evaluating the performance of an inexpensive, commercially available, NFC-powered and smartphone controlled potentiostat for electrochemical sensing. *Electroanalysis* **2023**, *35* (6). DOI: 10.1002/elan.202200552.

(157) Gonzalez-Macia, L.; Li, Y.; Zhang, K.; Nunez-Bajo, E.; Barandun, G.; Cotur, Y.; Asfour, T.; Olenik, S.; Coatsworth, P.; Herrington, J.; Güder, F. NFC-enabled potentiostat and nitrocellulose-based metal electrodes for electrochemical lateral flow assay. *Biosensors & bioelectronics* **2024**, *251*, 116124. DOI: 10.1016/j.bios.2024.116124. Published Online: Feb. 12, 2024.

(158) Krorakai, K.; Klangphukhiew, S.; Kulchat, S.; Patramanon, R. Smartphone-Based NFC Potentiostat for Wireless Electrochemical Sensing. *Applied Sciences* **2021**, *11* (1), 392. DOI: 10.3390/app11010392.

(159) Lathiya, P.; Wang, J. Near-Field Communications (NFC) for Wireless Power Transfer (WPT): An Overview. In *Wireless Power Transfer – Recent Development, Applications and New Perspectives*; Zellagui, M., Ed.; IntechOpen, 2021. DOI: 10.5772/intechopen.96345.

(160) Gu, Y.; Chen, C.-C. Eliminating the Interference of Oxygen for Sensing Hydrogen Peroxide with the Polyaniline Modified Electrode. *Sensors (Basel, Switzerland)* **2008**, *8* (12), 8237–8247. DOI: 10.3390/s8128237. Published Online: Dec. 12, 2008.

(161) Etienne, M.; Le, T. X. H.; Nasir, T.; Herzog, G. Electrochemical Filter To Remove Oxygen Interference Locally, Rapidly, and Temporarily for Sensing Applications. *Anal. Chem.* **2020**, *92* (11), 7425–7429. DOI: 10.1021/acs.analchem.0c00395. Published Online: May. 11, 2020.

(162) Giaretta, J. E.; Duan, H.; Oveissi, F.; Farajikhah, S.; Dehghani, F.; Naficy, S. Flexible Sensors for Hydrogen Peroxide Detection: A Critical Review. *ACS applied materials & interfaces* **2022**, *14* (18), 20491–20505. DOI: 10.1021/acsami.1c24727. Published Online: Apr. 29, 2022.

(163) Temoçin, Z. Designing of a stable and selective glucose biosensor by glucose oxidase immobilization on glassy carbon electrode sensitive to H₂O₂ via nanofiber interface. *J Appl Electrochem* **2021**, *51* (2), 283–293. DOI: 10.1007/s10800-020-01502-4.

(164) Kassal, P.; Kim, J.; Kumar, R.; Araujo, W. R. de; Steinberg, I. M.; Steinberg, M. D.; Wang, J. Smart bandage with wireless connectivity for uric acid biosensing as an indicator of wound status. *Electrochemistry Communications* **2015**, *56*, 6–10. DOI: 10.1016/j.elecom.2015.03.018.

(165) Ahmad, T.; Iqbal, A.; Halim, S. A.; Uddin, J.; Khan, A.; El Deeb, S.; Al-Harrasi, A. Recent Advances in Electrochemical Sensing of Hydrogen Peroxide (H₂O₂) Released from Cancer Cells. *Nanomaterials (Basel, Switzerland)* **2022**, *12* (9). DOI: 10.3390/nano12091475. Published Online: Apr. 26, 2022.

(166) Safaei, M. M.; Gravely, M.; Roxbury, D. A Wearable Optical Microfibrous Biomaterial with Encapsulated Nanosensors Enables Wireless Monitoring of Oxidative Stress. *Adv. Funct. Mater.* **2021**, *31* (13), 2006254. DOI: 10.1002/adfm.202006254.

(167) Klassen, N. V.; Marchington, D.; McGowan, H. C. H₂O₂ Determination by the I₃- Method and by KMnO₄ Titration. *Anal. Chem.* **1994**, *66* (18), 2921–2925. DOI: 10.1021/ac00090a020.

(168) Sunil, K.; Narayana, B. Spectrophotometric determination of hydrogen peroxide in water and cream samples. *Bulletin of environmental contamination and toxicology* **2008**, *81* (4), 422–426. DOI: 10.1007/s00128-008-9477-7. Published Online: Jul. 2, 2008.

(169) Şansal, Ü.; Somer, G. Detection of H₂O₂ in food samples by FTIR. *Food Chemistry* **1999**, *65* (2), 259–261. DOI: 10.1016/S0308-8146(98)00224-6.

(170) Su, J.; Zhang, S.; Wang, C.; Li, M.; Wang, J.; Su, F.; Wang, Z. MACA Fast and Efficient Method for Detecting H₂O₂ by a Dual-Locked Model Chemosensor. *ACS omega* **2021**, *6* (23), 14819–14823. DOI: 10.1021/acsomega.1c00384. Published Online: May. 28, 2021.

(171) Cooper, W. J.; Moegling, J. K.; Kieber, R. J.; Kiddie, J. J. A chemiluminescence method for the analysis of H₂O₂ in natural waters. *Marine Chemistry* **2000**, *70* (1-3), 191–200. DOI: 10.1016/S0304-4203(00)00025-6.

(172) Ali, M.; Tahir, M. N.; Siwy, Z.; Neumann, R.; Tremel, W.; Ensinger, W. Hydrogen peroxide sensing with horseradish peroxidase-modified polymer single conical nanochannels. *Anal. Chem.* **2011**, *83* (5), 1673–1680. DOI: 10.1021/ac102795a. Published Online: Feb. 4, 2011.

(173) Lin, J.; Peng, Z.; Liu, Y.; Ruiz-Zepeda, F.; Ye, R.; Samuel, E. L. G.; Yacaman, M. J.; Yakobson, B. I.; Tour, J. M. Laser-induced porous graphene films from commercial polymers. *Nature communications* **2014**, *5*, 5714. DOI: 10.1038/ncomms6714. Published Online: Dec. 10, 2014.

(174) Huang, L.; Su, J.; Song, Y.; Ye, R. Laser-Induced Graphene: En Route to Smart Sensing. *Nano-micro letters* **2020**, *12* (1), 157. DOI: 10.1007/s40820-020-00496-0. Published Online: Aug. 3, 2020.

(175) Deng, H.; Zhang, C.; Xie, Y.; Tumlin, T.; Giri, L.; Karna, S. P.; Lin, J. Laser induced MoS₂ /carbon hybrids for hydrogen evolution reaction catalysts. *J. Mater. Chem. A* **2016**, *4* (18), 6824–6830. DOI: 10.1039/C5TA09322H.

(176) Chhetry, A.; Sharifuzzaman, M.; Yoon, H.; Sharma, S.; Xuan, X.; Park, J. Y. MoS₂-Decorated Laser-Induced Graphene for a Highly Sensitive, Hysteresis-free, and Reliable Piezoresistive Strain

Sensor. *ACS applied materials & interfaces* **2019**, *11* (25), 22531–22542. DOI: 10.1021/acsami.9b04915. Published Online: Jun. 13, 2019.

(177) Rodrigues, J.; Zanoni, J.; Gaspar, G.; Fernandes, A. J. S.; Carvalho, A. F.; Santos, N. F.; Monteiro, T.; Costa, F. M. ZnO decorated laser-induced graphene produced by direct laser scribing. *Nanoscale advances* **2019**, *1* (8), 3252–3268. DOI: 10.1039/C8NA00391B. Published Online: Jul. 12, 2019.

(178) Sabzi, R. E.; Kant, K.; Losic, D. Electrochemical synthesis of nickel hexacyanoferrate nanoarrays with dots, rods and nanotubes morphology using a porous alumina template. *Electrochimica Acta* **2010**, *55* (5), 1829–1835. DOI: 10.1016/j.electacta.2009.10.075.

(179) Safavi, A.; Kazemi, S. H.; Kazemi, H. Electrochemically deposited hybrid nickel–cobalt hexacyanoferrate nanostructures for electrochemical supercapacitors. *Electrochimica Acta* **2011**, *56* (25), 9191–9196. DOI: 10.1016/j.electacta.2011.07.122.

(180) Yadav, M. D.; Dasgupta, K.; Kushwaha, A.; Srivastava, A. P.; Patwardhan, A. W.; Srivastava, D.; Joshi, J. B. Few layered graphene by floating catalyst chemical vapour deposition and its extraordinary H₂O₂ sensing property. *Materials Letters* **2017**, *199*, 180–183. DOI: 10.1016/j.matlet.2017.04.085.

(181) Liao, L. W.; Li, M. F.; Kang, J.; Chen, D.; Chen, Y.-X.; Ye, S. Electrode reaction induced pH change at the Pt electrode/electrolyte interface and its impact on electrode processes. *Journal of Electroanalytical Chemistry* **2013**, *688*, 207–215. DOI: 10.1016/j.jelechem.2012.08.031.

(182) Katsounaros, I.; Schneider, W. B.; Meier, J. C.; Benedikt, U.; Biedermann, P. U.; Auer, A. A.; Mayrhofer, K. J. J. Hydrogen peroxide electrochemistry on platinum: towards understanding the oxygen reduction reaction mechanism. *Physical chemistry chemical physics : PCCP* **2012**, *14* (20), 7384–7391. DOI: 10.1039/c2cp40616k. Published Online: Apr. 19, 2012.

(183) Li, X.; Heryadi, D.; Gewirth, A. A. Electroreduction activity of hydrogen peroxide on Pt and Au electrodes. *Langmuir : the ACS journal of surfaces and colloids* **2005**, *21* (20), 9251–9259. DOI: 10.1021/LA0508745.

(184) Peng, M.; Zhao, Y.; Chen, D.; Tan, Y. Free-Standing 3D Electrodes for Electrochemical Detection of Hydrogen Peroxide. *ChemCatChem* **2019**, *11* (17), 4222–4237. DOI: 10.1002/cctc.201900913.

(185) Xu, F.; Sun, Y.; Zhang, Y.; Shi, Y.; Wen, Z.; Li, Z. Graphene–Pt nanocomposite for nonenzymatic detection of hydrogen peroxide with enhanced sensitivity. *Electrochemistry Communications* **2011**, *13* (10), 1131–1134. DOI: 10.1016/j.elecom.2011.07.017.

(186) Sun, Y.; He, K.; Zhang, Z.; Zhou, A.; Duan, H. Real-time electrochemical detection of hydrogen peroxide secretion in live cells by Pt nanoparticles decorated graphene–carbon nanotube hybrid paper electrode. *Biosensors & bioelectronics* **2015**, *68*, 358–364. DOI: 10.1016/j.bios.2015.01.017.

Published Online: Jan. 8, 2015.

(187) Tajabadi, M. T.; Sookhakian, M.; Zalnezhad, E.; Yoon, G. H.; Hamouda, A.; Azarang, M.; Basirun, W. J.; Alias, Y. Electrodeposition of flower-like platinum on electrophoretically grown nitrogen-doped graphene as a highly sensitive electrochemical non-enzymatic biosensor for hydrogen peroxide detection. *Applied Surface Science* **2016**, *386*, 418–426. DOI: 10.1016/j.apsusc.2016.06.045.

(188) Yang, Y.; Fu, R.; Yuan, J.; Wu, S.; Zhang, J.; Wang, H. Highly sensitive hydrogen peroxide sensor based on a glassy carbon electrode modified with platinum nanoparticles on carbon nanofiber heterostructures. *Microchim Acta* **2015**, *182* (13-14), 2241–2249. DOI: 10.1007/s00604-015-1558-9.

(189) Han, K. N.; Li, C. A.; Bui, M.-P. N.; Pham, X.-H.; Kim, B. S.; Choa, Y. H.; Seong, G. H. Development of Pt/TiO₂ nanohybrids-modified SWCNT electrode for sensitive hydrogen peroxide detection. *Sensors and Actuators B: Chemical* **2012**, *174*, 406–413. DOI: 10.1016/j.snb.2012.08.066.

(190) Sahin, O. G. Microwave-assisted synthesis of PtAu@C based bimetallic nanocatalysts for non-enzymatic H₂O₂ sensor. *Electrochimica Acta* **2015**, *180*, 873–878. DOI: 10.1016/j.electacta.2015.09.015.

(191) Chou, T.-C.; Wu, K.-Y.; Hsu, F.-X.; Lee, C.-K. Pt-MWCNT modified carbon electrode strip for rapid and quantitative detection of H₂O₂ in food. *Journal of food and drug analysis* **2018**, *26* (2), 662–669. DOI: 10.1016/j.jfda.2017.08.005. Published Online: Sep. 23, 2017.

(192) Shang, N. G.; Papakonstantinou, P.; McMullan, M.; Chu, M.; Stamboulis, A.; Potenza, A.; Dhesi, S. S.; Marchetto, H. Catalyst-Free Efficient Growth, Orientation and Biosensing Properties of Multilayer Graphene Nanoflake Films with Sharp Edge Planes. *Adv. Funct. Mater.* **2008**, *18* (21), 3506–3514. DOI: 10.1002/adfm.200800951.

(193) Maksuk, C.; Tinala, C.; Somboot, W.; Jakmunee, J.; Marken, F.; Kanyanee, T. Rapid Determination of Hydrogen Peroxide in Milk with Non-enzymatic Amperometric Sensor Based on Porous Gold Modified Screen-printed Electrode in Online Dialysis System. *Electroanalysis* **2022**. DOI: 10.1002/elan.202100691.

(194) Ribeiro, J. A.; Fernandes, P. M. V.; Pereira, C. M.; Silva, F. Electrochemical sensors and biosensors for determination of catecholamine neurotransmitters: A review. *Talanta* **2016**, *160*, 653–679. DOI: 10.1016/j.talanta.2016.06.066. Published Online: Jul. 1, 2016.

(195) Chen, X.; Noy, A. Antifouling strategies for protecting bioelectronic devices. *APL Materials* **2021**, *9* (2), 20701. DOI: 10.1063/5.0029994.

(196) Wang, X.; Zhang, H.; Wang, E.; Han, Z.; Hu, C. Phosphomolybdate-polypyrrole composite bulk-modified carbon paste electrode for a hydrogen peroxide amperometric sensor. *Materials Letters* **2004**, *58* (10), 1661–1664. DOI: 10.1016/j.matlet.2003.10.044.

(197) Wang, J.; Han, D.; Wang, X.; Qi, B.; Zhao, M. Polyoxometalates as peroxidase mimetics and their applications in H₂O₂ and glucose detection. *Biosensors & bioelectronics* **2012**, *36* (1), 18–21. DOI: 10.1016/j.bios.2012.03.031. Published Online: Apr. 10, 2012.

(198) Salimi, A.; Korani, A.; Hallaj, R.; Khoshnavazi, R.; Hadadzadeh, H. Immobilization of Cu(bpy)2Br₂ complex onto a glassy carbon electrode modified with alpha-SiMo12O40(4-) and single

walled carbon nanotubes: application to nanomolar detection of hydrogen peroxide and bromate. *Analytica chimica acta* **2009**, *635* (1), 63–70. DOI: 10.1016/j.aca.2009.01.007. Published Online: Jan. 10, 2009.

(199) Zhang, B.; Zhao, M.; Qi, Y.; Tian, R.; Carter, B. B.; Zou, H.; Zhang, C.; Wang, C. The Intrinsic Enzyme Activities of the Classic Polyoxometalates. *Scientific reports* **2019**, *9* (1), 14832. DOI: 10.1038/s41598-019-50539-9. Published Online: Oct. 16, 2019.

(200) Yokuş, Ö. A.; Kardaş, F.; Akyıldırım, O.; Eren, T.; Atar, N.; Yola, M. L. Sensitive voltammetric sensor based on polyoxometalate/reduced graphene oxide nanomaterial: Application to the simultaneous determination of l-tyrosine and l-tryptophan. *Sensors and Actuators B: Chemical* **2016**, *233*, 47–54. DOI: 10.1016/j.snb.2016.04.050.

(201) Bruckschlegel, C.; Pasquier, C.; Toquer, G.; Girard, L.; Odorico, M.; Lautru, J.; Diat, O.; Bauduin, P. Toward Distinguishing between the Superchaotropic and Hydrophobic Characters of Nanometric-Sized Ions in Interaction with PEGylated Surfaces. *The journal of physical chemistry letters* **2024**, *15* (15), 4229–4236. DOI: 10.1021/acs.jpclett.4c00710. Published Online: Apr. 11, 2024.

(202) Delplanque, A.; Henry, E.; Lautru, J.; Leh, H.; Buckle, M.; Nogues, C. UV/ozone surface treatment increases hydrophilicity and enhances functionality of SU-8 photoresist polymer. *Applied Surface Science* **2014**, *314*, 280–285. DOI: 10.1016/j.apsusc.2014.06.053.

(203) Jaleh, B.; Parvin, P.; Wanichapichart, P.; Saffar, A. P.; Reyhani, A. Induced super hydrophilicity due to surface modification of polypropylene membrane treated by O₂ plasma. *Applied Surface Science* **2010**, *257* (5), 1655–1659. DOI: 10.1016/j.apsusc.2010.08.117.

(204) Buchecker, T.; Schmid, P.; Renaudineau, S.; Diat, O.; Proust, A.; Pfitzner, A.; Bauduin, P. Polyoxometalates in the Hofmeister series. *Chemical communications (Cambridge, England)* **2018**, *54* (15), 1833–1836. DOI: 10.1039/C7CC09113C.

(205) Marcus, Y. Effect of ions on the structure of water: structure making and breaking. *Chemical reviews* **2009**, *109* (3), 1346–1370. DOI: 10.1021/cr8003828.

(206) Assaf, K. I.; Nau, W. M. The Chaotropic Effect as an Assembly Motif in Chemistry. *Angewandte Chemie (International ed. in English)* **2018**, *57* (43), 13968–13981. DOI: 10.1002/anie.201804597. Published Online: Sep. 27, 2018.

(207) Yee, C.; Scotti, M.; Ulman, A.; White, H.; Rafailovich, M.; Sokolov, J. One-Phase Synthesis of Thiol-Functionalized Platinum Nanoparticles. *Langmuir : the ACS journal of surfaces and colloids* **1999**, *15* (13), 4314–4316. DOI: 10.1021/la9814283.

(208) Micheau, C.; Dedovets, D.; Bauduin, P.; Diat, O.; Girard, L. Nanoparticle foam flotation for caesium decontamination using a pH-sensitive surfactant. *Environ. Sci.: Nano* **2019**, *6* (5), 1576–1584. DOI: 10.1039/c9en00188c.

(209) Weinstock, I. A.; Schreiber, R. E.; Neumann, R. Dioxygen in Polyoxometalate Mediated Reactions. *Chemical reviews* **2018**, *118* (5), 2680–2717. DOI: 10.1021/acs.chemrev.7b00444. Published Online: Dec. 1, 2017.

(210) Wang, S.-S.; Yang, G.-Y. Recent advances in polyoxometalate-catalyzed reactions. *Chemical reviews* **2015**, *115* (11), 4893–4962. DOI: 10.1021/cr500390v. Published Online: May. 12, 2015.

(211) Dashtian, K.; Shahsavarifar, S.; Usman, M.; Joseph, Y.; Ganjali, M. R.; Yin, Z.; Rahimi-Nasrabadi, M. A comprehensive review on advances in polyoxometalate based materials for electrochemical water splitting. *Coordination Chemistry Reviews* **2024**, *504*, 215644. DOI: 10.1016/j.ccr.2023.215644.

(212) Rajeev, R.; Datta, R.; Varghese, A.; Sudhakar, Y. N.; George, L. Recent advances in bimetallic based nanostructures: Synthesis and electrochemical sensing applications. *Microchemical Journal* **2021**, *163*, 105910. DOI: 10.1016/j.microc.2020.105910.

(213) Mahshid, S. S.; Mahshid, S.; Dolati, A.; Ghorbani, M.; Yang, L.; Luo, S.; Cai, Q. Template-based electrodeposition of Pt/Ni nanowires and its catalytic activity towards glucose oxidation. *Electrochimica Acta* **2011**, *58*, 551–555. DOI: 10.1016/j.electacta.2011.09.083.

(214) Li, M.; Bo, X.; Mu, Z.; Zhang, Y.; Guo, L. Electrodeposition of nickel oxide and platinum nanoparticles on electrochemically reduced graphene oxide film as a nonenzymatic glucose sensor. *Sensors and Actuators B: Chemical* **2014**, *192*, 261–268. DOI: 10.1016/j.snb.2013.10.140.

(215) Sun, Y.; Yang, H.; Yu, X.; Meng, H.; Xu, X. A novel non-enzymatic amperometric glucose sensor based on a hollow Pt–Ni alloy nanotube array electrode with enhanced sensitivity. *RSC Adv.* **2015**, *5* (86), 70387–70394. DOI: 10.1039/C5RA13383A.

(216) Gao, H.; Xiao, F.; Ching, C. B.; Duan, H. One-step electrochemical synthesis of PtNi nanoparticle-graphene nanocomposites for nonenzymatic amperometric glucose detection. *ACS applied materials & interfaces* **2011**, *3* (8), 3049–3057. DOI: 10.1021/am200563f. Published Online: Jul. 18, 2011.

(217) Panda, A. K.; Keerthi, M.; Sakthivel, R.; Dhawan, U.; Liu, X.; Chung, R.-J. Biocompatible Electrochemical Sensor Based on Platinum-Nickel Alloy Nanoparticles for In Situ Monitoring of Hydrogen Sulfide in Breast Cancer Cells. *Nanomaterials (Basel, Switzerland)* **2022**, *12* (2). DOI: 10.3390/nano12020258. Published Online: Jan. 14, 2022.

(218) Panda, A. K.; Murugan, K.; Sakthivel, R.; Dhawan, U.; Lin, L.-Y.; Duann, Y.-F.; He, J.-H.; Chung, R.-J. A biocompatible electrochemical sensor based on PtNi alloy nanoparticles-coupled N-GQDs for in situ monitoring of dopamine in glioma cells. *Materials Today Chemistry* **2023**, *27*, 101283. DOI: 10.1016/j.mtchem.2022.101283.

(219) Liu, P.; Zhang, Y.; Ye, L.; Huang, M.; Zeng, T.; Yang, J.; Tian, F.; Wu, Z.; Zhang, X.; Hu, C.; Yang, N. Laser-induced graphene decorated with Ni Pt alloy nanoparticles for non-enzymatic electrochemical quantification of glucose. *Diamond and Related Materials* **2024**, *146*, 111205. DOI: 10.1016/j.diamond.2024.111205.

(220) Guan, H.; Zhao, Y.; Zhang, J.; Liu, Y.; Yuan, S.; Zhang, B. Uniformly dispersed PtNi alloy nanoparticles in porous N-doped carbon nanofibers with high selectivity and stability for hydrogen

peroxide detection. *Sensors and Actuators B: Chemical* **2018**, *261*, 354–363. DOI: 10.1016/j.snb.2018.01.169.

(221) Perju, A.; Holzhausen, F.; Lauerer, A.-M.; Wongkaew, N.; Baeumner, A. J. Flow-Through Carbon Nanofiber-Based Transducer for Inline Electrochemical Detection in Paper-Based Analytical Devices. *ACS applied materials & interfaces* **2023**, *15* (38), 44641–44653. DOI: 10.1021/acsami.3c07314. Published Online: Sep. 13, 2023.

(222) Abbasnia Tehrani, M.; Ahmadi, S. H.; Alimohammadi, S.; Sasanpour, P.; Batvani, N.; Kazemi, S. H.; Kiani, M. A. Continuous glucose monitoring using wearable non-enzymatic sensors in a physiological environment. *Biosensors and Bioelectronics: X* **2024**, *18*, 100482. DOI: 10.1016/j.biosx.2024.100482.

(223) Shirley, D. A. High-Resolution X-Ray Photoemission Spectrum of the Valence Bands of Gold. *Phys. Rev. B* **1972**, *5* (12), 4709–4714. DOI: 10.1103/PhysRevB.5.4709.

(224) Scofield, J. H. Hartree-Slater subshell photoionization cross-sections at 1254 and 1487 eV. *Journal of Electron Spectroscopy and Related Phenomena* **1976**, *8* (2), 129–137. DOI: 10.1016/0368-2048(76)80015-1.

(225) Regis, J.; Vargas, S.; Irigoyen, A.; Bramasco-Rivera, E.; Bañuelos, J. L.; Delfin, L. C.; Renteria, A.; Martinez, U.; Rockward, T.; Lin, Y. Near-UV light assisted green reduction of graphene oxide films through l-ascorbic acid. *International Journal of Smart and Nano Materials* **2021**, *12* (1), 20–35. DOI: 10.1080/19475411.2021.1887396.

(226) Sun, J.; Li, T.; Li, X.; Pan, J.; Hao, X.; Zhu, T. Investigation of the thermal stability of PtO₂ and dislocations in Pt wire. *Journal of Alloys and Compounds* **2020**, *831*, 154871. DOI: 10.1016/j.jallcom.2020.154871.

(227) Da Moreira Silva, C.; Girard, A.; Dufond, M.; Fossard, F.; Andrieux-Ledier, A.; Huc, V.; Loiseau, A. Nickel platinum (Ni x Pt_{1-x}) nanoalloy monodisperse particles without the core-shell structure by colloidal synthesis. *Nanoscale advances* **2020**, *2* (9), 3882–3889. DOI: 10.1039/D0NA00450B. Published Online: Jul. 9, 2020.

(228) Richardson, J. X-ray diffraction study of nickel oxide reduction by hydrogen. *Applied Catalysis A: General* **2003**, *246* (1), 137–150. DOI: 10.1016/S0926-860X(02)00669-5.

(229) Johra, F. T.; Lee, J.-W.; Jung, W.-G. Facile and safe graphene preparation on solution based platform. *Journal of Industrial and Engineering Chemistry* **2014**, *20* (5), 2883–2887. DOI: 10.1016/j.jiec.2013.11.022.

(230) Wei, G.; Yu, J.; Gu, M.; Tang, T. B. Dielectric relaxation and hopping conduction in reduced graphite oxide. *Journal of Applied Physics* **2016**, *119* (22). DOI: 10.1063/1.4953357.

(231) Chen, X.; Wang, X.; de Fang. A review on C1s XPS-spectra for some kinds of carbon materials. *Fullerenes, Nanotubes and Carbon Nanostructures* **2020**, *28* (12), 1048–1058. DOI: 10.1080/1536383X.2020.1794851.

(232) Rani, S.; Byron, C.; Teplyakov, A. V. Formation of silica-supported platinum nanoparticles as a function of preparation conditions and boron impregnation. *The Journal of chemical physics* **2020**, *152* (13), 134701. DOI: 10.1063/1.5142503.

(233) Chang, H.-W.; Tsai, Y.-C.; Cheng, C.-W.; Lin, C.-Y.; Wu, P.-H. Preparation of platinum/carbon nanotube in aqueous solution by femtosecond laser for non-enzymatic glucose determination. *Sensors and Actuators B: Chemical* **2013**, *183*, 34–39. DOI: 10.1016/j.snb.2013.03.115.

(234) Liu, W.; Chen, Q.; Huang, Y.; Wang, D.; Li, L.; Liu, Z. In situ laser synthesis of Pt nanoparticles embedded in graphene films for wearable strain sensors with ultra-high sensitivity and stability. *Carbon* **2022**, *190*, 245–254. DOI: 10.1016/j.carbon.2022.01.020.

(235) Jiménez-Pérez, R.; Agrisuelas, J.; Gomis-Berenguer, A.; Baeza-Romero, M. T.; Valero, E. One-pot electrodeposition of multilayered 3D PtNi/polymer nanocomposite. H₂O₂ determination in aerosol phase. *Electrochimica Acta* **2023**, *461*, 142683. DOI: 10.1016/j.electacta.2023.142683.

(236) Hu, T.; Li, P.; Zhang, W.; Ye, Y.; Liu, J.; Cai, Y.; Zhang, G.; Dai, K.; Liang, C. Laser irradiation induced platinum-based bimetallic alloy nanoparticles in liquids for electrocatalytic hydrogen production. *Journal of Alloys and Compounds* **2023**, *934*, 167914. DOI: 10.1016/j.jallcom.2022.167914.

(237) Saurel, D.; Segalini, J.; Jauregui, M.; Pendashteh, A.; Daffos, B.; Simon, P.; Casas-Cabanas, M. A SAXS outlook on disordered carbonaceous materials for electrochemical energy storage. *Energy Storage Materials* **2019**, *21*, 162–173. DOI: 10.1016/j.ensm.2019.05.007.

(238) Siburian, R.; Sihotang, H.; Lumban Raja, S.; Supeno, M.; Simanjuntak, C. New Route to Synthesize of Graphene Nano Sheets. *Orient. J. Chem* **2018**, *34* (1), 182–187. DOI: 10.13005/ojc/340120.

(239) Yasin, G.; Arif, M.; Shakeel, M.; Dun, Y.; Zuo, Y.; Khan, W. Q.; Tang, Y.; Khan, A.; Nadeem, M. Exploring the Nickel–Graphene Nanocomposite Coatings for Superior Corrosion Resistance: Manipulating the Effect of Deposition Current Density on its Morphology, Mechanical Properties, and Erosion-Corrosion Performance. *Adv Eng Mater* **2018**, *20* (7). DOI: 10.1002/adem.201701166.

(240) Li, R.; Deng, X.; Xia, L. Non-enzymatic sensor for determination of glucose based on PtNi nanoparticles decorated graphene. *Scientific reports* **2020**, *10* (1), 16788. DOI: 10.1038/s41598-020-73567-2. Published Online: Oct. 8, 2020.

(241) Shang, N. G.; Papakonstantinou, P.; McMullan, M.; Chu, M.; Stamboulis, A.; Potenza, A.; Dhesi, S. S.; Marchetto, H. Catalyst-Free Efficient Growth, Orientation and Biosensing Properties of Multilayer Graphene Nanoflake Films with Sharp Edge Planes. *Adv Funct Materials* **2008**, *18* (21), 3506–3514. DOI: 10.1002/adfm.200800951.

(242) Gaffney, E. M.; Lim, K.; Minteer, S. D. Breath biosensing: using electrochemical enzymatic sensors for detection of biomarkers in human breath. *Current Opinion in Electrochemistry* **2020**, *23*, 26–30. DOI: 10.1016/j.coelec.2020.02.014.

(243) Jadhav, M. R.; Wankhede, P. R.; Srivastava, S.; Bhargaw, H. N.; Singh, S. Breath-based biosensors and system development for noninvasive detection of diabetes: A review. *Diabetes & metabolic syndrome* **2024**, *18* (1), 102931. DOI: 10.1016/j.dsx.2023.102931. Published Online: Dec. 20, 2023.

(244) Karyakin, A. A.; Nikulina, S. V.; Vokhmyanina, D. V.; Karyakina, E. E.; Anaev, E. K.; Chuchalin, A. G. Non-invasive monitoring of diabetes through analysis of the exhaled breath condensate (aerosol). *Electrochemistry Communications* **2017**, *83*, 81–84. DOI: 10.1016/j.elecom.2017.09.005.

(245) Vasilescu, A.; Hrinczenko, B.; Swain, G. M.; Peteu, S. F. Exhaled breath biomarker sensing. *Biosensors & bioelectronics* **2021**, *182*, 113193. DOI: 10.1016/j.bios.2021.113193. Published Online: Mar. 26, 2021.

(246) Ligor, T. Analytical Methods for Breath Investigation. *Critical Reviews in Analytical Chemistry* **2009**, *39* (1), 2–12. DOI: 10.1080/10408340802569498.

(247) Adabi, M.; Adabi, M. Electrodeposition of nickel on electrospun carbon nanofiber mat electrode for electrochemical sensing of glucose. *Journal of Dispersion Science and Technology* **2021**, *42* (2), 262–269. DOI: 10.1080/01932691.2019.1678483.

(248) Wei, M.; Qiao, Y.; Zhao, H.; Liang, J.; Li, T.; Luo, Y.; Lu, S.; Shi, X.; Lu, W.; Sun, X. Electrochemical non-enzymatic glucose sensors: recent progress and perspectives. *Chemical communications (Cambridge, England)* **2020**, *56* (93), 14553–14569. DOI: 10.1039/D0CC05650B. Published Online: Oct. 29, 2020.

(249) Jahromi, Z.; Mirzaei, E.; Savardashtaki, A.; Afzali, M.; Afzali, Z. A rapid and selective electrochemical sensor based on electrospun carbon nanofibers for tramadol detection. *Microchemical Journal* **2020**, *157*, 104942. DOI: 10.1016/j.microc.2020.104942.

(250) Huan, K.; Li, Y.; Deng, D.; Wang, H.; Wang, D.; Li, M.; Luo, L. Composite-controlled electrospinning of CuSn bimetallic nanoparticles/carbon nanofibers for electrochemical glucose sensor. *Applied Surface Science* **2022**, *573*, 151528. DOI: 10.1016/j.apsusc.2021.151528.

(251) Bukhari, Q. U. A.; Della Pelle, F.; Alvarez-Diduk, R.; Scroccarello, A.; Nogués, C.; Careta, O.; Compagnone, D.; Merkoci, A. Laser-assembled conductive 3D nanozyme film-based nitrocellulose sensor for real-time detection of H₂O₂ released from cancer cells. *Biosensors & bioelectronics* **2024**, *262*, 116544. DOI: 10.1016/j.bios.2024.116544. Published Online: Jun. 29, 2024.

(252) Pidal, J. M. G.; Fiori, S.; Scroccarello, A.; Della Pelle, F.; Maggio, F.; Serio, A.; Ferraro, G.; Escarpa, A.; Compagnone, D. Laser-induced 2D/0D graphene-nanoceria freestanding paper-based films for on-site hydrogen peroxide monitoring in no-touch disinfection treatments. *Microchim Acta* **2024**, *191* (6), 361. DOI: 10.1007/s00604-024-06427-9. Published Online: Jun. 1, 2024.

(253) Della Pelle, F.; Bukhari, Q. U. A.; Alvarez Diduk, R.; Scroccarello, A.; Compagnone, D.; Merkoçi, A. Freestanding laser-induced two dimensional heterostructures for self-contained paper-

based sensors. *Nanoscale* **2023**, *15* (15), 7164–7175. DOI: 10.1039/D2NR07157F. Published Online: Apr. 13, 2023.

(254) Silveri, F.; Scroccarello, A.; Della Pelle, F.; Del Carlo, M.; Compagnone, D. Rapid pretreatment-free evaluation of antioxidant capacity in extra virgin olive oil using a laser-nanodecorated electrochemical lab-on-strip. *Food Chemistry* **2023**, *420*, 136112. DOI: 10.1016/j.foodchem.2023.136112. Published Online: Apr. 8, 2023.

(255) Franceschini, F.; Taurino, I. Nickel-based catalysts for non-enzymatic electrochemical sensing of glucose: A review. *Physics in Medicine* **2022**, *14*, 100054. DOI: 10.1016/j.phmed.2022.100054.

(256) Chen, X.; He, X.; Gao, J.; Jiang, J.; Jiang, X.; Wu, C. Three-dimensional porous Ni, N-codoped C networks for highly sensitive and selective non-enzymatic glucose sensing. *Sensors and Actuators B: Chemical* **2019**, *299*, 126945. DOI: 10.1016/j.snb.2019.126945.

(257) Liu, H.; Wu, X.; Yang, B.; Li, Z.; Lei, L.; Zhang, X. Three-Dimensional Porous NiO Nanosheets Vertically Grown on Graphite Disks for Enhanced Performance Non-enzymatic Glucose Sensor. *Electrochimica Acta* **2015**, *174*, 745–752. DOI: 10.1016/j.electacta.2015.06.062.

(258) Liu, Q.; Zhong, H.; Chen, M.; Zhao, C.; Liu, Y.; Xi, F.; Luo, T. Functional nanostructure-loaded three-dimensional graphene foam as a non-enzymatic electrochemical sensor for reagentless glucose detection. *RSC Adv.* **2020**, *10* (56), 33739–33746. DOI: 10.1039/d0ra05553k. Published Online: Sep. 11, 2020.

(259) Meng, A.; Yuan, X.; Li, Z.; Zhao, K.; Sheng, L.; Li, Q. Direct growth of 3D porous (Ni-Co)3S4 nanosheets arrays on rGO-PEDOT hybrid film for high performance non-enzymatic glucose sensing. *Sensors and Actuators B: Chemical* **2019**, *291*, 9–16. DOI: 10.1016/j.snb.2019.04.042.

(260) Wang, F.; Feng, Y.; He, S.; Wang, L.; Guo, M.; Cao, Y.; Wang, Y.; Yu, Y. Nickel nanoparticles-loaded three-dimensional porous magnetic graphene-like material for non-enzymatic glucose sensing. *Microchemical Journal* **2020**, *155*, 104748. DOI: 10.1016/j.microc.2020.104748.

(261) Shackery, I.; Patil, U.; Pezeshki, A.; Shinde, N. M.; Kang, S.; Im, S.; Jun, S. C. Copper Hydroxide Nanorods Decorated Porous Graphene Foam Electrodes for Non-enzymatic Glucose Sensing. *Electrochimica Acta* **2016**, *191*, 954–961. DOI: 10.1016/j.electacta.2016.01.047.

(262) Cheshideh, H.; Nasirpour, F. Cyclic voltammetry deposition of nickel nanoparticles on TiO₂ nanotubes and their enhanced properties for electro-oxidation of methanol. *Journal of Electroanalytical Chemistry* **2017**, *797*, 121–133. DOI: 10.1016/j.jelechem.2017.05.024.

(263) Jayashree, R. S.; Kamath, P. Nickel hydroxide electrodeposition from nickel nitrate solutions: mechanistic studies. *Journal of Power Sources* **2001**, *93* (1-2), 273–278. DOI: 10.1016/S0378-7753(00)00568-1.

(264) Bagheri, A. R.; Aramesh, N.; Chen, J.; Liu, W.; Shen, W.; Tang, S.; Lee, H. K. Polyoxometalate-based materials in extraction, and electrochemical and optical detection methods: A review. *Analytica chimica acta* **2022**, *1209*, 339509. DOI: 10.1016/j.aca.2022.339509. Published Online: Jan. 18, 2022.

(265) Puetz, P.; Behrent, A.; Baeumner, A. J.; Wegener, J. Laser-scribed graphene (LSG) as new electrode material for impedance-based cellular assays. *Sensors and Actuators B: Chemical* **2020**, *321*, 128443. DOI: 10.1016/j.snb.2020.128443.

Curriculum Vitae

Personal Data

Name	Christoph Johannes Bruckschlegel
Address	Sinzenhoferstraße 14, 93142 Maxhütte-Haidhof
Date of birth	22.08.1997
Place of birth	Burglengenfeld
Nationality	German

School & Academic Education

12/2021 – 11/2024	Ph.D. studies “Developing Novel Functional Laser-Induced Carbon Nanofibers for Miniaturized Electroanalytical Biosensors”. University of Regensburg (Institute of Analytical Chemistry, Chemo- and Biosensors)
10/2021 – 11/2021	Research assistant. University of Regensburg (Institute of Analytical Chemistry, Chemo- and Biosensors)
10/2019 – 9/2021	Master of Science Complex Condensed Materials and Soft Matter (COSOM) University of Regensburg
2/2021 – 7/2021	Master thesis ”Origin of the superchaotropic effect of nano-ions investigated by QCM”. Institut de Chimie Séparative de Marcoule (ICSM)
10/2016 – 9/2019	Bachelor of Science Chemistry University of Regensburg
9/2004 – 7/2016	Elementary school in Maxhütte-Haidhof & grammar school (JMF-Gymnasium) in Burglengenfeld.

Scholarships

2021	Erasmus, BayFrance (Starter Kit)
2022-2024	BayFrance (cooperation in teaching and research)
2024	DAAD funding for Pittcon

Conferences and Externals Stays During Ph.D.

21-24 Jun. 2022	Analytica, Munich, poster presentation.
3-19 Mar. 2023	Research stay, ICSM (France), SAXS measurements to characterize electrode materials and investigate liposomes.
27-30 Aug. 2023	European BioSensor Symposium, Aachen, poster presentation.
27-29 Sep. 2023	Fraunhofer Institute for Cell Therapy and Immunology, Branch Bioanalytics and Bioprocesses IZI-BB, Potsdam, poster presentation.
2-10 Feb. 2024	Research stay, ICSM (France), SAXS measurements (electrode material, liposomes and hydrogels).
24-28 Feb. 2024	Pittcon, San Diego, oral research presentation.
2-10 Aug. 2024	Research stay, ICSM (France), SAXS measurements (liposomes and hydrogels), development of an electrochemical sensor prototype for measurements in foam during flotation.
30 Sep.-2 Oct. 2024	Fraunhofer Institute for Cell Therapy and Immunology, Branch Bioanalytics and Bioprocesses IZI-BB, Potsdam, seminars

Additional Working Experience

Jul. - Sep. 2016	BMW (Randstad, Regensburg): Shift work in assembly.
Feb. - Oct. 2024	Sofatutor: Freelance writer for learning texts.
Since Aug. 2024	Springer Nature: Assistant Editor.

Publications

Bruckschlegel et al., Investigating nanocatalyst-embedding laser-induced carbon nanofibers for non-enzymatic electrochemical sensing of hydrogen peroxide. <i>Analytical And Bioanalytical Chemistry</i> , 2023 , 415(18), 4487–4499.
Bruckschlegel et al., Toward Distinguishing between the Superchaotropic and Hydrophobic Characters of Nanometric-Sized Ions in Interaction with PEGylated Surfaces. <i>The Journal of Physical Chemistry Letters</i> , 2024 , 4229–4236.
Research paper submitted: “Laser generated Pt/Ni nanocatalysts-carbon nanofibers enabling ratiometric enzyme-free glucose detection at physiological pH” (First Author).
Research paper in preparation: “Laser-induced carbon nanofibers as a permeable non-enzymatic electrode for development of biomarker detection in breath aerosol”(Co-authored, equal contribution)
Review in preparation: “Non-enzymatic electrochemical sensors for point-of-care testing: Current status, challenges, and future prospects” (First Author).

Eidesstattliche Erklärung

(1) Ich erkläre hiermit an Eides statt, dass ich die vorliegende Arbeit ohne unzulässige Hilfe Dritter und ohne Benutzung anderer als der angegebenen Hilfsmittel angefertigt habe; die aus anderen Quellen direkt oder indirekt übernommenen Daten und Konzepte sind unter Angabe des Literaturzitats gekennzeichnet.

(2) Bei der Auswahl und Auswertung des in „Declaration of Collaborations“ aufgeführten Materials haben mir die aufgeführten Personen in der jeweils beschriebenen Weise entgeltlich/unentgeltlich geholfen.

(3) Weitere Personen waren an der inhaltlich-materiellen Herstellung der vorliegenden Arbeit nicht beteiligt. Insbesondere habe ich hierfür nicht die entgeltliche Hilfe eines Promotionsberaters oder anderer Personen in Anspruch genommen. Niemand hat von mir weder unmittelbar noch mittelbar geldwerte Leistungen für Arbeiten erhalten, die im Zusammenhang mit dem Inhalt der vorgelegten Dissertation stehen.

(4) Die Arbeit wurde bisher weder im In- noch im Ausland in gleicher oder ähnlicher Form einer anderen Prüfungsbehörde vorgelegt.

Ort, Datum

Unterschrift